Assessment of Plasma Sprayed Coatings to Modify Surface Friction for Railroad Applications

Heidi Lynn Davis

B.S., University of Washington
Seattle, Washington, 1992

A dissertation submitted to the faculty of the
OGI School of Science & Engineering
Oregon Health & Science University
in partial fulfillment of the
requirements for the degree
Doctor of Philosophy
in
Materials Science and Engineering

June 2002

The dissertation "Assessment of Plasma Sprayed Coatings to Modify Surface Friction for Railroad Applications" by Heidi Lynn Davis has been examined and approved by the following Examination Committee:

Paul Clayton (Posthumous)
Professor and Thesis Advisor

Milton Scholl
Associate Professor and Thesis Advisor

David G. Atteridge
Adjunct Professor
Columbia Basin College

Lemmy L. Meekisho
Associate Professor
Portland State University

Daniel Danks
Consultant
Danks Tribological Services

ACKNOWLEDGEMENTS

First I would like to thank my thesis advisors, Dr. Paul Clayton and Dr. Milton Scholl, for their extraordinary patience and support in helping to complete this work. When Paul became Provost at OGI, leaving the day-to-day operations of the project behind, Milt took over the job of helping direct my research. I appreciate all the work he and Paul have done on my behalf over the past several years.

Next, I would like to express my appreciation for the tireless efforts of Dr. David Atteridge. He has been a wonderful resource, both professionally and personally, during my time at OGI. Dave kept me on track when I started to derail (pun intended). I also thank Dr. Lemmy Meekisho and Dr. Daniel Danks for providing valuable feedback on the completion of this manuscript.

I am extremely grateful to the Association of American Railroads for providing the funding, materials and testing facilities that enabled this research to be completed.

And finally, a special thanks goes to my family, friends and colleagues: my parents, who provided a safe place from which to explore the world, Tom van Laak, who started "the whole ball of wax" and to whom I am eternally grateful, Jessie Atteridge, my Mom-away-from-home, Eileen Brown, whose friendship has grounded me in what's important in life, Graham Tewksbury, who provided the extra push to the finish line, and most importantly, to Vivek Dixit, who has believed always.

Dedicated to the memory of Paul Clayton

TABLE OF CONTENTS

LIST OF TABLES

LIST OF FIGURES

ABSTRACT

For the past hundred years, railroads have been an important means of transportation for passengers and freight. Over the years train traffic, speeds, and loads have increased steadily leading to a more severe wheel/rail environment that exceeds the design limits of the steels thus causing increased wear, decreased rail life, and higher maintenance costs. The cost of controlling friction and the resulting damage is an area of ever-increasing concern. One potential method of modifying friction is by changing the surface properties of the rail. The work reported herein was carried out as part of a larger effort to modify surface friction of rails.

The original focus of this research was to use high velocity air plasma spraying to develop friction enhancing coatings for the rail surface. Using the methodology developed at the Oregon Graduate Institute, the plasma spray parameters were optimized and the coatings were tested on the Amsler machine under rolling/sliding wear conditions to determine viability prior to full scale testing. Stainless steel and composite 1080 steel were investigated as potential materials for increasing friction. Poor results with these coatings shifted the research focus to understanding the durability of the coatings and to failure analysis of initial 1080 steel full scale samples tested by the Facility for Accelerated Service Testing that had failed prematurely. After re-optimization of parameters and preparation methodologies further full scale samples (1080 steel/nylon) were tested and failure analysis was performed. Optical and scanning electron microscopy were used to evaluate the microstructure of coatings from the tested samples.

The laboratory scale Amsler test did not appear to be a good indicator of the performance of the coating in full scale tests, because variations in microstructure were caused by differences in sample size, geometry and spraying methods when scaling up from a small Amsler roller to a large rail sample. The damage in tested Amsler rollers and full scale test samples included coating delamination, substrate/coating debonding, oxide and metal lamellae cracking and surface deformation. The presence of a nylon coating layer on Amsler rollers increased coating durability, however, the results were inconclusive for full scale tests.

CHAPTER 1

INTRODUCTION AND BACKGROUND

1.1 INTRODUCTION

For the past hundred years railroads have been an important means of transportation for passengers and freight. While rail travel has given way to air travel as the preferred method of transportation for people, the demand for rail transportation of goods has steadily risen. To make rail transportation more economical, axle loads have become heavier allowing more goods to be transported [1-5]. Train traffic and speeds have increased as well, making the wheel/rail environment more severe than it was originally intended [6, 7]. As a consequence, the design limits of the steel have been exceeded leading to increased wear, decreased rail life, and higher line maintenance costs [3].

1.1.1 Improving Rail Performance

Since the beginning, the railroad industry has continually sought to improve rail quality and to obtain longer lasting, lower maintenance rails. Upgrading materials by changing the type of material was one way of improving rail quality. The first metal rails, made of cast and wrought iron, were replaced by Bessemer steel in the middle of the nineteen century [8-11]. More recently, the chemistry of the rail material was changed to improve the quality. Alloying elements, such as chromium, molybdenum, vanadium and silicon, were added to improve microstructural characteristics [9, 12]. In addition, advances in steelmaking and rail processing, such as vacuum degassing,

continuous casting, and in-line head hardening, have improved material properties by producing cleaner, more homogenous microstructures [9]. Advances in materials testing methods, both laboratory and full scale, and development of rail characterization methods have led to more uniform rail properties [13]. The use of profile grinding extends rail life greatly when it is tailored to the specific conditions the rail is normally subjected to, i.e., track curvature, track quality, tonnage [6, 14, 15]. These changes have improved the overall quality of the rails and enabled them to better withstand the more severe service conditions of the modern railroad.

1.1.2 Rail Environment

The environment that rails encounter is a very aggressive one for any material. Weather conditions are extreme and temperatures range from very hot to very cold [16]. Loading conditions are also extreme and include both normal and impact loading. Impact loading occurs as cars bounce up and down along the track as a result of the height misalignments of the track and wheel flats. The heavy loads seen by the rails contribute to high contact stresses that cause deformation to occur. It has been estimated that loads can exceed 1600 MPa in the area of contact between the wheel and rail [17, 18].

Of the two types of track, tangent (straight) and curved, loading conditions found in tangent track are generally less severe. In tangent track, ideally, the wheel contacts the center of the rail head and the stresses are distributed through the head, web and base to the supporting track structure [6]. The main damage modes found in tangent track are the result of long term accumulation of damage such as rolling contact fatigue, rail head wear, and corrugations [19].

As shown in Figure 1.1.2.1, in curved track, the outside rail or high rail, is elevated above the inside, or low rail. The inside face of the high rail is called the gage face, which usually experiences the most severe loading conditions due to a number of

factors. In curves, and to a lesser degree in tangent track, track misalignment and axle rigidity lead to hunting of the cars, which is the continual back and forth lateral oscillation motion as the axles hunt for the correct tracking position [20, 21]. As a result of hunting, the wheel flange rubs against the gage face leading to not only wear and increased resistance to rolling, but also to lateral scraping of the gage face and sideways impact loading.

Different types of wear may occur depending on the location on the rail [22]. In tangent track, on the top surface of the rail, rolling wear occurs. During starting and stopping of the train, sliding wear, which is more severe than rolling wear, can also occur due to inertia of the locomotive and cars. In curves, sliding wear occurs on the gage face of the high rail along with a combination of rolling and sliding wear occurring on the top of both of the rails.

1.1.3 Methods of Controlling Friction

While other aspects of rail technology have advanced to meet the increasing demands put on the rails, methods of controlling friction have changed little over the years. Lubrication is the common method used to reduce friction between the rail gage face and the wheel flange. The level of friction can vary widely depending on the condition of the rail. The dry rail coefficient of friction assumed typical by Sawley et al. [18] in their study of hollow worn wheels was 0.45. In lubricated tests, Clayton et al. [23] found the coefficient of friction to be 0.11 ± 0.02 for a variety of lubricants using the Amsler twin disk testing machine, while Beret et al. [24] found similar results, 0.107 to 0.145, for various greases using a tribometer. With proper lubrication, not only is friction reduced, but so is gage face wear, by a factor of 5 ranging up to 100 in some conditions [25]. Another benefit of lubrication is reduced rolling resistance, and subsequently reduced fuel consumption [26].

Of the two methods used to lubricate rails, trackside lubricators are the most common. Trackside lubricators, which have been used for over 60 years, apply grease to the flanges and are activated by the passing wheels of the train [24]. Trackside lubricators are used on curves although curve lubrication is not always effective and reliable, even when properly maintained.

The other type of lubricator, developed in the 1980's, is the on-board lubricator, which is mounted outside the rail car. The lubricant is sprayed onto the wheel flanges, transferred to the gage face of the rail and then carried on down the track [26]. These types of lubricators can be used on both curved and tangent track but are not as effective in curves as the trackside lubricators.

As mentioned previously, trackside and on-board lubricators are not always effective methods of lubrication. Rails experience wide extremes in temperature and a variety of weather conditions. In cold conditions, the lubricants can become too thick to pump and nozzles can become plugged. In hot conditions, grease can become too thin to stick to the rails. Rain and snow can be problems by washing the grease off the track. Lubricators located in remote locations of track are difficult to service properly. Compatibility between the greases used in the two different types of lubricators can also be a problem. Other problems can occur when the grease migrates to the top of the rail where it reduces traction and the ability to brake. Environmental concerns from the grease dripping off the track is an important consideration since grease consumption in the early 1990's was at 1800 metric tons and expected to rise to 4,500 metric tons by the end of the decade [24].

1.1.4 Cost of Friction and Wear

The cost of controlling friction, and the subsequent damage caused by it, can be high. Lubrication costs an estimated $1,250/kilometer and for lubricating curves of greater than three degrees, it takes an estimated $14 million yearly [27]. Replacement of worn rail in curved track costs approximately $180 million yearly [27]. In addition, derailments caused by poor curve lubrication result in the loss of $4 million yearly [27]. Another benefit of lubrication is lower fuel costs. An estimated $2 billion in diesel fuel is consumed by Class I railroads yearly [27]. Lubrication of the wheel flange lowers fuel usage by 5 to 15% [24].

1.1.5 Surface Engineering

Surface engineering techniques change the surface properties of a material or component while leaving the bulk material in its original state. Surface enhancing materials can be applied to specific sites on a surface leaving adjacent areas unaffected. In some cases, the materials used to enhance surface properties are more expensive than the bulk material. It may not be economical, or even desirable, to make the entire component of the special materials. A wide range of surface engineering methods exists, Figure 1.1.5.1, their use depending on the application. The two basic categories of surface engineering are surface treatments and coating processes. Examples of surface treatments are nitriding or carburising while coating processes include chemical vapor deposition and evaporation.

Surface engineering techniques were targeted as a way of controlling friction at the wheel/rail interface. The materials applied to the surface needed to provide friction levels below those found normally between the gage face and wheel flange in curves. Also important was increasing friction on the top of the low rail in curves to help prevent low rail rollover. Several factors were important to consider when choosing a surface

engineering method to meet these requirements. Modifying the surface of existing track necessitated a method that was portable and able to be performed in the field. A high deposition rate was needed and the ability to produce coatings of a millimeter or more of thickness. Also the ability to put down different types of materials in varying forms was important. The method must not adversely affect the rail substrate during processing.

Hyper-velocity air plasma spraying was the method deemed to fulfill these requirements. With this method, a wide range of materials could be sprayed including metals, ceramics, and polymers as well as multiple feedstocks like wire or powder. The deposition parameters were widely variable and flexible, and, most important, the method had the potential to be used from a high-rail vehicle.

1.1.6 Evaluating Coating Performance

To assess the effectiveness of the surface modification technique chosen for this project, a methodology was required to evaluate the coatings. The methodology needed to evaluate the coatings under conditions similar to those found in the rail environment. Ideally, running the tests on rails under service conditions would have been the most relevant, however, this was not practical for the following reasons. Service scale testing is extremely expensive and time-consuming, and, if failures occur, extremely hazardous. Interactions between the multiple variables affecting performance make it next to impossible to determine the influence of individual variables. Service scale tests would have also required development of the high-rail vehicle plasma spraying equipment in advance without an understanding of the spraying parameters and coating requirements.

The next best alternative would be have been to test the coatings in a full scale rail test facility such as the Facility for Accelerated Service Testing (FAST). However, tests performed at FAST are also expensive and the variables are not easily controlled. Furthermore FAST is designed for evaluating selected materials that exhibit high

potential for success, not for developmental and feasibility studies for new materials. Due to these limitations, it was not practical to conduct multiple tests at FAST without prior laboratory assessment.

While laboratory scale test methods were less expensive and more practical compared to the above alternatives, other pitfalls existed. The rail wear environment is difficult to simulate in laboratory scale tests. Only one aspect or damage mode at a time (i.e., wear or rolling contact fatigue) can be simulated and the test conditions are rarely as severe as those found under actual rail conditions. Despite the problems the most reasonable laboratory test available for assessment of wear damage was the Amsler test, a twin disk laboratory scale test machine that could be used to simulate dry or lubricated rolling/sliding wear, rolling contact fatigue, and deformation.

The Amsler test has been successfully used at the Oregon Graduate Institute of Science and Technology (OGI) for over a decade to assess rail materials and to understand the failure mechanisms observed in rails [28-31]. Various research projects at OGI have shown excellent correlations in the failure mechanisms and the relative performance of various steels between the Amsler test and rails in service under rolling/sliding wear and rolling contact fatigue conditions. However, all these results refer to tests carried out on solid steel materials, not coatings.

Research into the Amsler testing of coatings began with the work of McMurchie [32] and his development of a plain carbon 1080 steel coating that was to act as a lubricant reservoir. The work performed by McMurchie [32], and later continued by Niebuhr [33], laid the foundations in establishing the Amsler test parameters to test plasma spray coatings in the laboratory. McMurchie [32] found that the plasma spray coatings could indeed be tested in the manner of solid steel coatings as long as debonding from edge effects could be controlled. One of the goals of the work reported here was to correlate Amsler test results to service scale testing at FAST.

1.1.7 Project Goals and Background

The current research for a better alternative to conventional wheel/rail lubrication methods began in the early 1990's with the start of the "Friction Modification" research project at OGI and sponsored by the Association of American Railroads (AAR). The multi-year project, under the direction of Dr. Paul Clayton, sought to develop new approaches to replace, or be combined with, existing trackside and on-board lubrication methods [34, 35]. Finding materials that could be applied to a rail using surface modification technology, and that would modify the frictional characteristics of the surface, was necessary.

The ultimate goal of the "Friction Modification" research project was to use plasma sprayed coatings to control the friction level between the wheel and the rail. An important aspect of the project was to develop coatings that would reduce friction along the rail gage face and thereby reduce wear. Another important aspect was to investigate methods for improving traction on the rail top to prevent low rail rollovers. The focus of the research project was divided into four areas:

1. to produce steel coatings with a rough surface to act as a lubricant reservoir,
2. to develop friction reducing coatings containing Cu or graphite,
3. to develop friction reducing coatings containing polymeric materials deposited on top of steel coatings and
4. to develop friction increasing coatings using pure Ti or stainless steel, either alone or as part of a steel composite coating.

The general guidelines, based on economic considerations, assumed a friction reducing coating would be considered successful if it achieved a coefficient of friction ranging from 0.05 to 0.15. For a friction increasing coating, the coefficient of friction would be successful if the range was between 0.25 and 0.5. All coatings needed to meet the minimum durability of 10 MGT (700 trains of 100 cars) but the preferred durability was 25 MGT (1700 trains of 100 cars). Durability was considered the interval between when the coating was applied and when the friction exceeded 0.25 for friction reducing coatings and went below 0.20 for friction increasing coatings.

In order to meet the project goals, the technology had to be developed to produce metal, polymer and composite coatings that would be able to withstand the conditions encountered in the rail environment. The research spanned the work of several students and to date has produced two other doctoral theses [32, 33]. While these other theses dealt with controlling the frictional properties by decreasing them, the laboratory work reported herein was oriented towards increasing friction. A detailed assessment of the coatings applied to full scale rail tests is also reported. Both friction increasing and friction decreasing coatings were assessed in this phase of the study. The work reported in this document is the culmination of the "Friction Modification" research project.

1.2 BACKGROUND

The body of the Background is broken down into several sections. It contains a discussion of generic friction and wear, materials for friction control, and plasma spray coating technology. Next, coating characteristics are described and characterization criteria for evaluating the plasma sprayed coatings are discussed.

1.2.1 Friction and Wear

Friction is defined as the resistance to tangential motion between two solid surfaces [36, 37]. The motion can be rolling, rubbing, or sliding contact [37]. A simple case of friction can be shown by Figure 1.2.1.1 in which an object with a normal force P is placed upon a surface and loaded with tangential force F. The force opposing motion of the block is the frictional force. There are two situations that can exist. In the case of static friction, the tangential force, F, is less than or equal to the normal force so that the block remains stationary. In the case of dynamic friction, the tangential force is greater than the normal force and the block moves. The coefficient of friction is given by the limiting tangential force divided by the normal force [36].

Friction between two objects is related to the nature of their surfaces. Surfaces in the real world are not smooth; they are rough and contain irregularities. Surface roughness can be visible to the eye in the form of scratches, pits, or dimples. In addition, there exist surface features, called asperities, which are only visible at high magnification under the microscope. Typically, the angle of the asperity with the surface is between 3 to 20 degrees [38]. Figure 1.2.1.2 shows an exaggerated picture of surface asperities. The surfaces of the asperities have superimposed on them roughness features called asperities of the second or higher orders.

When two surfaces move against each other, the asperities interlock, Figure 1.2.1.3 [38]. For motion to occur, several things may happen. The asperities may either be moved up, over, and past each other, they may deform plastically, or they may fracture. The asperities may also adhere together and form junctions as shown in Figure 1.2.1.4. For motion to occur, either the junction strength must be overcome or one of the materials must fracture. However, surface roughness and the interactions of asperities cannot completely explain the measured friction forces alone, since a wide range of variables influence friction behavior [39-41].

1.2.2 Surface Film Formation

Most practical wear applications occur in conditions where surface films are present to some degree [36]. The films present on a typical metal surface are shown in Figure 1.2.2.1. Very clean surfaces can be maintained only under high vacuum at 10^{-10} torr; at 10^{-6} torr species begin to adsorb onto the surface once again [37]. Clean surfaces are highly reactive and energetic causing them to be unstable. There are three common types of reactions on clean surfaces: physical adsorption, chemisorption, and oxidation.

Physical adsorption is a relatively weak process that typically involves van der Waal forces. Figure 1.2.2.2 (a) shows this process. It can take place at any temperature and on all types of surfaces. The adsorbing species can be present as a single layer or as multiple layers on the surface. Gases are a typical example of physically adsorbing species [37]. Oxygen, argon, sulfur, water, and carbon monoxide are common adsorbed species of this type. It takes little energy to remove physically adsorbed species.

Chemisorption is a process that involves the sharing or exchange of electrons as shown in Figure 1.2.2.2 (b). Chemical bonding occurs between the surface and the adsorbing species, but the species retains its own identity and can be removed [37, 42]. A great deal of energy is required to remove the adsorbate, the amount of which is a function of the species and the surface [37]. Chemisorption is a monolayer process that requires a specific activation energy and is dependent on the purity of the surface [42]. After the monolayer forms, further adsorption may occur by physical or chemical reaction.

Chemical reaction is a process where absorbed species react with the surface to form chemical compounds, Figure 1.2.2.2 (c). For the surface and the species to react, the temperature and the concentration have to be greater than a critical value. Chemical reaction is always preceded by chemisorption [42]. The absorbed species cannot usually

be recovered once the chemical reaction takes place [37]. A common example of a chemical reaction process is the formation of oxides. With iron, one or more of three compounds of the oxide can be formed, FeO, Fe_2O_3, and Fe_3O_4, each having a different coefficient of friction.

1.2.3 Wear Processes

Wear is defined as the progressive loss of material from the surface of a body as a result of relative motion at the surface [43]. The three main types of wear that are of interest for this project are adhesive wear, abrasive wear and fatigue wear. Other types of wear include corrosive, cavitation, and erosive wear. In many cases the differences between the various types of wear are hard to distinguish and may all be acting simultaneously [38].

In adhesive wear surface damage is caused by the transfer of material back and forth between the surfaces. The resulting surfaces are extremely rough and contain voids, cavities, pits, and valleys. In adhesive wear, asperities of one surface plow the surface film on another, break through the film, and expose new surfaces [37, 38]. If the film cannot repair itself, metal-to-metal contact can occur. This exposed metal is very reactive and interacts with the other surface [37]. Junctions can occur between the two surfaces by cold welding and further sliding or rolling motion causes the junction to be destroyed [38].

The junctions formed in adhesive wear can be destroyed in several ways [36]. If the junction is weaker than both the materials, the interface separates and little wear occurs. If the junction is stronger than one or both of the materials, then the weakest material will fracture and the particle will adhere to the strongest material, Figure 1.2.3.1. More material may adhere to the particle until it reaches a size where it can break loose from the surface. At this point it may adhere back onto the original surface, and then

transfer back and forth causing material loss from both surfaces. Build-up of transferred material can lead to increases in friction. Particles that become work hardened can embed into one surface, and, if they are sharp and at the proper angle, can plow the other surface exposing fresh new material thus continuing the adhesive wear process.

Abrasive wear is another type of wear that is often found in practical tribological operations [37]. It occurs from the removal of material by hard asperities or particles caught between two surfaces, Figure 1.2.3.2 [37]. The amount of abrasive wear that occurs between surfaces depends on the particle shape, size, and orientation. Other factors that contribute to the amount of wear are the load, hardness, and sliding distance [43]. Low penetration by a particle causes less damage than greater penetration that causes plowing. The plowing action displaces material that in turn can become wear particles, especially if the material has low ductility. The wear particles that are formed can become blunt or dull thus causing less wear damage than particles that fracture and remain sharp.

Fatigue wear occurs with surfaces subject to repeated and high stresses [43]. When a part is loaded the surface is in compression, but below the surface the material is in shear causing microcracks to form, usually at a defect or an inclusion. Repeated loading causes the cracks to grow and form networks until they reach a critical size. At this point the cracks turn upward to the surface and flat sheet-like wear particles are created [38, 44]. Fatigue cracks can also be initiated at surface defects. The cracks propagate down into the material, form networks and when returning to the surface cause large wear particles, or spalling [38].

1.2.4 Wear Reduction Control

One way of reducing wear between two surfaces is by adding a lubricant film that reduces the coefficient of friction [37]. The lubricant acts as a contaminant that reduces the clean solid-to-solid contact between surfaces. Lubricants can also provide a low shear strength barrier between surfaces so that the shear occurs in the lubricant film thus reducing friction.

Lubricants can be gases, liquids, or solids, but the common factor between them is that they all reduce friction, adhesion and wear between surfaces [37, 42]. The most effective measure of a lubricant's performance is the coefficient of friction, and, in general, a good conventional lubricant lowers the coefficient of friction to 0.1 or below [37]. The amount of wear experienced by the surface is another method for measuring the lubricant's effectiveness.

A wide range of lubricants is used to control wear of metals. These can be classified according to basic composition and formulation. One type is mineral oils that are hydrocarbons obtained mainly from distilling crude oil [38]. The properties of these lubricants depend on the structure, chain length and degree of refining. They can be either liquids or solids, such as mineral waxes. Another type of lubricant is natural fats and oils. These are derived from animal or vegetable sources and were probably the first lubricants in use. Oils are liquid at room temperature and natural fats are semi-solid. Some of the natural fats and oils include beeswax, palm oil, lard, tallow, and lanolin.

Synthetic, compounded, and aqueous lubricants are three other types of lubricants used to control wear. Synthetic lubricants can be either mineral oil derivatives or silicon compounds. Compounded lubricants are those containing various additives that enhance the tribological properties of the lubricant. Additives are used to enhance the

corrosion resistance, oxidation resistance, and detergency of the lubricant. Aqueous lubricants are those containing water, a dispersed oil or oily phase, stabilizers, and corrosion and bacteria inhibitors.

Coatings are another type of lubricant used to reduce wear. Useful coatings come in a wide variety of forms such as metal, polymer, bonded, and conversion coatings. Metal coatings may be used alone but are more effective with a liquid or semi-solid lubricant. For metal/lubricant systems, the coating serves as a lubricant reservoir. Tin, zinc, copper, and sometimes silver or gold are used. Polymer coatings can be bonded or deposited onto a surface and used either alone or with a liquid lubricant. Some of the common polymers used are polytetrafluoroethylene (Teflon™), polyethylene, polypropylene, and polymethyl methacrylate. Figure 1.2.4.1 shows the mer chemical structures of these polymers [45].

Bonded coatings are a combination of a bonding agent, usually a polymer, and a solid lubricant, such as MoS_2 or graphite. The bonding agent helps to keep the solid lubricant as a continuous film that increases its effectiveness. Another class of lubricant coatings is conversion coatings that, while they do not serve as lubricants, instead act as lubricant carriers. Examples of conversion coatings are oxide films, chrome films, oxalate, and phosphate coatings.

Of the various lubrication states, the one considered to be the dominant mechanism in low speed rolling contact is boundary lubrication [46]. In boundary lubrication, the lubricant forms a thin film that only partially separates the two surfaces [36]. The thin film allows contact to occur between the asperities thus causing the coefficient of friction to be a function of both the lubricant and the surface material [38, 43].

1.3 MATERIALS OF INTEREST

A variety of materials were investigated for their friction modifying properties for use under rolling/sliding wear conditions. The materials of interest center around two types: non-steel materials that are lubricant-resistant and hard particle multi-phase materials. Both types are discussed below.

1.3.1 Lubricant-resistant Materials

Lubricant-resistant materials are those that have commonly been found to be difficult to lubricate. For the materials that were investigated as possible friction enhancing coatings, it was important to balance the high friction properties against other material properties such as wear resistance and toughness.

Much of the literature and scientific effort dealt with materials that reduce friction between surfaces. Limited work on high friction materials was also available, most of which had been developed for use in transportation systems [43]. High friction materials are important for brakes, clutches, wheels, and tires. Prior to the 1900's, wood, felt and leather were used for traction, but these did not have high temperature capability. Woven cotton impregnated with resin, asphalt, or bitumen worked but also had poor thermal characteristics. A method of improving these materials was the addition of metal wires that helped to conduct heat away and to improve strength. Asbestos was introduced in the early twentieth century and led the way for modern high friction materials [43].

Other types of high friction materials have since been developed. Sintered materials such as bronze with lead, iron, graphite, or silica are used for heavy duty brake and clutch conditions. They have good mechanical properties, low wear rates, good thermal conductivity and can even be used while immersed in oil. Cermets are used for

aircraft brakes and have good thermal conductivity, wear properties, and high temperature capability. Rubber is another high friction material that has been used for tires, belt drives, and footwear.

Lubricant-resistant materials of particular interest to this project were titanium and stainless steel. Titanium is a lightweight, high strength, corrosion resistant material used for a variety of applications including aerospace, biomedical, and chemical processing [47]. Titanium is especially noted for its difficulty to lubricate and its poor tribological properties [48]. In metalworking operations, the high adhesion of titanium causes increased levels of friction, galling and material transfer. It especially adheres badly to steel [38].

Several studies of the tribological properties of titanium and its alloys have been made. Tian et al. found that by undulating titanium surfaces in sliding wear the ability of common lubricants to decrease the coefficient of friction improved [49]. The coefficients of friction measured were:

Fluid	Mineral Oil	Oleic Acid	Turbo Oil	Silicone	Halocarbon Oil	Methylene Iodide
Coefficient of Friction	0.50	0.45	0.48	0.50	0.18	0.17

Lebedeva investigated the dry sliding wear of an alpha titanium alloy containing 3.5 to 5% aluminum, 1.0% C and 1.5% Cr against steel, and found the coefficient of friction to be 0.5 in air and 0.2 in vacuum [50].

Various types of wear tests have been performed to investigate the tribological properties of titanium and its alloys. The fretting behavior of titanium alloys has been studied by Fayeulle et al. who found a friction coefficient greater than one in all cases [51]. Budinski studied the fretting behavior as well as the galling, abrasion

resistance, and sliding wear of titanium and recommended that pure titanium be avoided for titanium tribosystems [52]. The coefficient of friction found for self-mated titanium in galling tests was 0.40. Mercer and Hutchings performed abrasion testing on titanium and Ti-6Al-4V alloy to evaluate the effect of atmosphere on wear and the coefficient of friction. In air, the wear rate was linear and the coefficient of friction approximately 0.6 for all test conditions [53].

Several investigators have studied the effects of adding non-metals such as carbon and nitrogen to titanium and titanium alloys to improve wear characteristics. Ayers investigated the effect of a carbide injected titanium alloy on abrasive and erosive wear and found the coefficient of friction to decrease as volume percent of titanium-carbide increased [54]. Fayeulle investigated the effect of nitrogen implanted titanium alloy on friction behavior [55]. Wear resistance and coefficient of friction showed no appreciable difference.

Little information existed on plasma spraying of pure titanium, and even less on the tribological properties of these coatings. Some work has been done using laser plasma spraying of titanium. Kaneta et al. investigated the effect of argon and nitrogen atmospheres on the friction and wear of titanium coatings formed by laser thermal spraying [56]. The coefficient of friction in argon varied from 0.56 to 0.36 as the coating thickness increased from 20 to 80 μm. In nitrogen, coatings had a coefficient of friction that remained approximately constant at 0.38 as coating thickness increased. The decrease was believed due to the formation of titanium-nitride that hardened the surface.

Other investigators have looked into the plasma spraying of titanium-carbide with titanium to improve wear resistance [57]. Smith and Mohanty investigated the wear resistance of commercially pure titanium and titanium-carbide/titanium plasma sprayed coatings in both air and vacuum [58]. The wear performance was found to improve with increased titanium-carbide content.

Another type of material examined for its lubricant-resistant ability was stainless steel. Both austenitic and martensitic stainless steels are traditionally used for wear applications, however, they have a tendency for galling and adhesion [38]. Austenitic stainless steels used for wear applications are the 200 and 300 series [59]. The 200 series stainless steels use nitrogen or manganese to replace part of the chromium content that is found in the 300 stainless steel series. Martensitic stainless steels are the 400 series, which have a low nickel content and chromium levels greater than 11.5%. Because of the martensitic structure, they have a better resistance to galling than the austenitic stainless steels, but corrosion resistance is reduced.

A wide body of research existed for stainless steels under a wide range of conditions. Smith investigated the sliding wear of austenitic 316 stainless steel in air at varying temperatures, using a standard pin and flat geometry [60]. The coefficient of friction peaked during the first few cycles and was dependent upon temperature with values of 0.78, 1.13, 1.34, 1.34 at 100 °C, 200 °C, 300 °C and 400 °C, respectively. The coefficient of friction then decreased to a constant value of 0.35 to 0.45 that was independent of temperature. At temperatures over 300 °C, Smith noted glazing of the surface and prows of transferred material that accumulated from a groove on the opposite surface.

Slifka et al. investigated the sliding wear of 440C martensitic stainless steel in oxygen over a wide range of temperatures, loads, and sliding speeds [61]. The transition from mild oxidative wear to severe wear with galling occurred as sliding speed and load increased. Sun et al. examined the wear behavior of martensitic 440C under rolling/sliding wear [62]. The wear rate increased nonlinearly with increasing loading and changes in wear rate corresponded to a change in wear mechanism. Smith studied the unlubricated reciprocating wear of a high strength martensitic steel at various temperatures [63]. The friction coefficient of the self-mated material was found initially to be around 0.2 and then increased to fluctuate between 0.7 to 0.85.

Yang et al. compared the sliding wear in argon of 304 and 310 stainless steels against M2 tool steel [64]. The value of the coefficient of friction for 304 varied from approximately 0.4 to 0.5 as load increased; for 310 stainless steel the coefficient of friction increased from 0.65 to 0.8. Hsu et al. studied the sliding wear in argon of 304 and 316 stainless steels against 440C stainless steel [65]. The coefficient of friction for both 304 and 316 was found to average at 0.5.

Wear testing of plasma sprayed stainless steel coatings has not been extensively investigated. Dallaire et al. investigated the abrasion resistance of arc sprayed 304 stainless steel and composite titanium-boride/stainless steel coatings [66]. The wear resistance of the coatings was dependent on the amount, size and hardness of the sprayed particles and the titanium-boride composite coatings showed a fourfold increase in wear resistance over bulk stainless steel.

Titanium-nickel was the other material investigated for its lubricant-resistant properties. Titanium-nickel is a material known for its shape memory properties rather than its tribological properties [67].

1.3.2 Hard Particle Coatings

The other friction enhancing technique investigated was the use of hard particle multi-phase coatings. The use of hard particles in a soft matrix is a common method for enhancing wear resistance [68]. Hard particle coatings consist of a matrix binder that provides toughness and adhesion, and the hard particle phases that provide the increased wear resistance. When the hard particles slide against a softer surface, they dig into it and shear the softer material [36]. The extra energy required to deform the material is reflected in the force required to move the surfaces.

Materials that were of interest for hard phases were titanium and stainless steel in a matrix phase of 1080 steel. The titanium and stainless steel hard particles may serve a dual role since they are contaminant resistant as well. At this stage no references were available on the plasma spraying of these types of multi-phase materials.

1.4 SURFACE MODIFICATION BY PLASMA SPRAYING

Today there exists a wide range of surface and coating treatments that can be used to modify surfaces. These include chemical vapor deposition, physical vapor deposition, welding, and thermal spraying. High velocity plasma spraying is just one of the many types of thermal spraying techniques used for coating and surface modification. High velocity plasma spraying is especially suited for developing and producing friction enhancing coatings. The major advantages of this technique are the ability to spray a wide variety of materials and to spray multiple types of feedstocks simultaneously. Other advantages of using plasma spraying for this project are the process can be performed in the lab as well as the field, and surface properties can be enhanced without affecting bulk material properties.

1.4.1 Plasma Sprayed Coating Development

Plasma spraying is a process that combines the melting of particles, solidification, and consolidation all in one operation [69]. Particles of the sprayed material are melted in the plasma jet and accelerated towards the substrate. The molten particles strike the substrate surface, at a rate of 10^6 particles per second [70], where they spread out to form splats as they cool. Figure 1.4.1.1 schematically shows the flattening and solidification of an individual splat. Splat cooling rates are usually from 10^5 to 10^6 °C per second [69]. As more particles impinge on the substrate surface, they form layers of interlocking splats

or lamellae. In addition to metal splats, the coating contains oxide particles, inclusions, unmelted or partially melted particles, as well as porosity. Figure 1.4.1.2 shows the constituents of a typical plasma sprayed coating.

The porosity in a coating is a result of incomplete melting and wetting of the particles that prevents them from filling in the gaps between previously deposited splats [69]. Figure 1.4.1.3 shows schematically how this occurs [71]. Oxides and nitride inclusions can result from reactions of the molten metal with the spraying environment.

In general, bonding between substrate/particle (adhesion) and particle/particle (cohesion) can be a combination of one or more bonding mechanisms [69]. The degree that one operates versus another is a function of the materials and the process variables. The splats can be bonded to the surface by three basic mechanisms. One mechanism is mechanical bonding which is a result of the mechanical interlocking of the molten particles with the surface irregularities. As they cool the molten particles assume the surface topography of the substrate. Major variables of mechanical bonding are surface roughness and cleanliness [72].

Mechanical bonding can be enhanced by grit blasting that not only cleans the substrate surface but increases surface roughness [69]. In addition, grit blasting induces local plastic deformation, which is thought to increase the energy of the surface [71]. A variety of different types and sizes of grit media can be used to optimize surface conditions depending on the requirements of the material and the application. Figure 1.4.1.4 shows the differences in surface roughness from two different sizes of grit blasting media.

Other bonding mechanisms are metallurgical bonding and physical bonding [71]. Metallurgical bonding is a result of diffusion between the coating and substrate atoms creating a diffusion zone or an intermediate compound. Physical bonding is due to mechanical interlocking between the sprayed material and the substrate.

1.4.2 Plasma Spray Equipment

Plasma spray equipment consists of several components [69, 73-75]. Perhaps the most important component is the plasma spray gun that creates and directs the energy for the spray process. Contained inside the gun are the electrodes. The negative electrode, the cathode, is a long cone shaped projection usually made of thoriated tungsten. The positive electrode, the anode, is a water cooled copper cylinder which has a small cylindrical channel inside that contains the cathode. The anode also acts as a nozzle that constricts and directs the plasma gas jet.

Gas enters the gun chamber and the arc is struck between the electrodes. Arc length is usually 25 to 30 mm long in conventional systems and 75 to 100 mm long in high energy systems. The temperatures range from 5000 to 30,000 °C. The length of the arc is a function of operating voltage [76]. The temperature of the arc is a function of current. As the gas heats up, it expands and the pressure of the incoming gas forces the plasma out the nozzle end of the gun.

The typical plasma spray gun also has a gas injection system, an insulating body to protect the electrodes, cooling water passages, and powder and/or wire feed systems, Figure 1.4.2.1 [72]. While plasma torches can be operated from either AC or DC current, DC current is more stable, and, as a consequence, most commercial plasma spray guns operate on DC current.

High velocity plasma guns, such as the one used at OGI, operate at high voltages and low currents [77, 78]. They typically operate in ranges of 300 to 450 V and 200 to 500 A and produce power levels of over 200 kW. The higher power level provides more energy that allows increased quantities of materials to be sprayed and allows the efficient utilization of multiple feedstocks. The lower currents decrease heating of the gun and contribute to longer gun life [34]. In addition, the high voltage and low current result in the development of increased arc lengths inside the gun body. The longer gun body required to house the arc causes the gases to reside longer and results in higher acceleration of gases and particles. Increased heating of the plasma gases coupled with the higher gas flow rates, gives supersonic exit gas velocities. Plasma gas exit velocities can exceed Mach 3, enabling higher particle velocities producing harder and denser coatings than are produced by conventional plasma spray systems.

Plasma spray feedstocks are introduced into the spray system external to the gun. They can be injected in various ways and at varying points within the plume: back injected, perpendicular or at an angle to the jet axis, and downstream of the jet [79]. This affects the amount of time the powder particles are in the plume, and, as a consequence, the degree of melting. Proper introduction of the powder and wire into the plasma jet is important in obtaining optimum melting which affects coating properties and deposition efficiency.

In addition to the plasma gun, other supporting equipment is needed [72, 75]. This includes the power supplies (usually DC rectifiers), water cooling circuit, powder or wire feeders, gas supply, and control console to meter powder, gas, and water. Auxiliary equipment that may be needed includes ventilation spray booths, acoustic protection, radiation protection (infrared and UV), and tooling to manipulate substrate or gun. Figure 1.4.2.2 shows the components of a basic plasma spray system [72]. Plasma spray guns typically use Ar, N_2, Ar/He, Ar/H_2, and N_2/H_2 gas mixtures, which are chosen for their inertness and energy content [75].

1.4.3 Plasma Spray Parameters

A wide range of process variables, or parameters, can affect the quality of a plasma spray coating [79]. Table 1.4.3.1 shows a list of these parameters that can be broken roughly into equipment related parameters and material related parameters. Many of the equipment related parameters center around particle heating and acceleration. The material related parameters are associated with the characteristics of the feedstocks used to make the coatings.

1.4.3.1 Equipment related parameters

Equipment related parameters that affect particle heating and acceleration are the primary and secondary gas composition, the gas flow rates, the power input, and the working distance. These are important parameters since, if the thermal and kinetic energy of particles is too low or too high, it can result in poor coating quality. For example, if particles are subjected to an excess of thermal energy, they can be vaporized in the plume rather than arriving at the substrate in the fully molten condition [32]. If the particles receive too little thermal energy, they arrive at the substrate in an unmelted condition and will rebound. Too much kinetic energy will also cause particles to rebound off the surface or shatter rather than flatten, spread out, and freeze. If too low a velocity is imparted to the particles, they will not spread out to fill in the gaps between splats causing porosity and low deposition efficiency.

The plasma source gas, or the primary gas, affects the heat content and velocity of the plasma jet. Lower gas flow rates lead to higher plasma temperatures [80]. This is because a smaller volume of gas has to be heated. The smaller volume of gas present leads to decreased plasma velocity. Increased gas flow rates cause the plasma temperatures to become cooler [34]. However, increased velocity also results since the plasma density increases.

The source gas is usually nitrogen or argon [73]. Nitrogen has the advantage of being less expensive as well as having a higher heat content due to its diatomic nature. Argon, while more expensive, leads to higher plasma jet velocities and temperatures. Also, argon can be used in cases where the formation of nitrides is likely to be a problem.

A secondary gas, usually hydrogen or helium, can be used to increase the temperature and velocity of the plasma jet [80]. The addition of the secondary gas causes the arc to lengthen. This lengthens the exposure of the gas to the arc. Proper adjustment of the ratio of the primary gas to the secondary gas flow rates optimizes particle heating and acceleration. During parameter optimization, much time is spent in adjusting this ratio.

Varying the power input, or amperage and voltage, controls the temperature and velocity of the plasma jet. Increasing the voltage causes the arc length to increase [76]. Gas is then exposed to the arc for a longer time thus raising temperature and velocity. Increasing the amperage increases the diameter of the arc and thus increases the temperature of the arc. The velocity is also increased as a result of the higher heat content and more rapid expansion of the gas.

The working distance, or the distance from the gun tip to the substrate surface, is an equipment parameter that affects how long the particles are in the flame and how much velocity they have as they strike the surface. Longer working distances give slower particle velocities and cooler particles than shorter working distances. The working distance usually ranges from 200 to 300 mm. Working distance adjustments can be made after the optimum primary to secondary gas flow rates are obtained to fine tune the resulting coating.

Injector configuration is another important equipment spraying parameter. Feedstocks can be set up to enter the plume at various distances from the gun tip, at

various angles, and using single or multiple injectors. Where and how the particles enter the plume affect particle heating and velocity. Wire feed rate and powder carrier gas flow rates both affect where the particles enter the plasma plume. For example, when powder carrier gas flow rates are too low, particles can't penetrate the plume and will bounce back off. For flow rates that are too high, the particles will have too high of a velocity and shoot through the plume. Both conditions contribute to low deposition efficiencies, where the deposition efficiency is defined as the ratio of the amount of powder in the coating with respect to the total amount of powder sprayed.

1.4.3.2 Material related parameters

In addition to the equipment related parameters, a wide variety of material parameters also affect the plasma spraying process. Material parameters include the type of material, the chemical and physical properties of the material, and the form of the material. The types of materials that can be sprayed are metals, ceramics, polymers, and composites. Each has different requirements with respect to optimum parameters.

Chemical properties include homogeneity and purity [81]. For example, homogeneity, as well as purity, is important since differences in the material composition can lead to different melting behavior in the plasma jet. Physical properties include melting temperature and thermal conductivity. A higher melting material is more suited to the high temperature conditions while lower melting point materials may require lower spray temperatures.

Material forms are the types of feedstocks that can be plasma sprayed. They are wire, powder, or rod [82]. Some materials are more suited for a particular form than others. For example, a ductile material could be found in wire or powder form while a ceramic would be found in only powder or rod form. The various forms of feedstocks require different operating parameters and give different coating results.

Size factors are another aspect of material form that requires consideration when optimizing parameters. Powder size and wire diameter have a significant affect on the plasma spraying process [83]. For example when spraying wire feedstock, the larger the wire diameter, the larger the molten droplets that are created, and thus the wider the spray pattern [76]. While this is an advantage for some applications such as those requiring high deposition rates, it can be a disadvantage for applications requiring a finer coating morphology.

Powder characteristics are particularly important considerations in the plasma spray process because of the close relationship between powder characteristics and coating properties [84]. Some of the more important powder characteristics include particle shape and size, particle size distribution, state of agglomeration, surface roughness and particle flow properties [81, 83]. Powder characteristics directly affect coating properties such as microstructure, porosity, surface roughness, and adhesion [84]. Powder feedstocks can include a wider range of material types including plastics, ceramics, and metals.

Particle size and shape are some of the most fundamental powder characteristics [81]. Powder sizes vary from a few micrometers to over 100 μm, the size depending on the material used and the application requirements [83]. Particles that are too small will vaporize in the hot plasma jet while particles that are too large will not melt fully. Particle shapes can be classified into a simple system as shown in Figure 1.4.3.1 [81]. Some of the concepts that help in analyzing shapes are particle dimensionality, surface contour, and aspect ratio.

The size distribution of a powder is another parameter that affects the coating quality. For most coating applications, a fairly narrow size distribution is ideal to achieve optimum coating properties. This is because a given set of plasma spray parameters will fully melt only a narrow range of particles sizes. Particles with too great a diameter will

not melt completely and will either bounce back off the coating, contributing to lower deposition efficiency, or will embed in the coating as unmelted particles [83]. Particles that are too fine will either bounce off the plasma plume or will vaporize before they reach the substrate, again lowering deposition efficiency. The ideal size range for a particular material depends on the melting point of the material and the particle shape.

Often, describing a powder using a single average size value can give an incorrect picture of a powder's characteristics. Mean and modal diameter values are sometimes used, but, with large ranges of diameters, size distribution curves, which relate particle size to the weight fraction of particles, are most useful [81]. Some of the various types of distributions are shown in Figure 1.4.3.2 [81].

Another factor that affects the particle size distribution is particle agglomeration [84]. Difficulties that can arise from agglomeration are inconsistent feed rates due to clogging. Also, unmelted particles can result from the larger sized agglomerations that are outside the particle size range of the optimum parameters. Particle agglomeration can adversely affect the heat transfer in the plasma jet due to air spaces between the agglomerated particles. Such agglomeration results in higher coating porosity.

Surface roughness, i.e., irregularities and protuberances on the particle surface, is another important material parameter. Surface topography has great influence on the frictional forces between particles during particle flow. For example, a mechanically or chemically reduced powder usually has sharp, irregular protuberances compared to an atomized powder that has finer, more rounded surface features. Another consideration of surface roughness is that chemical reactivity is increased the higher the surface roughness so that particle/particle and particle/environment reactions are increased.

The flow properties of a powder are a characteristic that can greatly affect coating properties [83]. Inconsistent flow rates make it difficult to control the amount of material being sprayed. Some of the variables affecting flow rate are size and shape of particles, surface roughness, particle density, humidity, electrostatic charging, and type of material.

1.5 COATING CHARACTERIZATION

Since the primary goal of this project was to assess the potential for increasing the coefficient of friction between two surfaces in rolling/sliding wear, it was necessary to evaluate the coatings' performance. Proper evaluation of the plasma sprayed coatings' ability to increase the coefficient of friction between the two surfaces required an investigation of the plasma spray coatings' character and behavior. Thus two focal points for this investigation were coating characterization and wear performance testing.

Coating characterization for this project required an understanding of the coatings' microstructure. It was necessary to examine the coating microstructure in the as-sprayed condition, and it was also important at various stages during and after the wear testing. This helped in understanding the wear mechanisms and in designing a coating that exhibited modified friction. The techniques for characterizing the coating microstructure included optical microscopy and scanning electron microscopy.

An understanding of the coatings' tribological properties was necessary to understand coating behavior. This portion of the work was important for determining the success or failure of a particular coating in regard to friction modification. Amsler testing was the method for evaluating the coatings' tribological behavior. With this equipment, wear rate, coefficient of friction, and wear mechanism were evaluated. Using a wide variety of testing parameters, especially different lubrication conditions, the success of the coating spray parameters was evaluated.

For a coating to be considered successful, four basic criteria had to be met. The criteria were:

1. homogeneous microstructure,
2. adherence to the substrate,
3. durability and
4. increased/decreased coefficient of friction.

The methods for characterizing the coatings are discussed below with respect to each of the success criteria.

1.5.1 Homogeneity

Homogeneity is important to coating quality because of the requirement for uniform properties within the coating. The method of forming plasma sprayed coatings causes them to be heterogeneous by nature. Homogeneity is especially important for materials being used for wear applications since uniform wear is desirable. Depending on the type of coating, whether single or multi-phase, the requirements for homogeneity can be different.

For a single component coating, homogeneity requires the microstructure of the coating be uniform throughout. This means that oxides, porosity, melted particles, and unmelted particles need to be distributed uniformly within the coating microstructure. For example, having regions of high coating porosity would lower coating strength or having oxides at the interface would decrease coating adhesion.

For a multi-phase coating, the same requirements exist, but, in addition, it is important to have a fine distribution of the second phase hard particles throughout the coating. The hard particles of the multi-phase coatings need to be uniformly distributed

so that the friction modifying properties are uniform in the coating. Having particles distributed on the macro-scale is a fairly easy task but to have them distributed evenly on the micro-scale is more difficult.

In order to determine the degree of homogeneity present in the coatings, several techniques were used including the various types of microscopy and chemical analysis (energy dispersive spectroscopy, x-ray mapping). Microscopy enabled determination of distribution and uniformity of the coatings while chemical analysis identified the components of the coating. Mapping was used to see the distributions of the various elements in the coating and was performed both at high and low magnifications to verify uniform distributions.

1.5.2 Adherence

Adherence describes how well the coating bonds to the substrate. This is a function of surface preparation and the material itself. For example, a cleaner, rougher surface promotes improved coating adherence. However, others factors may contribute to coating adherence as well. Such factors may include the formation of tenacious oxide layers on the substrate surface or differences in the thermal properties between the coating material and the substrate.

Two methods were used to evaluate coating adherence. The first was microscopy. Using microscopy, the existence of contaminant particles was seen and by using chemical analysis the composition was found. Mechanical testing was the second method that was used to evaluate coating adherence. The strength of the coating bond was measured by tensile tests. In addition, coating adherence was evaluated indirectly using the Amsler machine. Coatings that survived testing showed coating adherence but only in a qualitative manner. The results of Amsler testing were used as a screening device to determine which coatings were not likely to meet the adherence criteria.

1.5.3 Durability

Durability describes how well the coating is able to withstand continuous rolling/sliding wear conditions. An inherent part of durability is the cohesive strength of the coating. Durability was tested using the Amsler machine. By using a wide variety of testing conditions such as contact pressure, slide/roll ratios, and lubrication, an understanding of which factors have the greatest effect on the coating life was found. The duration of the test gave some idea of coating durability.

Characterization of the coatings after Amsler testing was an important part of understanding durability. Understanding why the coating failed to meet durability criteria can help in designing a more durable coating. Using both optical and scanning electron microscopy, the tested coatings were examined to determine the condition of the wear track and types of wear debris. These gave clues as to what types of wear mechanisms were occurring in the coating. Debonded coating pieces were examined on both inner and outer surfaces for evidence of coating failure mechanism.

1.5.4 Coefficient of Friction

The most important criterion to evaluate was the coefficient of friction. Without a change in the coefficient of friction, the project's goals would not be met, no matter how well the coating met the other criteria. Two different friction studies were required for full investigation of the friction coefficient. The first dealt with the friction coefficient of the solid materials (monolithic rail steel, stainless steels and titanium) and the second with the friction coefficient of the sprayed coatings.

The friction coefficients of the materials in their solid metal forms were found using the Amsler machine. Since friction data varied widely depending on the testing apparatus, conditions and techniques, these experiments enabled direct comparison of the

coating friction data with solid materials. The solid materials were tested using the same range of conditions as the coatings. Both self-mated pairs and dissimilar pairs of materials were tested. A large part of this study dealt with the friction coefficient obtained when tested against a steel bottom roller.

The second part of the friction study dealt with investigating the friction coefficient of the sprayed coating materials. Coating materials were tested using the same parameters as for monolithic steel specimens from the baseline friction study. In this portion of Amsler testing, the top rollers contained the friction modifying plasma sprayed coatings while the bottom rollers were uncoated steel. A successful test was one that met or exceeded the friction coefficient of monolithic steels under dry testing and was in the range from 0.2 to 0.5 for lubricated conditions. Ideally, the wear rates of a successful coating at least met the values currently obtained for the monolithic steel specimens.

Table 1.4.3.1. Selected material and equipment related plasma spray parameters.

Equipment Parameters	Material Parameters
Volts	Feedstock material
Amps	Wire diameter
Working distance	Powder size
Primary gas	Powder shape
Secondary gas	Powder size distribution
Anode geometry	Particle flow properties
Injector position	Chemical purity
Injector diameter	Melting point
Gas flow rates	Surface roughness
Wire feed rates	Agglomeration

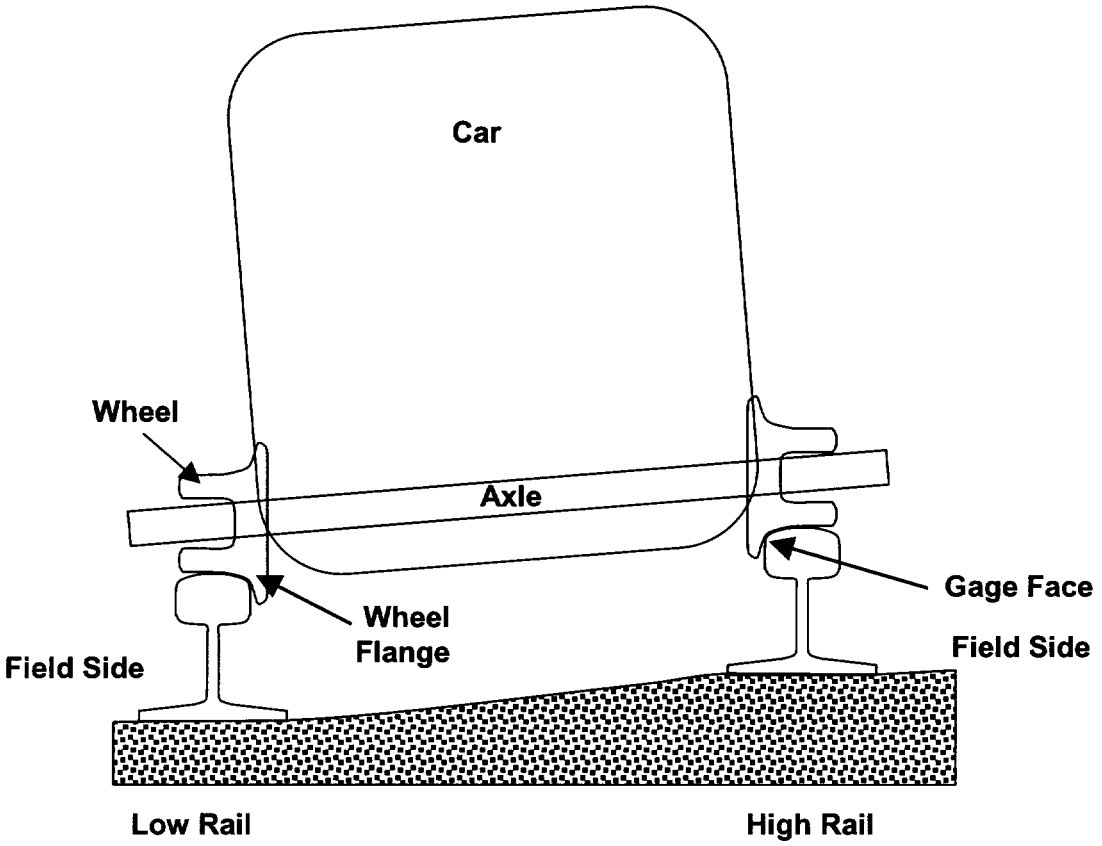

Figure 1.1.2.1. Schematic of rail in curved track.

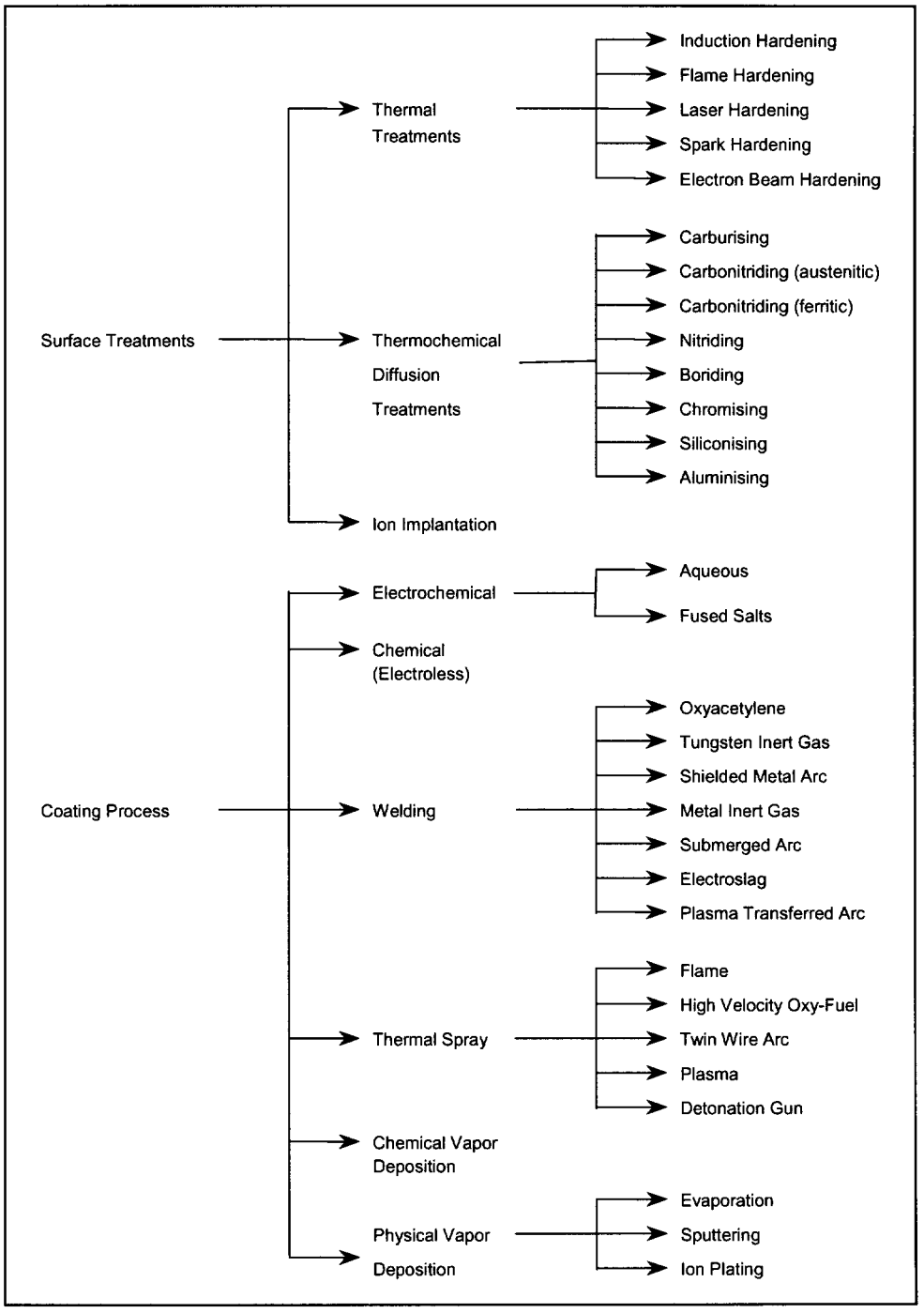

Figure 1.1.5.1. Surface engineering processes.

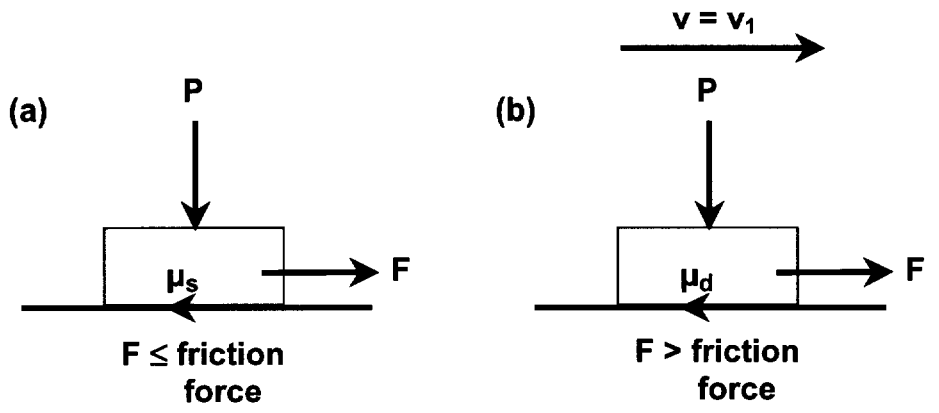

Figure 1.2.1.1. Schematic of (a) static and (b) dynamic friction.

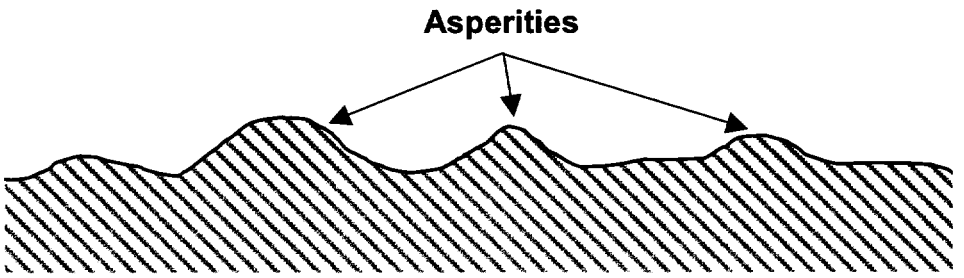

Figure 1.2.1.2. Exaggerated surface asperities.

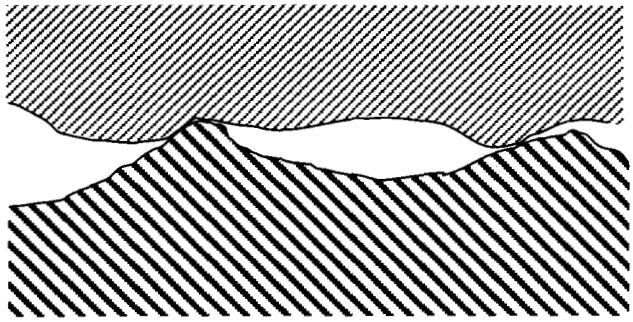

Figure 1.2.1.3. Interlocking of asperities [38].

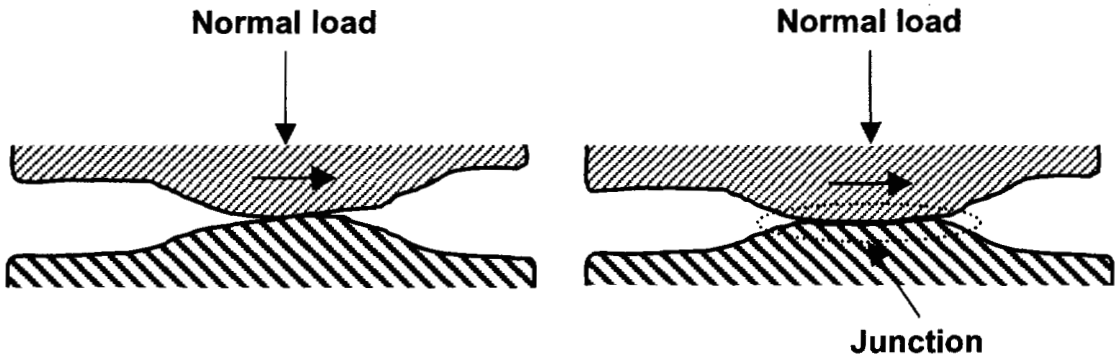

Figure 1.2.1.4. Formation of a junction between asperities.

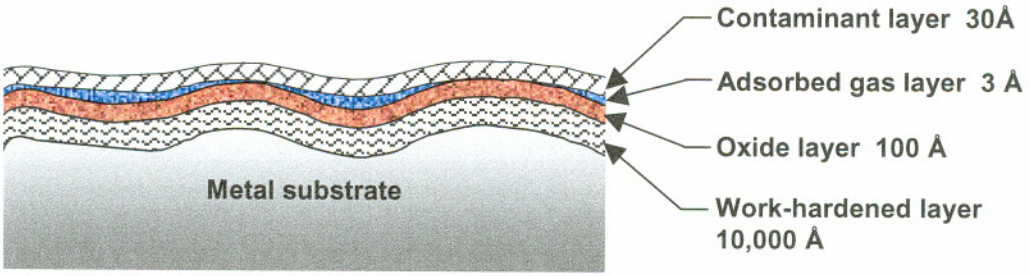

Figure 1.2.2.1. Typical films on a surface.

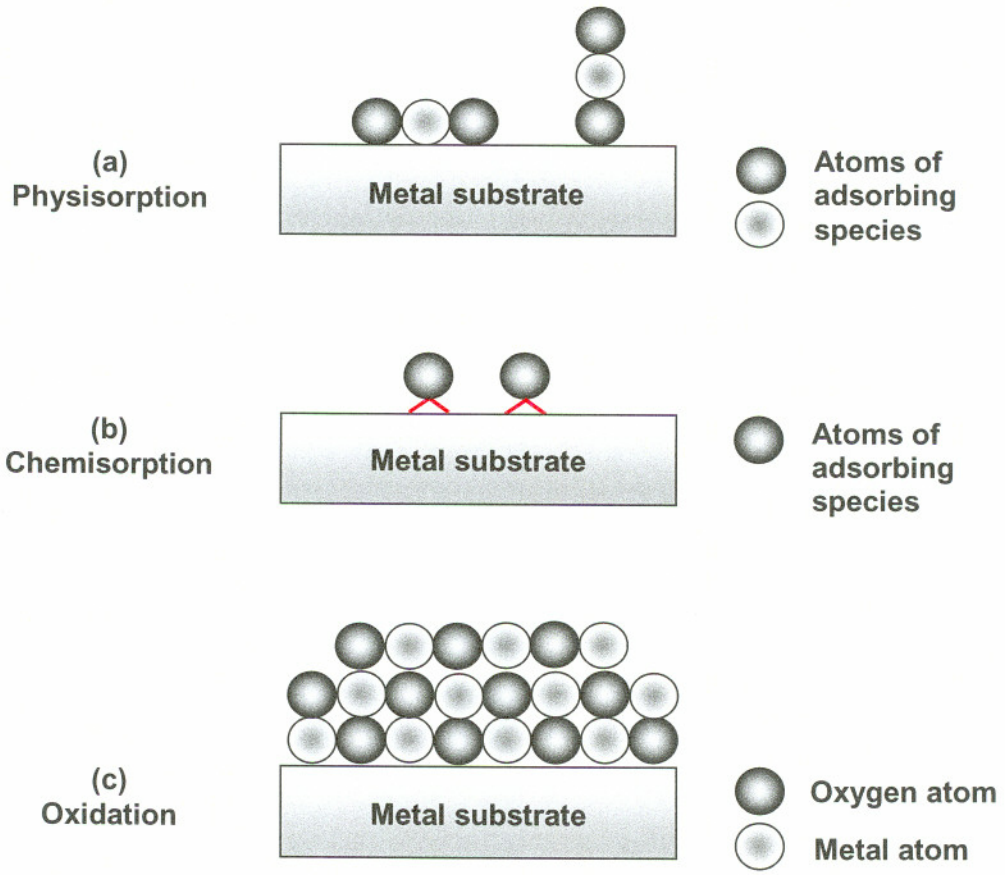

Figure 1.2.2.2. Schematic of (a) physisorption, (b) chemisorption, and (c) chemical reaction.

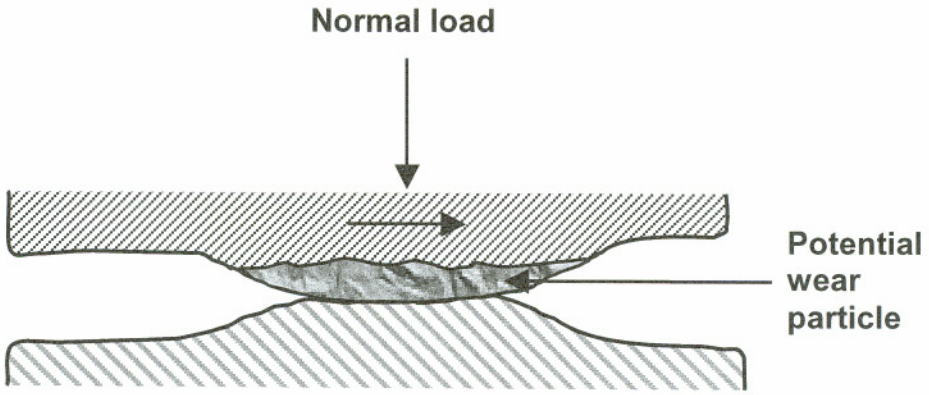

Figure 1.2.3.1. Wear particle being formed from junction.

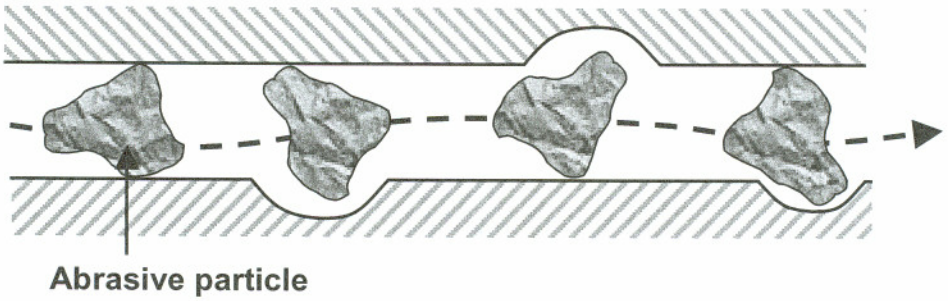

Figure 1.2.3.2. Abrasive wear mechanism.

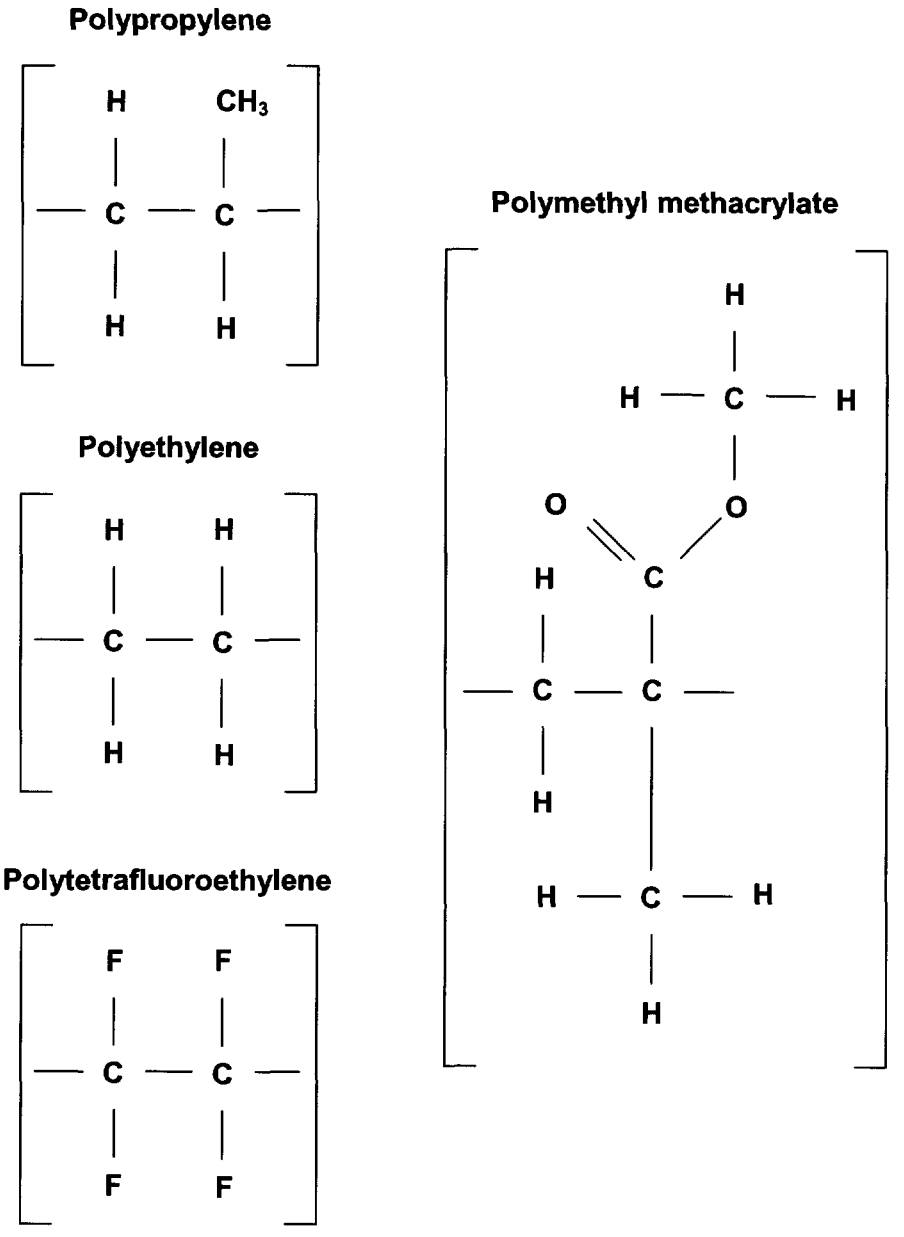

Figure 1.2.4.1. Mer chemical structure of polytetrafluoroethylene, polyethylene, polypropylene, and polymethyl methacrylate [45].

Reprinted with permission from ASM Engineered Materials Handbook, Vol. 2 Engineering Plastics, (1998), ASM International, Materials Park, OH 44073-0002, polymethyl methacrylate, page 49; polytetrafluoroethylene, page 49; polyethylene, page 50; polypropylene, page 50.

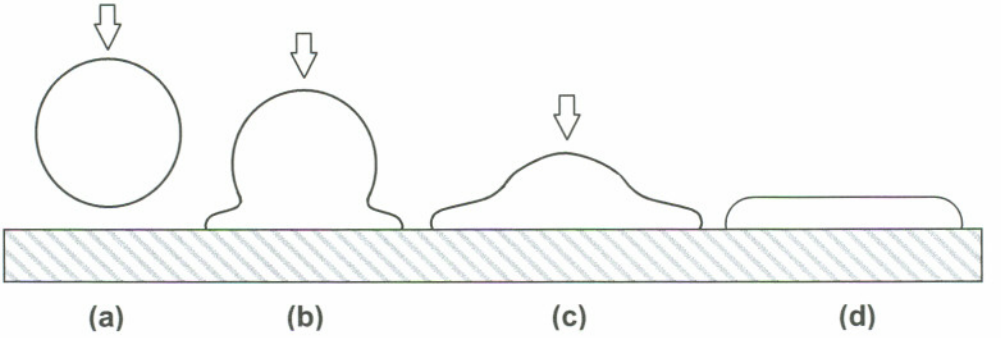

Figure 1.4.1.1. Flattening and solidification of a splat during plasma spray.

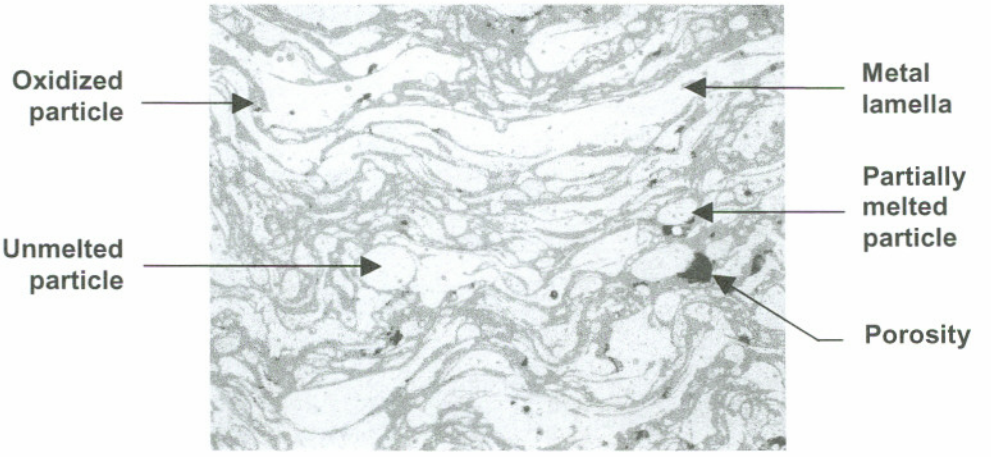

Figure 1.4.1.2. Constituents of a plasma sprayed coating.

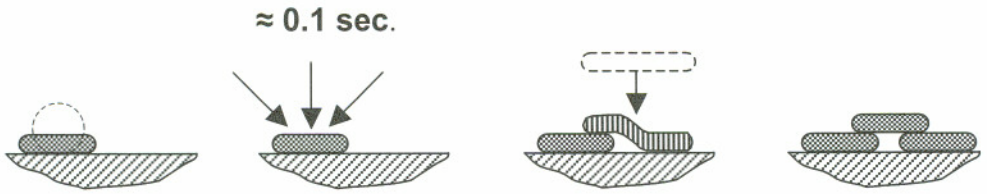

Figure 1.4.1.3. Schematic of the formation of porosity in a coating [71].

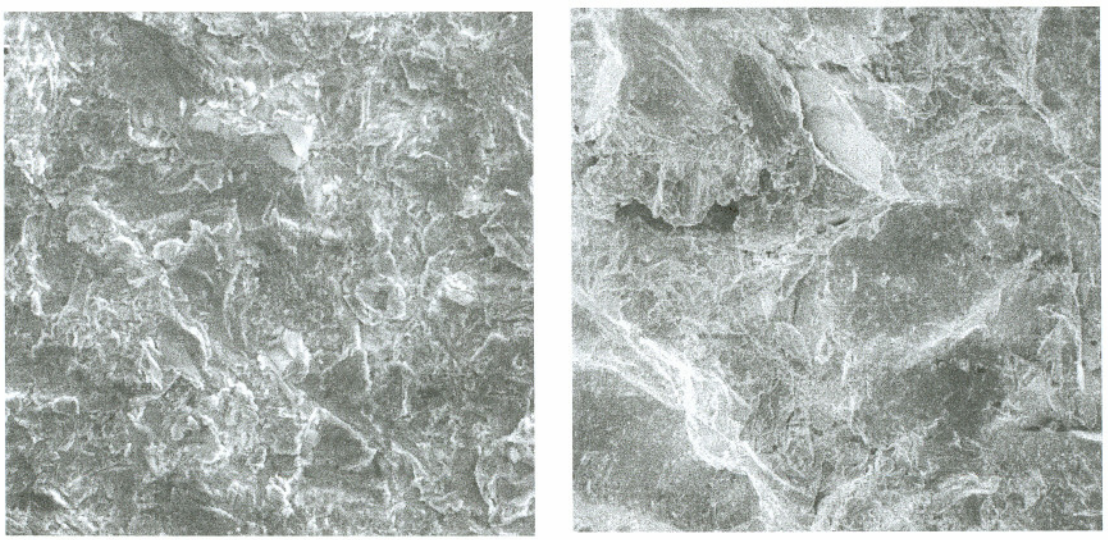

(a) (b)

Figure 1.4.1.4. Comparison of the surface roughness produced by two different grit sizes, (a) 50-70 mesh SiO_2, and (b) 20 grit Al_2O_3. 500x, secondary electron images.

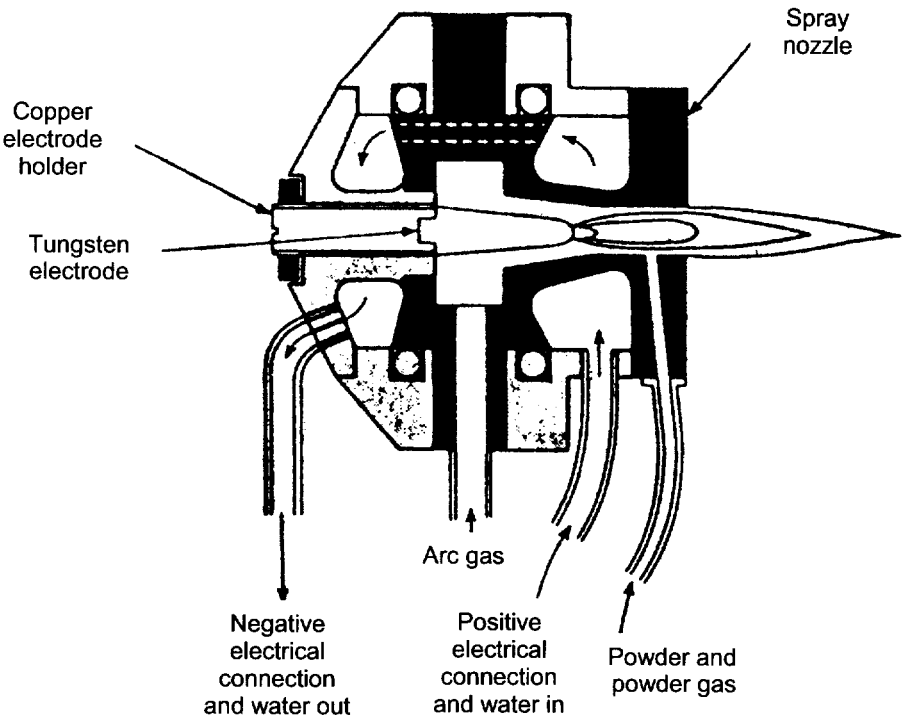

Figure 1.4.2.1. Typical plasma spray gun [72].

Reprinted with permission from *ASM Handbook, Vol. 5, Surface Engineering*, ASM International, Materials Park, OH 44073-0002, fig. 3, pg. 363.

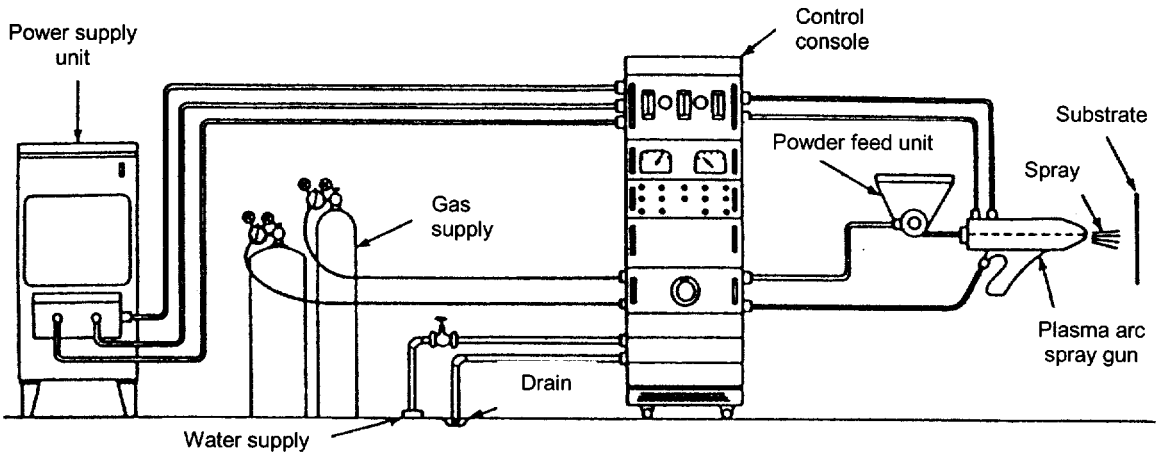

Figure 1.4.2.2. Components of a plasma spray system [72].

Reprinted with permission from *ASM Handbook, Vol. 5, Surface Engineering*, ASM International, Materials Park, OH 44073-0002, fig. 4, pg. 364.

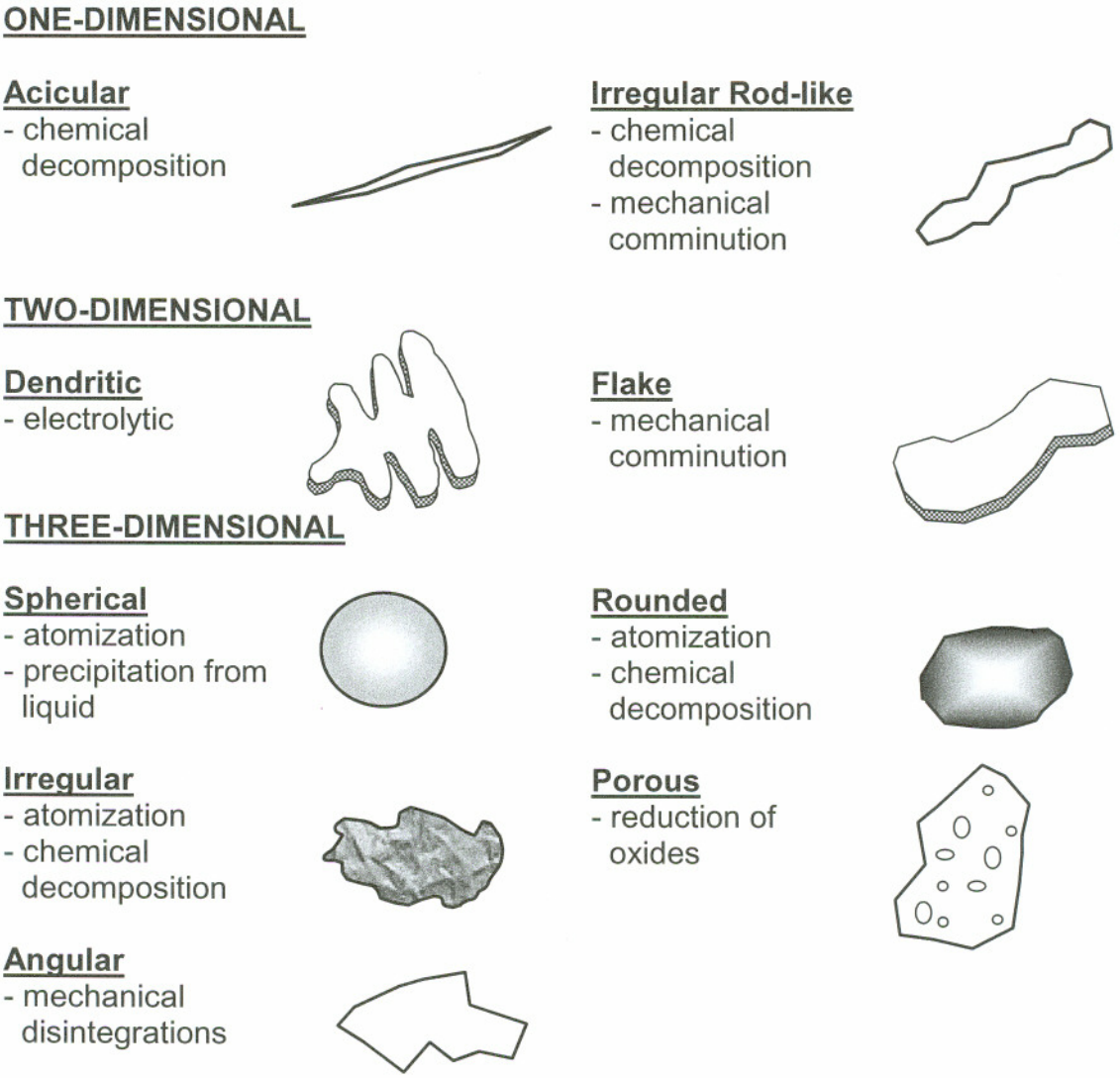

Figure 1.4.3.1. Simple classification of particle shapes [81].

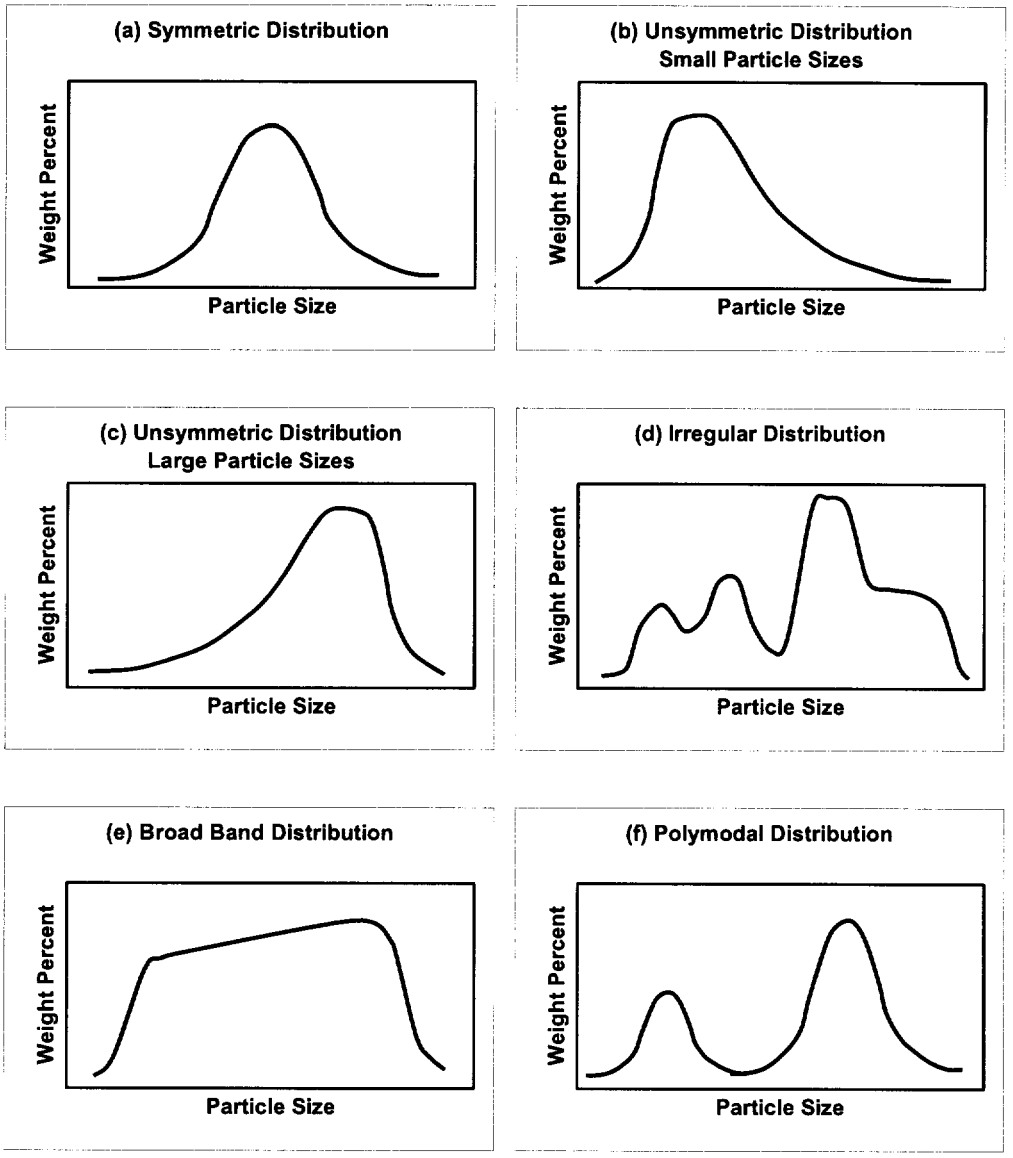

Figure 1.4.3.2. Particle distributions, (a) symmetric, (b) unsymmetric, small particle sizes, (c) unsymmetric, large particle sizes, (d) polymodal, (e) broad band, and (f) irregular [81].

References for Chapter 1

1. Knupp, G. G., Chidley, W. H., Giove, J. L., Hartman, H. H., Morris, G. F., and Taylor, C. W., A Review of the Manufacture, Processing and Use of Rail Steels in North America – A Report of AISI Technical Sub-committee on Rails and Accessories. *Rail Steels – Developments, Processing and Use*, D. H. Stone and G. G. Knupp, Editors, ASTM, STP 644, 1976, pp. 7-20.

2. Stone, D. H., and Steele, R. K., The Effect of Mechanical Properties Upon the Performance of Railroad Rails. *Rail Steels – Developments, Processing and Use*, D. H. Stone and G. G. Knupp, Editors, ASTM, STP 644, 1976, pp. 21-47.

3. O'Rourke, M. D., Engineering Effects of Increasing Axle Loads. *Proceedings of the 2nd International Heavy Haul Conference, Colorado Springs, CO, 1982*, Association of American Railroads, 1983, pp. 91-98.

4. Brown, D. N., and Brown, J. H., Optimizing Operational Modes on the Mt. Newman Mining Company Railroad. *Proceedings of the 2nd International Heavy Haul Conference, Colorado Springs, CO, 1982*, Association of American Railroads, 1983, pp. 77-82.

5. Burger, W. P., Doubling the Capacity of the Heavy Haul Coal Line to Richards Bay. *Proceedings of the 2nd International Heavy Haul Conference, Colorado Springs, CO, 1982*, Association of American Railroads, 1983, pp. 56-67.

6. Shedd, T., Profile Grinding is Cost Effective. *Modern Railroads*, Vol. 44, May 1989, pp. 45-49.

7. Paulsson, B., Assessing the Track Costs of 30 Tonne Axleloads. *Railway Gazette International*, Vol. 154, No. 11, November 1998, pp. 785-786.

8. *Rail Defect Manual*, Sperry Rail Services, 1964.

9. Bramfitt, B. L., Symposium Review – Rail Steels for the 21st Century. *Iron and Steelmaker*, Vol. 22, No. 2, February 1995, pp. 33-35.

10. Dinsdale, C., Steel Rails. *Iron and Coal Trades Review*, September 1946, pp. 447-454.

11. Dearden, J., The Centenary of the Steel Rail. *Railway Steel Topics*, Vol. 4, No. 1, 1957, pp. 11-24.

12. Bouse, G. K., Bernstein, I. M., and Stone, D. H., Role of Alloying and Microstructure on the Strength and Toughness of Experimental Rail Steels. *Rail Steels – Developments, Processing and Use*, D. H. Stone and G. G. Knupp, Editors, ASTM, STP 644, 1976, pp. 145-161.

13. McLean, M., Harder Heads Reduce Rail Wear. *Railway Gazette International*, Vol. 153, 1997, p. 607.

14. Kalousek, J., and Magel, E., Rail Profile Grinding: Heavy-haul and Freight Applications. *Railway Track and Structures*, Vol. 93, July 1997, pp. 21-22.

15. Leary, J. F., America Adopts Worn Wheel Profiles. *Railway Gazette International*, Vol. 146, No. 7, July 1990, pp. 526-527.

16. Kramer, J., Demanding the Best: Track Maintenance in Severe Environments. *Railway Track and Structures*, Vol. 92, January 1996, pp. 24-26.

17. Johnson, K. L., *Contact Mechanics*, Cambridge University Press, 1985.

18. Sawley, K. J., Oliva-Maal, D., and LoPresti, J., Effect of Hollow Worn Railroad Wheels on Fuel Use and Track Damage. *RTD, Rail Transportation*, Vol. 15, 1998, pp. 71-75.

19. Clayton, P., Allery, M. P. B., and Bolton, P. J., Surface Damage Phenomena in Rails. *Contact Mechanics and Wear of Rail/Wheel Systems*, University of Waterloo Press, 1982, pp. 419-443.

20. Fahey, W. R., Williams, E. H., Haby, I., and Adamson, W. J., Derailments on a Heavy Haul Railway. *Proceedings of the Heavy Haul Railways Conference, Perth, Western Australia, September 1978*, Australian Institute of Engineering, Session 315, Paper E.4.

21. Nisich, G. L., and Oliver, B. D., Transposing as a Measure to Combat Hunting. *Proceedings of the Heavy Haul Railways Conference, Perth, Western Australia, September 1978*, Australian Institute of Engineering, Session 316, Paper I.11.

22. Kalousek, J., and Bethune, J., Rail Wear Under Heavy Traffic Conditions. *Rail Steels – Developments, Processing and Use*, D. H. Stone and G. G. Knupp, Editors, ASTM, STP 644, 1976, pp. 63-79.

23. Clayton, P., Danks, D., and Steele, R. K., Laboratory Assessment of Lubricants for Wheel/Rail Applications. *Journal of the Society of Tribologists and Lubrication Engineers*, Vol. 45, No. 8, 1989, pp. 501-506.

24. Beret, S., and Trabert, G. R., Railroad Wheel and Track Lubrication: Assessment of Effectiveness. *NLGI Spokesman*, Vol. 55, May 1991, pp. 43-47.

25. Steele, R., Performance Requirements of Railroad Rail. *Mechanical Working and Steel Processing XXVIII: Proceedings of the 32nd Mechanical Working and Steel Processing Conference, Cincinnati, OH, October 21-24, 1990*, pp. 131-142.

26. Anonymous, What Rail Lubrication Means for Rail Wear. *Railway Track and Structures*, Vol. 86, August 1990, pp. 25-26.

27. Sawley, K., Plasma Arc Coatings: Review of Progress and Options for Future. Communication to Dr. Milton Scholl of the Oregon Graduate Institute of Science and Technology, March 1997.

28. Danks, D., *Wear and Microstructure of Eutectoid Steels*, Ph.D. Thesis, Oregon Graduate Center, 1989.

29. Ramaswamy, D., *Wear Behavior of Bainitic Steels*, Ph.D. Thesis, Oregon Graduate Institute of Science and Technology, 1991.

30. Dikshit, V. A., *Rolling Contact Fatigue Behavior of Pearlitic Rail Steel*, Ph.D. Thesis, Oregon Graduate Institute of Science and Technology, 1992.

31. Danks, D., and Clayton, P., Comparison of the Wear Processes for Eutectoid Rail Steels: Field and Laboratory Tests. *Wear*, Vol. 120, 1987, pp. 233-250.

32. McMurchie, D., *Development of a 1080 Steel Plasma Sprayed Coating for Slide/Roll Conditions*, Ph.D. Thesis, Oregon Graduate Institute of Science and Technology, 1996.

33. Niebuhr, D. V., *Development of a Self-lubricating Plasma Sprayed Coating for Rolling/Sliding Wear*, Ph.D. Thesis, Oregon Graduate Institute of Science and Technology, 1997.

34. Clayton, P., Scholl, M., and McMurchie, D., Potential Use of Plasma Spray Coatings for Wheel/Rail Friction Modification. Preliminary Report to Association of American Railroads, Oregon Graduate Institute of Science and Technology, June 1995.

35. Clayton, P., Coatings for Controlling Wheel/Rail Friction. Proposal to Association of American Railroads, Oregon Graduate Institute of Science and Technology, December 1995.

36. Rabinowitz, E., *Friction and Wear of Materials*, John Wiley and Sons, Inc., 1966.

37. Buckley, D. H., *Surface Effects in Adhesion, Friction, Wear, and Lubrication*, Elsevier Scientific Publishing Co., 1981.

38. Schey, J. A., *Tribology in Metalworking: Friction, Lubrication, and Wear*, ASM International, 1983.

39. Krim, J., Friction at the Atomic Scale. *Lubrication Engineering*, Vol. 53, January 1997, pp. 8-13.

40. Czichos, H., *Tribology*, Elsevier Scientific Publishing Co., 1980.

41. Ludema, K. C., *Friction, Wear, Lubrication: A Textbook in Tribology*, CRC Press, 1996.

42. Iliuc, I., *Tribology of Thin Layers*, Elsevier Scientific Publishing Co., 1980.

43. Dowson, D., *History of Tribology*, Longman Inc., 1979.

44. Suh, N. P., An Overview of the Delamination Theory of Wear. *Wear*, Vol. 44, 1977, pp. 1-16.

45. Clements, L. L., Polymer Science for Engineers. *Engineered Materials Handbook, Engineering Plastics, Vol. 2*, ASM International, 1988, pp. 49-50.

46. Holmberg, K., The Mechanism of Lubrication in Low Speed Rolling Contacts. *Journal of Tribology*, Vol. 111, October 1989, pp. 703-707.

47. Destefani, J. D., Introduction to Titanium and Titanium Alloys. *Metals Handbook, 10th Edition, Vol. 2*, 1990, pp. 586-591.

48. Polmear, I. J., *Light Alloy: Metallurgy of the Light Metals, 2nd Edition*, Edward Arnold, Great Britain, 1989.

49. Tian, H., Saka, N. and Suh, N., Boundary Lubrication Studies on Undulated Titanium Surfaces. *Tribology Transactions*, Vol. 32, No. 3, 1989, pp. 289-296.

50. Lebedeva, I. L. and Presnyakova, G. N., Adhesion Wear Mechanisms Under Dry Friction of Titanium Alloys in Vacuum. *Wear*, Vol. 148, 1991, pp. 203-210.

51. Fayeulle, S., Blanchard, P. and Vincent, L., Fretting Behavior of Titanium Alloys. *Tribology Transactions*, Vol. 36, No. 2, 1993, pp. 267-275.

52. Budinski, K. G., Tribological Properties of Titanium Alloys. *Wear*, Vol. 151, 1991, pp. 203-217.

53. Mercer, A. P. and Hutchings, I. M., The Influence of Atmospheric Composition on the Abrasive Wear of Titanium and Ti-6Al-4V. *Wear*, Vol. 124, 1988, pp. 165-176.

54. Ayers, J. D., Wear Behavior of Carbide-injected Titanium and Aluminum Alloys. *Wear*, Vol. 97, 1984, pp. 249-266.

55. Fayeulle, S., Tribological Behaviour of Nitrogen-implanted Materials. *Wear*, Vol. 107, 1986, pp. 61-70.

56. Kaneta, M., Matsuda, K., Matsuda, J. and Utsumi, A., Friction and Wear Properties of Titanium Films Formed on Aluminum by Laser Thermal Spraying. *Wear*, Vol. 156, 1992, pp. 161-173.

57. Dallaire, S. and Cliche, G., Tribological Properties of TiC-Fe Coatings Obtained by Plasma Spraying Reactive Powders. *Journal of Thermal Spray Technology*, Vol. 2, No. 1, March 1993, pp. 39-44.

58. Smith, R. W. and Mohanty, M., Lightweight TiC/Ti Alloy Wear Resistant Coatings for Lightweight Materials in Aerospace Applications. *Proceedings of the 7th National Thermal Spray Conference, Boston, MA, June 1994*, pp. 73-77.

59. Glaeser, W. A., *Materials for Tribology*, Elsevier Scientific Publishing Co., 1992.

60. Smith, A. F., The Sliding Wear of 316 Stainless Steel in Air in the Temperature Range 20-500 °C. *Tribology International*, Vol. 18, No. 1, February 1985, pp. 35-43.

61. Slifka, A. J., Morgan, T. J., Compos, R. and Chaudhuri, D. K., Wear Mechanism Maps of 440C Martensitic Stainless Steel. *Wear*, Vol. 162-164, 1993, pp. 614-618.

62. Sun, Y., Bell, T. and Wood, G., Wear Behavior of Plasma-nitrided Martensitic Stainless Steel. *Wear*, Vol. 178, 1994, pp. 131-138.

63. Smith, A. F., The Unlubricated Reciprocating Sliding Wear of a Martensitic Stainless Steel in Air and CO_2 Between 20 and 300 °C. *Wear*, Vol. 123. 1988, pp. 313-331.

64. Yang, Z. Y., Naylor, M. and Rigney, D. A., Sliding Wear for 304 and 310 Stainless Steels. *Wear*, Vol. 105, 1985, pp. 73-86.

65. Hsu, K. L., Ahn, T. M. and Rigney, D. A., Friction, Wear and Microstructure of Unlubricated Austenitic Stainless Steel. *Wear*, Vol. 60, 1980, pp. 13-37.

66. Dallaire, S., Legoux, J. G. and Levert, H., The Abrasion-wear Resistance of Arc Sprayed Stainless Steel and Composite Stainless Steel Coatings. *Proceedings of the 7th National Thermal Spray Conference, Boston, MA, June 1994*, pp. 609-614.

67. Hodgson, D. E., Wu, M. H. and Biermann, R. J., Shape Memory Alloys. *Metals Handbook, 10th Edition*, Vol. 2, ASM International, 1990, pp. 897-902.

68. Föhl, J., Weissenberg, T. and Wiedemeyer, J., General Aspects for Tribological Applications of Hard Particle Coatings. *Wear*, Vol. 130, 1989, pp. 275-288.

69. *Plasma Processing of Materials*, National Materials Advisory Board, National Research Council, National Academy Press, 1985.

70. Herman, H., Plasma-sprayed Coatings. *Scientific American*, Vol. 259, September 1988, pp. 112-117.

71. Zaat, J., A Quarter of a Century of Plasma Spraying. *Annual Review of Materials Science, Vol. 13*, Annual Reviews, 1983, pp. 9-42.

72. Clare, J. H. and Crawmer, D. E., Thermal Spray Coatings. *Metals Handbook, 9th Edition, Vol. 5*, ASM International, 1982, pp. 361-374.

73. Kearns, W., Editor, *Welding Handbook, 7th Edition, Vol. 2*, American Welding Society, 1976, pp. 367-393.

74. Knight, R., Smith, R. and Apelian, D., Applications of Plasma Arc Melting Technology to Processing of Reactive Metals. *International Materials Reviews*, Vol. 36, No. 6, 1991, pp. 221-252.

75. Apelian, D., Paliwal, M., Smith, R. and Schilling, W., Melting and Solidification in Plasma Spray Deposition - Phenomenological Review. *International Metals Review*, Vol. 28, No. 5, 1983, pp. 271-294.

76. McMurchie, D., Friction Modification Through Surface Engineering. Presentation, Oregon Graduate Institute of Science and Technology, Portland, OR, October 1995.

77. Scholl, M., Clayton, P., Elmore, E., Wooten, J., Sprayforming by High-power, High-velocity Plasma Spraying. *Proceedings of the Fourth National Thermal Spray Conference, Pittsburgh, PA, May 1991*, pp. 281-288.

78. Atteridge, D. G., Refining Technology for the Recycling of Stainless Steel Radioactive Scrap Metals. *DOE Subcontract #C85-110709-002, Report No. 5*, Oregon Graduate Institute of Science and Technology, Portland, OR, 1995.

79. Pfender, E., Fundamental Studies Associated with the Plasma Spray Process. *Proceedings of the National Thermal Spray Conference, September 1987*, pp. 1-10.

80. McMurchie, D., Friction Modification Through Surface Engineering. Qualifier Presentation, Oregon Graduate Institute of Science and Technology, Portland, OR, May 1994.

81. Hirschhorn, J. S., *Introduction to Powder Metallurgy*, American Powder Metallurgy Institute, Colonial Press, 1969.

82. Scholl, M., Plasma Spraying with Wire Feedstock. *Proceedings of the 7th National Thermal Spray Conference, Boston, MA, June 1994*, pp. 491-496.

83. Herman, H., Powders for Thermal Spraying Technology. *KONA*, No. 9, 1991, pp. 187-199.

84. Kollenberg, W. and Decker, J., Influence of Powder Characteristics on the Microstructure of Ceramic Plasma Spray Coatings. *Fresenius' Journal of Analytical Chemistry*, Vol. 346, 1993, pp. 327-333.

CHAPTER 2

EXPERIMENTAL METHODOLOGY AND PROCEDURES

Since the goal of this research was to develop plasma sprayed coatings to modify surface friction of rails, the first focus of the research was to develop suitable coatings. Prospective coating materials were optimized, sprayed, and then tested using the Amsler test machine. After coatings demonstrated required wear properties on the Amsler, they were then tested in full scale tests. At various points in the process, coatings were examined and characterized using a variety of techniques. After full scale testing, failure analysis of the coatings sought to understand the coatings' wear performance.

Several types of plasma spray coating systems were examined during the course of this research. Some of the coatings were sprayed of a single layer metal using a wire feedstock while others were composite coatings that were sprayed using both wire and powder feedstocks. Multi-layered coatings were created by first spraying a base metal coating using wire feedstocks followed by a second layer of polymer using powder feedstocks.

The experimental chapter is divided into two major topics. In the first section, the equipment and the standard procedures that were used for coating characterization and wear performance testing are described. This is followed by sections describing parameter optimization and preparation of substrates. The final sections describe the laboratory scale testing and analysis, and failure analysis of full scale test specimens.

2.1 EQUIPMENT AND PROCEDURES

Contained in the following section are descriptions of the equipment and procedures used during this research project. The equipment and standard procedures include a variety of testing, measurement, and analysis techniques including plasma spraying, Amsler testing, optical and scanning electron microscopy.

2.1.1 Plasma Spraying

The plasma spraying section describes the type of plasma spraying equipment and set-up used at OGI. This is followed by the procedures used to spray Amsler rollers, full scale specimens and tensile test specimens. The types of feedstock materials are also covered.

2.1.1.1 Plasma spray equipment

A Plazjet II 200 kW high velocity plasma spray system was used for this research. A high velocity system can spray high density, low porosity coatings and is capable of higher deposition rates, ten times that of a conventional system [1]. The higher power output of the system allows the deposition of multiple wire and powder feedstocks while still maintaining a relatively cool substrate. The supersonic plasma velocities in the Plazjet impart sonic or near sonic velocities to the sprayed particles. Plasma temperatures, which range from 10,000 °C to 50,000 °C, allow full melting of high melting point oxide powders.

Two 100 kW DC rectifiers, connected in series, provide power at 200 V and 500 A. The entire plasma spray system is housed in a 6.8 m^3 acoustic room equipped with a 1.8 m water curtain for collecting overspray. Other features of the system include a material recycle tent with a high efficiency particulate after-filter. The plasma gun is a non-

transferred DC arc type. Figure 2.1.1.1 shows a schematic of the OGI hyper-velocity plasma spray gun. Both wire and powder feedstocks enter the plasma stream external to the gun, Figure 2.1.1.2. Power conversion in the gun is estimated at 75% [2].

A three channel mass flow control is used to regulate primary and secondary gas flow rates. Various gases can be used for spraying with this system, and thus gas characteristics can be tailored to suit particular project applications. Generally, standard grade nitrogen was used as the primary gas and powder carrier gas due to its lower cost. The secondary gas was standard grade hydrogen. Air, carbon dioxide, or argon, chosen for a particular application and heat capacity, were used to cool the samples during spraying. The gas supply pressures were usually in the range of 1.25 to 1.38 MPa to obtain a 300 slpm gas flow volume.

Two different types of powder feeders were used with the OGI plasma spray system, a Plasma-dyne Rotohopper wheel type powder feeder and a Sylvester Mark XV screw type powder feeder. The Mark XV was equipped with a 4 turns/2.5 cm auger screw. This feeder assisted powder flow and prevented segregation of different particle sizes and weights. Powder spraying efficiency was approximately 50%. The Plasma-dyne Rotohopper was equipped with either a high volume or a low volume feed wheel allowing a greater control of the amount of powder added to the sprayed coating. Wire was fed using one or two push-pull wire feed units which allowed simultaneous powder and wire deposition. Figure 2.1.1.3 shows the OGI plasma spray system schematically.

2.1.1.2 Set-up

Depending on the configuration of the substrate sprayed, different arrangements of fixtures, cooling lines, and feed tubes were used. Figures 2.1.1.4 (a) to (c) show the fixtures used to hold substrates during plasma spraying. Figure 2.1.1.4 (a) shows the fixture used for spraying Amsler rollers. The fixture was a round piece of bar stock having the same

diameter as the Amsler rollers' inside diameter. One end of the bar was placed in a chuck that rotated at 200 rpm. An overspray tube was placed at the end followed by a maximum of five Amsler rollers and a witness sample. A graphite washer was placed between each roller and the overspray tubes to make removal of the coated rollers possible without damaging them. A second overspray tube completed the assembly and was held tightly in place in the threaded end of the fixture using a bolt and washer. Figure 2.1.1.4 (b) shows the fixture used for flat steel coupons, which were 10 by 1.25 by 0.65 cm. Flat coupons sat on a small ledge and were held against the flat surface using washers and screws. Figure 2.1.1.4 (c) shows the fixture used for spraying tensile testing samples. The tensile bar fixture was a piece of angle iron with threaded holes at intervals. The round substrates were placed on the sides, surfaces aligned to the same working distance, and held in place with a metal strap. Washers were used as spacers to keep the bars from touching each other.

Cooling jets were placed at different locations relative to the substrate depending on specimen geometry. For round specimens coated on the outside diameter, cooling tubes were located behind the centerline as shown in Figure 2.1.1.5 (a). This was termed backside cooling and was performed with CO_2 or air. For substrates that presented a flat face to the plasma jet, the cooling tubes were placed in front of the substrate on opposite sides of the plume, Figure 2.1.1.5 (b). This allowed the cooling gas to strike the surface of the substrate after it was sprayed, thus, reducing the temperature before the next pass. In some cases no cooling gas was used, such as with very thin coatings sprayed for short times.

The location of the feed tubes was a parameter that was varied depending on the material being sprayed. For all the wire feedstocks, the wire entered the plume as close to the gun tip as possible, 10 to 15 mm away at a 45 degree angle. For the dual wire feedstocks, the tubes were placed on opposite sides of the gun to reduce perturbations in the plume. Powder injectors were placed farther away from the gun tip than the wire injectors. Table 2.1.1.1 lists the powder injector locations for the various materials sprayed. Two powder feed tubes were

placed on opposite sides at angles of either 45 or 90 degrees to the plume. Figure 2.1.1.6 (a) shows the location of the wire feed tubes and the powder feed tubes along the perimeter of the gun tip, while Figure 2.1.1.6 (b) shows the entry points along the plume.

The working distance from the gun tip to the substrate surface also required adjustment prior to spraying. The path of the gun was adjusted so that the gun traversed parallel to the substrate faces. All the substrates were sprayed at 90 degrees to the gun. Table 2.1.1.2 lists the working distances for each of the coating materials sprayed.

2.1.1.3 Procedure for spraying Amsler rollers

After parameters were optimized, Amsler roller surfaces were prepared for grit blasting by washing with detergent and water, drying with compressed air, rinsing with acetone, and drying with compressed air. After grit blasting, the rollers were rinsed with acetone, dried with compressed air and then plasma sprayed. Each set of up to five rollers was sprayed along with a witness sample, a low carbon steel roller in the same dimensions as the Amsler roller but without the top hat profile. Witness samples were used to verify the microstructure of the coatings for different spray batches.

Coating thickness was controlled during spraying by the number of passes back and forth across the roller surfaces. By maintaining a constant traverse speed, increasing or decreasing the number of passes varied the coating thickness. The traverse speeds ranged from 25 to 35 passes per minute. A 1 mm coating was the target thickness for most Amsler rollers. A special study was undertaken to examine the effect of coating thickness on wear properties, for thickness ranging from 0.25 to 1.5 mm. For the composite coatings, a 15 to 20 pass bond coat was sprayed before the second phase material was added. After the rollers were cooled, they were removed from the fixture and the next batch of rollers was sprayed.

2.1.1.4 Procedure for spraying full scale samples and rail

Plasma spraying of the full scale samples was performed on three different types of substrates depending on the test performed. For the track lab tests (designated TL1 to TL4) the substrates were 61 by 5.7 by 7.6 cm 4340 steel coupons. These were machined in the profile of the railhead. For the rolling load tests (designated RL1 to RL5), the substrates were 90 cm sections of either standard carbon rail or new head-hardened rail. The FAST rail substrate was a 3.6 m section of new rail. Initially, full scale test surfaces were prepared by the same methods used for the Amsler rollers, which was washing with detergent and rinsing with water, then drying with a blast of compressed air. An acetone rinse and air drying followed to remove any oils. Next the surface was grit blasted with alumina, rinsed with acetone and dried with compressed air.

The full scale test samples were initially sprayed using the parameters 230/30/235 for N_2, H_2, and working distance, respectively. (The first number in this series indicates the primary gas flow rate in slpm, the next refers to the secondary gas flow rate in slpm and the final number indicates the working distance in mm. This convention will be followed in the rest of the document.) In some cases, the plasma sprayed steel coating was further coated with nylon as a friction reduction coating using the parameters of 200/250/255. Special fixturing was developed which enabled the coupon and rail specimens to be held firmly and rotated during spraying so that both the running surfaces and gage faces could be sprayed. Figure 2.1.1.7 shows the fixturing for the 3.7 m FAST rail, with the gage face of the rail towards the plasma spray gun. Spraying was performed by traversing along the length of the stationary rail surface; at the end of the traverse, the substrate was rotated slightly and spraying continued. Spraying was continued until the gage face and running surfaces of the samples were completely coated and the coating thickness built up to the desired level.

After testing of the first three full scale samples, TL1, TL2, and RL1, was completed, surface preparation and plasma spraying parameters were re-optimized to improve coating

performance. To improve coating adhesion, the grit blasting method was changed from a single step Al_2O_3 process to a two-stage process of Al_2O_3 to clean the surface, followed by steel grit to increase the roughening of the surface. For the FAST rail, the surface was wire brushed prior to grit blasting. The re-optimized wire spraying parameters were 230/75/235. Details supporting the need for parameter re-optimization are included in the results sections on failure analysis of TL1, TL2, and RL1.

2.1.1.5 Plasma spraying tensile test specimens (for coating adherence)

Tensile test specimens were made from 3.6 cm round steel bar stock approximately 15 to 30 cm in length. The ends of the bars were machined flat on a lathe, polished, then prepared for plasma spraying using previously described preparation procedures. The test matrix for the coatings examined three problems, viz., the effect of surface preparation, the effect of plasma spray parameters, and the effect of second phase particles, Table 2.1.1.3. To examine the effect of surface preparation on tensile strength, samples were sprayed with 1080 steel after grit blasting with either alumina, iron shot, steel shot, a 50/50 mixture (by volume) of alumina and steel shot or the two-stage process. The two-stage process consisted of first grit blasting with alumina to clean the surface followed by steel shot to roughen the surface. This technique was later also used for preparing full scale specimens after re-optimization of the grit blasting process.

To examine the effect of spray parameters, samples were sprayed with 1080 steel using 230/30/235, 230/75/235, or 300/75/235. Titanium and stainless steel powder were added to 1080 steel to test the effect of second phase additions on coating strength. Three samples were made for each of the conditions investigated. After plasma spraying, the tensile bars were rinsed in acetone and dried with a blast of compressed air. A second set of unsprayed bars was prepared as mating surfaces for the sprayed bars. These were also grit blasted and cleaned according to standard procedures. A plasma sprayed and unsprayed bar

were joined together with a thermosetting epoxy adhesive (3M 2214 Hi-Density Epoxy Adhesive). Figure 2.1.1.8 shows a schematic of the tensile test specimens. To verify the epoxy strength, two uncoated bars were glued together. The tensile specimens were placed in a furnace and cured for 1 to 2 hours at 190 °C.

2.1.1.6 Feedstock materials

A variety of feedstocks were used for this project including wire, powder, and combinations of both wire and powder. For the stainless steel work, a single 1.6 mm 308L Si welding wire (Arcos Alloys) was sprayed. The wire feeder was placed at a setting of 1.5 resulting in an expected feed rate of 33 g per minute. The actual wire deposition rate fluctuated from 19.0 to 23.8 g per minute. For the composite steel coatings, two 1.6 mm 1080 steel wires were sprayed. Table 2.1.1.4 [3, 4] lists the elemental composition of the 1080 steel wire. The titanium powder was pure titanium and the stainless steel powder was a 316 austenitic stainless, Table 2.1.1.4. Neat Nylon 11 powder was used to spray polymeric coatings.

2.1.2 Grit Blasting

Grit blasting was performed using a suction blast system, manufactured by Davis Sandblasting. In this system, compressed air, typically between 0.55 to 0.69 MPa, was used to propel the abrasive medium through the 7 mm inner diameter nozzle. The compressed air line contained an oil and water filter system to minimize possible contamination during the drying step. After the abrasive was sprayed over the work-piece, it was returned to the hopper and recycled. Coarse contaminants were filtered out of the abrasive by a screen, while fine contaminants remain suspended in the air and were carried to a dust collector.

2.1.3 Amsler Testing

2.1.3.1 Amsler testing machine

Wear testing was performed using an Amsler twin disk tribometer, Figure 2.1.3.1, that generates rolling/sliding wear. Test rollers are placed on two parallel, horizontal shafts, Figure 2.1.3.2. The bottom shaft is driven by a motor; the top shaft is geared to the bottom shaft. The gearing is such that the bottom shaft rotates 1.104 times faster than the top shaft. For this research the top hat roller profile was used, Figure 2.1.3.3.

Since the rollers are moving at different tangential speeds, sliding occurs at the contact surface. The slide/roll ratio, γ, is defined by

$$\gamma = \frac{d_s}{d_r}$$

where d_s is the sliding distance relative to the contact surface and d_r is the average rolling distance of the top and bottom rollers. The slide/roll ratio can be calculated by

$$\gamma = \frac{2\,(1.104\,D_2 - D_1)}{1.104\,D_2 + D_1}$$

where D_1 and D_2 are the diameters of the top and bottom rollers, respectively. By varying the diameters of the top and bottom rollers, the slide/roll ratio can be changed.

A load is applied to the roller surfaces through a coil spring mechanism. Contact pressures ranged from 900 MPa to 1220 MPa. The maximum Hertzian contact pressure, P_o can be determined by

$$P_O = 0.418\left(\frac{L\,E}{W\,R}\right)^{\frac{1}{2}}$$

where L is the contact load, E is the Young's Modulus of the material, W is the contact width of the rollers (5 mm), and R is the effective radius given by

$$\frac{1}{R} = \frac{1}{R_1} + \frac{1}{R_2}$$

where R_1 and R_2 are the radii of the top and bottom rollers, respectively.

The number of revolutions during the test was measured by a counter connected to the bottom shaft. A strip chart recorder connected to a torque dynamometer measured the torque during the test. From the strip chart, the coefficient of friction was measured using the relationship

$$\mu = \frac{2.75\,M}{W\,L\,R_2}$$

where M = deflection/8, W is the contact width, L is the contact load, and R_2 is the radius of the bottom roller in meters. The number 2.75 is a constant adjusted for this specific Amsler machine. Figure 2.1.3.4 shows a schematic of a typical strip chart with the definition of deflection. After the initial run-in period, wearing of the surfaces takes place and the friction stabilizes to a steady state value.

2.1.3.2 Wear testing procedures

For this investigation, the top rollers were plasma spray coated. The top roller was the tested specimen since the wear behavior of the top simulates revenue rail wear [5]. The bottom roller was uncoated wheel steel with a machined finish. Prior to the test, both rollers were cleaned with detergent and water, dried with a hot air gun, then rinsed with acetone and dried with compressed air. Measurements were made of the initial weights and diameters of the rollers. Subsequent weight and diameter measurements were made periodically by stopping the test. The weight loss of the rollers was calculated and the data graphed with weight loss as a function of revolutions.

Rollers used in this investigation were machined into the top hat configuration shown in Figure 2.1.3.3. Amsler top rollers were machined from standard carbon rail material with the roller axis parallel to the longitudinal direction of the rail as shown in Figure 2.1.3.5 (a). The uncoated top rollers ranged in diameter from 32 to 34.5 mm depending on the final coating thickness. The coating thickness plus the roller diameter were targeted for a 35 mm top roller diameter. The bottom rollers were machined from a Class C wheel with the roller orientation as shown in Figure 2.1.3.5 (b). Diameters for the bottom rollers were either 33.3 mm or 45 mm for 5% and 35% slide/roll ratio tests, respectively. The composition of the wheel steel and the rail steel are shown in Table 2.1.3.1 [5].

2.1.4 Full Scale Tests

Full scale testing of 1080 plasma sprayed steel and stainless steel coatings was performed to evaluate the coatings' performance in rolling/sliding wear. Full scale tests are designed to approximate the type of conditions found in revenue rail service. After plasma spraying the rails at OGI, the full scale samples were sent to the Association of American Railroads Transportation Technology Center in Pueblo, Colorado. Table 2.1.4.1 lists the full scale samples and coating data for samples sent to AAR for testing. Three types of full

scale tests were performed: rolling load machine, track lab, and tests at the FAST track. After testing was completed, the rail samples were returned to OGI for failure analysis. The factors contributing to the coating wear process were investigated.

2.1.4.1 Rolling load tests

Five coupons underwent rolling load testing, one tested with the old rolling load machine and four coupons using the new rolling load machine. The first rolling load coupon (RL1), tested on the old rolling load rig, was a 90 cm long section of rail which had been plasma sprayed over the center 60 cm of the rail head. Each of the new rolling load coupons was 1.8 m long rail sections with a 60 cm long sprayed section in the middle of each half. Figure 2.1.4.1 shows schematically how the rolling load machine works. For these tests, a wheel loaded with 155 to 200 kN is rolled over the specimen, either by moving the wheel or the coupon as shown. Pure rolling or rolling/sliding testing can be performed, however, the amount of the slide/roll ratio was unknown due to equipment problems.

2.1.4.2 Track lab tests

Four specimens were tested in the outdoor track lab at the Pueblo, Colorado facility. The 60 cm long test coupons were machined from 4340 steel into a form that mimics the rail head shape. Coatings were sprayed over the entire length of the coupons. Track lab test set-up and specimen are shown schematically in Figure 2.1.4.2. For this test, a 4-axle car with wheel loads of 228 MPa passed back and forth over the coupon in pure rolling. Speeds of the car ranged from 16 to 24 kmph. The track lab test is performed outdoors.

2.1.4.3 FAST track tests

The FAST test sample was a 3.7 m long section of rail which was plasma sprayed over the center 3 m of the rail. Figure 2.1.4.3 shows the outdoor FAST track schematically. The rail was placed at the entrance to section 2 of the high tonnage loop where the curvature is 2 to 3 degrees. The train consisted of 4 locomotives and 75 cars under heavy axle loads (350 kN per train pass). The train speed was 64 kmph on all but the first pass which was between 16 to 24 kmph. The outside temperature was 7 °C.

2.1.5 Tensile Testing

Tensile testing was performed using a Satec Universal testing machine equipped with quick release grips. The load limit range was set at 10,900 kg. Samples were loaded until failure and the maximum load to failure recorded. The ultimate tensile strength was calculated by dividing by the joint surface area. After testing, the failed coatings were examined for evidence of adhesive and cohesive failure. Both halves of the failed joints were sectioned, mounted in phenolic, and prepared for metallography using standard metallographic procedures. Samples were examined using both an optical microscope and a scanning electron microscope (SEM).

2.1.6 Hardness Measurements

Microhardness testing was performed on polished samples using a Leco MP401 tester with a Knoop diamond indenter. A load of 300 g was used with a dwell time of 15 seconds. In some cases, such as testing individual splats or very thin coatings, lighter loads ranging from 15 to 50 g were used. Both the substrate and the coating were measured at locations in and outside the wear track. Substrate hardness measurements were made parallel to the surface and coating hardness measurements, unless otherwise indicated, were made perpendicular to the surface. Coating measurements performed perpendicular to the surface

were found to average the coating hardness better because they span more lamellae. Microhardness indents made parallel to the coating surface span fewer lamellae. Figure 2.1.6.1 shows microhardness indents running parallel and perpendicular to the coating surface. Measurements of individual lamellae were made parallel to the coating surface. Ten or more measurements were made and the average and standard deviation calculated.

2.1.7 Surface Roughness Measurements

Surface roughness was measured using a Mitutoyo Surftest 401 profilometer. An analyzer was used to collect and to calculate the various surface roughness parameters as well as to print surface profiles. Measurements were taken in random locations and orientations on the sample surfaces. Five or more measurements were made and the average and standard deviation calculated. The samples tested were either flat coupons or sections of rail. For the rail sections, readings were taken across the flat portion of the railhead. The measurement parameters for range and sampling length varied depending on the size of the sample. The number of sampling lengths was five, the highest possible, since the higher number of sampling lengths produces a more repeatable surface roughness value. Surface roughness parameters were measured according to DIN standards.

2.1.8 Metallographic Specimen Preparation

Metallographic specimens were prepared by different techniques depending on two factors: the type of testing the samples underwent and the purpose of the metallographic investigation. Some of the tests imparted greater amounts of damage to the coatings' microstructure. The friable oxide phase of the coating was susceptible to cracking and pullout if not prepared carefully. By using different sectioning and mounting techniques, this damage was reduced. Preparation techniques that resulted in the least amount of pullout possible were preferable when porosity measurements were to be performed.

Sample sectioning was performed using four different methods. For gross sectioning of large pieces, such as the rails, a band saw was used. Smaller pieces were sectioned using a Leco abrasive saw. The abrasive saw was used only for cutting samples to size, not for cutting faces that were to be mounted, since, in most cases, the surface damage induced by the blade was found to be too extensive. Sectioning for mounted faces was performed using a high speed "slice and dice" saw equipped with a diamond blade. For debonded coating samples, a slow speed diamond saw was used.

Wear tested Amsler rollers were sectioned to show the coating microstructure both longitudinal and transverse to the rolling direction as shown in Figure 2.1.8.1 (a). Witness samples were sectioned longitudinally only. The parameter optimization coupons were sectioned perpendicular to the spraying direction as shown in Figure 2.1.8.1 (b).

The mounting technique used also depended on the samples' test history. Cold mounting, in epoxy, under pressure or vacuum, was used for coatings that had undergone Amsler or full scale wear testing. Cold mounting in epoxy was found to preserve the original coating condition without introducing further damage. Hot mounting in phenolic was used for witness samples, tensile tested samples and 3M epoxy/aluminum strip reinforced samples. Also hot mounting was used in cases where potential cracking induced by the mounting process was not critical. In some cases, the samples were prepared in the unmounted condition.

After mounting, the samples were ground and polished. The grinding procedure was wet grinding with silicon carbide paper at 120, 240, 400, 600, and 800 grit. Polishing was performed using 6 μm diamond paste followed by 1 μm diamond paste on a "hard" synthetic napless cloth. Final polish consisted of 0.05 μm neutral pH alumina suspension used on a neoprene cloth. After polishing, samples were cleaned with detergent and water and dried with compressed air. To remove water spots, the samples were rinsed with methanol and dried under a hot air gun. Where necessary, samples were etched using 2% Nital.

2.1.9 Optical Microscopy

Optical methods were used to investigate the overall features of the coatings and as a screening device for coatings requiring further investigation in the SEM. The optical microscope was also used to scan the samples for debonded regions in the coatings. The samples were examined in the polished condition.

Optical characterization was performed using a Nikon Epiphot inverted stage microscope and a Nikon SMZ-U Zoom stereomicroscope. The Epiphot was used at magnifications of 50x to 400x and the stereomicroscope at 4x to 75x. Bright field imaging was used in all cases. Samples were imaged in the unetched condition unless otherwise indicated. The stereomicroscope was used for single splat analysis while the inverted stage microscope was used for image analysis and coating phase distribution studies.

2.1.10 Scanning Electron Microscopy

A Zeiss DSM 960 scanning electron microscope, equipped with a Link X-ray Analytical energy dispersive spectrometer, was used for sample imaging, energy dispersive spectroscopy, and mapping. Samples were imaged in the as-received and mounted condition. Both secondary electron (SE) and backscattered electron (BSE) imaging were used to examine the samples. Mounted samples, as well as powder samples, were sputter coated with 200 Å of Au-Pd or carbon to reduce charging caused by the mounting materials and coating oxides.

A variety of SEM parameters were used for investigating the samples depending on the coating and the goal of the experiment. Working voltages ranged from 5 to 30 kV and working distances from 11 to 31 mm. For imaging, the shorter working distances were used while for energy dispersive spectroscopy longer working distances were used. Lower working voltages were used to examine samples that were susceptible to charging and for

energy dispersive spectroscopy of the lighter elements. Higher working voltages were used for energy dispersive spectroscopy of heavier elements and for imaging when charging wasn't a concern.

Energy dispersive spectroscopy was performed on the samples to investigate coating constituents. The Link Pentafet light element detector was operated using the "no window" turret position when performing analysis of materials thought to contain oxygen or carbon. Backscattered electron imaging mode was used during spectra collection in order to distinguish between constituents having different average atomic numbers. The higher the average atomic number of a material, the lighter the appearance of the phase. Semi-quantitative analysis was performed using the ZAF-4/FLS program's "normalized processing for all the specified elements" option.

The interface between the coating and the substrate was examined for evidence of contamination and debonding. The SEM was used to image and identify the contaminants present at the interface. Mounted and unmounted samples were examined in the unetched condition.

2.1.11 Image Analysis

A Leco 2001 image analysis system was used to quantify many of the coating characteristics. The Leco was directly coupled to the Nikon Epiphot for imaging mounted samples. For particle size analysis, the Leco was coupled to the Nikon stereomicroscope. Digitally collected SEM images were dealt with in one of two ways. They were either transferred to the Leco system or processed in a Macintosh based image analysis program. The disadvantage in transferring digital images to the Leco is that it can only handle images 512 x 512 pixels in size.

Coating thickness was measured for wear tested rail as well as witness samples. Samples were examined in the unetched condition at magnifications of 50x to 100x. A routine, or sequence of image analysis operations needed to obtain quantitative information on coating thickness, was developed which allowed a consistent measurement methodology for all samples. User defined values for histogram modification, thresholding, and length limiting were entered as part of the set-up for each sample. The results given are an average of 10 or more random fields of measurement, each of which was measured at 10 or more locations within the field.

Porosity was measured using unetched mounted samples of the coatings. Images were collected and adjusted for contrast and brightness. After sharpening was performed, the images were threshholded to obtain only the porosity, which showed as black in the image. An average of 10 or more fields were measured.

The amount of second phase in the multi-phase steel coatings was found using mounted samples which were etched in 2% Nital. Images were collected and contrast and brightness adjusted. Sharpening was performed followed by thresholding to obtain the second phase particles that showed as white regions in the image. The results given are an average of over 10 or more random fields of measurement.

2.2 PARAMETER OPTIMIZATION STUDY

This section describes the procedures used in optimizing the plasma spray parameters to obtain the best quality coatings. Parameters were optimized using a variety of methods. The methods used were single splat analysis, coupon verification or a combination of both.

The single splat analysis technique consisted of passing glass microscope slides rapidly through the plasma stream so that a small number of molten particles were collected

from the center of the plasma plume at the correct working distance. The individual splats collected on the glass slides were evaluated for appearance. The stereomicroscope was used to examine the splats, since, when illuminated using side lighting, the three-dimensional nature of the particles was emphasized. Splat characteristics such as flatness, shape, size and size distribution were noted. These characteristics indicated whether particle velocity and heating were optimized for the particular material being sprayed. Parameters were adjusted and new slides made to check the results until optimum splat morphology was obtained.

Coupon verification consisted of spraying flat steel coupons and then performing metallography on the resulting coating. Coating characteristics were evaluated for porosity, inclusions, oxides, and melted and unmelted particle content. Parameters were adjusted as in single splat analysis; however, the process of iteration was more time-consuming.

The main parameters that were varied during optimization were the primary gas flow rate, the secondary gas flow rate and the working distance. The primary gas was nitrogen and the secondary gas was hydrogen for all coatings sprayed for this research. Other parameters, which were varied once the main ones were finalized, were those relating to feedstock injection into the plasma stream such as injector location and angle of injection.

Parameter optimization for the stainless steel work used the parameters developed by McMurchie [6] for 1080 steel coatings. The matrix of parameters tested using single splat analysis is shown in Table 2.2.1, with those suggested by McMurchie in bold characters. The primary and secondary gases were varied while the working distance was held at 225 mm. A single wire was used for all the stainless steel plasma spraying work.

The parameters used as a starting point for optimization of 1080 steel composite coatings were originally developed for friction reduction coatings [7]. These parameters, 230/30/235, were developed for a single wire feed, while for this research a dual wire feed was used. Parameter optimization for dual wire feed presented additional challenges.

Difficulties were also encountered when both powder and wire feedstocks were co-sprayed. Poor powder characteristics were also a problem during plasma spraying. Powder feed and carrier gas rate parameters were studied during initial parameter optimization of the composite coatings.

The coupon test matrix for composite 1080 steel coatings is shown in Table 2.2.2. Single splat analysis was used to verify the 1080 steel parameters and the powder parameters separately due to difficulties in distinguishing between the two types of particles. Once the optimum spray parameters were narrowed down, low carbon steel flat coupons, 10 by 1.25 by 0.65 cm in size, were sprayed and analyzed. Flat coupons provided an inexpensive method for verifying the coating produced from a set of parameters instead of using machined Amsler rollers.

The microstructure of the coupon coatings was evaluated optically for characteristics such as distribution of the phases, porosity, unmelted particles and oxide content. For the composite coatings, a 2% Nital etch was performed to distinguish between the steel and the second phase materials. By over-etching the steel, the second phases, titanium and stainless steel, which did not etch, were resolved more easily using optical methods.

2.3 PREPARATION OF SUBSTRATES (GRIT BLASTING STUDY)

Prior to plasma spraying, the surfaces of the substrates need to be prepared to ensure that the coatings adhere properly. Various methods have previously been investigated at OGI for preparing the surfaces, from machining grooves into the surface [6] to using different types of grit media and blasting parameters. The investigation into the effectiveness of the various grit media and blasting parameters is described in the following sections. Included in this study is a detailed assessment of a variety of surface cleaning and roughening techniques on subsequent coating quality.

2.3.1 Grit Blast Media and Impact Angle Experiments

Three different types of grit blast media and two impact angles were tested using 3.8 cm diameter by 5.1cm long sections of steel. The end surfaces of eleven round bars were machined flat and then polished to a 400 grit finish to create a blemish free surface. The sections were cleaned with detergent, rinsed in water and dried with compressed air. A final flush wash with acetone and drying with compressed air completed the pre-grit blast preparations. Grit blasting was performed on ten of the samples using different grit media and impact angles. One sample was used as a control. The grit materials used were alumina, silica and steel shot and the impact angles were 45 and 90 degrees. Table 2.3.1.1 shows the various grit blasting conditions tested. After grit blasting, the samples were rinsed in acetone and dried with compressed air to remove residual grit blasting debris.

The grit blasted surfaces were examined in the SEM at both high and low magnification. Surface morphology and the presence of any embedded grit particles were noted. Fresh, unused 25 and 36 grit alumina particles were mounted onto aluminum stubs using graphite tabs, plated with 200 Å Au-Pd, and examined in the SEM. Energy dispersive spectroscopy was performed on the grit blasted samples and grit media to identify chemistries.

The Mitutoyo Surftest 401 profilometer with a skidless probe was used to determine the surface roughness of each sample. A total of five measurements were taken at varying locations and directions on each sample and the average calculated. The measuring parameters were: range = 20, $\lambda c = 2.5$ mm, and $L = 5$. Strip charts were plotted for each of the sample surface profiles.

2.3.2 Substrate Hardness

The effect of substrate hardness on the surface roughness was investigated. Two types of rail were used for this study, new low hardness, hot-rolled rail and worn high hardness, head-hardened rail. Pieces of new and worn rail were cut into 10 to 15 cm lengths, then scrubbed with a detergent, rinsed in water and dried with compressed air. Then a solvent rinse and air dry followed. The new and worn rail samples were grit blasted with the various surface preparation methods listed in Table 2.3.2.1. The surface preparation methods were alumina, Fe shot, steel shot, a 50/50 mixture of alumina and steel shot and a two-stage process (alumina followed by steel shot). Approximately 2 minutes of total grit blasting time was required to prepare the surfaces of each rail section. The sections were then rinsed in acetone and dried with compressed air to clean off grit blasting debris.

The surface roughness was measured with the Mitutoyo Surftest 401 profilometer using a skidless probe. The measuring parameters were: range = 20, λc = 2.5 mm, and L = 5. A total of ten measurements were made on each rail surface in different locations and orientations. A representative strip chart of the surface profile was recorded for each sample.

2.3.3 Dwell Time

Grit blasting was performed on lengths of flat steel strip for times ranging from 1 to 120 seconds. The material used was 36 grit alumina. Alumina was chosen for this study because of the high contrast in backscattered imaging mode between the steel substrate and the alumina. During grit blasting, the distance from the substrate to the gun was held at approximately 2.5 cm with an impact angle of 90 degrees. The gun was held stationary for the test duration so that only one location was grit blasted. The grit blasted strip was then rinsed in acetone to remove loose debris and dried with compressed air.

The surface roughness of each grit blasted area was measured with the Mitutoyo Surftest 401 profilometer using the skidless probe. An average of ten measurements, in various directions, were performed on each spot. The profilometry parameters were: range = 20, $\lambda c = 0.8$ and L = 5.

After profilometry, the grit blasted surfaces were examined in the SEM using 20 kV at 11 to 13 mm working distances in secondary imaging mode. Representative photographs were taken of each surface to compare the amount of contamination.

Random cross-sections were cut from each grit blasted area and mounted in phenolic. Standard metallographic procedures were used to prepare the samples. A 200 Å thick Au-Pd coating was sputtered onto the mounts prior to SEM examination. The surfaces of each cross-section were examined for evidence of grit contamination and disturbed material. Under backscattered imaging the embedded alumina appeared dark gray compared to the light gray of the steel test coupons, making it easier to determine the amount of contamination. Energy dispersive spectroscopy was performed to verify the contaminant chemistry.

A section of each sample cross-section was randomly selected and a series of images were digitally collected at 500x using NIH Image 1.60. The images were printed and a composite image of the length of sample surface was made. The composite images were used to measure the amount of surface contamination present using lineal analysis. Calipers were used to measure the length of uncontaminated surface. The lengths were totaled and divided by the total surface under examination to get the percentage of uncontaminated surface. The error in the reading was found to be approximately 5%.

2.3.4 Tensile Testing

The adhesive strength of a coating is an important factor in a coating's durability. Spalling of a rail coating during wear testing has been shown to cause full scale failure. Various methods of surface preparation can affect the ability of a coating to adhere to the substrate. Tensile testing is one method of quantifying the strength of a coating prepared by different surface preparation processes. Test samples were made by gluing a plasma spray coated surface to an uncoated surface and the joint tested under tension. Obtaining the coating strength value required failure of the coating before glue failure.

A series of tensile bars were made to test the adhesive strength of 1080 steel coatings prepared using different grit blasting processes. The different grit processes used are shown in Table 2.1.1.3. The two-stage process used first alumina to clean the surface from scale and debris, followed by steel shot to provide greater surface roughness. The 50/50 mixture consisted of a physical mixture by volume of alumina and steel shot. The 3.6 cm diameter tensile bars were prepared by machining the face flat, polishing with 400 grit paper to remove machining grooves, then grit blasting. After grit blasting the surfaces were rinsed with acetone and dried with compressed air.

Plasma spraying parameters for the 1080 steel were the same as those used for the plasma sprayed rails [7]. Table 2.3.4.1 lists the spraying parameters for this experiment. The tensile bar fixture was a piece of angle iron with threaded holes at intervals as described in Section 2.1.1.2. Approximately 15 to 20 passes were made to achieve a 0.5 mm coating. The bar ends were sprayed in halves (top, then bottom) with the exception of one set that was sprayed in thirds (top, middle, bottom). These spraying patterns attempted to provide a uniform coating thickness on the faces of the tensile bars. Difficulties were encountered in obtaining a uniform coating thickness.

The bars were prepared for tensile tests by gluing one plasma spray coated bar to an uncoated bar. The uncoated bar surfaces were grit blasted with the same media. Both sets of bars were then cleaned with acetone and dried with compressed air. The pairs of bars were glued together with 3M 2214 High Density Epoxy Adhesive. After gluing, the bar sets were placed in a furnace at 190 °C for 1 to 2 hours until cured. Six pairs of tensile bars were glued at a time along with a set of two uncoated bars for testing the strength of the epoxy. After the bars had cured, they were removed from the furnace and allowed to air cool.

Tensile testing was performed using the Satec testing machine equipped with quick release grips. The load range was 10,900 kg. Bars were installed in the grips and a load applied until failure occurred. The maximum load was recorded as well as failure mode, although, this was sometimes hard to determine from visual inspection alone. The ultimate strength of the coatings was calculated by dividing the maximum load by the surface area of the glued joint. Cross-sectional metallographic samples were prepared from each of the bars following standard procedures and were examined for mode of failure.

2.3.5 Amsler Testing

To determine whether surface preparation affects the coating durability under wear conditions, two different series of Amsler rollers were made. One group of rollers was sprayed with 1.6 mm 1080 steel wire and the other group was sprayed with 1.6 mm 308L Si wire. For each group of rollers, different grit blasting processes were used to prepare the surfaces of the rollers prior to spraying. All the rollers were prepared for grit blasting by washing with detergent, rinsing thoroughly with water and drying with a blast of compressed air. This was followed by flushing with a solvent, acetone or ethanol, and then once again drying with compressed air. The grit blasting impact angle was 90 degrees. After grit blasting, the rollers were rinsed in acetone to remove grit particles and dried with compressed air.

For the 1080 steel, four sets of three Amsler rollers and a witness sample were made. Each set was grit blasted with one specific process, either 36 grit alumina, 25 grit steel shot, Fe shot, or a two-stage process consisting of alumina followed by steel shot. The 1080 steel spraying parameters are shown in Table 2.3.5.1. The average number of passes in 4 minutes was 120. The average coating thickness was 0.48 ± 0.06 mm.

For the 308 L Si stainless steel, four rollers were made. Three rollers were grit blasted with 20 grit alumina, 36 grit alumina, 25 grit steel shot. The fourth roller was polished to a 400 grit surface finish. In some cases, a second grit blast was performed just prior to plasma spraying. The spraying parameters for stainless steel are shown in Table 2.3.5.2. Coating thickness ranged from 1.2 to 1.4 mm and the number of passes ranged from 115 to 160.

Amsler testing was performed at 1220 MPa and at both 5% and 35% slide/roll. Prior to Amsler testing, both the top and bottom rollers were cleaned in acetone and dried with compressed air. Test durability, i.e., number of revolutions to failure of the coating by debonding, was used as a means to assess the effectiveness of the different grit blasting methods. Strip charts showing deflection over number of revolutions were recorded for each test from which the coefficient of friction was calculated.

2.3.6 Full Scale and Rail Testing

Prior to grit blasting the full scale rail substrates were cleaned by first scrubbing the surfaces with water and a detergent, and then rinsing thoroughly with water. The substrates were then dried with either a hot air gun or a blast of compressed air. This was followed by rinsing with a solvent, acetone or ethanol, and drying with compressed air to further ensure a clean, oil-free surface.

Initially, roughening of the substrate surface was accomplished by grit blasting, with either 20 or 36 grit alumina. After re-optimization of grit blasting procedures the full scale samples were grit blasted with the two-stage process (alumina followed by steel shot) that was found to improve surface roughening. The angle of impact of the grit was 90 degrees to the surface with a standoff distance of approximately 2.5 cm. A 7 mm inside diameter nozzle was used and the grit blasting system pressure was held between 0.55 to 0.69 MPa. The grit blasting dwell time for any particular area was 5 to 10 seconds. After grit blasting, the surfaces were rinsed with acetone or ethanol and dried with a blast of compressed air. Following the cleaning and roughening operations, plasma spraying of the full scale and rail samples was performed as soon as possible in order to reduce re-contamination of the substrate surface.

2.4 LABORATORY SCALE TESTING AND ANALYSIS

2.4.1 Standard Wear Tests

During unlubricated testing, compressed air was aimed at the surfaces of both the top and bottom rollers to minimize heating and to remove wear debris from the contact zone. The Amsler testing parameters for the stainless steel plasma sprayed coatings and the composite steel coatings are shown in Table 2.4.1.1. Periodically, the tests were stopped and observations made on the roller surface condition and the weight and diameter of both rollers were measured. The total number of revolutions to failure was recorded as well as the failure mode. Failure was defined by coating debonding or by extreme surface wear, which led to excessive Amsler machine vibration. After wear testing, representative rollers were sectioned and both transverse and longitudinal metallographic sections were examined. Surface and subsurface characteristics were examined in the Nikon metallograph and the scanning electron microscope.

2.4.2 Lubricated Wear Tests

Lubricated tests were performed with distilled water that was dripped from overhead onto the surface of the top roller. The flow rate was adjusted to provide thorough wetting at the contact surface. At intervals, the tests were stopped and observations made on the roller surface condition and the weight and diameter of both rollers were measured. The total number of revolutions to failure was recorded as well as the failure mode. The same failure criteria was used as described in the previous section. Table 2.4.2.1 shows the test parameters for lubricated wear tests.

After wear testing, representative rollers were sectioned and both transverse and longitudinal metallographic sections were made. Surface and subsurface characteristics were examined optically and in the scanning electron microscope.

2.4.3 Interrupted Amsler Testing

A series of interrupted Amsler tests were performed in order to investigate the durability of 1080 steel coatings. All previously discussed tests could be considered "interrupted tests", as the total number of wear cycles these rollers were subjected to were interrupted multiple times in order to evaluate surface damage and determine weight changes. The specimens defined as "interrupted tests" in this thesis consist of a series of rollers that were rolled to various different predetermined number of wear cycles and then destructively tested. By interrupting (terminating) the Amsler test at various percentages of the coatings' total life, the microstructural changes as a function of test duration were examined. Three series of interrupted tests were conducted. Each series consisted of 8 to 10 Amsler tests using, 34 mm 1080 steel coated top rollers. The rollers were prepared following standard procedures and spraying practices. Sets of 4 to 5 rollers were sprayed at one time including a witness roller for metallography. Rollers were sprayed for 3.5 to 4 minutes with a total of 70 to 80 passes yielding a coating thickness of approximately 0.5 mm.

Prior to testing, rollers were cleaned according to standard practices. Interrupted Amsler test parameters are given in Table 2.4.1.1. To establish an average coating durability, 3 to 5 rollers of each set were tested without interruption to failure. The average coating life was calculated and this number was designated the 100% coating life. The number of revolutions corresponding to 5%, 10%, 25%, and 50% of the 100% coating life were calculated. Rollers were tested to these values without interruption.

The tested rollers and the witness samples were prepared for metallography. Transverse and longitudinal sections were cut on a high speed saw using a diamond blade. The coatings were cold mounted in epoxy under vacuum and polished using standard metallographic procedures. Mounted witness and test samples were examined optically and in the SEM to determine the extent of wear at the various coating test durations.

2.5 FAILURE ANALYSIS OF FULL SCALE TEST SPECIMENS

Failure analysis was performed on the full scale specimens tested by the AAR. In addition, coating debris from the tests were collected and sent to OGI for analysis. Finding the most successful sample preparation technique for the fragile wear coatings was a process of trial and error. This section covers sample preparation of the worn coatings and wear debris, and characterization methods used to examine the coatings.

2.5.1 Sample Preparation

On receipt of the full scale specimens and coupons at OGI, the wear surfaces were examined and photographed to record surface features and conditions. After documenting the as-received condition of the specimens, the surfaces were cleaned thoroughly. To remove embedded dirt and grease resulting from the tests, the surfaces were scrubbed gently with acetone and dried with a heat gun. A final rinse with methanol was performed to remove any

traces of contaminants followed by drying with a heat gun. Various methods were used to prepare the full scale tested coupons, specimens, and rail for metallography. Table 2.5.1.1 lists the metallographic preparation for each of the full scale test specimens investigated.

2.5.1.1 Rolling Load 1 (RL1)

A low viscosity 5-minute epoxy adhesive was applied to the complete surface of the wear tested coupon prior to sectioning. Two and a half centimeter thick sections were cut in the coupon at 25, 30, 38, 43, 53, 56, 58, 66, 74, 76 and 79 cm from one end. Sections were selected for sectioning based on individual features in the coating wear track. The 2.5 cm segments were further sectioned to remove all but the top portion of the coupon and then cut into quarters for mounting as shown in Figure 2.5.1.1. The segments were cold mounted in epoxy under low pressure.

2.5.1.2 Track Lab 1 (TL1)

A low viscosity 5-minute epoxy was applied to the surface of TL1 only at the outer edges where debonding occurred. The remainder of the sprayed coating was left unsealed. The specimen was cut into 2.5 cm slices at 13, 20, 33 and 43 cm along the length from one end. The top 2.5 cm of the rail was cut from the slice to reduce the size. The remaining slices were cut into halves and prepared for metallographic examination in the unmounted condition.

2.5.1.3 Track Lab 2 (TL2)

An aircraft epoxy adhesive was applied to the entire surface of the specimen. Sections 2.5 cm wide were cut at various locations along the specimen length, Figure 2.5.1.2. The sections were cut at 7, 15, 23, 28, 36, 46 and 53 cm from one end and

were selected to investigate specific wear features in the coating. The top 2.5 cm of the sections was removed and cut into thirds that were cold mounted in epoxy under low pressure.

2.5.1.4 Track Lab 3 (TL3)

Due to the lack of coating remaining in the wear track, only one section was removed from TL3. Band saw cuts were performed 2.5 cm to each side of the area of interest shown in Figure 2.5.1.3 (a) to keep from damaging the worn coating. After sectioning, 3M epoxy was applied to the worn coating surface. Aluminum strips were pressed into the 3M epoxy creating a protective layer of the epoxy and aluminum. After curing the epoxy in an oven, longitudinal and transverse cuts were made to isolate the wear coating region of interest. Samples were hot mounted in phenolic.

2.5.1.5 Track Lab 4 (TL4)

The same procedure was followed as for Track Lab 3. One section was removed from the specimen, coated with a layer of the 3M epoxy and aluminum strips, cured, then hot mounted in phenolic. Figure 2.5.1.3 (b) shows the region selected for metallography.

2.5.1.6 FAST rail

For the FAST rail, sectioning was performed in the as-received condition. Figure 2.5.1.4 shows 1.8 m of the 3.7 m rail prior to sectioning; only half of the rail was used for metallographic purposes. To assist in record keeping, the rail was marked in 2.5 cm increments along the length from one end. Sections were cut 2.5 cm wide at intervals along the length of the rail at 38, 64, 89, 114, 140 and 179 cm from the end. The top 2.5 cm of the rail was cut from the sections to reduce the overall height of the sections, Figure 2.5.1.5. The

sections were coated with 3M thermosetting epoxy, covered with aluminum strips and cured, Figure 2.5.1.6. After this, the sections were cut into thirds and hot mounted in phenolic. Figure 2.5.1.7 shows the sectioning technique for worn rail samples.

2.5.1.7 Wear debris preparation

The as-received wear debris were photographed to record the size and shape of the particles, Figure 2.5.1.8. Large pieces of wear debris were cleaned using an acetone wash followed by a methanol rinse, then dried with a heat gun (with the exception of the nylon debris which were air dried). Very small wear particles were cleaned and rinsed through filter paper. Two types of samples were prepared from the debris, metallographic mounts and SEM samples. For the SEM samples, both small particles and powdered debris, if available, were applied with graphite tabs to aluminum stubs. These were coated with 200 Å of Au-Pd. Representative debris were chosen for each test, coated completely with 3M thermosetting epoxy and sandwiched between aluminum strips to provide rigidity to the wear debris. After curing, two sections were made from each debris with orientations perpendicular to each other. Sections were hot mounted in phenolic.

2.5.2 Characterization

Standard metallographic procedures were used to prepare the worn coating and wear debris samples as described in Section 2.1.8. The samples were examined optically and in the SEM to evaluate the microstructure. Special attention was paid in the worn coatings to the progress of cracking from coating surface to interface. Backscattered imaging was used to resolve the steel and iron oxide phases of the coating. Energy dispersive spectroscopy was performed to identify constituents. Unless noted, samples were examined in the unetched condition. The entire coating and coating/substrate interface was examined and images were taken, either on film or digitally.

Table 2.1.1.1. Powder injector parameters for sprayed coatings.

Parameter	1080 Steel Composite	Nylon
Powder injector angle (degrees)	45	45
Powder injector location (mm)	35	43

Table 2.1.1.2. Working distances for sprayed coatings.

Coating	Working Distance (mm)
Stainless steel	225
1080 steel	225
1080 steel composite	235
Stainless steel/nylon	235
Nylon	255

Table 2.1.1.3. Tensile test matrix.

Effect of ...	Conditions Tested
Surface preparation	Alumina, steel shot, Fe shot, 50/50 mix and two-stage
Plasma spray parameters	230/30/235, 230/75/235 and 300/75/235
Second phase particles in 1080 steel	Titanium and stainless steel

Table 2.1.1.4. Nominal compositions for 1080 steel wire [3], 308 L Si stainless wire, and stainless steel powder [4].

Steel	C	Mn	Si	S	P	Cr	Ni	Cu	Mo
1080	0.75-0.88	0.60-0.90	-	0.05 max	0.04 max	-	-	-	-
308 L Si	0.02	1.70	0.87	0.01	0.02	20.0	10.1	0.06	0.08
304L	0.02	0.18	0.66	-	-	18.90	10.50	-	-
316L	0.02	0.18	0.83	-	-	17.0	12.75	-	2.15

Table 2.1.3.1. Class C wheel steel and standard carbon rail steel compositions [5].

Material	C	Mn	Si	S	P	Cr	Ni	Cu	Mo	B	Ti
Wheel	0.70	0.66	0.51	0.02	0.02	0.04	0.04	0.04	<0.001	0.001	<0.001
Rail	0.81	0.92	0.26	0.005	0.006	0.18	0.09	0.22	<0.01	<0.001	0.001

Table 2.1.4.1. Rails tested at Pueblo, Colorado by AAR.

Sample	Coating Type		Coating Thickness (μm)		Notes
	Base	Lubricant	Base	Lubricant	
RL1	1080 steel	None	1000	-	Abrupt ends
RL2	1080 steel	Nylon	1000	30-50	New head-hardened rail
RL3	1080 steel	Nylon	500	30-50	New head-hardened rail
RL4	1080 steel	Nylon	1000	30-50	New head-hardened rail
RL5	1080 steel	Nylon	500	30-50	New head-hardened rail
TL1	1080 steel	None	1000	-	Abrupt ends
TL2	1080 steel	None	1000	-	Feathered at ends
TL3	stainless steel	Nylon	500	30-50	Feathered at ends
TL4	1080 steel	Nylon	500	30-50	Feathered at ends
FAST	1080 steel	Nylon	250	30-50	Feathered at ends

Table 2.2.1. Stainless steel parameter optimization test matrix (working distance 225 mm).

Primary Gas (N_2, slpm)	Secondary Gas (H_2, slpm)
230	0, 10, 20, **30**, 40, 50
235	35
240	20, 30, 40
250	20, 30, 40

Table 2.2.2. Parameter optimization for 1080 steel composite coatings.

Parameter	Value
Primary gas, N_2 (slpm)	230
Secondary gas, H_2 (slpm)	30
Working distance (mm)	235
Carrier gas, N_2 (slpm)	15, 40
Powder feed setting (rpm)	2, 3, 4, 5, 15

Table 2.3.1.1. Tested grit materials and impact angles.

Grit Material	Grit Size	Impact Angle (degrees)
Al_2O_3	50-70, 36, 20	45, 90
SiO_2	50-70	45, 90
Steel shot	25	45, 90

Table 2.3.2.1. Grit blasting surface preparation procedures for new and worn head-hardened rails.

Test	Material Parameters		
	Material(s) Used	Size of Grit Blast Material	Blast Time (minutes)
Alumina	Crushed alumina	36 grit	2
Steel shot	Chilled steel shot	25 grit	2
50/50 mix	Mixture of steel shot and alumina	25 and 36 grit mixture	2
Two-stage	Alumina	36 grit	2
	Steel shot	25 grit	2
Fe shot	Crushed chilled Fe shot	50-70 grit	2

Table 2.3.4.1. Plasma spraying parameters for tensile bars.

Parameter	Value
Primary gas, N_2 (slpm)	230
Secondary gas, H_2 (slpm)	75
Working distance (mm)	235
Voltage (V)	410
Current (A)	355
Wire type	1080 steel, 1.6 mm
Wire injector(s)	1
Wire injector angle	45 degrees
Wire injector position (mm)	15, side
Wire speed	1.5
Number of passes	15-20
Cooling gas/location	Air/front

Table 2.3.5.1. 1080 steel spraying parameters for Amsler rollers.

Parameter	Value
Primary gas, N_2 (slpm)	230
Secondary gas, H_2 (slpm)	30
Working distance (mm)	235
Voltage (V)	410
Current (A)	350
Wire type	1080 steel, 1.6 mm
Wire injector(s)	1
Wire injector angle	45 degrees
Wire injector position (mm)	15, side
Wire speed	1.5
Time (minutes)	4
Number of passes	120
Cooling gas/location	CO_2/backside

Table 2.3.5.2. Spraying parameters for stainless steel Amsler tests.

Parameter	Value
Primary gas, N_2 (slpm)	240
Secondary gas, H_2 (slpm)	30
Working distance (mm)	225
Voltage (V)	380
Current (A)	350
Wire type	308LSi, 1.6 mm
Wire injector(s)	1
Wire injector angle	45 degrees
Wire injector position (mm)	10
Wire speed	1.5
Time (minutes)	3-6
Number of passes	115-160
Cooling gas/location	CO_2/backside

Table 2.4.1.1. Amsler testing parameters for coatings.

Coating	Contact Pressure (MPa)	Conditions	Slide/Roll Ratio (%)
Stainless steel	900, 1000, 1220	Dry as-sprayed Dry as machined Water	2, 5, 35
Stainless steel/nylon	1220	Dry	35
1080 steel, 1 wire	1220	Dry, water	5, 35
1080 steel, 2 wires	1220	Water	5, 35
1080 steel composite	1220	Dry	5
1080 steel interrupted	1220	Dry	35

Table 2.4.2.1. Lubricated Amsler wear test parameters.

Coating	Contact Pressure (MPa)	Slide/Roll Ratio	Coating Thickness (mm)
Stainless steel	1220	5, 35	0.8
1080 steel, 2 wire	1220	5	0.6, 1.3
1080 steel, 1 wire	1220	5	0.6

Table 2.5.1.1. Metallographic preparation for worn rail specimens.

Sample	Coating Preservation	Final Sectioning	Mounting
RL1	5-minute epoxy over complete surface	Quarters	Cold mount under pressure in epoxy
TL1	5-minute epoxy at debonded areas only	Halves	Unmounted
TL2	Aircraft epoxy over complete surface	Thirds	Cold mount under pressure in epoxy
TL3	3M thermoset epoxy/Al strips applied at specific sites of interest	Only one transverse and one longitudinal section made	Cold mount under pressure in epoxy
TL4	3M thermoset epoxy/Al strips at specific sites of interest	Only three transverse sections made	Cold mount under pressure in epoxy
FAST	3M thermoset epoxy/Al strips at specific sites of interest	Thirds at 30 cm intervals along railhead	Cold mount under pressure in epoxy

Note: only the wear debris from RL2 to RL5 were returned to OGI for failure analysis.

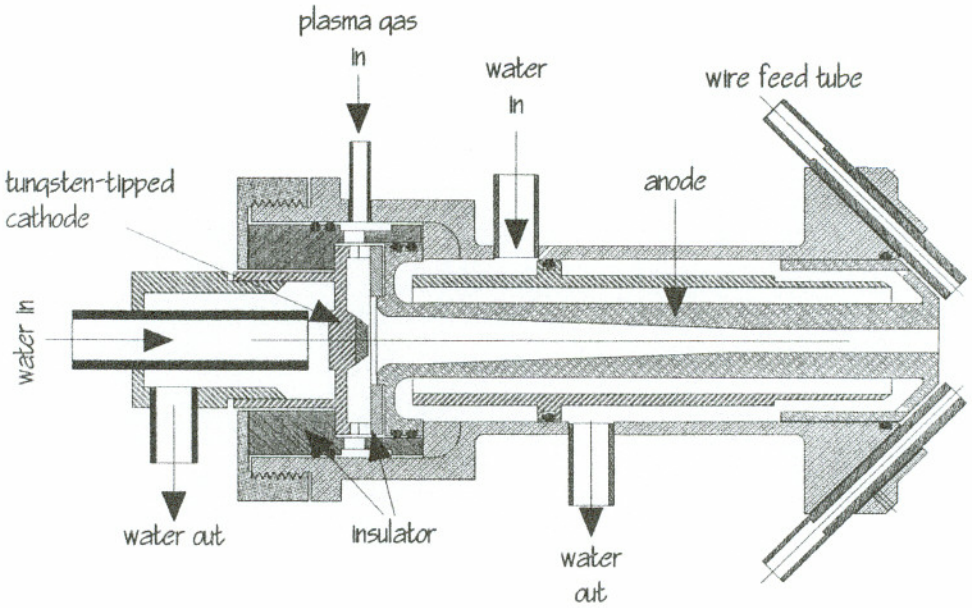

Figure 2.1.1.1. Schematic of OGI hyper-velocity plasma spray gun.

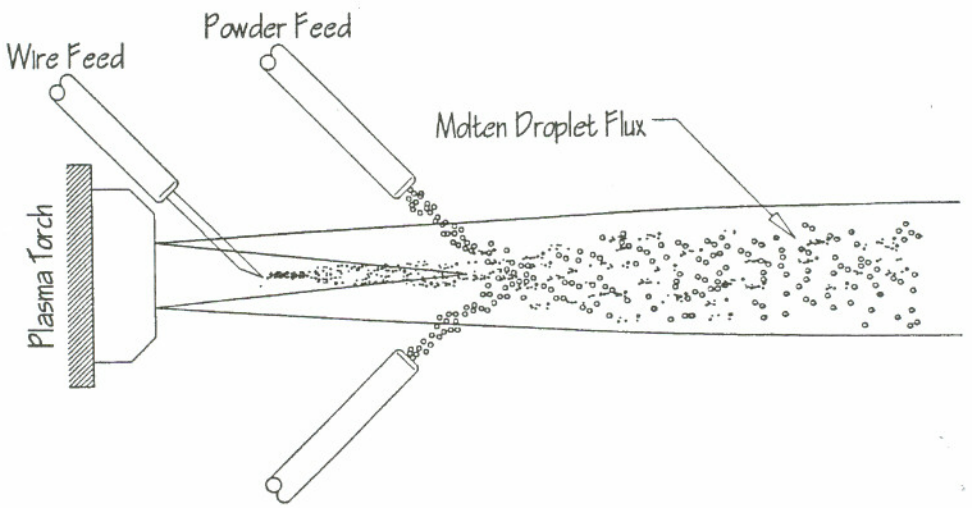

Figure 2.1.1.2. Wire and powder feed locations in plasma jet.

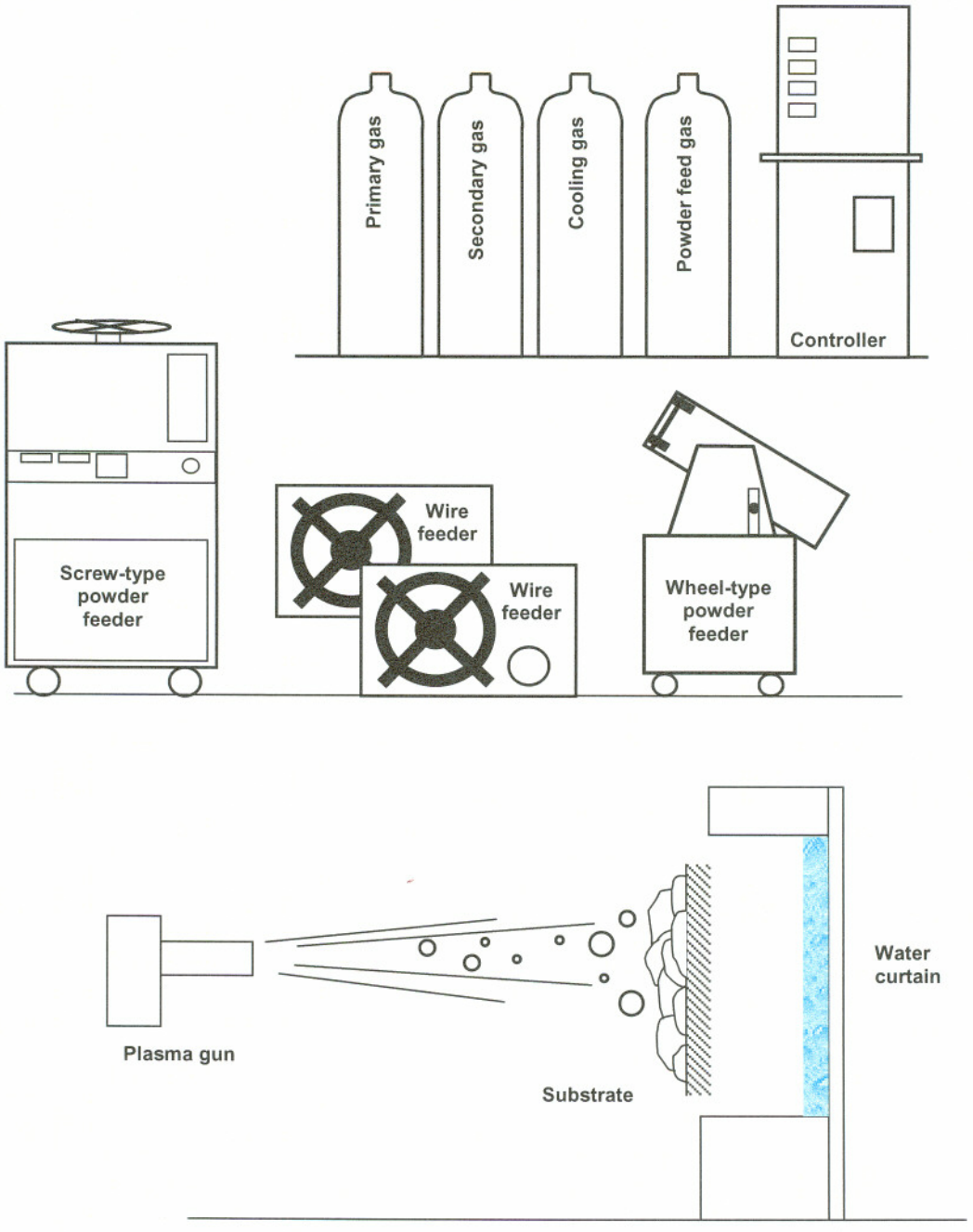

Figure 2.1.1.3. Schematic of OGI plasma spray system.

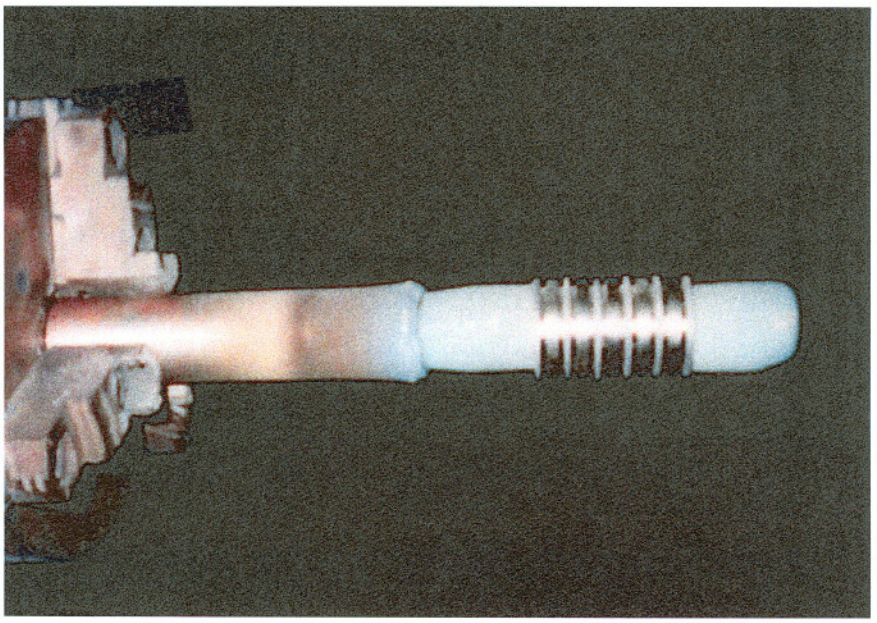

(a)

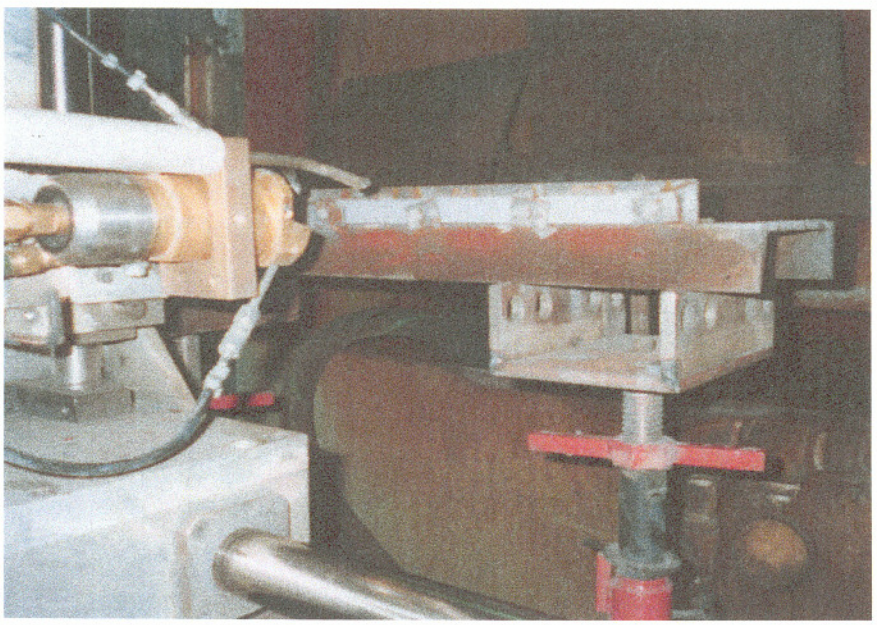

(b)

Figure 2.1.1.4. Typical sample fixture, (a) Amsler rollers, (b) flat coupons, and (c) tensile bars.

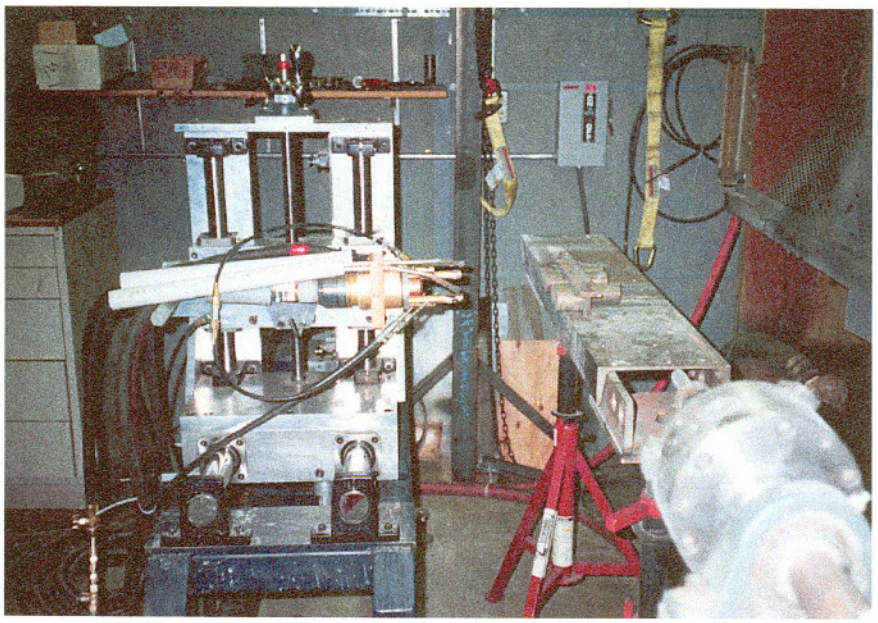

(c)

Figure 2.1.1.4. (Continued) Typical sample fixture, (a) Amsler rollers, (b) flat coupons, and (c) tensile bars.

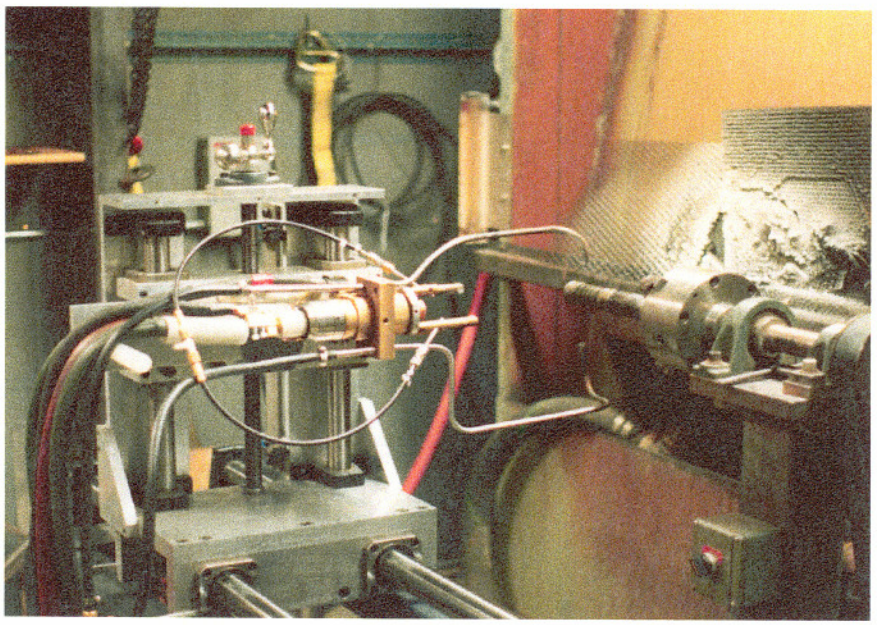

(a)

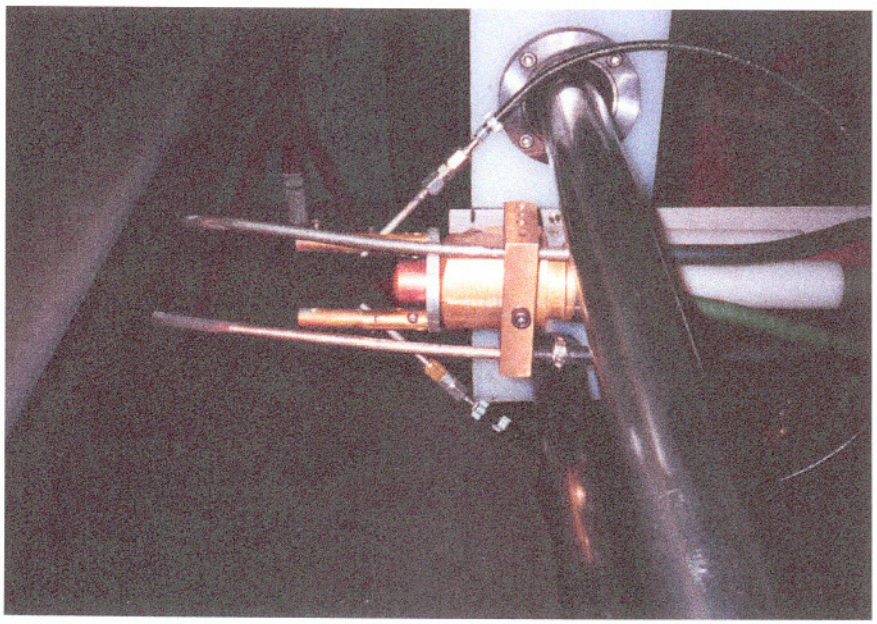

(b)

Figure 2.1.1.5. Cooling set-ups, (a) backside and (b) front.

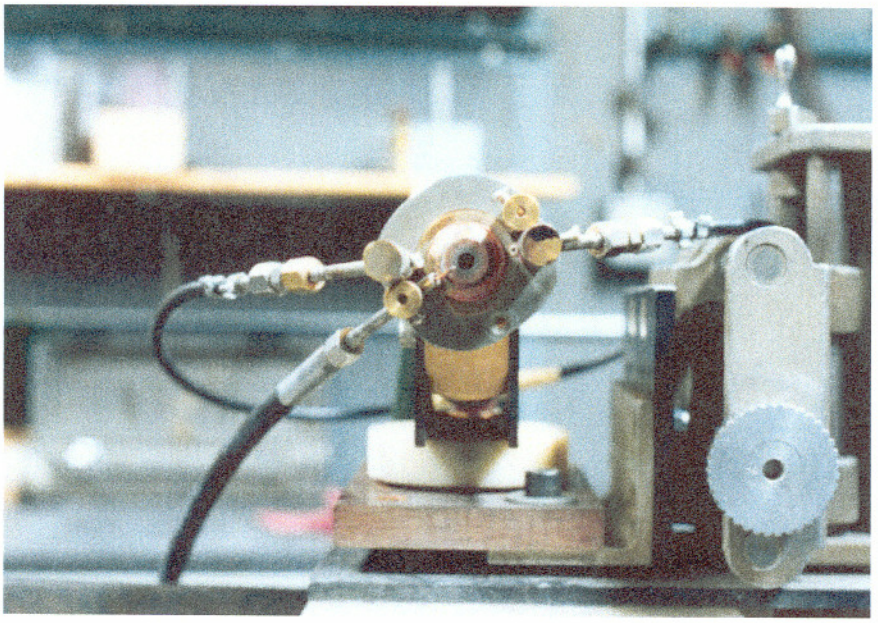

(a)

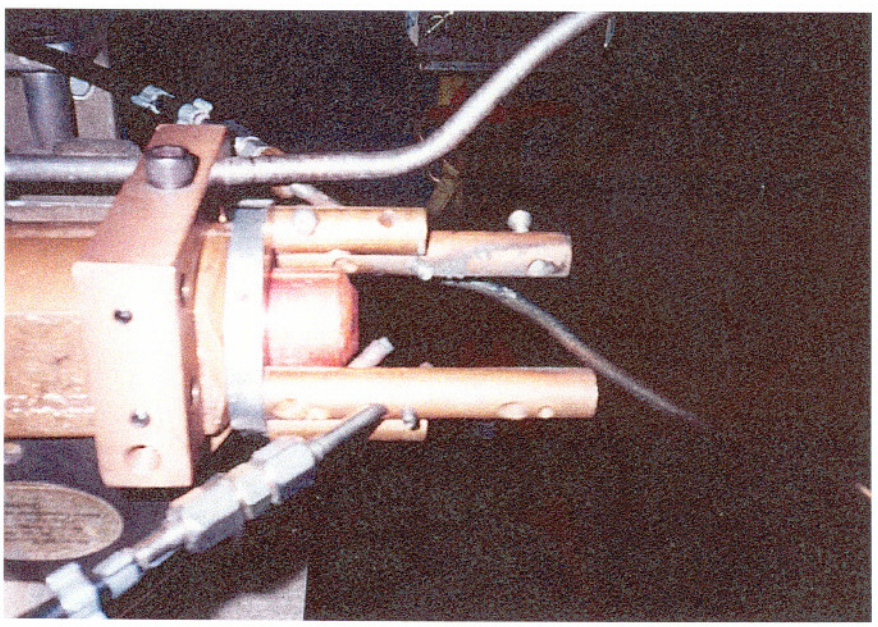

(b)

Figure 2.1.1.6. Wire and powder feed-tube locations, (a) around gun perimeter and (b) entry point along the plume.

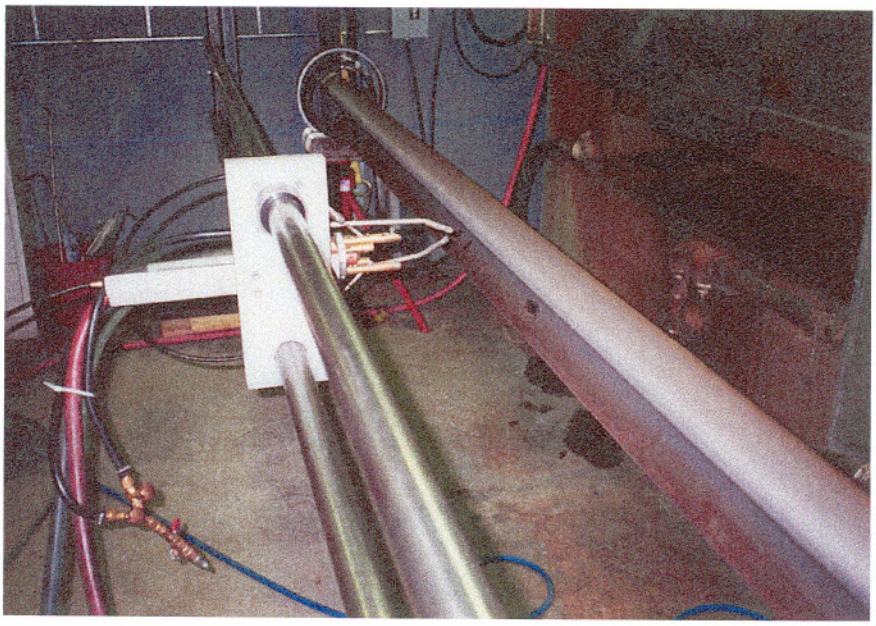

Figure 2.1.1.7. Plasma spraying of FAST rail.

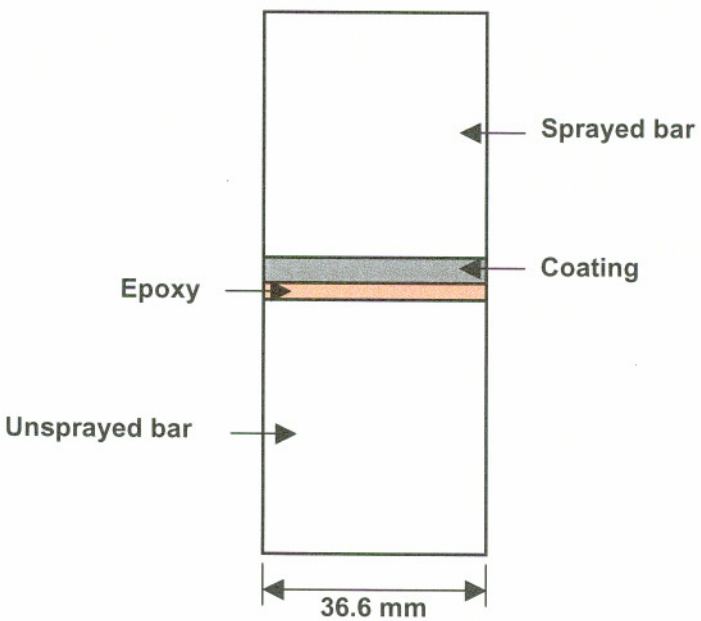

Figure 2.1.1.8. Schematic of tensile specimens.

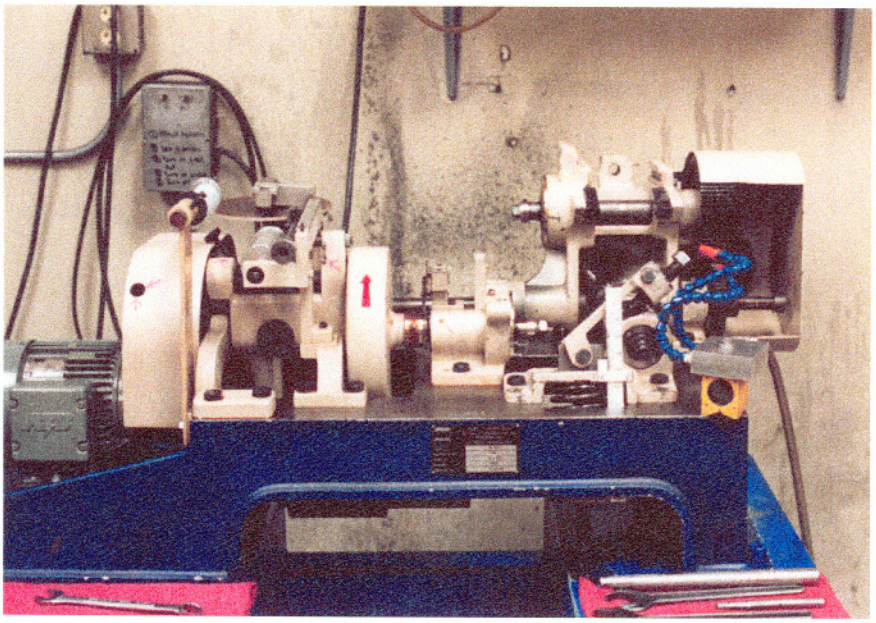

Figure 2.1.3.1. Amsler rolling/sliding wear testing machine.

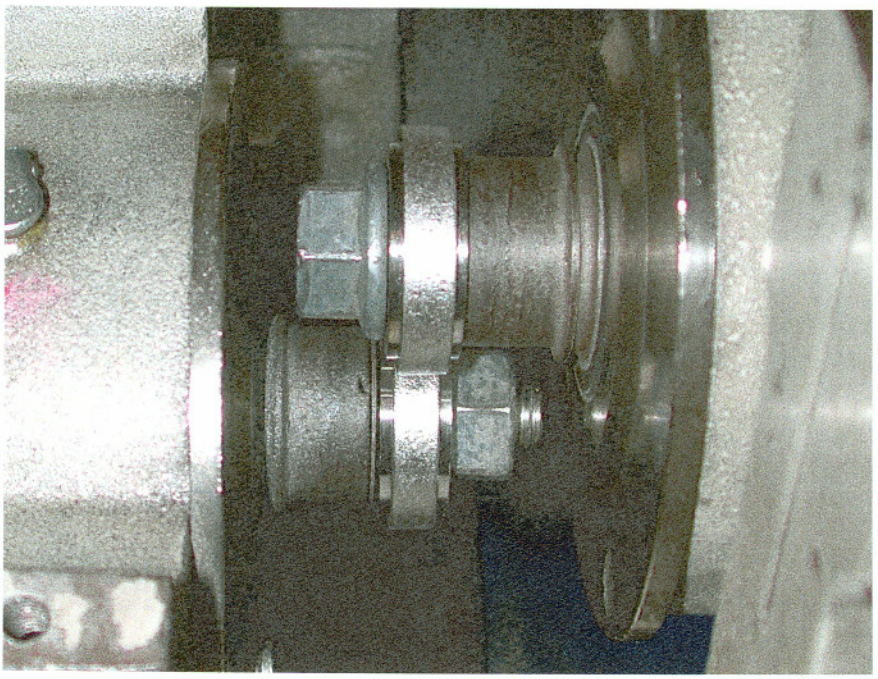

Figure 2.1.3.2. Amsler rollers on upper and lower shafts.

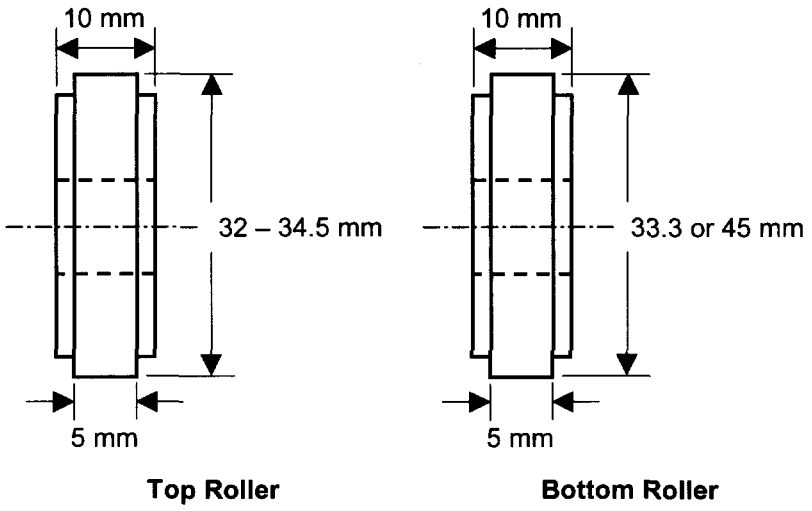

Figure 2.1.3.3. Roller top hat configuration and dimensions for top and bottom rollers.

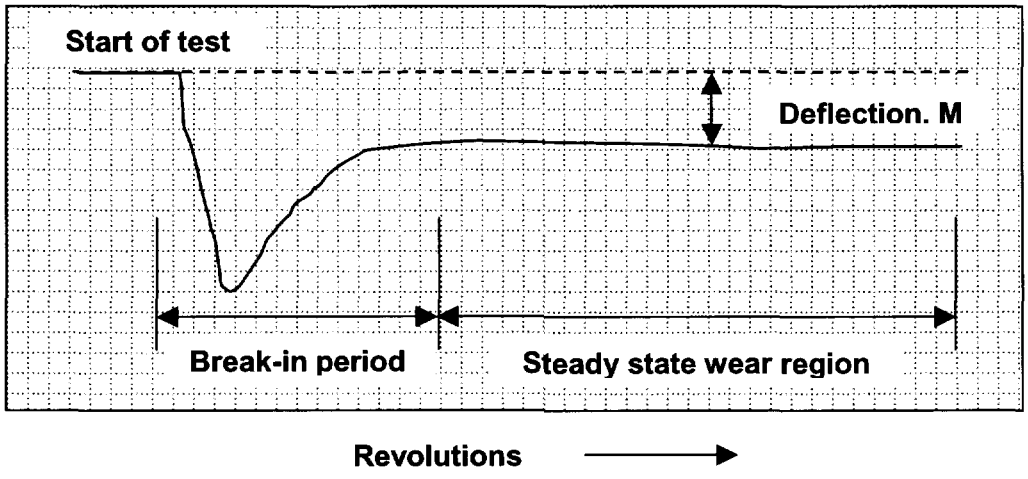

Figure 2.1.3.4. Schematic of a typical strip chart showing torque as a function of time.

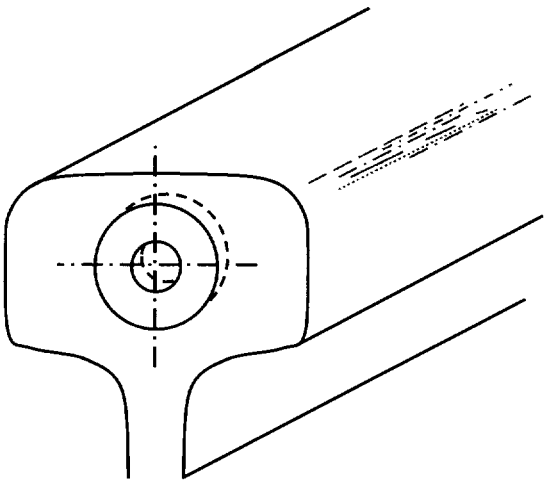

(a)

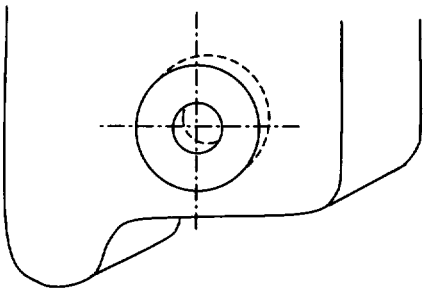

(b)

Figure 2.1.3.5. Orientation of (a) top roller taken from rail and (b) bottom roller machined from Class C wheel steel.

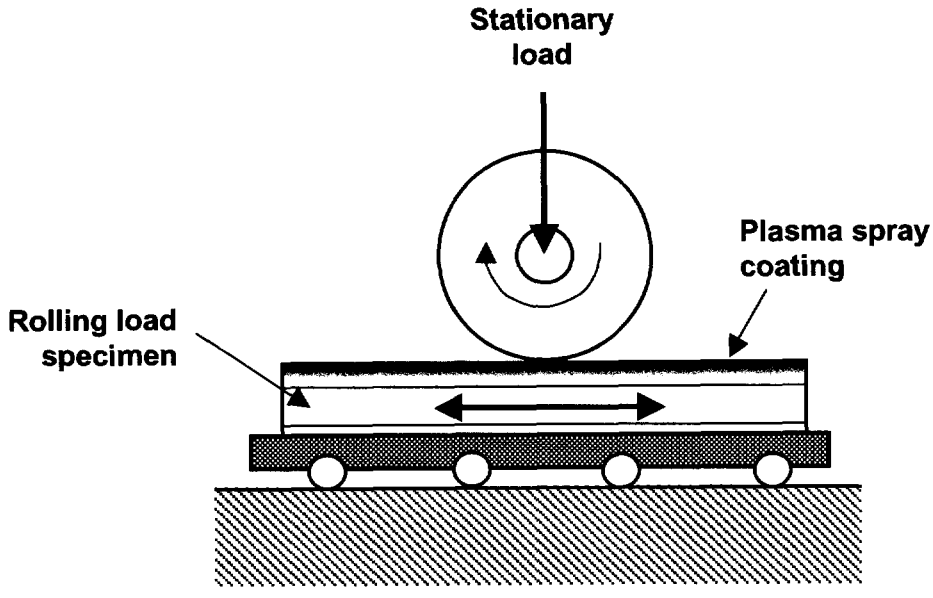

(a)

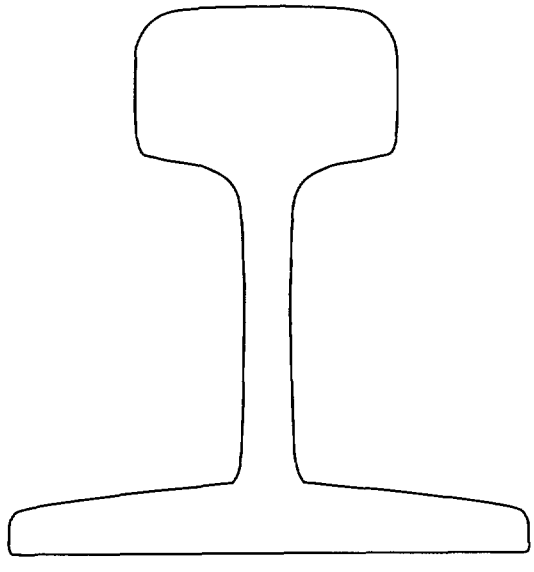

(b)

Figure 2.1.4.1. Schematic of (a) old rolling load and
(b) rolling load specimen configuration.

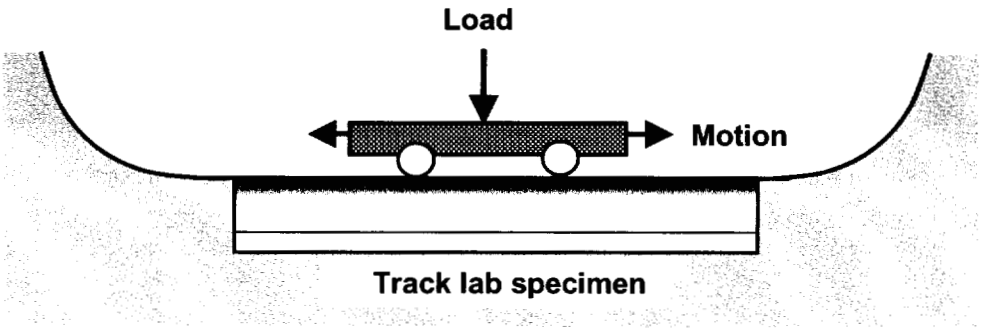

(a)

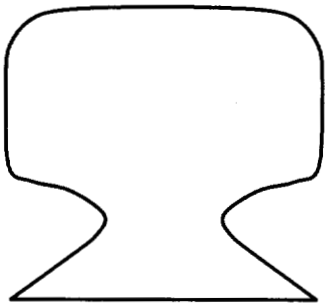

(b)

Figure 2.1.4.2. Schematic of (a) track lab test and
(b) track lab test coupon configuration.

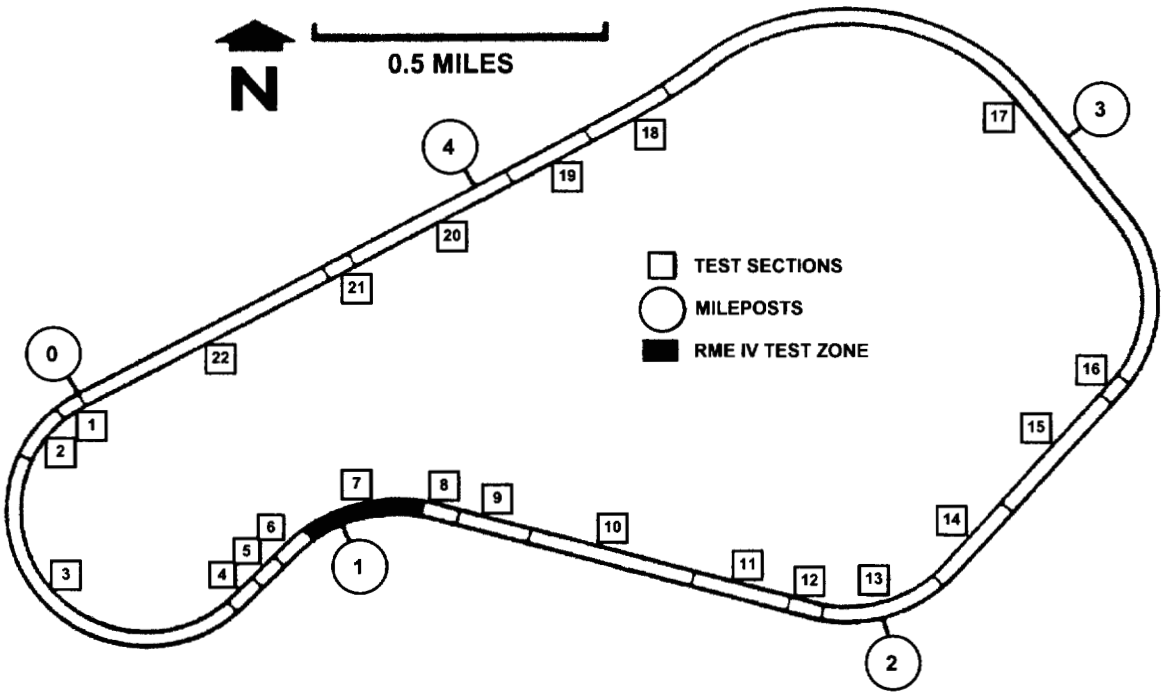

Figure 2.1.4.3. Map of Facility for Accelerated Service Testing (FAST) at Pueblo, Colorado.

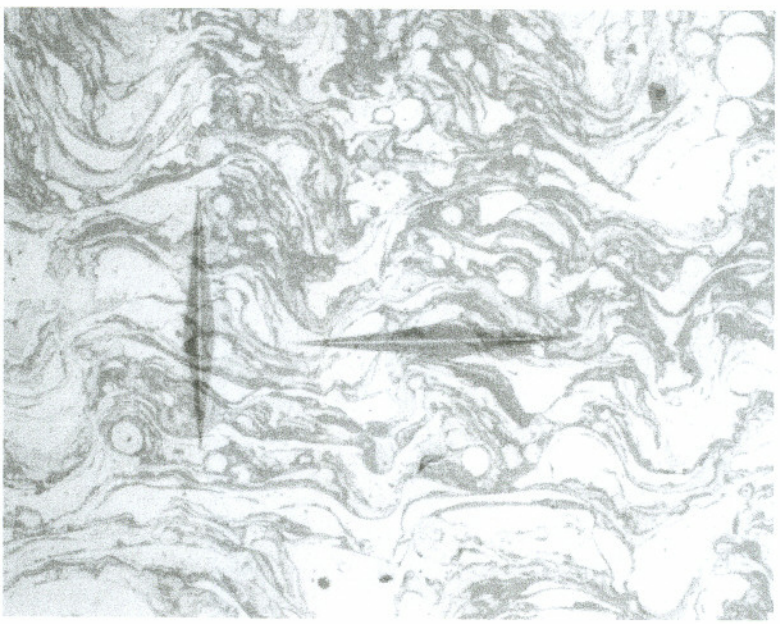

Figure 2.1.6.1. Microhardness indents perpendicular and parallel to the coating surface.

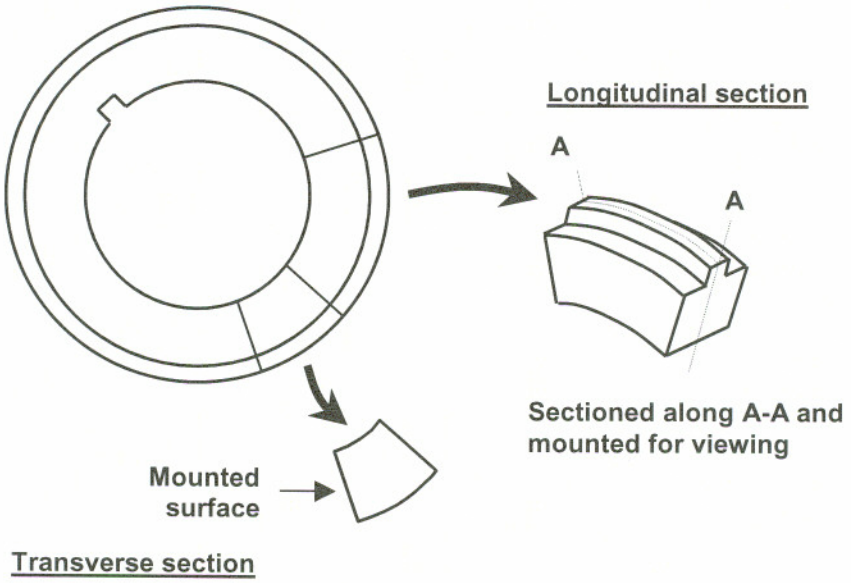

(a)

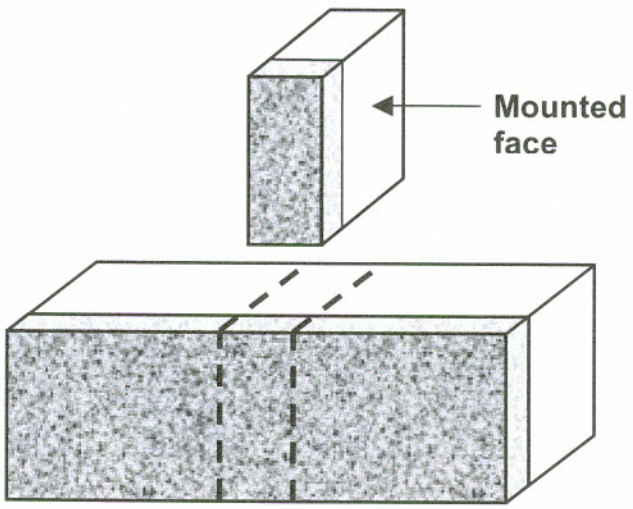

(b)

Figure 2.1.8.1. Sectioning of (a) Amsler rollers and (b) coupons.

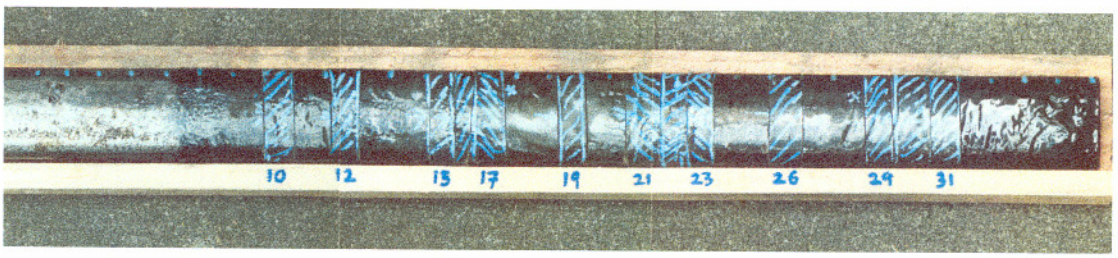

Figure 2.5.1.1. Sectioning of rolling load specimen, RL1.

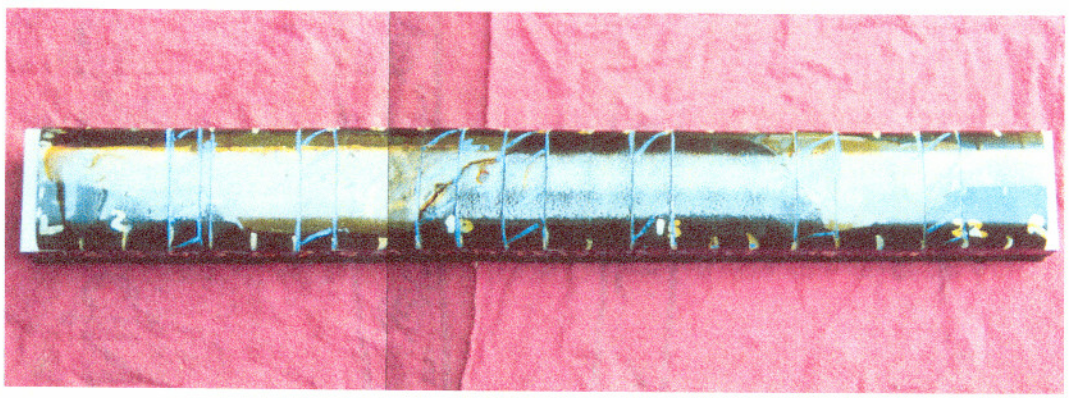

Figure 2.5.1.2. Sectioning of track lab coupon, TL2.

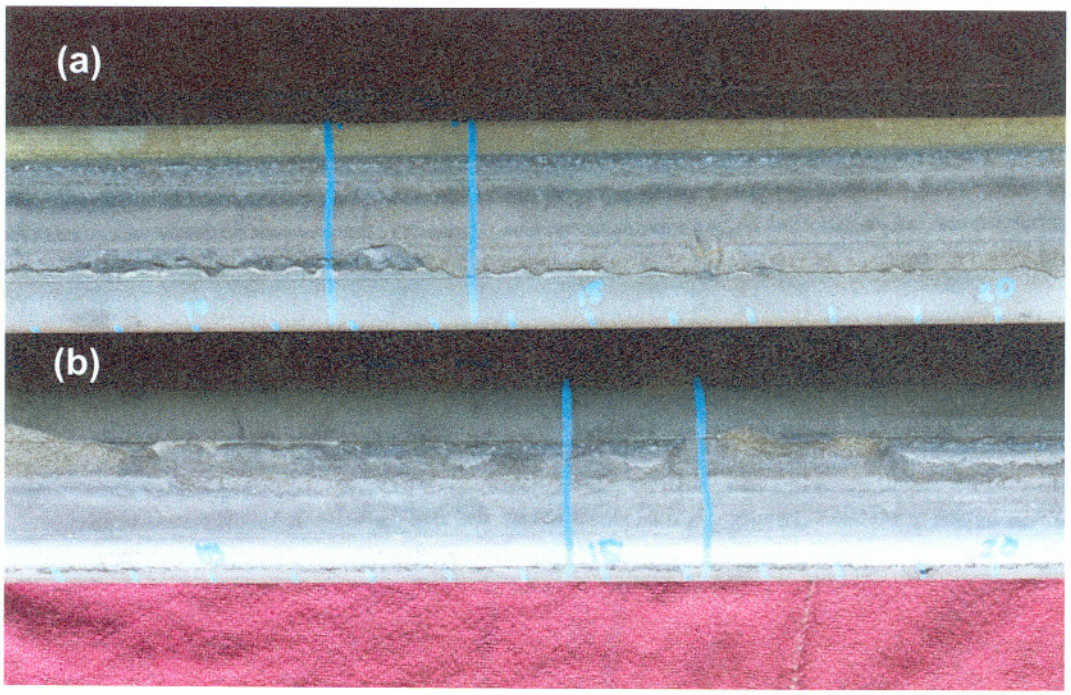

Figure 2.5.1.3. Sectioning of track lab coupons, (a) TL3 and (b) TL4.

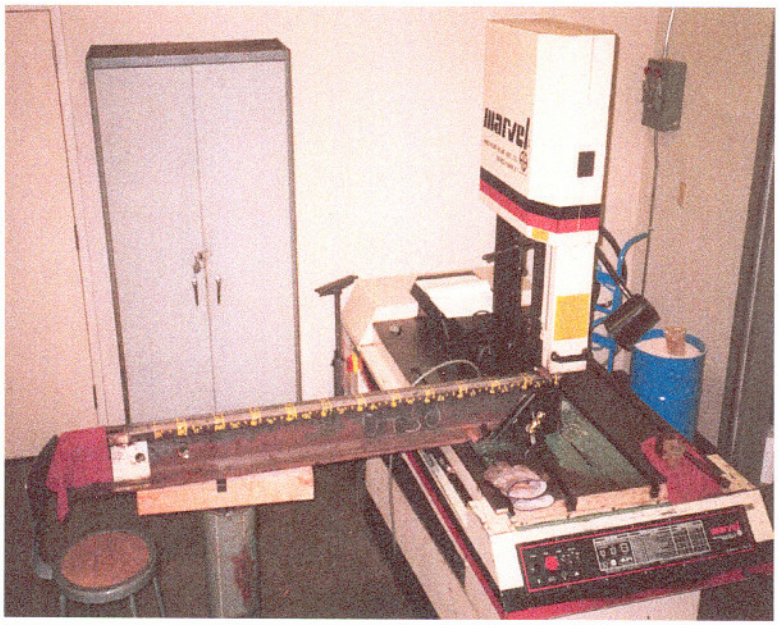

Figure 2.5.1.4. Worn FAST rail prior to sectioning.

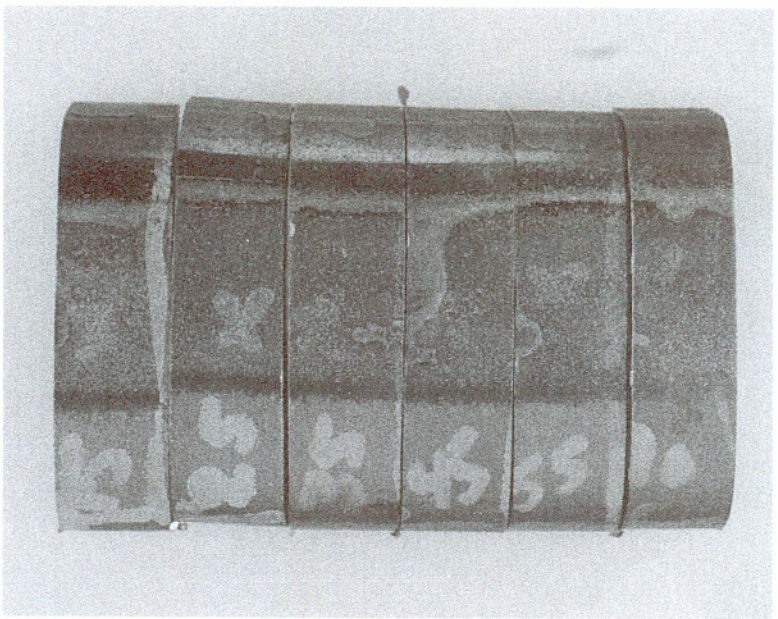

Figure 2.5.1.5. Sections cut from FAST rail.

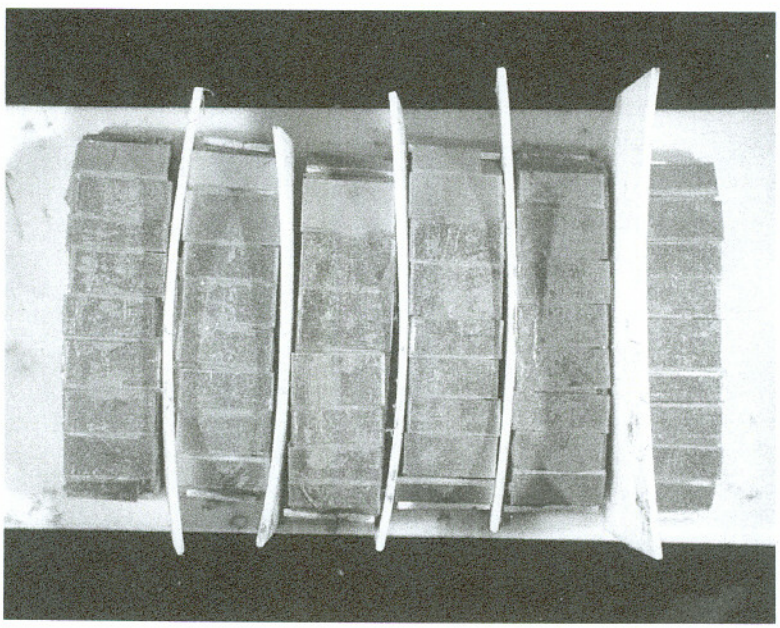

Figure 2.5.1.6. Coating protection applied to FAST sections.

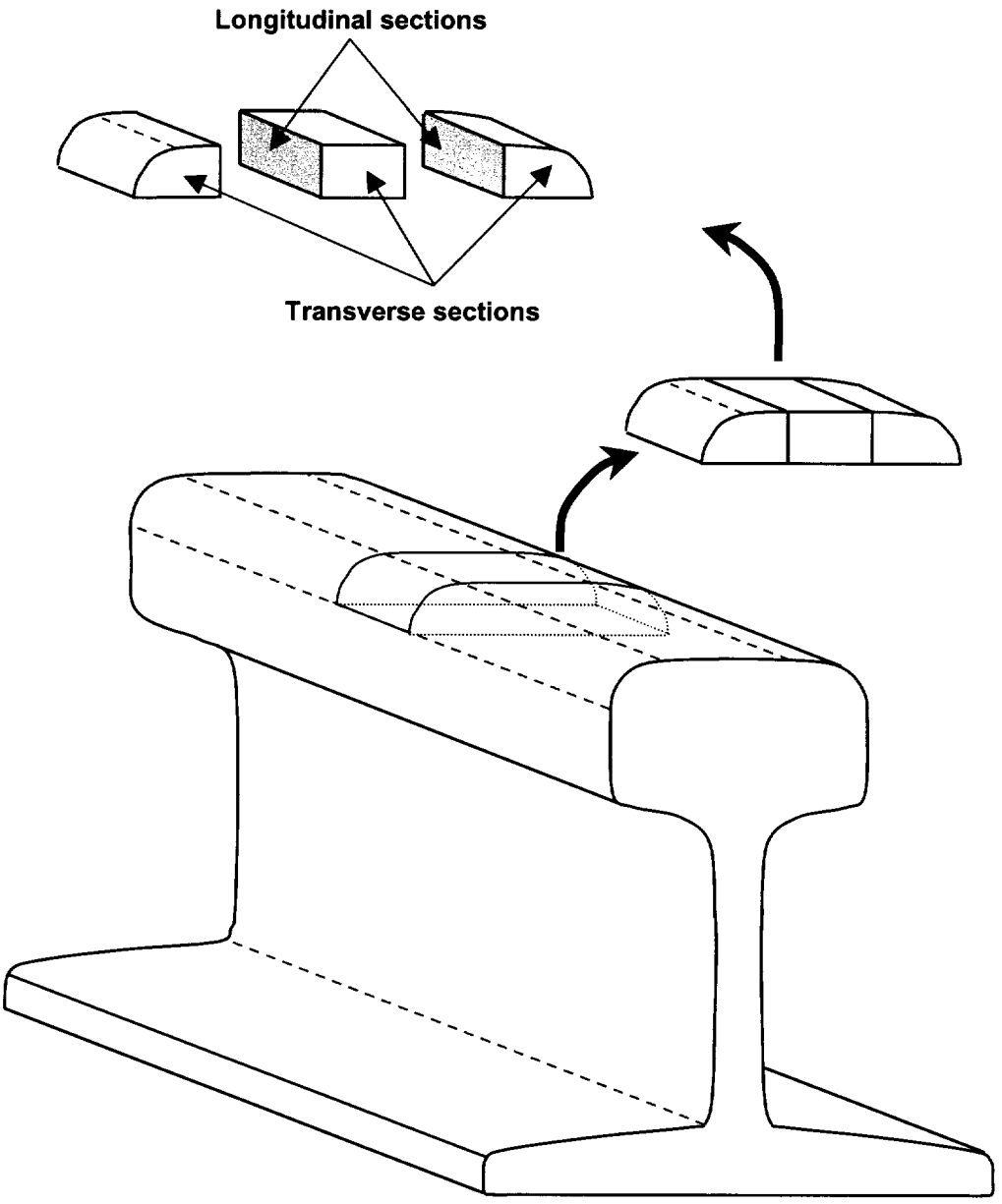

Figure 2.5.1.7. Schematic of sectioning techniques for full scale wear tests.

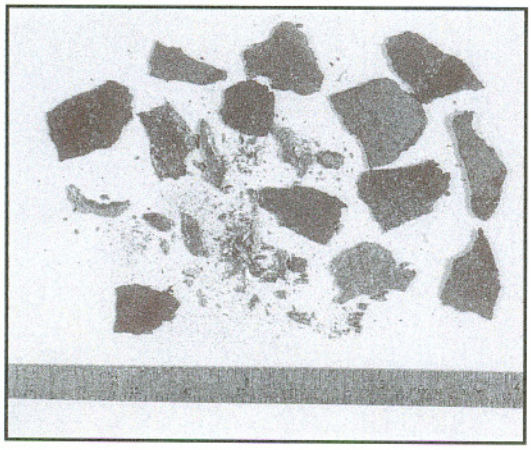

(a) RL2

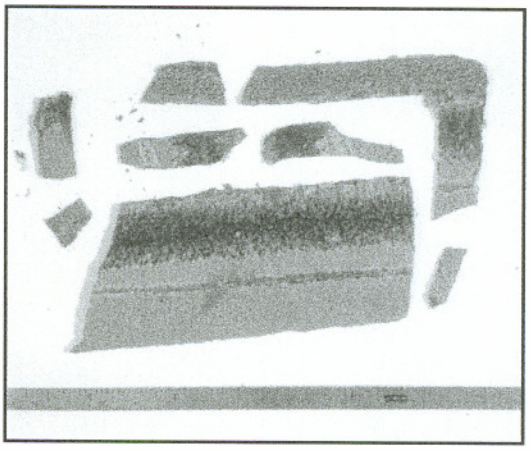

(b) RL4

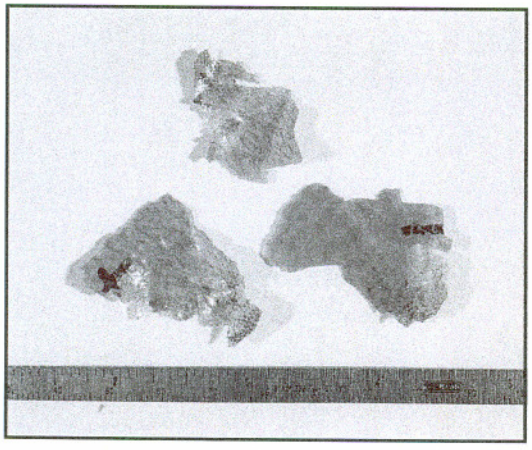

(c) RL5

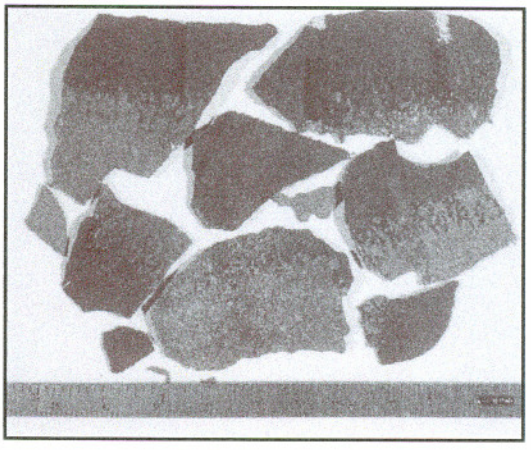

(d) TL2

Figure 2.5.1.8. As-received wear debris from, (a) RL2, (b) RL4, (c) RL5, (d) TL2, (e) TL3, (f) TL4 at 8,700 cycles, (g) TL4 at 18,723 cycles and (h) FAST.

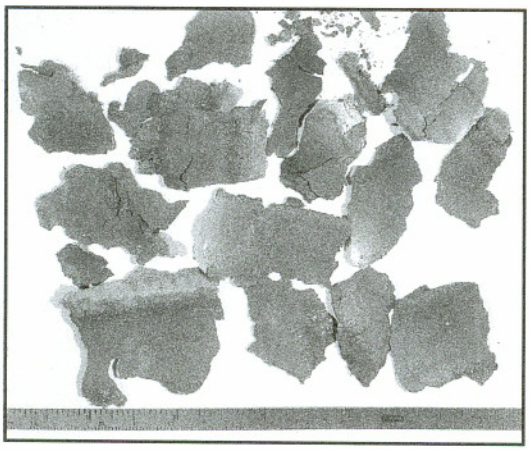

(e) TL3

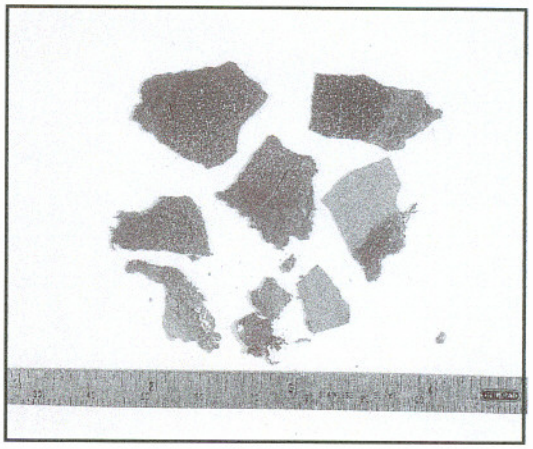

(f) TL4 at 8,700 cycles

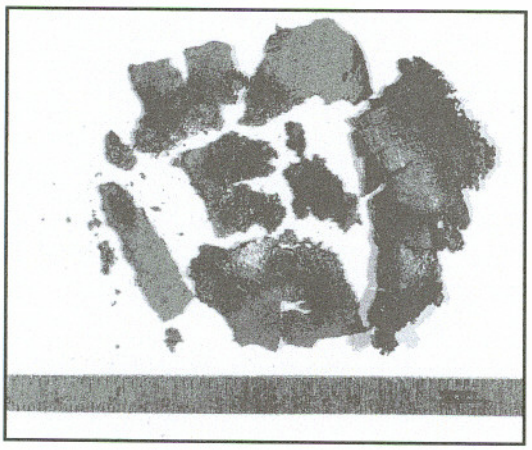

(g) TL4 at 18,723 cycles

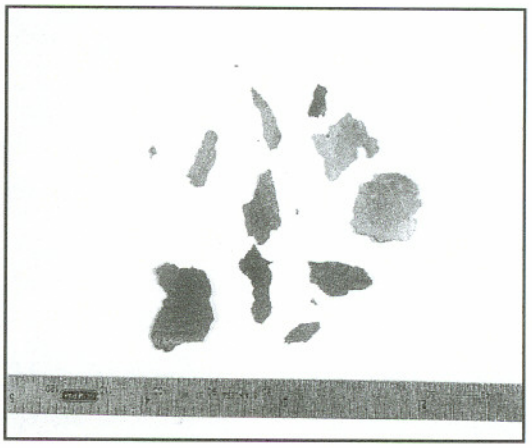

(h) FAST

Figure 2.5.1.8. (Continued) As-received wear debris from, (a) RL2, (b) RL4, (c) RL5, (d) TL2, (e) TL3, (f) TL4 at 8,700 cycles, (g) TL4 at 18,723 cycles and (h) FAST.

References for Chapter 2

1. Scholl, M., Clayton, P., Abrasive and Erosive Wear of Some Hypervelocity Air Plasma Sprayed Coatings. *Proceedings of the 4th National Thermal Spray Conference, Pittsburgh, PA, May 1991*, pp. 39-52.

2. Scholl, M., Clayton, P., Elmore, E., Wooten, J., Sprayforming by High-power, High-velocity Plasma Spraying. *Proceedings of the Fourth National Thermal Spray Conference, Pittsburgh, PA, May 1991*, pp. 281-288.

3. *Metals Handbook, 9th Edition, Vol. 1*, ASM International, p. 125.

4. Brandes, E. and Brook, G., Editors, *Smithells Metals Reference Book, 7th Edition*, Butterworth-Heinemann Ltd, 1992, p. 23-20.

5. Danks, D., *Wear and Microstructure of Eutectoid Steels*, Ph.D. Thesis, Oregon Graduate Center, 1989.

6. McMurchie, D., *Development of a 1080 Steel Plasma Sprayed Coating for Slide/Roll Conditions*, Ph.D. Thesis, Oregon Graduate Institute of Science and Technology, 1996.

7. Niebuhr, D. V., *Development of a Self-lubricating Plasma Sprayed Coating for Rolling/Sliding Wear*, Ph.D. Thesis, Oregon Graduate Institute of Science and Technology, 1997.

CHAPTER 3

RESULTS

3.1 PARAMETER OPTIMIZATION STUDY

This study sought to optimize parameters for coating systems to be used for Amsler tests and later for full scale tests. Parameters were re-optimized when the original Amsler roller parameters were found inadequate for full scale tests.

3.1.1 Lubricant-resistant Coatings (Stainless Steel)

The starting parameters used for optimizing the stainless steel plasma sprayed Amsler roller coatings were the same as those used by McMurchie in his 1080 steel single wire research [1]. These parameters were 230 slpm nitrogen, 30 slpm hydrogen, and a 225 mm working distance (230/30/225). Glass slides were sprayed for each of the test parameters shown in the test matrix in Table 3.1.1.1. Figures 3.1.1.1 (a) and (b) show the splat morphology of an optimized and non-optimized splat.

In order to verify the stainless steel parameters determined to be optimum by single splat analysis, flat steel coupons were sprayed. Figure 3.1.1.2 shows the microstructure of the stainless steel coupon sprayed with the optimized parameters 240/30/225. The microhardness of the optimized coating was 391 ± 38 HK_{500}.

3.1.2 Hard Particle Containing Coatings (Composite 1080 Steel)

The parameters used as a starting point for optimization were 230/30/235 and were developed by Niebuhr for his single wire friction reduction work [2]. Optimizing parameters for the hard particle composite coatings was more complicated since a twin wire feed was used instead of just a single wire feed as used in Niebuhr's research.

As a result of the initial parameter optimization studies, two of the candidate powder materials, stainless steel powder and titanium powder, were selected for in-depth testing. Powder carrier gas flow rates, 14 slpm and 42 slpm, were investigated during the initial parameter optimization tests using single splat analysis, Table 3.1.2.1. The 14 slpm rate was found to produce the best splat morphology and distribution for the materials tested.

Flat coupons and Amsler rollers were used in parameter optimization of the powder feed rates for 1080 steel/titanium and 1080 steel/stainless steel coatings. Powder feed rates were studied using two different feeder wheels at two different speeds, Table 3.1.2.2. Figures 3.1.2.1 (a) and (b) and Figures 3.1.2.2 (a) and (b) show typical microstructures for the 1080 steel/stainless steel and the 1080 steel/titanium samples, respectively, at different powder feed volumes. The high volume wheel at a speed of 1.0 was found to produce the best coatings without jamming the feeder.

The above tests were followed by a test matrix varying the powder injection point and the gas parameters. Table 3.1.2.3 shows the test matrix. Figures 3.1.2.3 (a) and (b) show that it was difficult to distinguish optically between the steel matrix and the powder (stainless steel and titanium) in the coatings. Figures 3.1.2.4 (a) and (b) and Figures 3.1.2.5 (a) and (b) compare the same location in secondary electron and backscattered imaging modes for the 1080 steel/stainless steel and 1080 steel/titanium composite coatings, respectively. Figures 3.1.2.6 (a) and (b) compare the unetched and etched microstructures of 1080 steel containing stainless steel powder.

Tables 3.1.2.4 and 3.1.2.5 show the results for the volume fraction of the second phase found in the 1080 steel composite coatings containing titanium and stainless steel, respectively. Tables 3.1.2.6 through 3.1.2.8 show the surface roughness data for coupons sprayed with both dual and single wire 1080 steel, and composite 1080 steel coatings containing either titanium or stainless steel. (The plasma spray parameters for the single and dual wire 1080 steel were both 230/30/235.) Figure 3.1.2.7 shows a typical example of the microstructure of the coupons sprayed with 1080 steel/stainless steel using these optimized spraying parameters.

3.1.3 Tensile Tests

Tensile tests were used to evaluate the effect of plasma spray parameters and second phase particles on coating adhesion strength. The test matrix of spray parameters examined and results found are given in Table 3.1.3.1. The results of second phase particle tensile tests are given in Table 3.1.3.2. Metallographic examination of the tested tensile bars showed that the failures occurred at the coating/substrate interface, i.e., adhesive failures. Figures 3.1.3.1 (a) and (b) show both sides of a typical tested tensile specimen. Figure 3.1.3.1 (a) shows some interlamellar separation, but not enough to lead to a cohesive failure.

3.1.4 Friction Reducing Coatings (1080 Steel/Nylon)

No parameter optimization was carried out for the friction reducing coatings. Rather, the parameters developed by Niebuhr were used for this work [2].

3.1.5 Full Scale Tests

The plasma spraying parameters used for the initial full scale tests (TL1, TL2, RL1) were developed by Niebuhr for his 1080 steel composite coatings. Premature coating failure during full scale tests made it necessary to re-optimize the spray parameters. A summary of the work follows.

Re-optimization of the plasma spraying parameters was performed using coupon verification. The coupons used for re-optimization were 5 cm thick sections of rail. Table 3.1.5.1 shows the test matrix used. The primary gas parameters were varied from 200 to 275 slpm nitrogen, the secondary gas parameters were varied from 0 to 75 slpm hydrogen, and the working distance was varied from 200 to 250 mm. The coupons were rotated to three different positions to obtain an even coating over the whole rail coupon surface. Approximately 50 to 60 passes were performed and the traverse speed was 20 passes per minute. Metallographic examination of the mounted and polished coatings from the center of the railhead showed the lowest oxide content and porosity in the 230/75/235 parameter set. Further fine tuning of this set of parameters was performed on the secondary gas by varying the hydrogen from 50 to 125 slpm. These tests confirmed that the 75 slpm hydrogen produced the optimum microstructure.

3.1.6 Final Plasma Spraying Parameters

The final parameters used for spraying each type of coating, stainless steel, 1080 steel, 1080 steel composites, and nylon are shown in Tables 3.1.6.1 through 3.1.6.4. Table 3.1.6.5 shows the parameters for the interrupted test Amsler rollers.

3.1.7 Full Scale Sample Plasma Spraying Parameters

Full scale samples were sprayed initially with a parameter set of 230/30/235 for the 1080 steel coatings sprayed on TL1, TL2, and RL1. After re-optimization the 1080 steel and stainless steel spray parameters used were 230/75/235. Nylon spray parameters were 200/50/255.

3.2 PREPARATION OF SUBSTRATES (GRIT BLASTING STUDY)

This portion of the research was aimed at assessing the roughening ability of various grit media and their ability to clean the original substrate surface while avoiding subsequent grit-induced contamination.

3.2.1 Grit Blast Media and Impact Angle Experiments

Table 3.2.1.1 presents the results of the profilometry tests for the eleven surface roughness samples. Figures 3.2.1.1 (a) to (e) compare the grit size and morphology of the alumina, silica and steel shot particles. Surfaces grit blasted at 45 and 90 degree impact angles showed little difference in the appearance of the surfaces when examined in the SEM. Contaminant particles were found to some degree on all the sample surfaces, Figure 3.2.1.2.

3.2.2 Substrate Hardness

The effect of substrate hardness on surface roughness was investigated. Table 3.2.2.1 lists the surface roughness measurements for the five different blasting media tested on new low hardness, hot-rolled rail and worn high hardness, head-hardened rail. Figure 3.2.2.1 shows the grit morphology for the Fe shot. Figure 3.2.2.2 compares the surfaces obtained by grit blasting steel with a variety of materials. Representative surface roughness profiles for

each of the grit blasting media are shown in Figure 3.2.2.3 through Figure 3.2.2.12. For comparison, Figure 3.2.2.13 through Figure 3.2.2.15 show the profile and surface morphology for a plasma sprayed coating.

3.2.3 Dwell Time

The effect of dwell time on surface roughness was investigated using a 36 grit alumina on plain steel. Table 3.2.3.1 shows the results of the surface roughness measurements for each dwell time. Table 3.2.3.2 shows the results of the measurements for surface contamination as a function of grit blast dwell time. Figure 3.2.3.1 shows, at low magnification, the contamination typically found on a grit blasted surface, while Figure 3.2.3.2 shows a close-up of a large grit particle and smaller particles embedded in the surface.

Figure 3.2.3.3 shows a cross-section of a typical grit contaminated surface at a low dwell time while Figure 3.2.3.4 shows a longer dwell time. It was found that at short dwell times the embedded alumina grit remained more intact, Figure 3.2.3.5, but the chance of oxide scale remaining was greater. Figure 3.2.3.6 shows a region where oxide scale and alumina particles were covered by a fold of metal during grit blasting. At longer dwell times, the oxides were removed but the grit particles became fragmented and regions of disturbed material resulted, Figure 3.2.3.7.

3.2.4 Tensile Testing

Table 3.2.4.1 shows the results of the tensile tests performed on the 1080 steel plasma sprayed coatings prepared using different grit media. Two different sets of alumina samples were prepared; one set was cleaned after grit blasting and the other set was left in the as-grit blasted condition.

3.2.5 Amsler Testing

Table 3.2.5.1 shows the results for the coating durability of 1080 steel Amsler tests. Table 3.2.5.2 shows the results of Amsler testing of stainless steel coatings prepared using the different grit media, in addition to a roller with a surface polished to 400 grit.

3.3 ROLLING/SLIDING WEAR TESTS USING THE AMSLER MACHINE

Amsler testing was used to assess the wear characteristics of the various coating systems. The baseline friction study sought coefficient of friction data on the various materials used and interrupted testing sought information on progression of wear for 1080 steel coatings.

3.3.1 Baseline Friction

The baseline friction section refers to the work performed to measure the coefficient of friction for the uncoated, monolithic materials of interest. Table 3.3.1.1 shows the baseline friction study test matrix. The tests marked with a "R" indicated that the bottom rollers were reused from another test. Due to a limited number of bottom rollers, rollers were reused when the surfaces showed no damage from the previous Amsler test. The highest load used for titanium rollers was 1175 MPa.

Tables 3.3.1.2 and 3.3.1.3 show the results for the titanium and stainless steel materials under investigation. Optical examination of the tested rollers showed a black film present on some of the water lubricated stainless steel roller surfaces, and, in some cases, over large areas of the surface. Figure 3.3.1.1 shows a black oxide film on the roller surface. Energy dispersive spectroscopy of the black film showed it to contain a higher amount of oxygen and silicon than in an area without the black film. In some of the water lubricated

steel tests, a light rust colored film was noted on the roller surfaces. Table 3.3.1.4 shows the coefficient of friction results for monolithic wheel and rail steels pairs at various contact pressures and slide/roll ratios under both dry and water lubricated conditions.

3.3.2 Lubricant-resistant Stainless Steel Coatings

Several factors were examined during Amsler testing of the various stainless steel plasma sprayed coatings, primarily, the effects of slide/roll ratio and contact pressure. Table 3.3.2.1 lists the test parameters and results for all the stainless steel coating tests. Failure was found to occur in three typical modes: by debonding from the substrate, by formation of edge cracks, and by bottom roller failure. Partial debonding of the coating from a tested Amsler roller is shown in Figure 3.3.2.1. Figures 3.3.2.2 (a) and (b) show the failure of the coating at the edges and the subsequent cracking induced by it. Figure 3.3.2.3 (a) shows the bottom roller surface for a plasma sprayed stainless steel test that failed due to excessive wear and material transfer to the bottom roller. For comparison, Figure 3.3.2.3 (b) shows the bottom roller surface of a plasma sprayed 1080 steel test that exhibited normal wear behavior.

3.3.3 Hard Particle Co-sprayed Composite Steel Coatings

Tables 3.3.3.1 and 3.3.3.2 show the test conditions and results obtained for Amsler tests on composite steel coatings containing stainless steel and titanium. The coatings failed by the transfer of material, starting with narrow, circumferential lines that widened until the complete surface was covered, Figure 3.3.3.1.

3.3.4 1080 Steel Interrupted Tests

Interrupted testing of 1080 steel coatings was carried out to understand the changes in microstructure as a function of test duration. Table 3.3.4.1 lists test and spray parameters for all the interrupted tests. Tables 3.3.4.2 through 3.3.4.4 show the test durations for the three different sets of interrupted tests. During testing, premature debonding frequently occurred. Figure 3.3.4.1 shows a cross-section of the worn surface of the bottom roller.

The microstructural characteristics of the tested coatings were measured. The coating thickness measurements for the tested rollers are shown in Tables 3.3.4.5 through 3.3.4.7. Tables 3.3.4.8 through 3.3.4.10 give the Knoop microhardness measurements for the tested rollers. Tables 3.3.4.11 through 3.3.4.13 give the porosity, oxide and metal fraction measurements for the tested rollers. Deformation depths for the tested rollers are shown in Tables 3.3.4.14 through 3.3.4.16.

3.3.5 1080 Steel Dual Wire Tests

Dual wire 1080 steel coatings were investigated with the objective of increasing the deposition rate, which would be a requirement for the high-rail concept vehicle. Wear tests were performed on rollers sprayed with dual steel wires to evaluate the impact of the increased deposition rate on coating performance. Table 3.3.5.1 shows the results of Amsler testing for dual wire steel coatings under water lubrication.

3.3.6 Stainless Steel/Nylon Coatings

A two layer plasma spray coating of stainless steel followed by nylon was assessed for friction and wear properties. These were compared to two layer 1080 steel and nylon coatings and to single layer stainless steel plasma sprayed coatings. The results of the Amsler tests for two layer stainless steel and nylon coatings are shown in Table 3.3.6.1.

Figure 3.3.6.1 shows a typical wear trace with the corresponding friction increase. The coefficient of friction, initially at 0.1, rose steadily as the wear test progressed to slightly greater than 0.2. For uncoated stainless steel, the friction coefficient ranged from 0.2 to 0.6 during wear testing depending on the amount of material transfer that occurred.

3.4 AS-RECEIVED FULL SCALE TEST RAIL AND SAMPLES

Tables 3.4.1 through 3.4.3 give a summary of the various full scale tests carried out at FAST in Pueblo, Colorado, along with notes about the failure modes and test conditions. Figure 3.4.1 through Figure 3.4.6 show the as-received rolling load coupon, each of the track lab specimens, and the FAST rail sections. The surface of Rolling Load 1 is shown with the coating spalled in large, thick chunks from the center of the rail around the wear track. Both Track Lab 1 and 2 showed debonding at the ends of the wear track. Differences in height between adjacent uncoated specimens in the track caused the coatings to spall in large, thick sections. For Track Lab 3 and 4, very little coating remained in the wear path. Only very small, thin pieces of the coating remained at the very edges of the wear track. The FAST rail showed debonding of the coating from the running surface and the gage face. The coating was found to spall in small, flake-like pieces.

For the specimens coated with nylon, bubbling of the nylon coatings was noted during initial stages of the wear tests. It was not known whether the bubbling indicated complete debonding of the nylon coating or whether it was simply excess nylon being sloughed from the running surface.

An in-depth characterization of each test specimen and wear debris is given in the following sections.

3.4.1 Characterization of Full Scale Test Rolling Load 1 (RL1)

3.4.1.1 Coating thickness measurements

The coating thickness measurements for RL1 are shown in Table 3.4.1.1. The unworn coating had a thickness ranging from 241 to 633 μm on the running surface of the coupon. The worn coating thickness ranged from 454 to 510 μm.

3.4.1.2 Microhardness

The Knoop microhardness values for RL1 are reported in Table 3.4.1.2. The unworn coating hardness ranged from 403 to 412 HK_{300}. The worn coating hardness was 445 HK_{300}. The substrate hardness was found to be 399 HK_{300}.

3.4.1.3 Microstructure

The microstructure of RL1 was found to be heterogeneous with high oxide concentrations in the form of bands that ran from the surface to the coating interface, Figure 3.4.1.1. Figure 3.4.1.2 shows a region of high oxide concentration and porosity. A low oxide region with interlamellar separation is shown in Figure 3.4.1.3. Figure 3.4.1.4 shows damage to the coating resulting from the breaking off of the protective epoxy layer during sectioning operations. Figures 3.4.1.5 and 3.4.1.6 show the wear surface of the coating. Figure 3.4.1.7 shows deformation at the coating surface.

Oxide cracking was found throughout the coatings, both in the worn and unworn samples, however, more extensive cracking was noted near the wear surfaces and in the regions where interface debonding occurred, Figure 3.4.1.8. Delamination was found to occur along the surfaces and in the vicinity of the coating/substrate interface as shown in Figures 3.4.1.9 and 3.4.1.10.

The coating was found to have a heterogeneous plasma sprayed microstructure. Regions of high oxide content were found concentrated in bands as shown in Figure 3.4.1.11. A large number of unmelted particles were noted, especially in the oxide bands, but also in the coating as a whole. Figure 3.4.1.12 shows the presence of inclusions in the coating microstructure. Both oxide and metallic inclusions were noted. The black features are the result of porosity and/or pullout of the oxides. Energy dispersive spectroscopy identified the dark gray phase as iron oxide.

Black contaminant particles were observed at the coating/substrate interface. This interface contamination, shown in Figure 3.4.1.13, was found by energy dispersive spectroscopy to be alumina that resulted from grit blasting operations.

3.4.2 Characterization of Full Scale Test Rolling Load 2 (RL2) Wear Debris

The RL2 full scale test sample was not returned to OGI for failure analysis. Only wear debris were received and examined for evidence of wear and deformation.

3.4.2.1 Microscopic analysis

The unmounted wear debris for RL2 were found to have a variety of morphologies, Figures 2.5.1.8 (a) and 3.4.2.1. While some of the particles were rounded, others had flat faces which appeared to result from wear of the coating. Energy dispersive spectroscopy of the particles found the presence of iron with trace amounts of Si, Al, C, Mn, and O.

In an unworn section of wear debris, Figure 3.4.2.2, oxide bands, porosity, and an intact nylon coating were found. A worn section of wear debris for RL2 showed delamination and cracking both in the coating interior, Figure 3.4.2.3, and at the surface, Figure 3.4.2.4. In one section of the worn coating debris, the coating was found to

be severely damaged with large, horizontal cracks running through it, Figure 3.4.2.5. Interlamellar debonding and cracking was commonly found throughout the debris coating samples, Figure 3.4.2.6.

A wear product was found mainly at the surface but also in the coating interior along cracks in the coating, Figures 3.4.2.7 and 3.4.2.4. Using backscattered electron imaging mode at high magnification, Figures 3.4.2.8 and 3.4.2.9, the debris was found to consist of various constituents of differing average atomic number. There appeared to be several different phases present, a lower atomic number material (black), a higher atomic number material (light gray), and white particles. In some cases the particles were finely compacted.

Energy dispersive spectroscopy was performed to identify the various constituents contained in the wear product. Bulk analysis found high amounts of Fe and C, with some O present. Spot analysis was performed on the higher and lower average atomic numbered materials in the wear product. Spot analysis found Fe, C, and O with trace amounts of Al, Si, Cr, and Mn in both cases.

3.4.2.2 Coating thickness

Table 3.4.2.1 shows the coating thickness for the RL2 wear debris. The coating thickness for the worn wear debris ranged from 719 to 963 μm. The worn coating thickness was 72 μm. The unworn nylon coating was found to be 144 ± 66 μm.

3.4.2.3 Microhardness

Table 3.4.2.2 shows the microhardness results for the RL2 wear debris. The unworn coating hardness ranged from 352 to 376 HK_{300}. The worn coating hardness was higher at 386 HK_{300} but showed a wider variation in the data.

3.4.3 Characterization of Full Scale Test Rolling Load 4 (RL4) Wear Debris

The RL4 full scale test sample was not returned to OGI for failure analysis. Only wear debris were received and examined for evidence of wear and deformation.

3.4.3.1 Microscopic analysis

The unmounted wear debris for RL4 are shown in Figure 3.4.3.1. The particles were irregular in shape with some particles showing flat surfaces indicating wear had occurred. The flat facets of these particles had the typical wear surface appearance containing cracks and lifted lamellae, Figure 3.4.3.2. Figure 3.4.3.3 shows the surface of a fractured particle displaying the lamellar coating structure. Figure 3.4.3.4 shows the surface of another wear particle with cracks and small wear debris particles on its surface.

Interlamellar debonding and oxide cracking were found in the mounted wear debris despite the coating being unworn. Figures 3.4.3.5 and 3.4.3.6 show cracking and inter-lamellar debonding of the coating surface.

Two different areas of an unworn wear debris particle are shown in Figure 3.4.3.7 and Figure 3.4.3.8. In Figure 3.4.3.7, taken towards the edge of the debris, oxides tended to be more banded. In the central, thicker sections of the debris, the coating had a more homogeneous microstructure, Figure 3.4.3.8, and there was less banding and porosity. Figure 3.4.3.9 compares a region of high and low oxides. Delamination was found between oxide and metallic lamellae, Figure 3.4.3.10.

A wear product was found at the surface of the RL4 coating, Figure 3.4.3.11. In backscattered imaging the wear product was found to consist of a lower average atomic numbered matrix with embedded higher atomic numbered particles. Energy dispersive

spectroscopy of the wear product found it to contain iron with trace amounts of C, Mn, Al, S, Ni, K, and Cl. The matrix material was found to contain the same elements but with much higher amounts of C.

3.4.3.2 Coating thickness

Table 3.4.3.1 shows the coating thickness values for the RL4 wear debris. The unworn steel coating thickness ranged from 1092 to 1200 μm. The unworn nylon thickness was 149 μm. The wear debris for RL4 was thick compared to the wear debris particles from other tests.

3.4.3.3 Microhardness

Microhardness for RL4 wear debris are presented in Table 3.4.3.2. The unworn coating hardness ranged from 349 to 401 HK_{300}.

3.4.4 Characterization of Full Scale Test Rolling Load 5 (RL5) Wear Debris

The full scale sample of RL5 was not returned to OGI for failure analysis. The wear debris received was in the form of debonded nylon coating. The wear debris resulted from the "bubbling up" of the nylon coating as described by AAR. Only SEM analysis was performed on the nylon wear debris.

A typical surface for the nylon wear debris is shown in Figure 3.4.4.1. Energy dispersive spectroscopy of the unmounted nylon wear debris found it to contain mainly C with small amounts of Si, S, and Cl. In some locations trace amounts of Fe and Ni were found, probably the result of small steel wear particles embedding in the nylon coating.

3.4.5 Characterization of Full Scale Test Track Lab 1 (TL1)

3.4.5.1 Microscopic analysis

Figure 3.4.5.1 shows the typical microstructure found in the TL1 tested coatings. The coatings, inside and outside the wear track, appeared similar in microstructure; the main difference was a rougher final surface topography compared to the coating towards the center of the rail. Contamination particles were found at the coating/substrate interface, Figure 3.4.5.1. Energy dispersive spectroscopy showed the particles to be alumina.

In Figure 3.4.5.2, the darker gray oxide constituent was found concentrated in bands. High porosity was also found in the coatings, in both the worn and the unworn sections. Examination of the samples showed that high porosity generally occurred in regions of high oxide content.

Examination in the SEM at high magnification showed oxides, in both the worn and unworn specimens, to contain microcracking. Figure 3.4.5.3 shows fine cracking of the oxide lamellae as well as cracking through the steel lamellae (light gray phase). Oxide cracking was found throughout the coatings both in and outside the wear track.

A section of TL1 was etched in order to determine whether any deformation had been introduced at the substrate surface during the test. Figure 3.4.5.4 shows the etched coating interface of a transverse worn section. Due to the fine microstructure of the substrate, no deformation was apparent in the microstructure. An etched longitudinal sample was also examined and deformation at the interface was not observed. However, as shown in Figure 3.4.5.5, damage in the near surface coating layers was observed.

The top surface of the worn coating is shown in Figure 3.4.5.6. Flat regions indicate worn metal particles while the small particles are fractured oxides. Flat, pancake-like wear particles and surface cracks in the oxides, Figure 3.4.5.7, were observed.

3.4.5.2 Coating thickness

Table 3.4.5.1 shows the coating thickness results for TL1. Thickness of the unworn steel coating ranged from 209 to 430 μm. The unworn steel coating thickness varied significantly with location of the sample. The worn steel coating thickness ranged from 390 to 469 μm.

3.4.5.3 Microhardness

Microhardness values are reported in Table 3.4.5.2. The unworn steel coating average hardness was 357 HK_{300}. The worn steel coating hardness was higher and the average ranged from 421 to 467 HK_{300}. The substrate was found to be 30 HRC (285 HB).

3.4.6 Characterization of Full Scale Test Track Lab 2 (TL2)

3.4.6.1 Microscopic analysis

Figure 3.4.6.1 shows the typical microstructure found in the TL2 sample. The microstructure was found to be heterogeneous with regions of oxide banding running from the coating/substrate interface to the coating surface. Both steel and oxide inclusions were found throughout the coating, Figure 3.4.6.2.

Figure 3.4.6.3 shows a region of high oxide content in the steel matrix along with high porosity. In comparison, Figure 3.4.6.4 shows a region of low oxide content. Unmelted and partially melted particles were also found concentrated in these regions.

Figure 3.4.6.5 shows the microcracking found near the surface of a worn coating. Figure 3.4.6.6 shows delamination of the lamellae near the worn surface. Figure 3.4.6.7 shows delamination of the coating at the coating/substrate interface.

Two types of wear surfaces were noted in the coatings examined. Figure 3.4.6.8 shows a wear surface that is smooth with the presence of deformation. The deformation, shown at higher magnification in Figure 3.4.6.9, shows flow of the steel lamellae and fracture of the brittle oxide lamellae. The other type of wear surface was rougher, as shown in Figure 3.4.6.10, where the coatings appeared to be disintegrating as wear occured.

3.4.6.2 Coating thickness

Table 3.4.6.1 lists the coating thickness values for several locations along the TL2 specimen. A high variation in the unworn coating thickness was found. The unworn steel coating thickness ranged from 672 to 1235 μm. The worn steel coating thickness ranged from 1047 to 1225 μm.

3.4.6.3 Microhardness

Knoop microhardness values for TL2 are reported in Table 3.4.6.2. The unworn steel coating hardness ranged from 339 to 382 HK_{300}. The worn steel coating had higher hardness which ranged from 474 to 498 HK_{300}.

3.4.6.4 Wear debris

The unmounted wear debris surfaces examined showed two different surface conditions. One was smooth and flat containing the typical pancake-like wear particles lifting from the surface. The other surface was rough, and, in places, was worn away revealing unmelted particles in the coating, Figures 3.4.6.11 and 3.4.6.12.

Table 3.4.6.3 shows the coating thickness for the TL2 wear debris. The unworn steel coating thickness was 582 μm. The worn steel coating thickness ranged from 436 to 704 μm. Table 3.4.6.4 shows the Knoop microhardness for the TL2 wear debris. The unworn steel coating microhardness was 375 HK_{300} while the worn coating hardness ranged from 378 to 460 HK_{300}.

Figure 3.4.6.13 shows a composite image of the wear debris which demonstrates the irregular nature of the coating microstructure. In Figures 3.4.6.14 and 3.4.6.15, a high oxide region containing unmelted particles and a low oxide region of the coating are compared. Figure 3.4.6.16 shows an unworn section of the wear debris with the nylon coating remaining and embedded with wear product. In Figure 3.4.6.17, backscattered imaging shows the composite nature of the wear product which contains metallic particles embedded within a lower average atomic number matrix.

Using energy dispersive spectroscopy, the higher average atomic numbered wear debris particles were found to contain Fe with traces of C, Cl, Cr, Si and Ni while the lower average atomic numbered particles contained Si with small amounts of Fe, Ni, O, and Al. The fines, with sizes on the order of a micron or less, were subjected to energy dispersive spectroscopy as well. These particles were found to consist of Fe and Si with traces of K, Ca, Al, C, Cu, Mg, Ni, and O. Other small particles contained S and C with traces of Fe, Ni, Cu, Si, P, Na, and O.

The mounted wear debris of TL2 had extensive cracking, not only at the wear surface, but throughout the bulk of the sample. Figure 3.4.6.18 shows cracking in the oxides within the coating bulk. Figure 3.4.6.19 shows the fractured wear surface of TL2. At the top of the surface is the wear product that was found in other coatings.

3.4.7 Characterization of Full Scale Test Track Lab 3 (TL3/N-2)

The Track Lab 3 and Track Lab 4 specimens received at OGI from AAR were labeled as "N-2" and "S-2". To identify which one was TL3 (listed as a stainless steel coating) and which one was TL4 (listed as a 1080 steel coating), energy dispersive spectroscopy was performed on both samples. Since the "N-2" sample showed the presence of nickel and chromium, while the "S-2" sample did not, the "N-2" sample was designated to be TL3 and the "S-2" sample was designated to be TL4.

3.4.7.1 Microscopic analysis

Figure 3.4.7.1 shows the microstructure of the TL3 coating at the field side edge of the wear track. Figure 3.4.7.2 shows the unworn coating outside the wear track on the field side. Plastic deformation of the wear surface and interlamellar debonding are seen in Figure 3.4.7.3. Figure 3.4.7.4 shows the stainless steel coating microstructure directly under the wear path. Interlamellar debonding and oxide cracking can be seen, as well as plastic deformation at the top of the image. Figure 3.4.7.5 shows a high oxide region.

3.4.7.2 Coating thickness

The thickness of the TL3 coating samples is shown in Table 3.4.7.1. The unworn steel coating thickness ranged from 190 to 285 μm. The worn steel coating thickness was 240 μm and the unworn nylon was 190 μm.

3.4.7.3 Microhardness

Microhardness values for TL3 are shown in Table 3.4.7.2. The hardness of the unworn steel coating ranged from 315 to 356 HK_{300}. The hardness of the worn steel coating

ranged from 322 to 332 HK_{300}. The coating measurements made perpendicular to the surface had a slightly lower hardness and narrower standard deviation than those made parallel. Substrate hardness measurements averaged 376 HK_{300}.

3.4.7.4 Wear debris

Energy dispersive spectroscopy of TL3 particles found them to contain Fe and Si with trace amounts of Al, C, and O indicating the material was plain carbon steel rather than stainless steel as was expected.

Table 3.4.7.3 shows the coating thickness of the TL3 wear debris. The unworn steel coating thickness was 228 μm while the worn coating thickness was higher at 342 μm. The nylon thickness was 209 μm. Table 3.4.7.4 shows the microhardness of the TL3 wear debris. The unworn steel coating hardness was 358 HK_{300} while the worn coating was higher at 416 HK_{300}.

The unmounted TL3 wear particles were found to have a variety of shapes and sizes ranging from rounded to flake-like, Figure 3.4.7.6. The red colored fines, around 1 μm in size, were examined and found to contain Fe, Si, S, and C with trace amounts of Cr, Al, Ni, Cu, Mn, P, S, K, Cl, Na, and O.

The examination of the mounted wear debris showed cracked oxides and interlamellar debonding. Figure 3.4.7.7 shows cracked oxides, surface deformation and interlamellar separation. Figure 3.4.7.8 shows both large and small cracks following along the oxides between the lamellae.

The microstructure of the TL3 wear debris showed it to be heterogeneous with high oxide regions appearing as bands, Figure 3.4.7.9. The top surface contained deformation and

wear particles indicating that most of the wear took place in this region, Figure 3.4.7.10. Figure 3.4.7.11 shows a region in the wear track with large band-like oxides and high porosity. Figure 3.4.7.12 shows a typical low oxide region of the coating.

3.4.8 Characterization of Full Scale Test Track Lab 4 (TL4/S-2)

3.4.8.1 Microscopic analysis

Energy dispersive spectroscopy identified the "S-2" track lab coupon as plain carbon steel thus it was labeled as TL4. Figure 3.4.8.1 shows the oxide patches rather than the banding that was found in other full scale test samples. Figure 3.4.8.2 shows the wear surface has a slight amount of plastic deformation very close to the surface.

For comparison, Figures 3.4.8.3 and 3.4.8.4 show two different worn sections of the TL4 coating, one a high oxide region and the other a low oxide region. Figure 3.4.8.5 shows interlamellar debonding in an unworn region well away from the wear track. Figure 3.4.8.6 shows debonding that occurred in lamellae away from the interface despite the presence of alumina contamination at the surface.

3.4.8.2 Coating thickness

The coating thickness of the TL4 samples is listed in Table 3.4.8.1. The unworn steel coating thickness was fairly consistent ranging from 165 to 188 μm. For the worn steel coating, the thickness ranged from 176 to 252 μm. The nylon coating thickness ranged from 136 to 142 μm. It was not possible to determine whether the nylon coatings were worn or unworn.

3.4.8.3 Microhardness

The microhardness values for TL4 are shown in Table 3.4.8.2. The unworn steel coating hardness ranged from 363 to 383 HK_{300}. The worn steel coating hardness was higher and ranged from 418 to 452 HK_{300}. The substrate hardness was found to be 389 HK_{300}.

3.4.8.4 Wear debris

Energy dispersive spectroscopy of TL4, both the 8,700 cycle and 18,723 cycle samples, showed the presence of Fe, Cr, and Ni indicating the samples were stainless steel, contrary to expectations.

Table 3.4.8.3 shows the coating thickness of the wear debris that were gathered at both 8,700 cycles and 18,723 cycles. At 8,700 cycles the unworn stainless steel coating thickness was 460 μm while the nylon thickness was 140 μm. At 18,723 cycles the unworn stainless steel coating thickness was 390 μm and the worn stainless steel coating ranged from 357 to 371 μm. The nylon coating was found to be 55 μm for the 18,723 cycle sample.

The microhardness for the wear debris are shown in Table 3.4.8.4. The unworn stainless steel coating hardness for wear debris at 8,700 cycles was 306 HK_{300}. The worn stainless steel coating hardness for wear debris at 18,723 cycles was 375 HK_{300}.

Two types of debris were found among the unmounted particles: flake-like particles and angular particles, Figure 3.4.8.7. The surface of an angular particle, Figure 3.4.8.8, shows the initiation of a flake-like particle from the wear surface. Figure 3.4.8.9 shows a typical microstructure of the wear debris for TL4 with large amounts of oxide in clumps rather than in bands. Throughout the coating both vertical and horizontal cracking occurred, and, at one end especially, the coating integrity was severely compromised, Figure 3.4.8.10.

Fractured and elongated oxide strings were found in regions where plastic deformation was evident, Figure 3.4.8.11. The nylon was intact at the unworn edges of the coating, Figure 3.4.8.12, and in some places large, highly deformed wear particles were embedded in the nylon, Figures 3.4.8.13 and 3.4.8.14.

The wear debris showed the contamination of the nylon coating by wear product similar to that found in other samples, Figure 3.4.8.15. A higher magnification of the fractured contaminant is shown in Figure 3.4.8.16. The wear product was found to contain what appeared to be small fractured lamellae. Energy dispersive spectroscopy showed the broken pieces to contain Fe with trace amounts of Cr, Al, Si, and Ni. Figure 3.4.8.17 shows the fracture of an oxide-rich region in the coating.

3.4.9 Characterization of Full Scale Test FAST Rail

3.4.9.1 Microscopic analysis

Figures 3.4.9.1 and 3.4.9.2 show representative cracks found in the wear track and gage face of the FAST rail substrate indicating the rail was worn rather than new as originally intended. Microhardness traverse measurements performed on the rail, Figure 3.4.9.3, from the interface to a depth of 6.0 mm showed a softened surface to a depth of 1.5 mm. Figure 3.4.9.4 shows a typical image of the FAST coating under the wear track. Some of the debonded regions showed break-up of the coating at the coating/substrate interface, Figure 3.4.9.5. No evidence of plastic deformation was found in the coatings.

Compared to the rail center, the gage face plasma sprayed coating had a much poorer microstructure. The same poor microstructure was found on the field side of the rail, however, very little wear was found, Figure 3.4.9.6. The dark region located just above the coating is unworn nylon. Contamination at the interface by alumina was found throughout the samples.

Figure 3.4.9.7 shows the interlamellar debonding in a low oxide region of the worn FAST coating. Figure 3.4.9.8 shows a high oxide region with the associated cracking of the friable oxides. Cracking was not just limited to the oxides. Figure 3.4.9.9 shows cracking in the steel lamellae seen at the right. Figure 3.4.9.10 shows the formation of a wear particle by interlamellar debonding. Figure 3.4.9.11 shows substrate cracking just below the debonded coating. Plastic flow in the coating surface was not found in these samples.

3.4.9.2 Coating thickness

The coating thickness measurements for the FAST rail are shown in Table 3.4.9.1. The coating thickness for the unworn steel ranged from 66 to 90 μm. The worn steel coating thickness ranged from 66 to 123 μm. The nylon coating thickness was found to be 48 μm.

3.4.9.3 Microhardness

Table 3.4.9.2 shows the microhardness values for the FAST rail. Due to the extremely thin nature of the coating remaining on the rail after wear testing, microhardness measurements were made parallel to the surface. The hardness of the unworn steel coating showed a wide variation ranging from 190 to 328 HK_{300}. The worn steel coating hardness ranged from 248 to 318 HK_{300}.

The substrate hardness was of concern after finding that the rail had been used in service and had cracking at the gage face and running surfaces. Figure 3.4.9.3 shows a microhardness traverse for a section of worn substrate that indicates a reduction in hardness for a depth of 1.5 mm.

3.4.9.4 Wear debris

Table 3.4.9.3 shows the coating thickness of the FAST wear debris. The unworn steel coating thickness was 76 μm while the worn steel coating thickness ranged from 82 to 103 μm. No nylon remained on the wear debris for measurement. Table 3.4.9.4 shows the microhardness for the FAST wear debris. The worn steel coating microhardness ranged from 254 to 334 HK_{300}.

A large particle of FAST debris was examined in the unmounted condition. The surface of the wear particle, Figure 3.4.9.12, shows a network of cracks resulting in wear particles lifting away from the bulk of the coating. Energy dispersive spectroscopy of the wear debris surface showed the presence of three different constituents. One constituent (light phase) contained Fe with traces of Mn, Ni, and Si. Another constituent was an oxide (gray phase) which was found to contain Fe and Si with traces of Al, Cr, Mn, Ni, Ca, and Cl. The third constituent (black phase) was found to consist mainly of Fe, C, and Si.

Examination of the mounted wear debris showed interlamellar separation and cracking in the oxides throughout the coating, Figure 3.4.9.13. Plastic deformation of the wear surface was not found. Figure 3.4.9.14 shows oxide cracking around an unmelted particle of steel. The interface between the oxide and steel lamellae was delaminated. Figure 3.4.9.15 shows the initiation of a wear particle as a result of interlamellar cracking. Energy dispersive spectroscopy of the FAST wear debris showed it to contain Fe and Si with small amounts of C and Al.

Figure 3.4.9.16 shows a region of high oxides, inclusions, and unmelted particles. For comparison, Figure 3.4.9.17 shows a region of coating where the oxides are more evenly distributed, although still high in inclusions. The wear debris examined for FAST appeared to have been worn on both sides as demonstrated by the smoothness of both the top and bottom surfaces, Figures 3.4.9.16 and 3.4.9.17.

Residual nylon coating was found inside cavities in the coating surface, as shown in Figure 3.4.9.18. No evidence of plastic deformation was noted. The coating showed high oxide regions and unmelted particles. Figure 3.4.9.19 shows the transition point from worn to unworn coating. On the right is the worn coating while on the left is the unworn coating still covered with nylon.

Figure 3.4.9.20 shows a wear product similar to that found in other samples. Wear products were found embedded between the coating and the substrate where the coating had separated from the substrate. Energy dispersive spectroscopy found the material to consist of particles having the same composition as the 1080 steel coating. Examination using the SEM at high magnification showed lamellar shaped debris.

Table 3.1.1.1. Stainless steel single splat analysis test matrix for parameter optimization for a working distance of 225 mm.

Primary Gas (N_2, slpm)	**Secondary Gas (H_2, slpm)**
230 [1]	0, 10, 20, **30** [1], 40, 50
235	35
240	20, 30, 40
250	20, 30, 40

[1] The highlighted values were the optimum parameters from McMurchie [1].

Table 3.1.2.1. Single splat parameter optimization for 1080 steel composite coatings using glass slides.

Parameter	**Value**
Primary gas, N_2 (slpm)	230
Secondary gas, H_2 (slpm)	30
Working distance (mm)	235
Carrier gas, N_2 (slpm)	14, 42
Powder feeder setting (rpm)	2, 3, 4, 5, 15

Table 3.1.2.2. Test matrix of powder feeder wheel and speed parameters.

Sample Number	Material	Powder Parameters (wheel type/rpm)	Test No.
2 [1]	1080 steel/stainless steel	Low Volume/15 rpm	A028
3		Low Volume/1 rpm	A029
6 [2]		High Volume/5 rpm	A030
7		High Volume/1 rpm	A031
4	1080 steel/titanium	Low Volume/1 rpm	A032
5		Low Volume/15 rpm	A033
8 [3]		High Volume/1 rpm	A034
9		High Volume/5 rpm	A035

[1] No bond coating.
[2] Cooling gas turned on late, runaway traverse.
[3] Spray interrupted for 2 minutes.

Table 3.1.2.3. Coupon test matrix for variation of powder injector points and gas parameters.

Gas Parameters	Powder Injector Distance from Gun Tip			
	35 mm	65 mm	90 mm	130 mm
230/30	✔	✔	✔	✔
250/33	✔	✔	✔	✔
275/36	✔	✔	✔	✔
295/40	✔	✔	✔	✔

Table 3.1.2.4. Volume fraction of second phase in 1080 steel/titanium composite coatings.

Sample I.D.	Injector Distance (mm)	Spray Parameters (N_2/H_2/WD)	Average Volume %
Ti1	35	230/30/235	8.9 ± 4.1
Ti2	35	250/33/235	5.0 ± 2.4
Ti3	35	275/36/235	2.6 ± 8.0
Ti4	35	295/40/235	25.7 ± 8.0
Ti5	65	295/40/235	2.5 ± 1.9
Ti6	65	275/36/235	2.5 ± 1.1
Ti7	65	250/33/235	2.9 ± 1.7
Ti8	65	230/30/235	2.2 ± 1.5
Ti9	90	230/30/235	10.2 ± 9.6
Ti10	90	250/33/235	5.9 ± 4.3
Ti11	90	275/36/235	8.7 ± 9.5
Ti12	90	295/40/235	7.5 ± 7.8
Ti13	130	295/40/235	10.7 ± 14.9
Ti14	130	275/36/235	1.1 ± 1.1
Ti15	130	250/33/235	2.7 ± 3.3
Ti16	130	230/30/235	1.2 ± 1.9

Table 3.1.2.5. Volume fraction of second phase in 1080 steel/stainless steel composite coatings.

Sample I.D.	Injector Distance (mm)	Spray Parameters (N_2/H_2/WD)	Average Volume %
SS1	60	230/30/235	38.9 ± 13.1
SS2	90	230/30/235	2.5 ± 0.8
SS3	130	230/30/235	3.4 ± 1.2
SS4	60	250/33/235	1.1 ± 0.8
SS5	60	275/36/235	2.8 ± 1.3
SS6	60	295/40/235	1.8 ± 0.7
SS7	90	250/33/235	1.1 ± 0.4
SS8	90	275/36/235	3.1 ± 1.9
SS9	90	295/40/235	2.4 ± 1.5
SS10	130	250/33/235	16.0 ± 13.3
SS11	130	275/36/235	4.1 ± 4.9
SS12	130	295/40/235	3.3 ± 4.3
SS13	35	230/30/235	3.0 ± 1.5
SS14	35	250/33/235	22.7 ± 15.9
SS15	35	275/36/235	1.5 ± 0.9
SS16	35	295/40/235	9.3 ± 3.8

Table 3.1.2.6. Surface roughness data for single and dual wire 1080 steel coatings.

Sample I.D.	Surface Roughness (μm)
Single	17.7 ± 2.9
Dual	18.9 ± 1.5

Table 3.1.2.7. Surface roughness for 1080 steel/titanium composite coatings.

Sample I.D.	Injector Distance (mm)	Spray Parameters (N_2/H_2/WD)	Surface Roughness (μm)
Ti1	35	230/30/235	24.4 ± 2.6
Ti2	35	250/33/235	24.9 ± 2.0
Ti3	35	275/36/235	24.8 ± 3.2
Ti4	35	295/40/235	25.2 ± 2.4
Ti5	65	295/40/235	27.8 ± 2.9
Ti6	65	275/36/235	25.9 ± 3.2
Ti7	65	250/33/235	25.3 ± 4.1
Ti8	65	230/30/235	20.0 ± 3.1
Ti9	90	230/30/235	26.5 ± 2.3
Ti10	90	250/33/235	23.0 ± 2.9
Ti11	90	275/36/235	24.4 ± 2.4
Ti12	90	295/40/235	24.0 ± 3.7
Ti13	130	295/40/235	23.0 ± 1.9
Ti14	130	275/36/235	21.1 ± 2.1
Ti15	130	250/33/235	22.6 ± 2.4
Ti16	130	230/30/235	23.8 ± 2.3

Table 3.1.2.8. Surface roughness for 1080 steel/stainless steel composite coatings.

Sample I.D.	Injector Distance (mm)	Spray Parameters (N_2/H_2/WD)	Surface Roughness (μm)
SS1	130	230/30/235	19.6 ± 1.8
SS2	90	230/30/235	26.0 ± 3.7
SS3	65	230/30/235	23.8 ± 3.4
SS4	65	250/33/235	20.5 ± 1.6
SS5	65	275/36/235	22.3 ± 2.9
SS6	65	295/40/235	18.6 ± 1.3
SS7	90	250/33/235	18.5 ± 3.0
SS8	90	275/36/235	23.7 ± 2.9
SS9	90	295/40/235	18.2 ± 1.4
SS10	130	250/33/235	19.1 ± 2.0
SS11	130	275/36/235	21.8 ± 2.3
SS12	130	295/40/235	23.3 ± 2.7
SS13	35	230/30/235	20.0 ± 2.2
SS14	35	250/33/235	20.7 ± 2.2
SS15	35	275/36/235	24.2 ± 4.6
SS16	35	295/40/235	25.5 ± 3.2

Table 3.1.3.1. Tensile test results for coatings created using three different spraying parameters.

Sample No.	Coating Bond Strength (MPa)		
	230/30/235	**230/75/235**	**300/75/235**
1	38.0	39.8	29.7
2	54.7	47.5	53.5
3	41.3	37.4	28.3
Average	**44.7**	**41.6**	**37.2**
Std. Dev.	**8.8**	**5.3**	**14.1**

Table 3.1.3.2. Tensile test results for composite coatings of 1080 steel with second phase titanium and stainless steel powders.

Sample No.	Coating Bond Strength (MPa)	
	Stainless Steel	**Titanium**
1	10.4	9.8
2	7.9	7.2
3	36.2	9.9
Average	**18.2**	**9.0**
Std. Dev.	**15.7**	**1.5**

Table 3.1.5.1. Full scale test plasma spray parameters test matrix.

Primary Gas (N_2, slpm)	**Secondary Gas (H_2, slpm)**	**Working Distance (mm)**	**Number of Passes**
60	275	30	235
60	200	30	235
60	230	0	235
50	230	75	235
55	230	30	200
58	230	30	250

Table 3.1.6.1. Spraying parameters for stainless steel and 1080 steel wire coatings.

Parameter	**Stainless Steel**	**1080 Steel**
Nitrogen (slpm)	240	230
Hydrogen (slpm)	30	30
Working distance (mm)	225	235
Voltage (V)	390	380
Current (A)	350	350
Wire type/diameter	308LSi/1.6 mm	1080/1.6 mm
Wire injector(s)	1	1
Wire injector angle (degrees)	45	45
Wire injector position (mm)	15	10
Wire speed	1.5	1.5
Time (minutes)	4-7	3-6
Number of passes	115-160	115-160
Cooling gas/location	CO_2/backside	CO_2/backside

Table 3.1.6.2. Spraying parameters for 1080 steel composite coatings.

Parameter	Condition
Nitrogen (slpm)	230
Hydrogen (slpm)	30
Working distance (mm)	235
Voltage (V)	380
Current (A)	350
Wire type/diameter	1080/1.6 mm
Wire injector(s)	2
Wire injector angle (degrees)	45
Wire injector position (mm)	15
Wire speed	1.5
Time (minutes)	2
Number of passes	65-75
Number of bond coat passes	15-20
Cooling gas/location	CO_2/backside
Powder type(s)	42F Austenitic stainless
	Titanium
Powder injector(s)	2
Powder injector angle (degrees)	45
Powder injector position (mm)	35

Table 3.1.6.3. Stainless steel parameters for stainless steel coated with nylon.

Parameter	Condition
Nitrogen (slpm)	230
Hydrogen (slpm)	50
Working distance (mm)	235
Voltage (V)	360
Current (A)	350
Wire type/diameter	308 L Si/1.6 mm
Wire injector(s)	1
Wire injector angle (degrees)	45
Wire injector position (mm)	15
Wire speed	1.5
Time (minutes)	7
Number of passes	130
Cooling gas/location	CO_2/backside

Table 3.1.6.4. Parameters for spraying nylon.

Parameter	Condition
Nitrogen (slpm)	200
Hydrogen (slpm)	50
Working distance (mm)	255
Voltage (V)	360
Current (A)	350
Bond coat	1080 steel
	Stainless steel
Cooling gas/location	Air/front
Powder	Nylon, neat
Powder injector(s)	2
Powder injector angle (degrees)	45
Powder injector position (mm)	43, Opposite
Powder feed wheel	High volume
Powder feed speed (rpm)	Full open
Powder carrier gas	N_2
Carrier gas flow rate (slpm)	42-56
Time (minutes)	Varied
Number of passes	16

Table 3.1.6.5. Plasma spraying parameters for interrupted tests.

Parameter	Condition
Nitrogen (slpm)	230
Hydrogen (slpm)	30
Working distance (mm)	235
Voltage (V)	360
Current (A)	350
Wire type/diameter	1080 steel/1.6 mm
Wire injector(s)	1
Wire injector angle (degrees)	45
Wire injector position (mm)	15, top
Wire speed	1.5
Time (minutes)	3.5
Number of passes	80
Cooling gas/location	CO_2/backside

Table 3.2.1.1. Results of the profilometry tests for the eleven surface roughness samples.

Grit Media	Grit Size (mesh)	Impact Angle (degrees)	Roughness, R_a, μm
Alumina	50-70	45	2.9 ± 0.2
		90	2.9 ± 0.3
Alumina	36	45	5.2 ± 0.7
		90	5.8 ± 0.3
Alumina	20	45	6.4 ± 0.7
		90	6.5 ± 0.9
Silica	50-70	45	2.2 ± 0.2
		90	2.1 ± 0.1
Steel Shot	25	45	7.5 ± 1.1
		90	6.2 ± 0.6
Polished	400	N/A	0.08 ± 0.02

Table 3.2.2.1. Surface roughness measurements for five different grit blast media on new and worn rail.

Blast Media	Rail Type	R_a (μm)	R_z (μm)	R_{max} (μm)	R_t (μm)	R_p (μm)	P_c (cm^{-1})	S_m (μm)	S (μm)
36 grit alumina	New	7.6	46	58	64	20	40	252	150
	Worn	4.8	33	40	45	14	49	204	115
Steel shot	New	9.0	58	69	74	27	40	250	172
	Worn	5.3	36	49	52	17	32	308	202
50/50 mix [1]	New	8.3	52	63	68	25	39	250	157
	Worn	5.2	36	44	48	17	46	216	128
Two-stage [2]	New	7.6	48	60	62	23	33	300	181
	Worn	5.4	35	45	50	16	33	298	197
Fe shot	New	7.4	47	58	62	21	31	321	172
	Worn	4.8	34	42	46	15	40	249	142
As-sprayed	N/A	18.3	87	107	115	41	29	345	201

Range = 20, except as-sprayed range = 50; $\lambda c = 0.8$; L = 5.

[1] 50/50 mix consisted of 36 grit alumina and steel shot by volume.

[2] Two-stage process used 36 grit alumina followed by steel shot.

Table 3.2.3.1. Surface roughness as a function of grit blasting dwell time using alumina.

Time (seconds)	R_a (µm)	R_z (µm)	R_{max} (µm)	R_t (µm)	R_p (µm)	P_c (cm^{-1})	S_m (µm)	S (µm)
5	7.5	41	48	50	19	49	200	130
10	7	38	44	48	17	47	211	130
15	7.5	41	54	57	20	47	215	151
20	6.7	38	52	54	18	45	221	138
25	7.7	44	56	60	21	51	196	154
30	6.9	39	48	51	18	45	225	134
45	7.1	40	48	51	20	49	205	136
60	7.3	42	54	56	20	48	209	151
120	7.3	42	54	56	20	49	203	149

Range = 20; $\lambda c = 0.8$; L = 5.

Table 3.2.3.2. Surface contamination as a function of grit blasting dwell time using alumina.

Dwell Time (seconds)	Measurement (cm)	Total Length (cm)	Uncontaminated Surface (%)
1 [1]	55	134	41
5	39	198	19
10	9	109	8
20	24	123	19
30	11	112	10
45	8	124	7
60	2	111	2
120	9	124	7

[1] Average of three readings.

Table 3.2.4.1. Tensile test results for different grit blast media.

Sample No.	Coating Bond Strength (MPa)						
	Alumina As-Grit Blasted	Alumina Cleaned Surface	Steel Shot	Fe Shot	Two-Stage [1]	50/50 Mix [2]	Glue Only
1	43.4	47.2	64.7	44.4	61.6	58.2	99.4
2	35.0	61.0	60.9	51.1	50.2	54.9	92.3
3	15.6	23.4	45.0	43.1	48.1	53.8	--
4	32.2	--	--	--	--	--	--
5	45.8	--	--	--	--	--	--
Average	**34.4**	**43.8**	**56.9**	**46.2**	**53.3**	**55.6**	**95.8**
Std. Dev.	**11.9**	**19.0**	**10.5**	**4.3**	**7.3**	**2.2**	**5.0**

[1] 50/50 mix consisted of 36 grit alumina and steel shot by volume.
[2] Two-stage process used 36 grit alumina followed by steel shot.

Table 3.2.5.1. Amsler test results for 1080 steel coatings prepared by various grit blasting processes.

Surface Preparation	Durability (revs.)	Friction Coefficient
20 grit alumina	1487 ± 393	0.45
36 grit alumina	4263 ± 620	0.44
Steel shot	1003 ± 121	0.44
Fe shot	5110 ± 3703	0.44
Two-stage [1]	1013 ± 389	0.45

[1] Two-stage process used 36 grit alumina followed by steel shot.

Table 3.2.5.2. Amsler test results for stainless steel coatings prepared using different grit media.

Surface Preparation	Slide/Roll (%)	Durability (revs.)	Friction Coefficient	Wear Rate (μg/m)
36 grit alumina [1]	34	326	0.54	56,954
20 grit alumina [1]	33	471	0.55	50,431
Polished (400) [2]	8	1621	0.43	5,058
Steel shot [2]	8	697	0.44	11,334

[1] Second grit blast just prior to spraying.
[2] Two bottom rollers used.

Table 3.3.1.1. Test matrix of slide/roll ratios for baseline friction study.

Test Pairs	Dry			Water		
	700 MPa	900 MPa	1220 MPa	700 MPa	900 MPa	1220 MPa
Ti/Ti	5%	5%	5% (1175) [1]	5%(R)	5%	5% (1175)
Ti/wheel steel	5%	5%	5% (1175)	5%	5%	5% (1175)
440C/440C	5%	5%(R)	5%(R)	5%	5%	5%
308/308	5%	5%(R)	5%(R)	5%	5%(R)	5%
308/wheel steel	5%	5%	5%	5%	5%	5%
Wheel/rail steel	5%, 20%, 35%	5%, 35%	5%, 20%, 35%	5%, 20%, 35%	5%, 35%	5%, 20%, 35%

[1] Numbers in parentheses indicate Ti tested value.

Table 3.3.1.2. Baseline coefficient of friction results for titanium.

Test Pairs	Dry			Water		
	700 MPa	900 MPa	1220 MPa	700 MPa	900 MPa	1220 MPa
Ti/Ti	0.33	0.35	0.34	0.36	0.34	0.30
Ti/wheel steel	0.36	0.34	0.26	0.36	0.32	0.28

Table 3.3.1.3. Baseline coefficient of friction results for stainless steel.

Test Pairs	Dry			Water		
	700 MPa	900 MPa	1220 MPa	700 MPa	900 MPa	1220 MPa
440C/440C	0.14	0.12	0.11	0.31	NA	0.24
308/308	0.13	0.10	0.10	0.10	0.08	0.27
308/wheel steel	0.10	0.16	0.15	0.40	0.36	0.30

Table 3.3.1.4. Baseline friction test results for wheel/rail roller pairs.

Contact Pressure (MPa)	Dry			Water		
	Load (N)	Slide/Roll (%)	Friction Coefficient	Load (N)	Slide/Roll (%)	Friction Coefficient
700	570	5	0.43	NA	5	NA
700	613	20	0.53	610	20	0.26
700	660	35	0.48	660	35	0.28
900	945	5	0.46	NA	5	NA
900	1090	35	0.60	1090	35	0.29
1220	1735	5	0.56	1730	5	0.29
1220	1860	20	0.53	1860	20	0.29
1220	2000	35	0.56	2000	35	0.26

Table 3.3.2.1. Test parameters and results for Amsler Tests.

Sample I.D.	Contact Pressure (MPa)	Slide/Roll Ratio (%)	Load (N)	Friction Coeff.	Wear Rate Top Roller (mg/m)	Wear Rate Top Roller (mg/m/mm)	No. Revs. Top Roller	Failure Mode	Coating Thickness (mm)	Wire Type/Diameter	Parameter Set N2/H2/WD/ Injector	Top Roller Material	Bottom Roller Material	Roller Conditions	Notes
A001	1220	35.0	2000	0.55	N/A	N/A	170	Debond	0.85	308L Si 1/16"	240/30/225/45 (10 mm)	X244	W10	Dry As-Sprayed	
A002	1220	36.0	2020	.22 to .60	N/A	N/A	290	Edge Cracks	0.86	308L Si 1/16"	240/30/225/45 (10 mm)	X244	W10	Dry Ground Flat	
A003	900	6.0	940	0.24	N/A	N/A	N/A	Debond	0.85	308L Si 1/16"	240/30/225/45 (10 mm)	X244	W9 (5%)	Dry As-Sprayed	
A004	900	5.3	940	0.33	782	156	2808	Debond	0.9	308L Si 1/16"	240/30/225/45 (10 mm)	X244	W9 (5%)	Dry As-Sprayed	
A005	900	36.0	1080	0.54	23868	4774	480	Debond	0.83	308L Si 1/16"	240/30/225/45 (10 mm)	X244	W10	Dry As-Sprayed	
A006	1220	5.0	1720	0.36	2241	448	571	Edge Cracks	0.87	308L Si 1/16"	240/30/225/45 (10 mm)	X244	W9 (5%)	Dry As-Sprayed	Edge cracking - stopped test.
A007	1220	33.0	2020	0.54	54433	10887	200	Edge Cracks	1.28	308L Si 1/16"	240/30/225/45 (10 mm)	X244	W10	Dry As-Sprayed	Edge cracking - stopped test.
A008	1220	33.0	1350	0.53	26797	5359	272	Edge Cracks	1.28	308L Si 1/16"	240/30/225/45 (10 mm)	X244	W10	Dry As-Sprayed	
A009	1220	34.0	2020	0.54	56954	11391	326	Debond	1.25	308L Si 1/16"	240/30/225/45 (10 mm)	X244	W10	Dry As-Sprayed	36 grit alumina.
A010	1220	33.0	2030	0.55	50431	10086	471	Debond	1.44	308L Si 1/16"	240/30/225/45 (10 mm)	X244	W10	Dry As-Sprayed	20 grit alumina.
A011	1220	2.0	1750	0.20	24	5	7554	None	1.51	308L Si 1/16"	240/30/225/45 (10 mm)	X244	W3 (5%)	Dry As-Sprayed	Successful test.
A012	1220	2.3	1750	0.31	580	116	9139	None	1.49	308L Si 1/16"	240/30/225/45 (10 mm)	X244	W3 (5%)	Dry As-Sprayed	Successful test.
A013	1220	6.8	1720	0.26	37	7	1420	Debond	0.7	308L Si 1/16"	240/30/225/45 (10 mm)	X244	W3 (5%)	Dry As-Sprayed	Multiple bottom rollers.
A014	1220	6.8	1720	0.40	87	17	553	N/A	0.69	308L Si 1/16"	240/30/225/45 (10 mm)	X244	W3 (5%)	Dry As-Sprayed	Multiple bottom rollers.
A015	1220	8.7	1700	0.44	8651	1730	353	Debond	0.38	308L Si 1/16"	240/30/225/45 (10 mm)	X244	W3 (5%)	Dry As-Sprayed	
A016	1220	8.6	1700	0.17	157	31	553	Error	0.39	308L Si 1/16"	240/30/225/45 (10 mm)	X244	W3 (5%)	Dry As-Sprayed	Multiple bottom rollers/ overspray fell off roller.
A017	1220	4.9	1730	0.38	935	187	2763	Debond	1.52	308L Si 1/16"	240/30/225/45 (10 mm)	X95	W3 (5%)	Dry As-Sprayed	Top roller 32.
A018	1220	5.1	1730	0.39	4356	871	1141	BR Failed	1.51	308L Si 1/16"	240/30/225/45 (10 mm)	X95	W3 (5%)	Dry As-Sprayed	Top roller 32.

Contact width was 5 mm and motor speed was 200 rpm for all tests.

Table 3.3.2.1. (Continued) Test parameters and results for Amsler Tests.

Sample I.D.	Contact Pressure (MPa)	Slide/Roll Ratio (%)	Load (N)	Friction Coeff.	Wear Rate Top Roller (mg/m)	Wear Rate Top Roller (mg/m/mm)	No. Revs. Top Roller	Failure Mode	Coating Thickness (mm)	Wire Type/Diameter	Parameter Set N2/H2/WD/ Injector	Top Roller Material	Bottom Roller Material	Roller Conditions	Notes
A019	1220	3.2	1750	0.44	1259	252	5734	Passed	1.84	308L Si 1/16"	240/30/225/45 (10 mm)	X244	W10 (5%)	Dry Ground Flat	Successful test.
A020	1220	3.3	1680	0.44	676	135	2726	Error	1.88	308L Si 1/16"	240/30/225/45 (10 mm)	X244	W10	Dry As-Sprayed	Stopped test due to dropped roller.
A021	1220	3.8	1740	0.38	1931	386	2274	Edge Cracks	1.66	308L Si 1/16"	240/30/225/45 (10 mm)	X244	W10	Dry As-Sprayed	Uneven wear on roller led to cracks.
A022	1220	6.1	1720	0.43	5862	1172	679	BR Failed	1.35	308L Si 1/16"	240/60/225/45 (10 mm)	X244	W10	Dry As-Sprayed	Data from BR 1/high h2 level.
A023	1220	6.4	1720	0.31	2210	442	4339	BR Failed	1.3	308L Si 1/16"	240/75/225/45 (10 mm)	X244	W10	Dry Ground Flat	Bottom roller failed/high H2 level.
A024	1220	8.3	1700	0.48	6511	1302	625	Debond	1.03	Cored 308L Si 1/16"	240/30/225/45 (10 mm)	X244	W10	Dry As-Sprayed	Cored wire/poor coatings.
A025	1220	8.3	1760	0.43	5058	1012	1621	Debond	1.36	308L Si 1/16"	240/30/225/45 (10 mm)	X244	W10	Dry As-Sprayed	400 grit/2 BR/thru cracks in coating.
A026	1220	8.3	1740	0.44	11334	2267	697	Debond	1.21	308L Si 1/16"	240/30/225/45 (10 mm)	X244	W10	Dry As-Sprayed	Steel shot/2 BR.
A027	1220	8.5	1700	N/A	161	32	118	N/A	0.88	308L Si 1/16"	240/30/225/45 (10 mm)	X244	W10	Dry As-Sprayed	Multiple BR/stopped test.
A028	1220	3.5	1750	0.52	28	6	1449	Debond	1.32	1080 1/16"	230/30/235	X244	W10	Dry As-Sprayed	1080 steel/stainless steel.
A029	1220	6.2	1730	0.48	514	103	851	Debond	0.84	1080 1/16"	230/30/235	X244	W10	Dry As-Sprayed	1080 steel/stainless steel.
A030	1220	6.1	1730	0.52	1963	393	453	Debond	0.8	1080 1/16"	230/30/235	X244	W10	Dry As-Sprayed	1080 steel/stainless steel.
A031	1220	5.6	1730	0.48	2446	489	625	Debond	1.11	1080 1/16"	230/30/235	X244	W10	Dry As-Sprayed	1080 steel/stainless steel.
A032	1220	6.4	1730	0.44	223	45	236	Debond	0.8	1080 1/16"	230/30/235	X244	W10	Dry As-Sprayed	1080 steel/titanium.
A033	1220	4.7	1740	0.49	99	20	299	Debond	1.11	1080 1/16"	230/30/235	X244	W10	Dry As-Sprayed	1080 steel/titanium.
A034	1220	6.9	1720	0.53	N/A	N/A	399	Debond	0.72	1080 1/16"	230/30/235	X244	W10	Dry As-Sprayed	1080 steel/titanium.
A035	1220	4.1	1730	0.46	88	18	906	Debond	1.12	1080 1/16"	230/30/235	X244	W10	Dry As-Sprayed	1080 steel/titanium.
A036	1220	7.6	1745	0.32	196	39	4611	Debond	0.85	308L Si 1/16"	240/30/225/45 (10 mm)	X244	W10	Water As-Sprayed	
A037	1220	7.5	1745	0.35	169	34	13170	Debond	0.86	308L Si 1/16"	240/30/225/45 (10 mm)	X244	W10	Water As-Sprayed	

Contact width was 5 mm and motor speed was 200 rpm for all tests.

Table 3.3.2.1. (Continued) Test parameters and results for Amsler Tests.

Sample I.D.	Contact Pressure (MPa)	Slide/Roll Ratio (%)	Load (N)	Friction Coeff.	Wear Rate Top Roller (mg/m)	Wear Rate Top Roller (mg/m/mm)	No. Revs. Top Roller	Failure Mode	Coating Thickness (mm)	Wire Type/Diameter	Parameter Set N2/H2/WD/ Injector	Top Roller Material	Bottom Roller Material	Roller Conditions	Notes
A038	1220	34.2	1990	0.57	85602	17120	299	High Vibration	0.91	308L Si 1/16"	240/30/225/45 (10 mm)	X244	W9	Water As-Sprayed	Extreme material transfer.
A039	1220	6.3	1700	0.22	N/A	N/A	634	Debond	0.64	1080 2 wire	230/30/235/45 (10 mm)	X244	W3	Water As-Sprayed	Want only coeff. of friction.
A040	1220	6.0	1700	0.23	N/A	N/A	399	Debond	0.65	1080 2 wire	230/30/235/45 (10 mm)	X244	W3	Water As-Sprayed	Want only coeff. of friction.
A041	1220	4.9	1770	0.22	711	142	471	Edge Cracks	1.32	1080 2 wire	230/30/235/45 (10 mm)	X244	W10	Water As-Sprayed	Want only coeff. of friction.
A042	1220	5.2	1765	0.21	521	104	543	Edge Cracks	1.27	1080 2 wire	230/30/235/45 (10 mm)	X244	W10	Water As-Sprayed	Want only coeff. of friction.
A043	1220	34.6	2000	0.50	N/A	N/A	N/A	Debond		1080 2 wire	230/30/235/45 (10 mm)	X244	W10	Dry As-Sprayed	Compare 1 & 2 wires.
A044	1220	34.6	200	0.53				Edge Cracks	0.5	1080 2 wire	230/30/235	X244	W10	Dry As-Sprayed	Edge cracking - stopped test.
A045	1220	37.0	2150	0.10 to 0.21				High Vibration	1.12/.002	308/Nylon	230/50/235	X252	W11	Dry As-Sprayed	Excessive vibration.
A046	1220	37.0	2150	0.10 to 0.21						308/Nylon	230/50/235	X252	W11	Dry As-Sprayed	Burnt Nylon.
A047	1220	37.0	2150	0.10 to 0.21					1.01/.002	308/Nylon	230/50/235	X252	W11	Dry As-Sprayed	Burnt Nylon.
A048	1220	34.6	2000	0.45				Debond	0.521	1080	230/30/235	X252	W11	Dry As-Sprayed	
A049	1220	35.0	2000	0.44				Debond	0.47	1080	230/30/235	X252	W11	Dry As-Sprayed	
A050	1220	35.0	2000	0.46				Debond	0.495	1080	230/30/235	X252	W11	Dry As-Sprayed	
A051	1220	35.0	2040	0.10 to 0.22				Debond	0.445	308/Nylon	230/50/235	X252	W11	Dry As-Sprayed	Friction only & max. revs.
A052	1220	35.0	2040	0.10 to 0.23				Debond	0.444	308/Nylon	230/50/235	X252	W11	Dry As-Sprayed	Friction only & max. revs.
A053	1220	35.0	2040	0.10 to 0.13				Debond	0.457	308/Nylon	230/50/235	X252	W11	Dry As-Sprayed	Friction only & max. revs.
A054	1220	35.1	2000	0.45				Debond	0.508	1080	230/30/235	X252	W11	Dry As-Sprayed	Two-stage prep.
A055	1220	35.0	1997	0.44				Debond	0.508	1080	230/30/235	X252	W11	Dry As-Sprayed	Two-stage prep.

Contact width was 5 mm and motor speed was 200 rpm for all tests.

Table 3.3.2.1. (Continued) Test parameters and results for Amsler Tests.

Sample I.D.	Contact Pressure (MPa)	Slide/Roll Ratio (%)	Load (N)	Friction Coeff.	Wear Rate Top Roller (mg/m)	Wear Rate Top Roller (mg/m/mm)	No. Revs. Top Roller	Failure Mode	Coating Thickness (mm)	Wire Type/Diameter	Parameter Set N2/H2/WD/ Injector	Top Roller Material	Bottom Roller Material	Roller Conditions	Notes
A056	1220	35.0	2000	0.45				Debond	0.47	1080	230/30/235	X252	W11	Dry As-Sprayed	Two-stage prep.
A057	1220	35.0	2000	0.44				Debond	0.483	1080	230/30/235	X252	W11	Dry As-Sprayed	Fe shot.
A058	1220	35.0	2000	0.44				Spalling	0.47	1080	230/30/235	X252	W11	Dry As-Sprayed	Fe shot.
A059	1220	35.0	2000	0.43				Debond	0.495	1080	230/30/235	X252	W11	Dry As-Sprayed	Fe shot.
A060	1220	35.4	2000	0.44				Debond	0.521	1080	230/30/235	X252	W11	Dry As-Sprayed	Steel shot.
A061	1220	35.0	2000	0.44				Debond	0.495	1080	230/30/235	X252	W11	Dry As-Sprayed	Steel shot.
A062	1220	35.0	2000	0.44				Debond	0.508	1080	230/30/235	X252	W11	Dry As-Sprayed	Steel shot.
A063	1220	35.7	1990	0.44				Edge Cracks	0.381	1080	230/30/235	X252	W11	Dry As-Sprayed	Alumina grit.
A064	1220	35.5	1990	0.44				Edge Cracks	0.381	1080	230/30/235	X252	W11	Dry As-Sprayed	Alumina grit.
A065	1220	35.6	1990	0.44				Edge Cracks	0.381	1080	230/30/235	X252	W11	Dry As-Sprayed	Alumina grit.

Contact width was 5 mm and motor speed was 200 rpm for all tests.

Table 3.3.3.1. Amsler test conditions and results for 1080 steel with stainless steel.

Test No./ Sample	Contact Load [1] (N)	Slide/Roll Ratio	Friction Coefficient	Test Duration (revs.)	Coating Thickness (μm)
A028/#2	1750	3.5	0.52	1600	1320
A029/#3	1730	6.2	0.48	940	830
A030/#6	1730	6.1	0.52	500	800
A031/#7	1730	5.6	0.48	690	1110

[1] These contact loads were chosen to give a contact pressure of 1220 MPa.

Table 3.3.3.2. Amsler test conditions and results for 1080 steel with titanium.

Test No./ Sample	Contact Load (N)	Slide/Roll Ratio	Friction Coefficient	Test Duration (revs.)	Coating Thickness (μm)
A032/#4	1730	6.4	0.44	260	800
A033/#5	1740	4.7	0.49	330	1110
A034/#8	1720	6.9	0.53	440	720
A035/#9	1730	4.1	0.46	1000	1120

Table 3.3.4.1. Test parameters and results for interrupted Amsler tests.

Sample I.D.	Contact Pressure (MPa)	Slide/Roll Ratio (%)	Load (N)	Friction Coeff.	No. Revs. Top Roller	Failure Mode	Contact Width	Motor Speed (rpm)	Coating Thickness (mm)	Wire Type/ Diameter	Parameter Set N2/H2/WD	Top Roller Material	Bottom Roller Material	Roller Conditions	Notes
I1-1	1220	31.0	2050	0.42	320	Debond	5	200	0.7	1080 1/16"	230/30/235	X244	W11	Dry As-Sprayed	Material x-fer started in 1st 100 revs.
I1-2	1220	37.6	1970	0.43	2560	Debond	5	200	0.66	1080 1/16"	230/30/235	X244	W10	Dry As-Sprayed	
I1-3	1220	37.8	1966	0.45	570	Debond	5	200	0.67	1080 1/16"	230/30/235	X252	W11	Dry As-Sprayed	BR had poor surface finish.
I1-4	1220	37.7	1965	0.43	670	Successful	5	200	0.67	1080 1/16"	230/30/235	X244	W11	Dry As-Sprayed	BR had poor surface finish.
I1-6	1220	38.2	1960	0.43	2260	Debond	5	200	0.56	1080 1/16"	230/30/235	X244	W10	Dry As-Sprayed	
I1-7	1220	38.3	1962	0.43	1340		5	200	0.56	1080 1/16"	230/30/235	X252	W11	Dry As-Sprayed	
I1-8	1220	38.2	1959	0.43	420		5	200	0.56	1080 1/16"	230/30/235	X252	W11	Dry As-Sprayed	BR had poor surface finish.
I1-10	1220	38.1	1960	0.43	260	Debond	5	200	0.58	1080 1/16"	230/30/235	X244	W10	Dry As-Sprayed	BR had poor surface finish.
I2-1	1220	34.9	1998	0.43	680		5	200	0.5	1080 1/16"	230/30/235	X252	W11	Dry As-Sprayed	BR had poor surface finish.
I2-2	1220	34.9	1998	0.43	510	Debond	5	200	0.5	1080 1/16"	230/30/235	X252	W11	Dry As-Sprayed	
I2-3	1220	35.1	1995	0.43	1780	Debond	5	200	0.45	1080 1/16"	230/30/235	X252	W11	Dry As-Sprayed	
I2-5	1220	35.3	1996	0.45	130		5	200	0.45	1080 1/16"	230/30/235	X252	W11	Dry As-Sprayed	
I2-6	1220	34.9	1998	0.43	600	Debond	5	200	0.49	1080 1/16"	230/30/235	X252	W11	Dry As-Sprayed	
I2-7	1220	35.0	1997	0.43	970	Debond	5	200	0.48	1080 1/16"	230/30/235	X252	W11	Dry As-Sprayed	
I2-9	1220	35.1	1995	0.43	1340	Debond	5	200	0.46	1080 1/16"	230/30/235	X252	W11	Dry As-Sprayed	
I2-10	1220	35.0	2000	0.43	340		5	200	0.47	1080 1/16"	230/30/235	X252	W11	Dry As-Sprayed	
I3-1	1220	35.5	1990	0.44	740	Debond	5	200	0.41	1080 1/16"	230/30/235	X252	W11	Dry As-Sprayed	
I3-2	1220	35.1	1995	0.44	620	Debond	5	200	0.48	1080 1/16"	230/30/235	X252	W11	Dry As-Sprayed	BR had poor surface finish.
I3-3	1220	35.0	1997	0.44	670	Debond	5	200	0.48	1080 1/16"	230/30/235	X252	W11	Dry As-Sprayed	BR had poor surface finish.
I3-4	1220	35.3	1996	0.45	510		5	200	0.47	1080 1/16"	230/30/235	X252	W11	Dry As-Sprayed	BR had poor surface finish.
I3-5	1220	35.1	1998	0.45	340		5	200	0.48	1080 1/16"	230/30/235	X252	W11	Dry As-Sprayed	BR had poor surface finish.
I3-6	1220	35.2	1997	0.45	170		5	200	0.5	1080 1/16"	230/30/235	X252	W11	Dry As-Sprayed	BR had poor surface finish.
I3-7	1220	35.0	1999	0.47	70		5	200	0.5	1080 1/16"	230/30/235	X252	W11	Dry As-Sprayed	BR had poor surface finish.

Table 3.3.4.2. Test durations for interrupted test Set 1.

Test Roller No.	Coating Life (%)	Durability (revs.)
I1-1	15 (D)	320
I1-2	100	2560
I1-3	25 (D)	570
I1-4	25	670
I1-6	100	2260
I1-7	50	1340
I1-8	15	420
I1-10	10 (D)	260

D = Premature debond failure.

Table 3.3.4.3. Test durations for interrupted test Set 2.

Test Roller No.	Coating Life (%)	Durability (revs.)
I2-1	40	680
I2-2	30 (D)	510
I2-3	100	1780
I2-5	10	130
I2-6	40 (D)	600
I2-7	60	970
I2-9	100	1340
I2-10	20	340

D = Premature debond failure.

Table 3.3.4.4. Test durations for interrupted test Set 3.

Test Roller No.	Coating Life (%)	Durability (revs.)
I3-1	100	740
I3-2	100	620
I3-3	100	670
I3-4	75	510
I3-5	50	340
I3-6	25	170
I3-7	10	70

Table 3.3.4.5. Coating thickness for interrupted test Set 1.

Test Roller No.	Durability (revs.)	Thickness (μm)
I1-1	320	599 ± 12
I1-2	2560	524 ± 9
I1-3	570	475 ± 13
I1-6	2260	427 ± 10
I1-10	260	414 ± 5

Table 3.3.4.6. Coating thickness for interrupted test Set 2.

Test Roller No.	Durability (revs.)	Thickness (μm)
I2-1	680	394 ± 9
I2-2	510	429 ± 12
I2-3	1780	345 ± 7
I2-6	600	404 ± 6
I2-7	970	339 ± 7

Table 3.3.4.7. Coating thickness for interrupted test Set 3.

Test Roller No.	Durability (revs.)	Thickness (μm)
I3-1	740	353 ± 7
I3-2	620	342 ± 5
I3-3	670	334 ± 5
I3-4	510	359 ± 7
I3-5	340	367 ± 9
I3-6	170	356 ± 6
I3-7	70	419 ± 11

Table 3.3.4.8. Knoop microhardness for interrupted test Set 1.

Test Roller No.	Durability (revs.)	Hardness (HK_{300})
I1-1	320	428 ± 12
I1-2	2560	402 ± 20
I1-3	570	427 ± 18
I1-6	2260	439 ± 26
I1-10	260	439 ± 43

Table 3.3.4.9. Knoop microhardness for interrupted test Set 2.

Test Roller No.	Durability (revs.)	Hardness (HK_{300})
I2-1	680	461 ± 18
I2-2	510	423 ± 22
I2-3	1780	431 ± 46
I2-6	600	442 ± 22
I2-7	970	446 ± 30

Table 3.3.4.10. Knoop microhardness for interrupted test Set 3.

Test Roller No.	Durability (revs.)	Hardness (HK_{300})
I3-1	740	420 ± 23
I3-2	620	430 ± 22
I3-3	670	455 ± 21
I3-4	510	424 ± 34
I3-5	340	444 ± 40
I3-6	170	432 ± 67
I3-7	70	410 ± 62

Table 3.3.4.11. Porosity, oxide and metal fractions for interrupted test Set 1.

Test Roller No.	Porosity (%)	Oxide (%)	Metal (%)
I1-1	0.33 ± 0.21	33.34 ± 2.63	66.32 ± 2.56
I1-2	0.28 ± 0.23	34.69 ± 2.71	65.03 ± 2.71
I1-3	0.13 ± 0.18	34.47 ± 2.71	65.40 ± 2.76
I1-6	0.20 ± 0.20	30.77 ± 2.38	69.03 ± 2.43
I1-10	0.16 ± 0.18	29.23 ± 2.26	70.61 ± 2.31

Table 3.3.4.12. Porosity, oxide and metal fractions for interrupted test Set 2.

Test Roller No.	Porosity (%)	Oxide (%)	Metal (%)
I2-1	0.64 ± 0.37	35.04 ± 4.37	64.32 ± 4.49
I2-2	1.02 ± 0.41	32.90 ± 5.53	66.08 ± 5.70
I2-3	0.78 ± 0.33	33.18 ± 5.37	66.04 ± 5.45
I2-6	0.73 ± 0.37	33.78 ± 5.29	65.49 ± 5.41
I2-7	0.81 ± 0.29	33.64 ± 4.80	65.55 ± 4.97

Table 3.3.4.13. Porosity, oxide and metal fractions for interrupted test Set 3.

Test Roller No.	Porosity (%)	Oxide (%)	Metal (%)
I3-1	1.07 ± 0.49	40.40 ± 8.66	58.53 ± 8.70
I3-2	0.56 ± 0.23	34.57 ± 5.08	64.88 ± 5.18
I3-3	0.55 ± 0.23	30.70 ± 4.29	68.75 ± 4.38
I3-4	0.57 ± 0.30	30.56 ± 5.17	68.87 ± 5.28
I3-5	0.88 ± 0.44	30.15 ± 4.32	68.97 ± 4.45
I3-6	0.42 ± 0.22	28.47 ± 5.30	71.10 ± 5.41
I3-7	0.90 ± 0.40	33.03 ± 4.92	66.07 ± 5.09

Table 3.3.4.14. Depth of deformation from surface for interrupted test Set 1.

Test Roller No.	Durability (revs.)	Deformation Depth (μm)
I1-1	320	74.24 ± 15.95
I1-2	2560	85.87 ± 26.44
I1-3	570	55.19 ± 14.99
I1-6	2260	49.33 ± 12.23
I1-10	260	40.13 ± 12.46

Table 3.3.4.15. Depth of deformation from surface for interrupted test Set 2.

Test Roller No.	Durability (revs.)	Deformation Depth (μm)
I2-1	680	28.61 ± 8.63
I2-2	510	40.89 ± 15.66
I2-3	1780	31.90 ± 12.50
I2-6	600	45.78 ± 13.53
I2-7	970	26.61 ± 8.89

Table 3.3.4.16. Depth of deformation from surface for interrupted test Set 3.

Test Roller No.	Durability (revs.)	Deformation Depth (μm)
I3-1	740	NA
I3-2	620	39.83 ± 11.71
I3-3	670	39.15 ± 10.27
I3-4	510	47.58 ± 13.03
I3-5	340	43.80 ± 16.49
I3-6	170	21.72 ± 8.25
I3-7	70	53.22 ± 14.07

Table 3.3.5.1. Amsler test results for water lubricated dual wire 1080 steel coatings.

Test No.	Contact Pressure (MPa)	Slide/Roll Ratio	Friction Coefficient	Thickness (μm)	Test Duration (revs.)
A039	1220	6	0.22	640	700
A040	1220	6	0.23	650	440
A041	1220	5	0.22	1320	520
A042	1220	5	0.21	1270	600

Table 3.3.6.1. Amsler test results for nylon coated stainless steel rollers tested at 1220 MPa and 35% slide/roll.

Test No.	Nylon Condition	Coating Thickness (μm)	Test Duration (revs.)
A045	burned	1120	4070
A046	burned	1090	4980
A047	burned	1010	3170
A051	good	450	13250
A052	good	440	12910
A053	good	460	11870

Table 3.4.1. Test data for rolling load samples tested at Pueblo, Colorado.

Sample	Coating Life (MGT)	Failure Mode	Test Conditions
RL1	2.2	Large scale debonding of steel coat from rail	45 kips pure rolling
RL2	0.2	Large scale debonding of steel coat from rail	45 kips varying slide/ roll ratio
RL3	0.24	Large scale break-up starting from one end	45 kips high slide/roll ratio
RL4	1.72	Large scale break-up, large pieces of coating	35 kips pure rolling

Table 3.4.2. Track lab data for samples tested at Pueblo, Colorado.

Sample	Coating Life (MGT)	Failure Mode	Notes
TL1	0.12	Steel debond	No debris collected
TL2	0.32	Steel debond	Fine black particles
TL3	6	Steel debond	Nylon bubbled off
TL4	0.8	Steel debond	Nylon bubbled off

Table 3.4.3. FAST test data for sample tested at Pueblo, Colorado.

Sample	Coating Life (MGT)	Failure Mode	Notes
FAST	1.7	Steel debond	Heavy axle loads in 2-3 degree curves

Table 3.4.1.1. Coating thickness for RL1.

Sample No.	Condition	Thickness (μm)
16B	Unworn	493 ± 44
22B	Unworn	241 ± 29
23B	Worn	454 ± 17
26B	Worn	510 ± 30
29B	Unworn	633 ± 56

Table 3.4.1.2. Knoop microhardness for RL1.

Sample No.	Location	Condition	Hardness (HK_{300})
10B	Coating	Unworn	403 ± 36
15B	Coating	Unworn	409 ± 41
23B	Coating	Worn	445 ± 27
26B	Coating	Worn	446 ± 32
30B	Coating	Unworn	412 ± 30

Table 3.4.2.1. Coating thickness for RL2 wear debris.

Sample No.	Location	Condition	Thickness (μm)
1A	Coating	Unworn	719 ± 100
1A	Nylon	Unworn	144 ± 66
1B	Coating	Unworn	963 ± 139
2A	Coating	Worn	72 ± 12

Table 3.4.2.2. Microhardness for RL2 wear debris.

Sample No.	Location	Condition	Hardness (HK_{300})
1A	Coating	Unworn	376 ± 45
1B	Coating	Unworn	352 ± 56
2A	Coating	Worn	386 ± 109

Table 3.4.3.1. Coating thickness for RL4 wear debris.

Sample No.	Location	Condition	Thickness (μm)
A	Coating	Unworn	1200 ± 45
A	Nylon	Unworn	149 ± 31
B	Coating	Unworn	1092 ± 80

Table 3.4.3.2. Microhardness for RL4 wear debris.

Sample No.	Location	Condition	Hardness (HK_{300})
A	Coating	Unworn	349 ± 87
B	Coating	Unworn	401 ± 47

Table 3.4.5.1. Coating thickness for TL1.

Sample No.	Location	Condition	Thickness (μm)
5-2	Coating	Unworn	430 ± 56
8-1	Coating	Worn	469 ± 28
8-2	Coating	Unworn	346 ± 48
13-1	Coating	Worn	390 ± 30
17-1	Coating	Worn	394 ± 32
17-2	Coating	Unworn	209 ± 49

Table 3.4.5.2. Knoop microhardness for TL1.

Sample No.	Location	Condition	Hardness (HK_{300})
5-2	Coating	Unworn	367 ± 31
8-1	Coating	Worn	421 ± 32
8-2	Coating	Unworn	338 ± 35
13-1	Coating	Worn	467 ± 40
13-2	Coating	Unworn	364 ± 38
17-1	Coating	Unworn	358 ± 41

Table 3.4.6.3. Coating thickness for TL2 wear debris.

Sample No.	Location	Condition	Thickness (μm)
A	Coating	Worn	704 ± 75
B	Coating	Unworn	582 ± 66
C	Coating	Worn	436 ± 39

Table 3.4.6.4. Microhardness for TL2 wear debris.

Sample No.	Location	Condition	Hardness (HK_{300})
A	Coating	Worn	460 ± 58
B	Coating	Unworn	375 ± 47
C	Coating	Worn	378 ± 47

Table 3.4.7.1. Coating thickness for TL3.

Sample No.	Location	Condition	Thickness (μm)
N2A	Coating	Unworn	255 ± 42
N2A	Nylon	NA	140 ± 55
N2A	Coating	Worn	240 ± 44
N2B	Coating	Unworn	285 ± 56
N2B	Nylon	Unworn	190 ± 58

Table 3.4.6.1. Coating thickness for TL2.

Sample No.	Location	Condition	Thickness (μm)
10A	Coating	Unworn	848 ± 188
10B	Coating	Unworn	1092 ± 118
10B	Coating	Worn	1225 ± 78
11B	Coating	Worn	1047 ± 100
11B	Coating	Unworn	1120 ± 61
11C	Coating	Unworn	672 ± 88
15A	Coating	Unworn	874 ± 186
15B	Coating	Unworn	962 ± 97
15C	Coating	Unworn	720 ± 54
18A	Coating	Unworn	1004 ± 55
18B	Coating	Unworn	1235 ± 123

Table 3.4.6.2. Knoop microhardness for TL2.

Sample No.	Location	Condition	Hardness (HK_{300})
10A	Coating	Unworn	376 ± 40
11B	Coating	Worn	498 ± 54
15A	Coating	Unworn	339 ± 66
15B	Coating	Worn	474 ± 37
18A	Coating	Unworn	382 ± 49

Table 3.4.7.2. Knoop microhardness for TL3.

Sample No.	Location	Condition	Hardness (HK_{300})
N2A	Coating	Worn	322 ± 34
N2A [1]	Coating	Worn	332 ± 42
N2A	Coating	Unworn	356 ± 24
N2B	Coating	Unworn	315 ± 61

[1] Measured parallel to the surface.

Table 3.4.7.3. Coating thickness for TL3 wear debris.

Sample No.	Location	Condition	Thickness (μm)
TL3A	Coating	Unworn	228 ± 48
TL3A	Nylon	Unworn	209 ± 118
TL3B	Coating	Worn	342 ± 10

Table 3.4.7.4. Knoop microhardness for TL3 wear debris.

Sample No.	Location	Condition	Hardness (HK_{300})
TL3A	Coating	Unworn	358 ± 40
TL3B	Coating	Worn	416 ± 48

Table 3.4.8.1. Coating thickness for TL4.

Sample No.	Location	Condition	Thickness (μm)
S2A	Coating	Worn	176 ± 31
S2A	Coating	Unworn	165 ± 41
S2A	Nylon	NA	142 ± 42
S2B	Coating	Worn	252 ± 12
S2B	Coating	Unworn	188 ± 45
S2B	Nylon	NA	136 ± 34
S2C	Coating	Worn	198 ± 22
S2C	Coating	Unworn	183 ± 36
S2C	Nylon	NA	142 ± 34

Table 3.4.8.2. Knoop microhardness for TL4.

Sample No.	Location	Condition	Hardness (HK_{300})
S2A	Coating	Unworn	377 ± 34
S2A	Coating	Worn	452 ± 44
S2B	Coating	Unworn	363 ± 60
S2B	Coating	Worn	424 ± 68
S2C	Coating	Unworn	383 ± 37
S2C	Coating	Worn	418 ± 46

Table 3.4.8.3. Coating thickness for TL4 wear debris.

Sample No.	No. of Cycles	Location	Condition	Thickness (μm)
TL4A	8700	Coating	Unworn	460 ± 30
TL4A	8700	Nylon	NA	140 ± 60
TL4B-A	18723	Nylon	NA	55 ± 23
TL4B-A	18723	Coating	Worn	357 ± 42
TL4B-B	18723	Coating	Worn	371 ± 31
TL4B-B	18723	Coating	Unworn	390 ± 66

Table 3.4.8.4. Knoop microhardness for TL4 wear debris.

Sample No.	No. of Cycles	Location	Condition	Hardness (HK_{300})
TL4A	8700	Coating	Unworn	306 ± 25
TL4B-A	18723	Coating	Worn	375 ± 47

Table 3.4.9.1. Coating thickness of FAST rail.

Sample No.	Location	Condition	Thickness (μm)
15B	Coating	Worn	66 ± 10
15C	Nylon	Unworn	48 ± 25
45C	Coating	Unworn	66 ± 31
35A	Coating	Worn	123 ± 12
35B	Coating	Worn	89 ± 17
35C	Coating	Unworn	90 ± 26
55A	Coating	Worn	82 ± 9
55B	Coating	Worn	75 ± 9
70B	Coating	Worn	72 ± 12
70C	Coating	Unworn	87 ± 26

Sample location A-gage face, B-running track, and C-field side.

Table 3.4.9.2. Knoop microhardness for FAST rail, measurements parallel to surface.

Sample No.	Location	Condition	Hardness (HK_{300})
15B	Coating	Worn	290 ± 73
15C	Coating	Unworn	328 ± 81
45C	Coating	Unworn	245 ± 100
55A	Coating	Worn	248 ± 37
55B	Coating	Worn	318 ± 45
55C	Coating	Unworn	312 ± 84
70B	Coating	Worn	279 ± 36
70C	Coating	Unworn	190 ± 85

Sample location A-gage face, B-running track, and C-field side.

Table 3.4.9.3. Coating thickness for FAST wear debris.

Sample No.	Location	Condition	Thickness (μm)
1A	Coating	Unworn	76 ± 20
1A	Coating	Worn	103 ± 4
1B	Coating	Worn	82 ±10

Table 3.4.9.4. Knoop microhardness for FAST wear debris.

Sample No.	Location	Condition	Hardness (HK_{300})
1A	Coating	Worn	254 ± 43
1B	Coating	Worn	334 ± 62

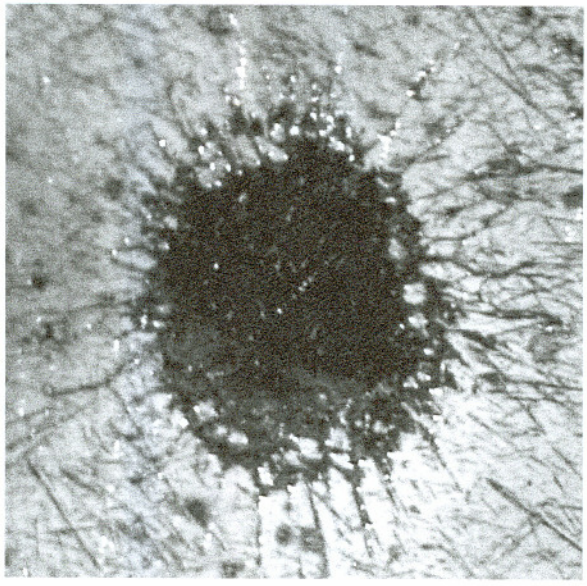

(a)

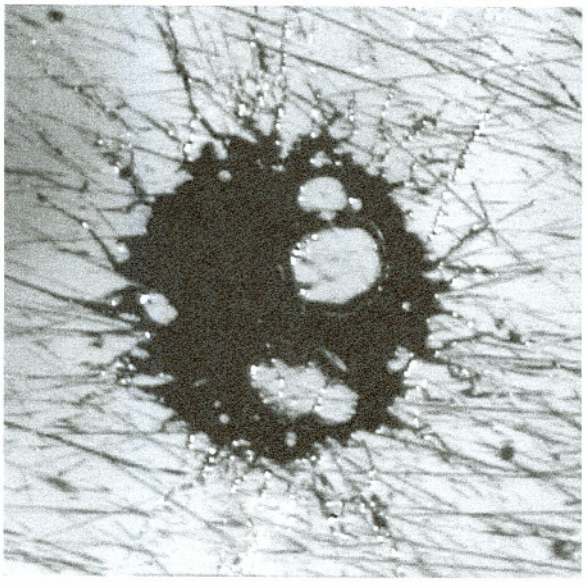

(b)

Figure 3.1.1.1. Splat morphology for (a) optimized parameters and (b) non-optimized parameters. 500x, optical micrographs.

Figure 3.1.1.2. Microstructure of the stainless steel coating sprayed using the parameters optimized by single splat analysis. 400x, optical micrograph.

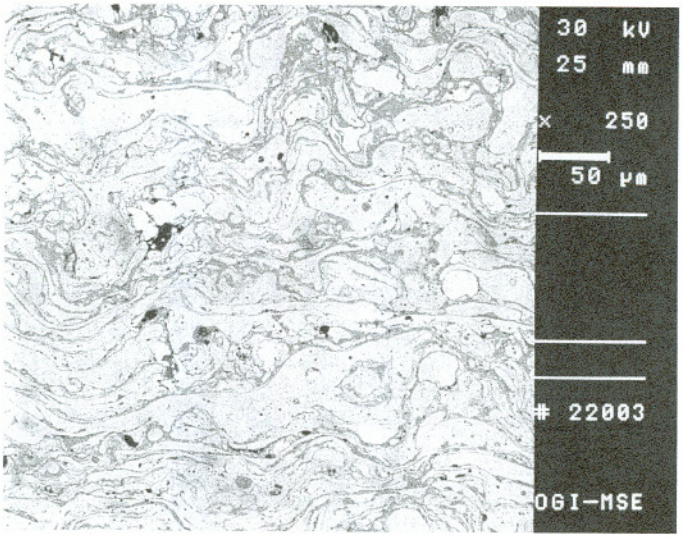

(a)

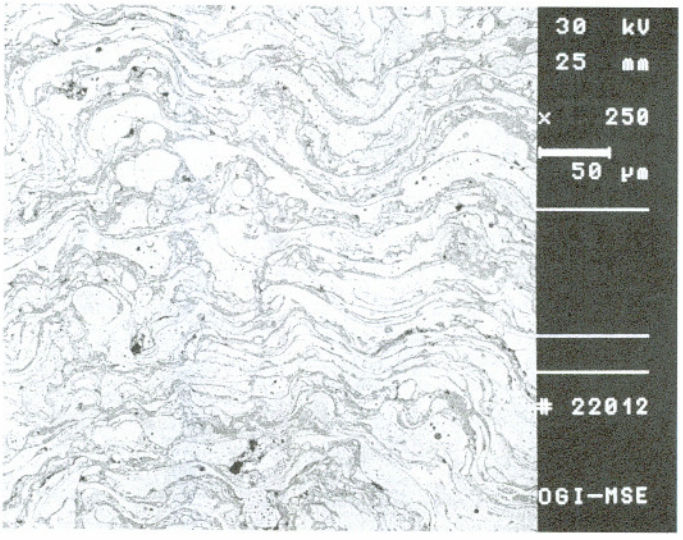

(b)

Figure 3.1.2.1. Typical microstructures for 1080 steel/stainless steel using (a) low volume feed wheel and (b) high volume feed wheel. 250x, backscattered electron images.

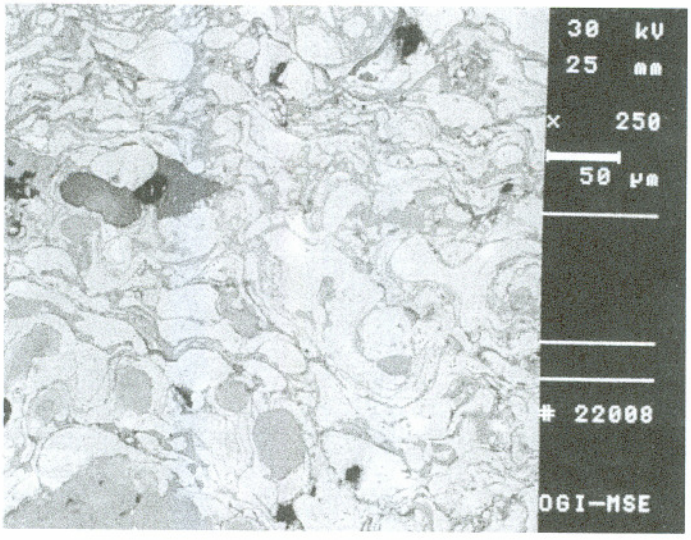

(a)

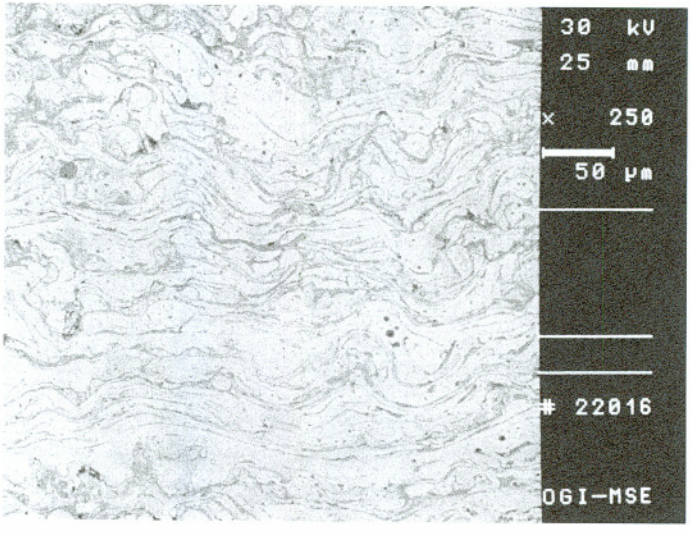

(b)

Figure 3.1.2.2. Typical microstructures for 1080 steel/titanium using (a) low volume feed wheel and (b) high volume feed wheel. 250x, backscattered electron images.

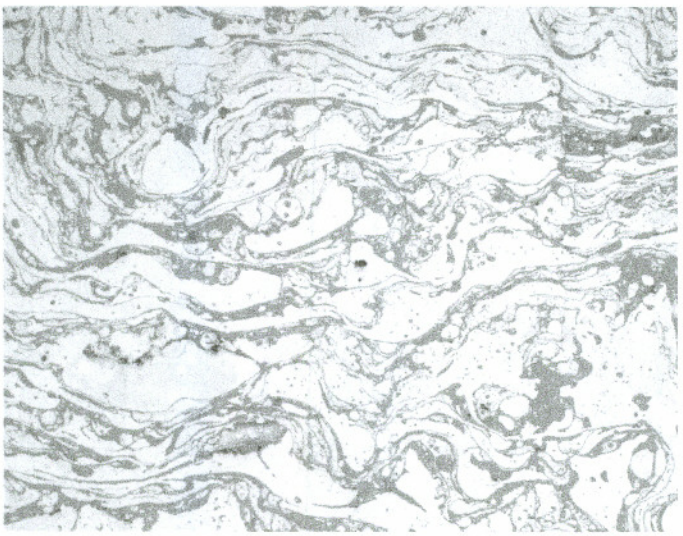

(a)

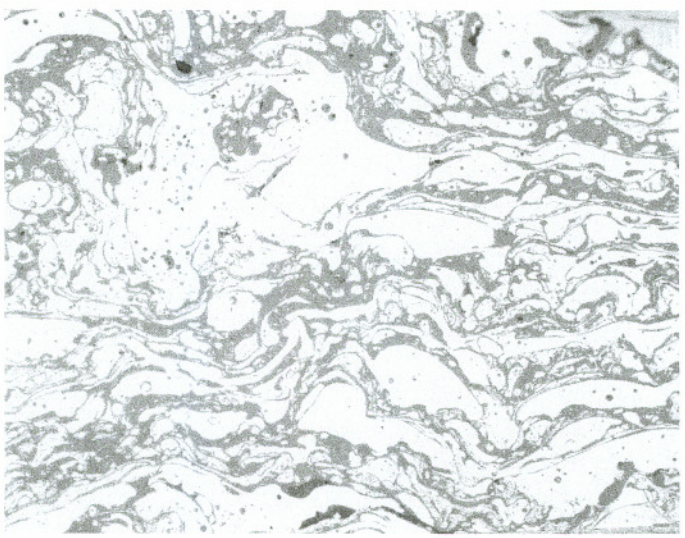

(b)

Figure 3.1.2.3. Optical photomicrographs showing little difference between the powder phases and the matrix phase of (a) 1080 steel/stainless steel and (b) 1080 steel/titanium. 400x, optical micrographs.

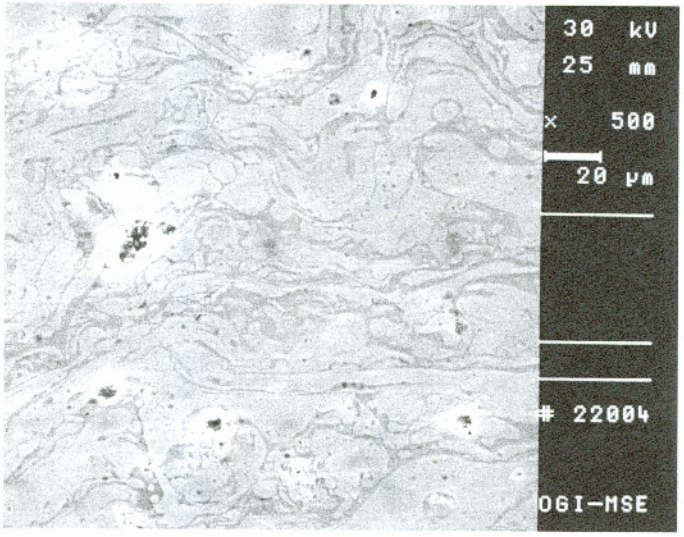

(a)

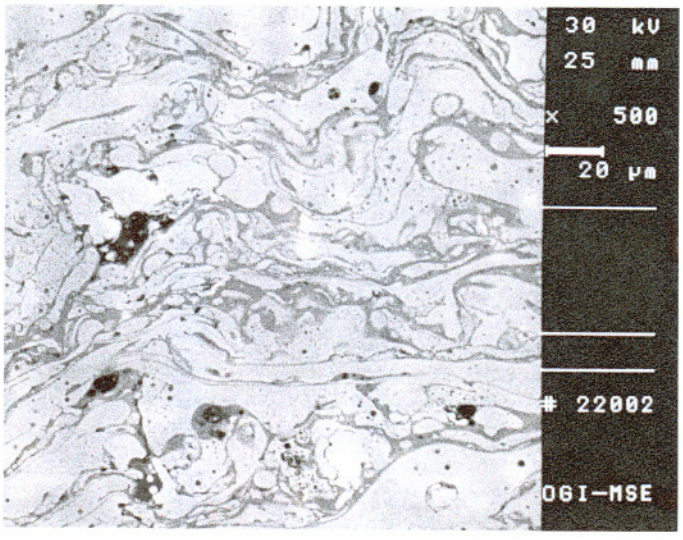

(b)

Figure 3.1.2.4. Scanning electron photomicrographs showing little difference between the stainless steel powder phase and the 1080 steel matrix phase, (a) 500x, secondary electron image and (b) 500x, backscattered electron image.

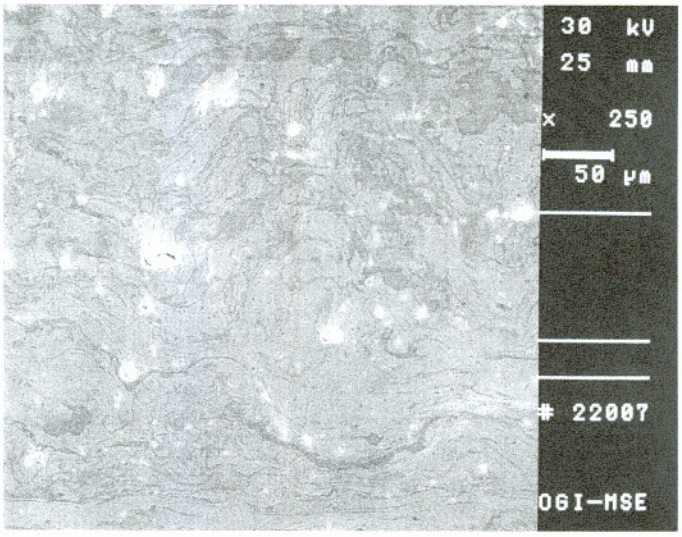

(a)

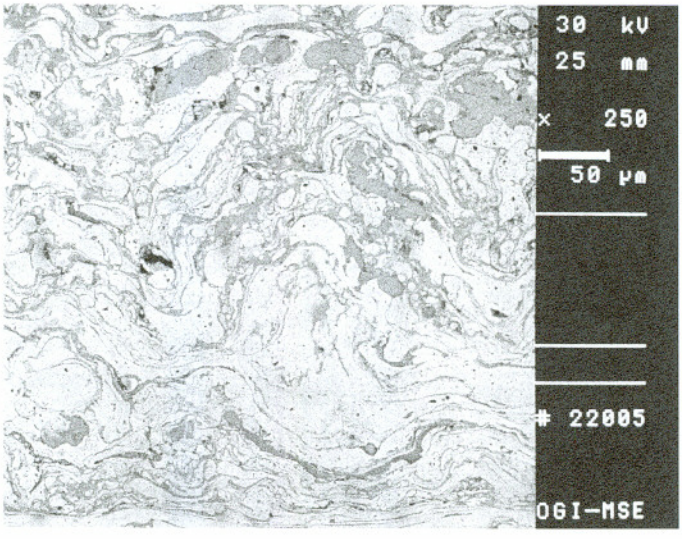

(b)

Figure 3.1.2.5. Scanning electron photomicrographs showing little difference between the titanium powder phase and the 1080 steel matrix phase, (a) 250x, secondary electron image and (b) 250x, backscattered electron image.

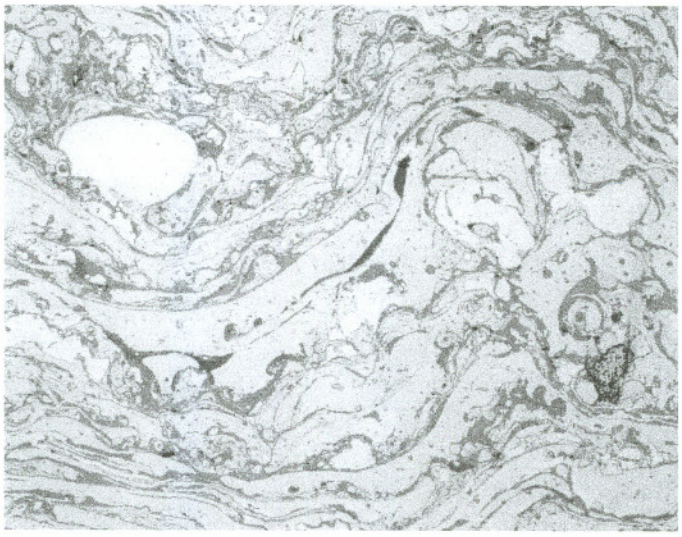

(a)

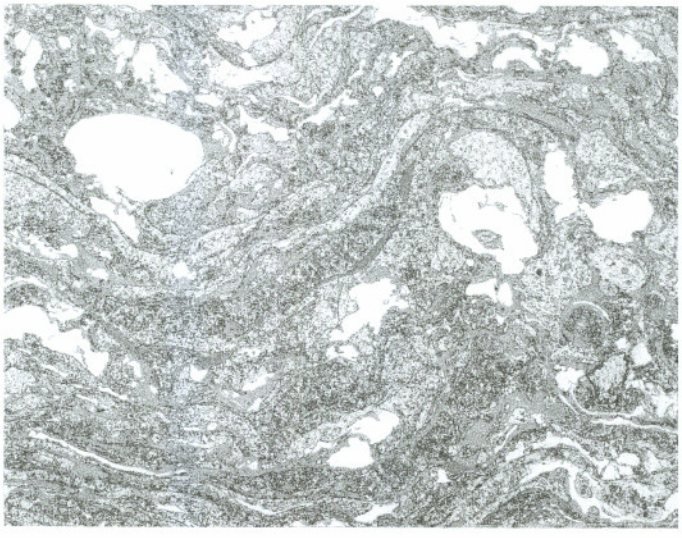

(b)

Figure 3.1.2.6. Comparison of (a) unetched and (b) etched microstructures of 1080 steel with stainless steel.
400x, optical micrographs.

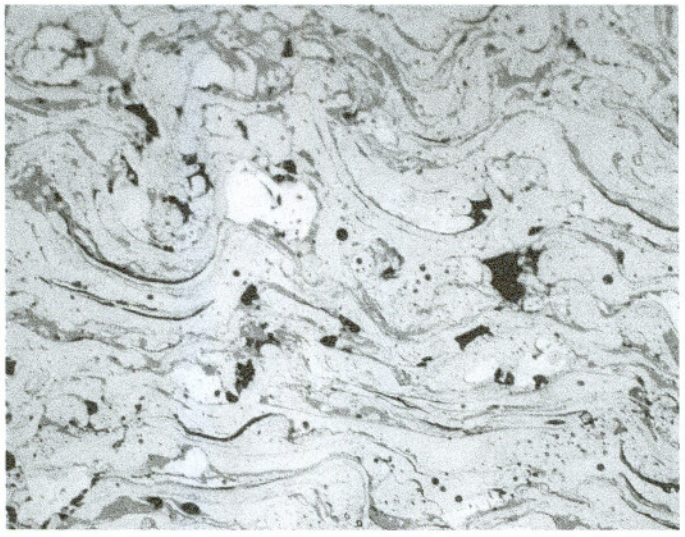

Figure 3.1.2.7. Typical microstructure of the 1080 steel/stainless steel composite coating coupons sprayed using 230/30/235, showing high porosity. 400x, optical micrograph.

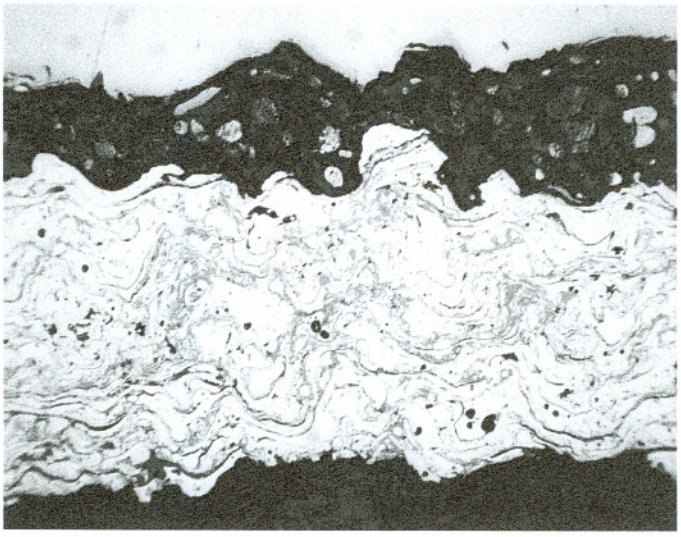

(a)

(b)

Figure 3.1.3.1. Photomicrographs of tested tensile bars showing adhesive failures occurring at the coating/substrate interface, (a) coating and 3M epoxy on one side of specimen and (b) bare substrate on other side of specimen. 100x, optical micrographs.

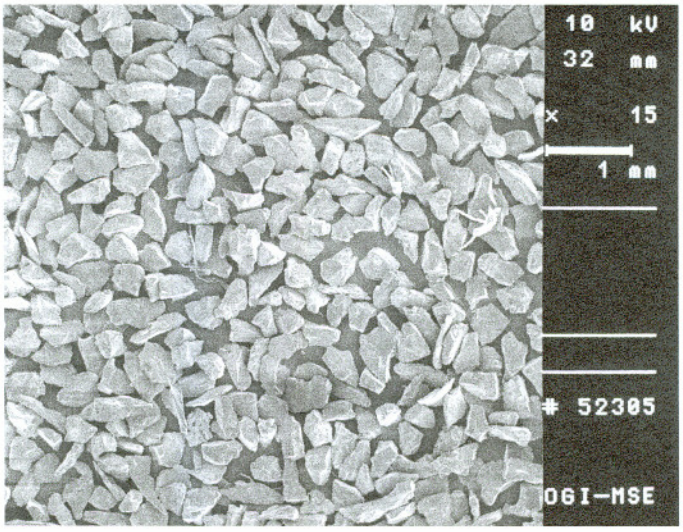

(a)

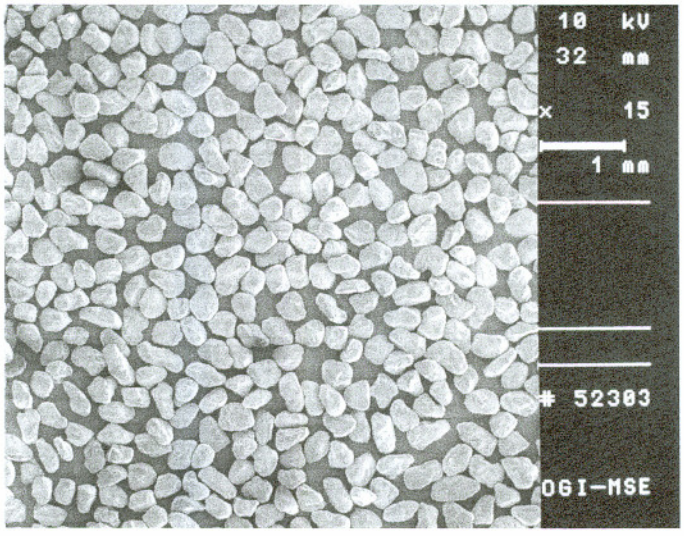

(b)

Figure 3.2.1.1. Comparison of particles, sizes and morphologies for (a) 50-70 grit alumina, (b) 50-70 grit silica, (c) 20 grit alumina, (d) 36 grit alumina and (e) 25 grit steel shot. 15x, secondary electron images.

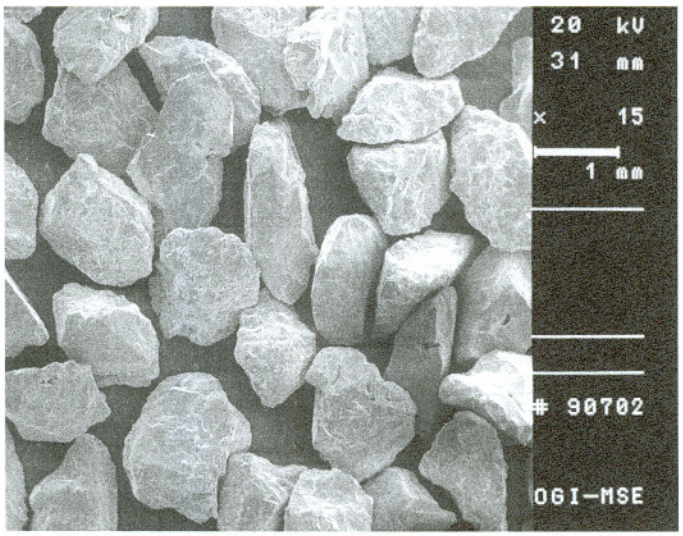

(c)

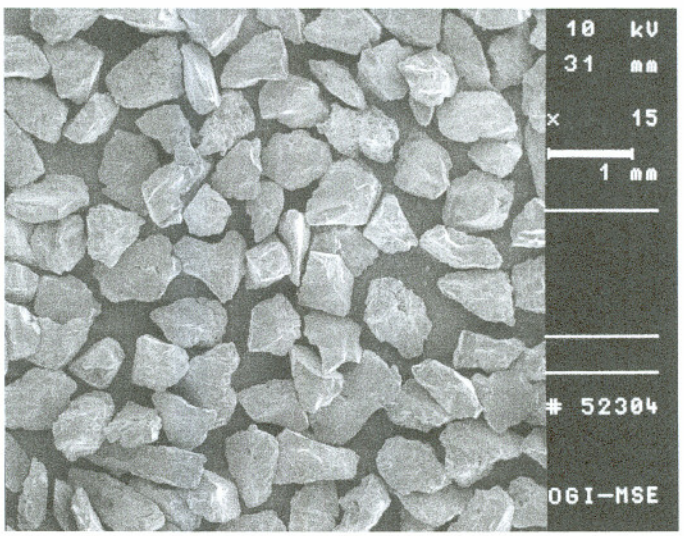

(d)

Figure 3.2.1.1. (Continued) Comparison of particles, sizes and morphologies for (a) 50-70 grit alumina, (b) 50-70 grit silica, (c) 20 grit alumina, (d) 36 grit alumina and (e) 25 grit steel shot. 15x, secondary electron images.

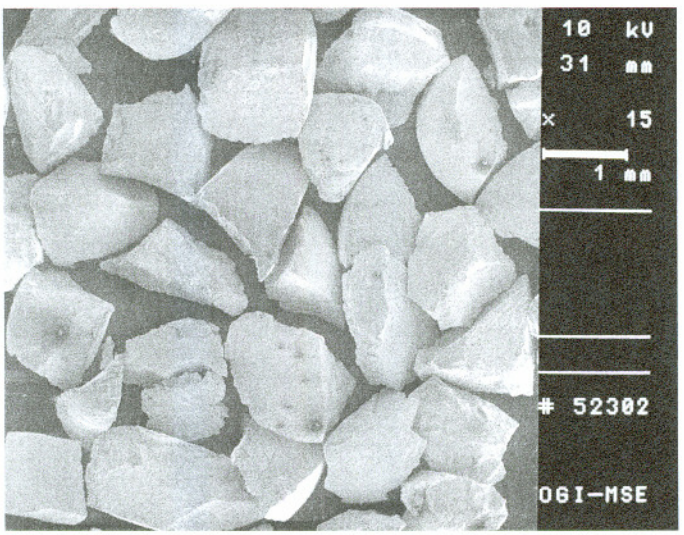

(e)

Figure 3.2.1.1. (Continued) Comparison of particles, sizes and morphologies for (a) 50-70 grit alumina, (b) 50-70 grit silica, (c) 20 grit alumina, (d) 36 grit alumina and (e) 25 grit steel shot. 15x, secondary electron images.

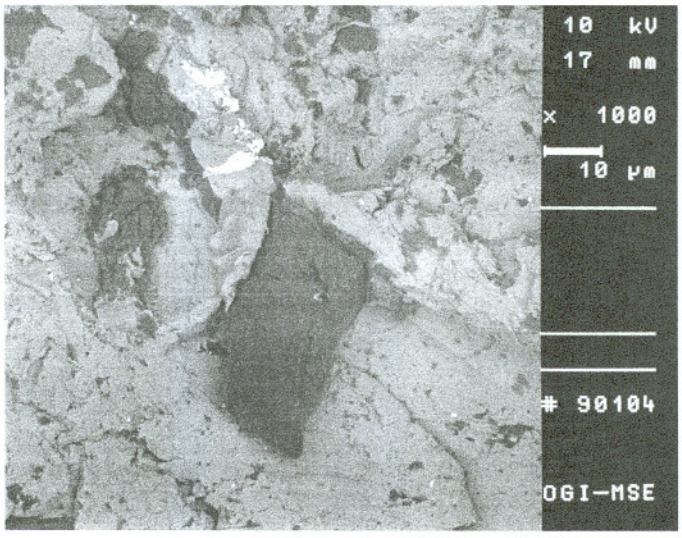

Figure 3.2.1.2. Embedded alumina particles and tungsten particles (white) from nozzle breakdown. 1000x, backscattered electron image.

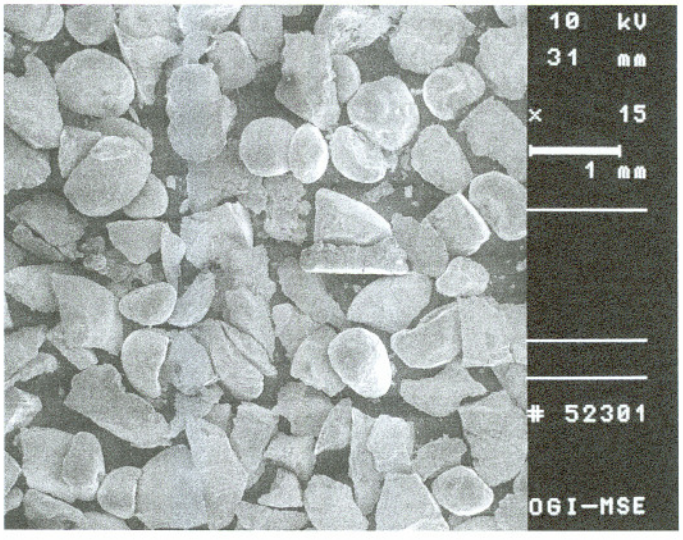

Figure 3.2.2.1. Grit particle sizes and morphologies for Fe shot. 15x, secondary electron image.

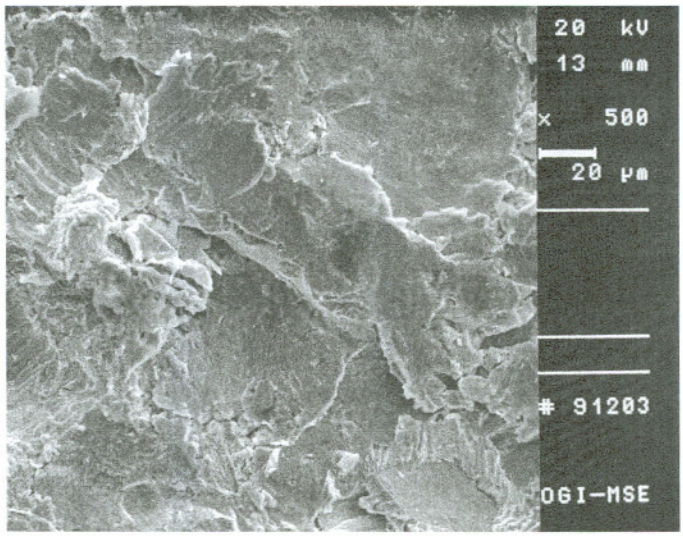

(a)

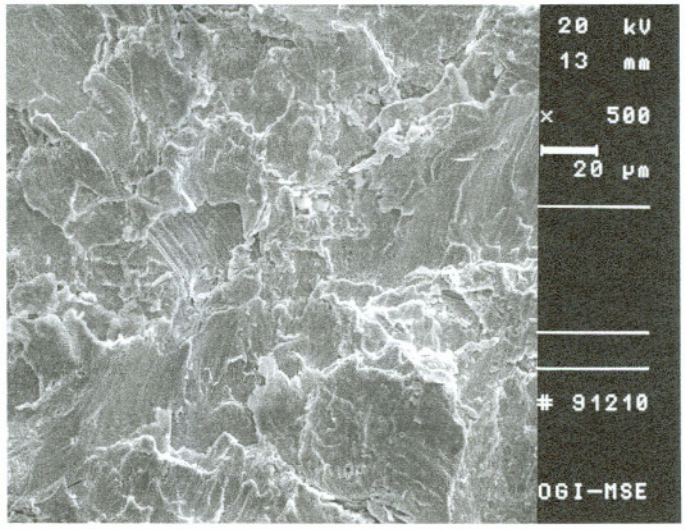

(b)

Figure 3.2.2.2. Comparison of surfaces from grit blasting with (a) Fe shot, (b) two-stage, (c) 50/50 mix, (d) steel, (e) 36 grit alumina and (f) 20 grit alumina. 500x, secondary electron images.

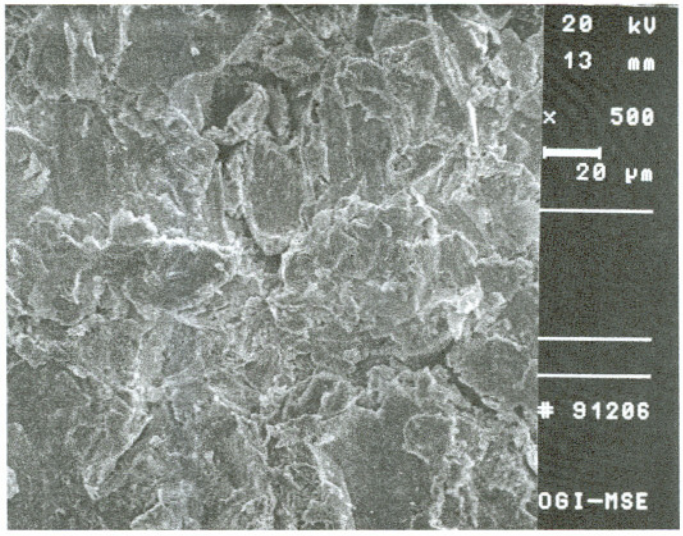

(c)

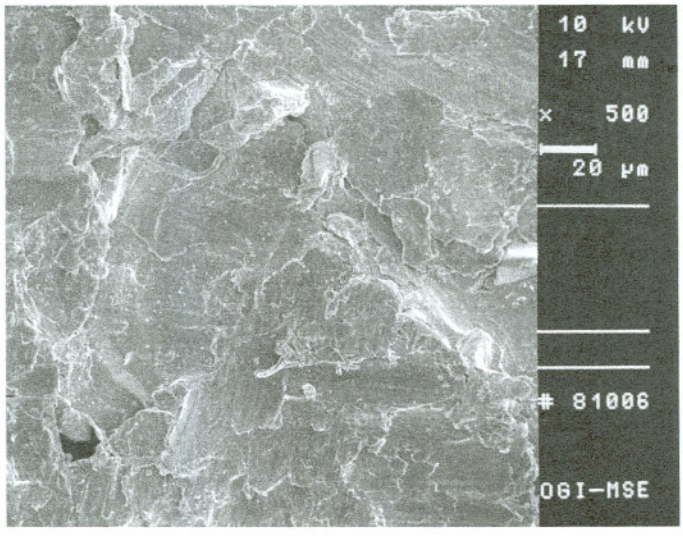

(d)

Figure 3.2.2.2. (Continued) Comparison of surfaces from grit blasting with (a) Fe shot, (b) two-stage, (c) 50/50 mix, (d) steel, (e) 36 grit alumina and (f) 20 grit alumina. 500x, secondary electron images.

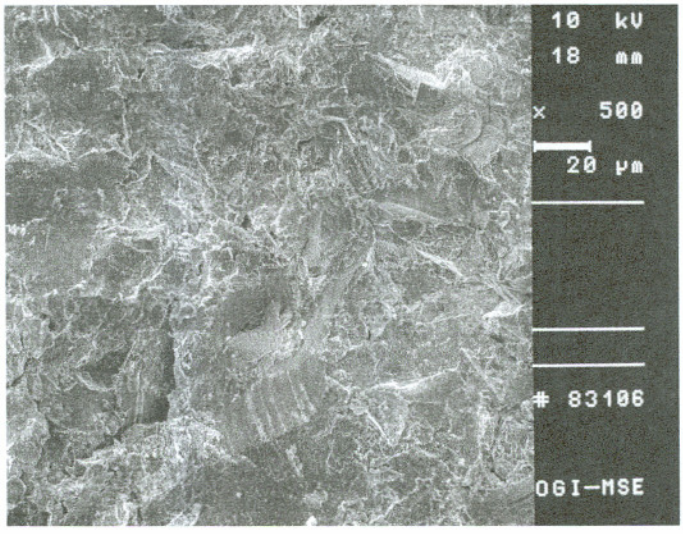

(e)

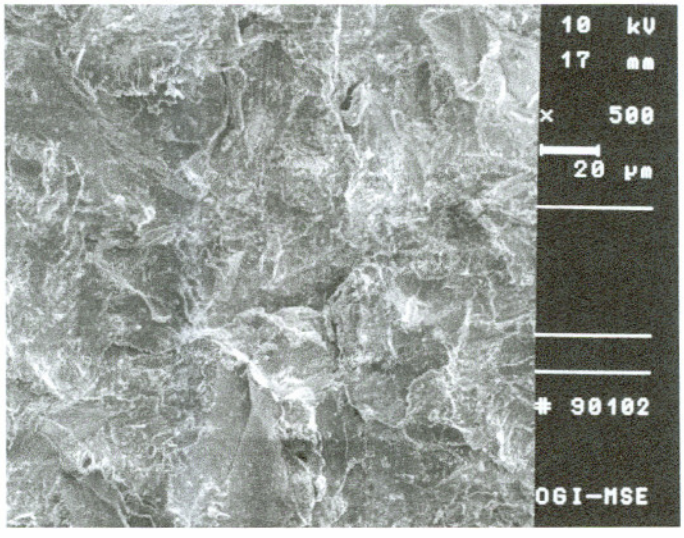

(f)

Figure 3.2.2.2. (Continued) Comparison of surfaces from grit blasting with (a) Fe shot, (b) two-stage, (c) 50/50 mix, (d) steel, (e) 36 grit alumina and (f) 20 grit alumina. 500x, secondary electron images.

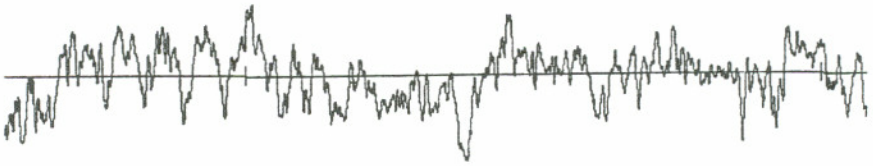

Figure 3.2.2.3. Surface roughness trace, alumina grit, new rail.
R_a = 7.6 μm, R_{max} = 58 μm.

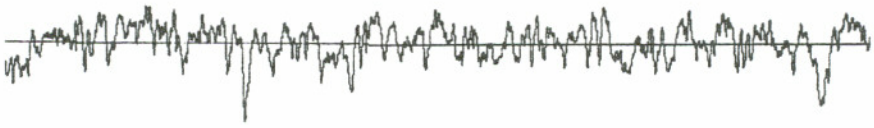

Figure 3.2.2.4. Surface roughness trace, alumina grit, worn rail.
R_a = 4.8 μm, R_{max} = 40 μm.

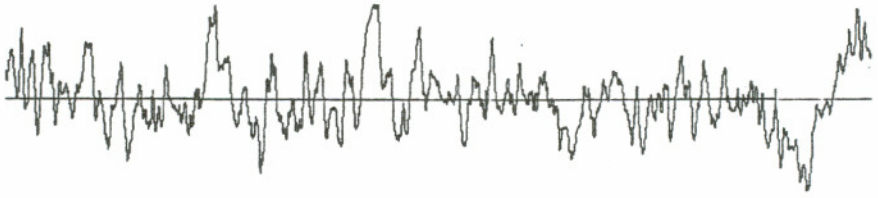

Figure 3.2.2.5. Surface roughness trace, steel shot, new rail.
R_a = 9.0 μm, R_{max} = 69 μm.

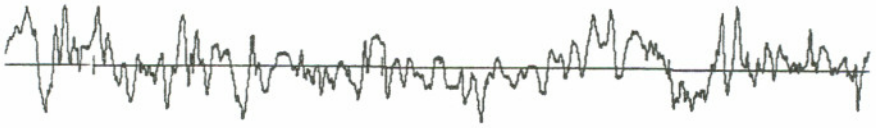

Figure 3.2.2.6. Surface roughness trace, steel shot, worn rail.
R_a = 5.3 μm, R_{max} = 49 μm.

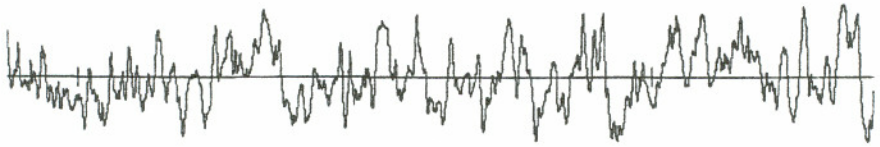

Figure 3.2.2.7. Surface roughness trace, 50/50 mix, new rail.
R_a = 8.3 μm, R_{max} = 63 μm.

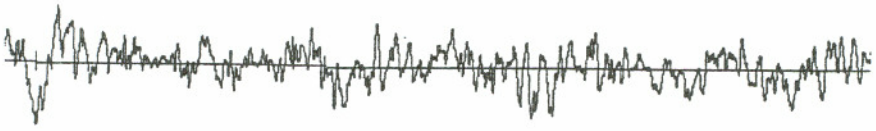

Figure 3.2.2.8. Surface roughness trace, 50/50 mix, worn rail.
R_a = 5.2 μm, R_{max} = 44 μm.

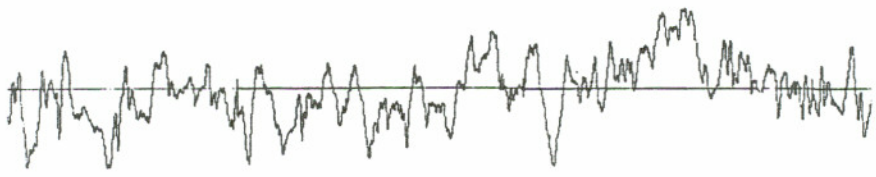

Figure 3.2.2.9. Surface roughness trace, two-stage process, new rail.
R_a = 7.6 μm, R_{max} = 60 μm.

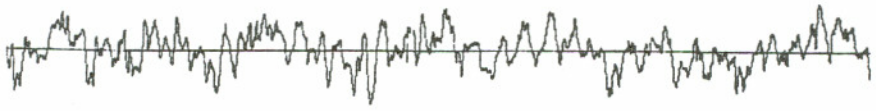

Figure 3.2.2.10. Surface roughness trace, two-stage process, worn rail.
R_a = 5.4 μm, R_{max} = 45 μm.

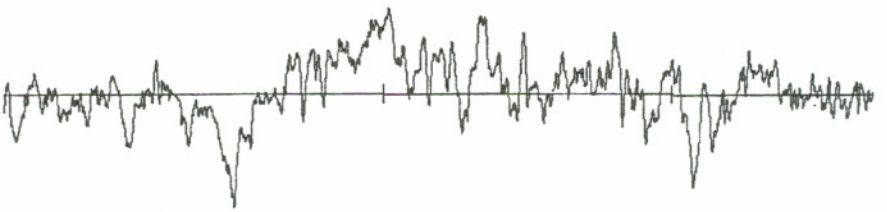

Figure 3.2.2.11. Surface roughness trace, Fe shot, new rail.
R_a = 7.4 μm, R_{max} = 58 μm.

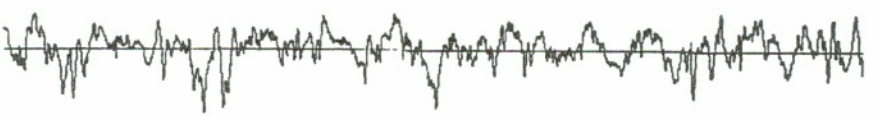

Figure 3.2.2.12. Surface roughness trace, Fe shot, worn rail.
R_a = 4.8 μm, R_{max} = 42 μm.

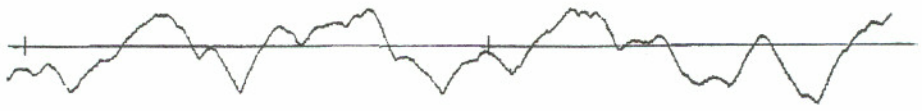

Figure 3.2.2.13. Typical plasma sprayed coating, 1 mm thick.
R_a = 18.3 μm, R_{max} = 107 μm.

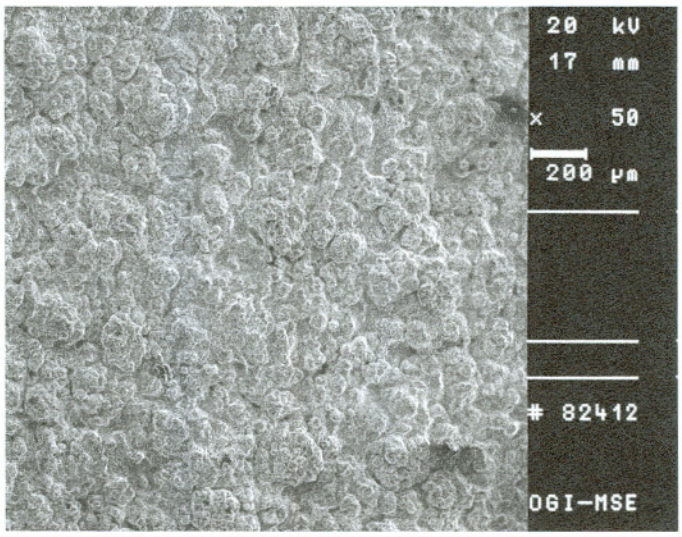

Figure 3.2.2.14. Typical plasma sprayed surface morphology.
50x, secondary electron image.

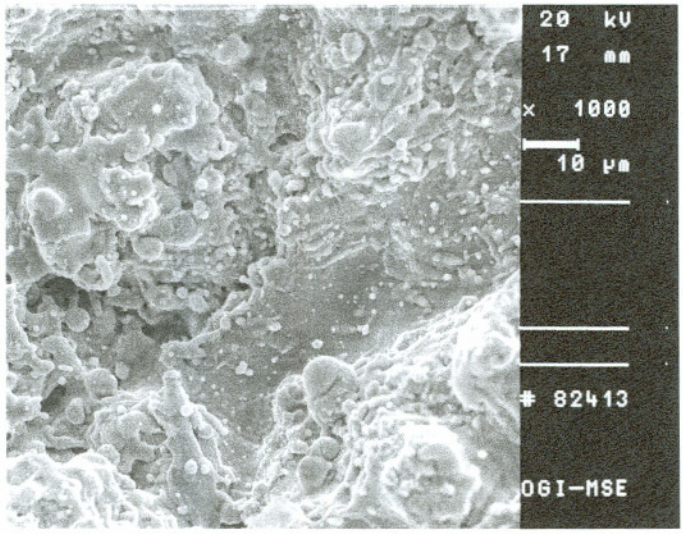

Figure 3.2.2.15. Typical plasma sprayed surface morphology.
1000x, secondary electron image.

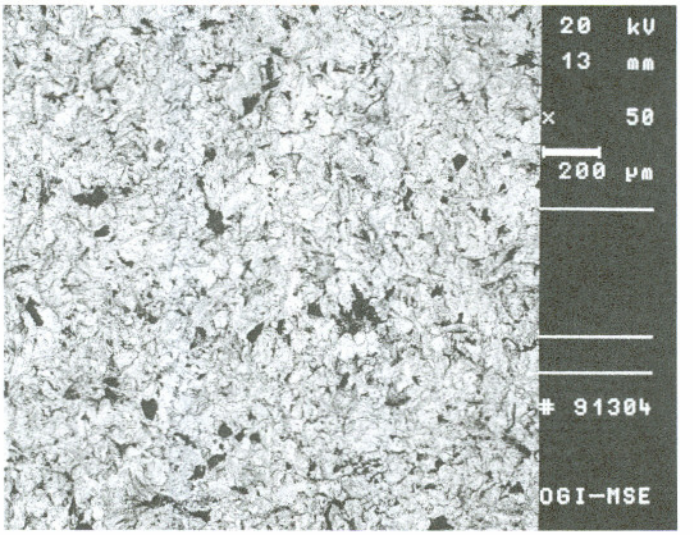

Figure 3.2.3.1. Grit blasted surface with alumina (dark gray) contamination. 50x, backscattered electron image.

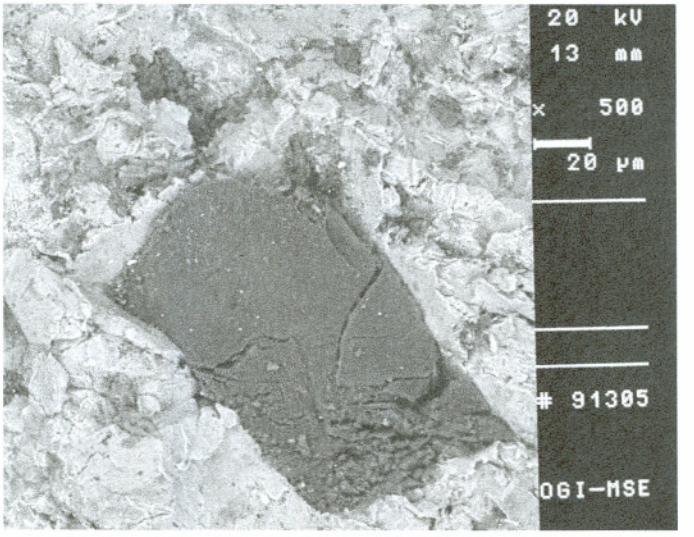

Figure 3.2.3.2. Embedded alumina contaminant particle in grit blasted surface. 500x, backscattered electron image.

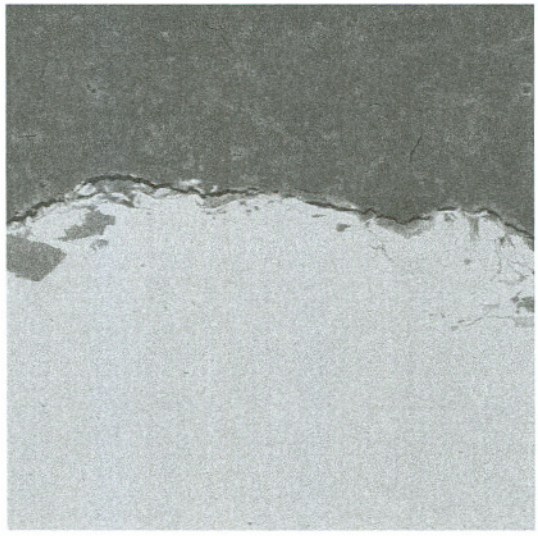

Figure 3.2.3.3. Typical cross-section of grit contaminated surface at short dwell time. 500x, backscattered electron image.

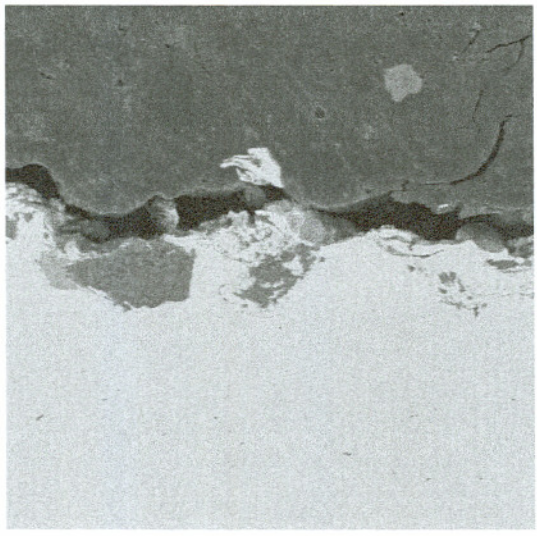

Figure 3.2.3.4. Typical cross-section of grit contaminated surface at long dwell time. 500x, backscattered electron image.

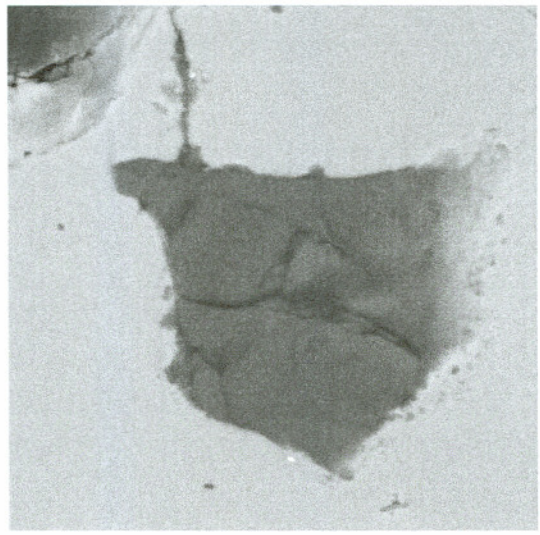

Figure 3.2.3.5. Intact embedded grit below the surface.
3000x, backscattered electron image.

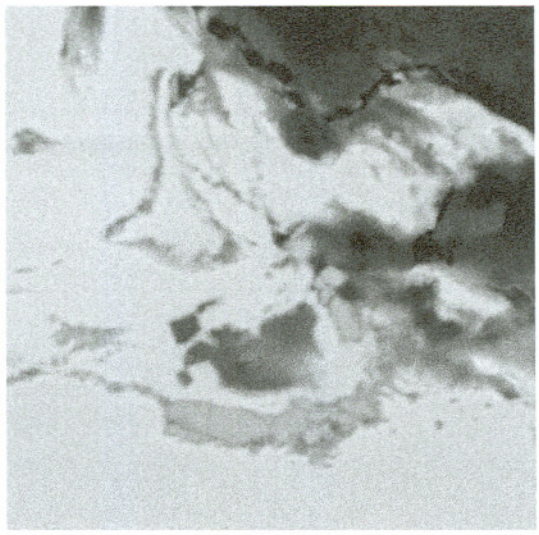

Figure 3.2.3.6. Embedded scale and alumina beneath surface at short dwell times.
2000x, backscattered electron image.

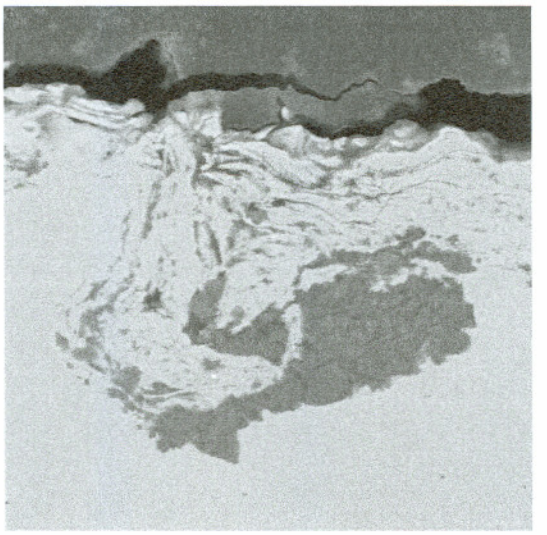

Figure 3.2.3.7. Disturbed material below grit blasted surface.
1250x, backscattered electron image.

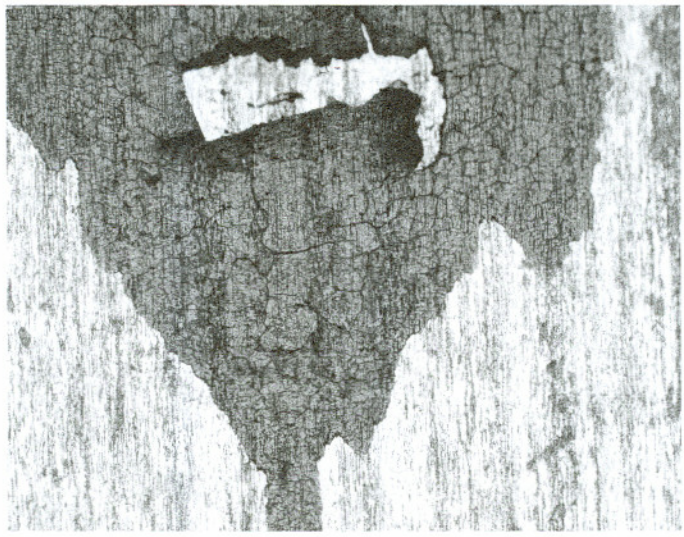

Figure 3.3.1.1. Black oxide film on a stainless steel roller surface.
100x, optical micrograph.

Figure 3.3.2.1. Partial debonding of stainless steel coating from Amsler roller.

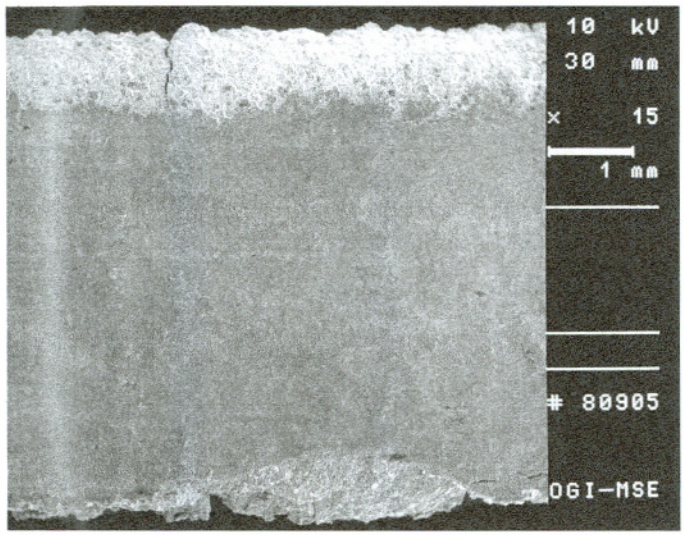

(a)

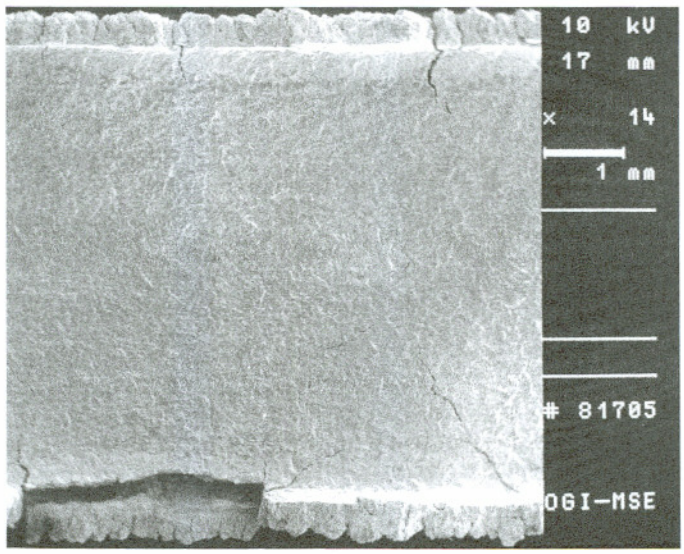

(b)

Figure 3.3.2.2. Debonded stainless steel coatings showing (a) edge effects and (b) network of cracks initiated at edge effects.
15x and 14x, secondary electron images.

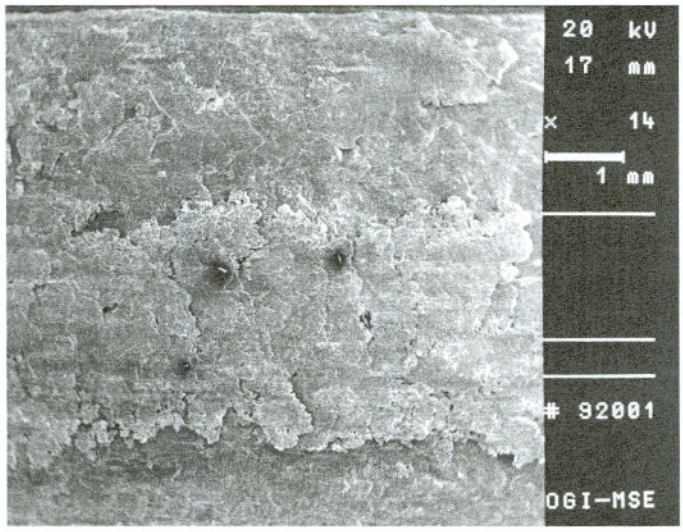

(a)

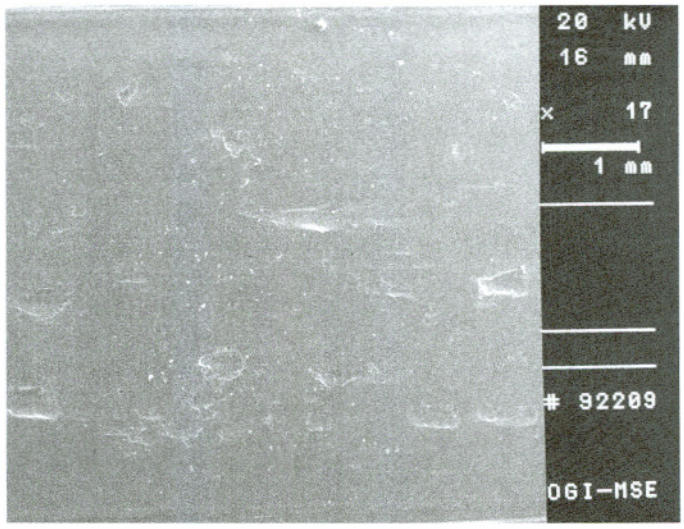

(b)

Figure 3.3.2.3. Wear surface of bottom rollers after testing showing (a) extreme wear and (b) normal wear. 14x and 17x, secondary electron images.

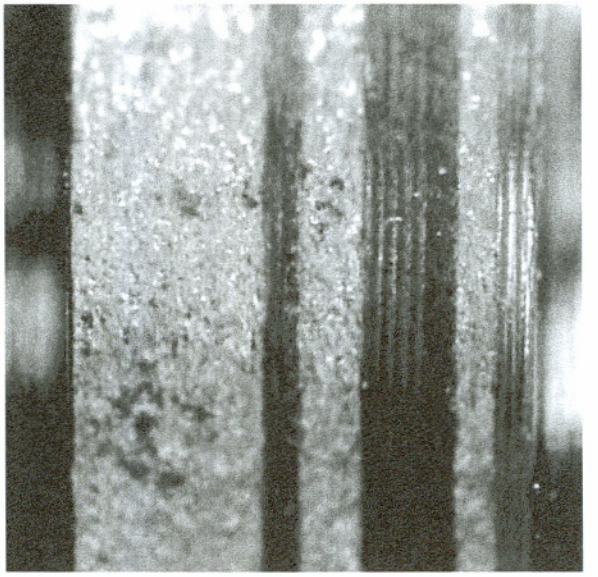

Figure 3.3.3.1. Material transfer and roughening of bottom roller surface.

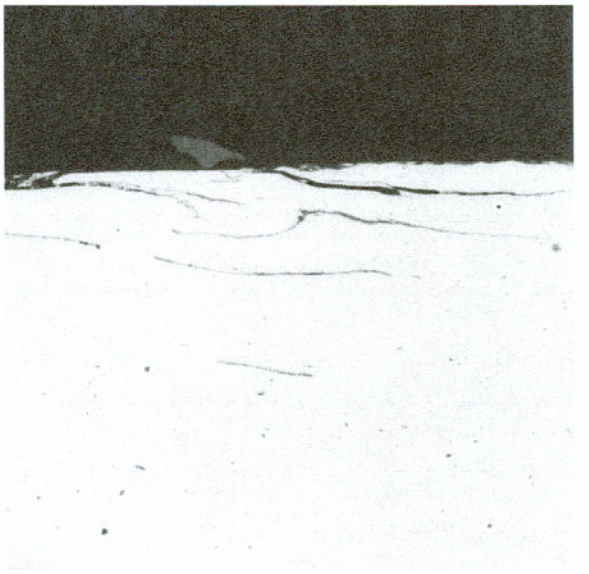

Figure 3.3.4.1. Worn surface of the bottom roller from I3-2 interrupted test. 400x, optical micrograph.

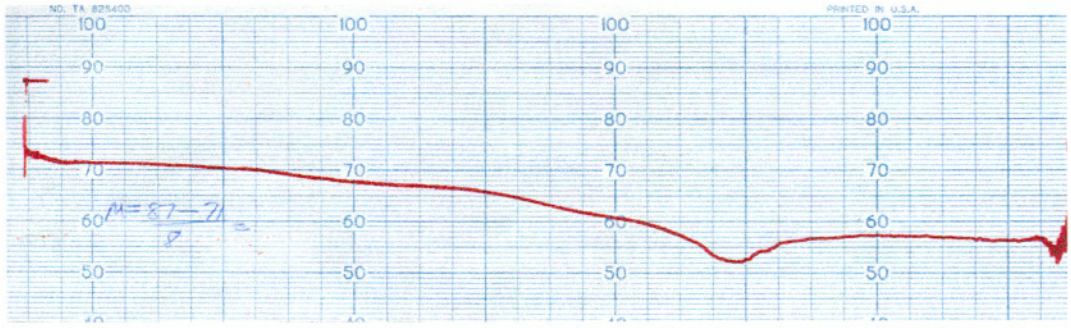

Figure 3.3.6.1. Typical wear trace for stainless steel with nylon showing corresponding friction increase.

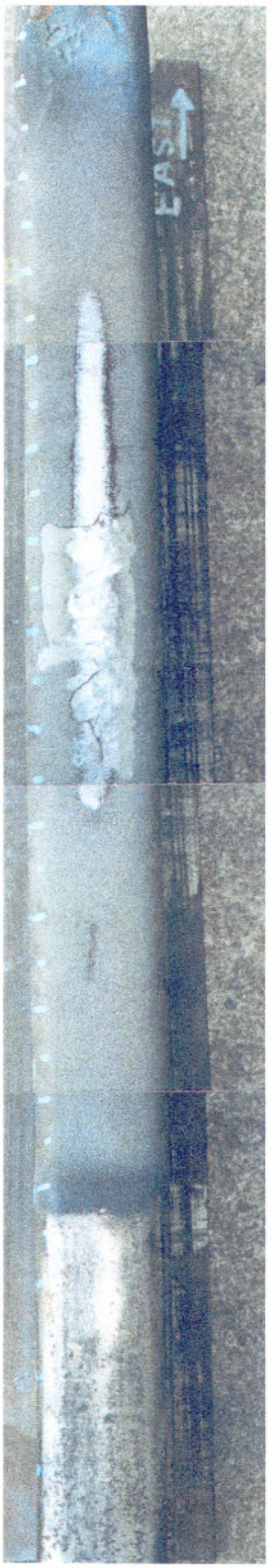

Figure 3.4.1. As-received Rolling Load Specimen 1 (RL1).

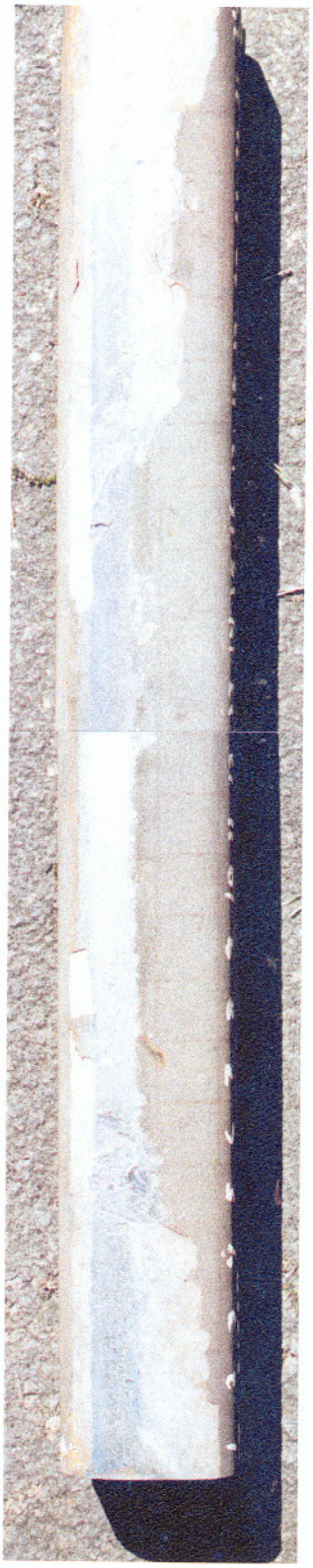

Figure 3.4.2. As-received Track Lab Coupon 1 (TL1).

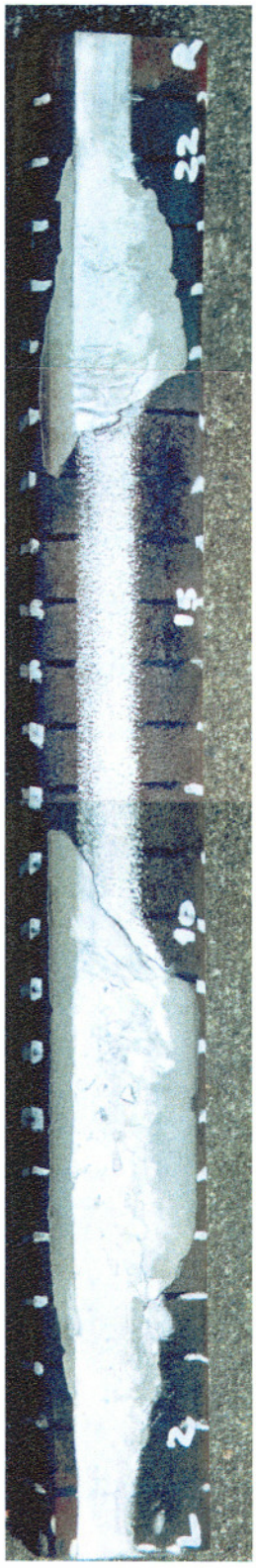

Figure 3.4.3. As-received Track Lab Coupon 2 (TL2).

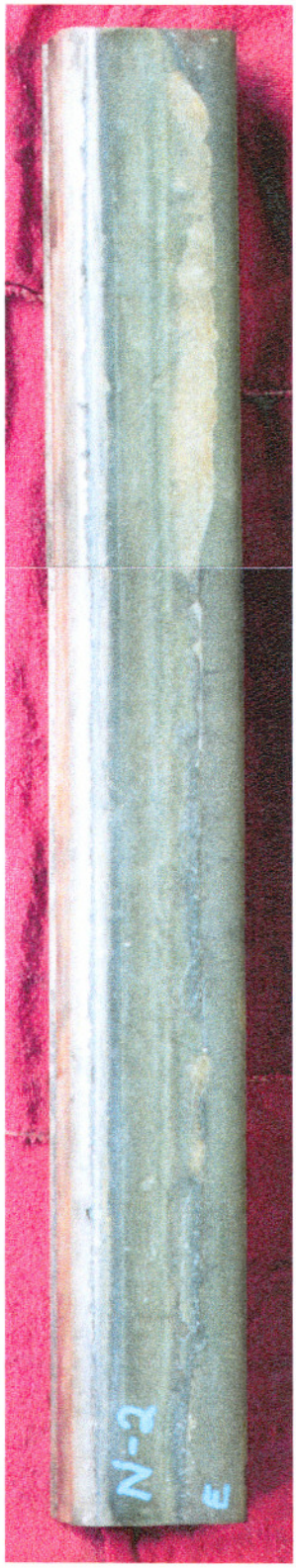

Figure 3.4.4. As-received Track Lab Coupon 3 (TL3/N-2).

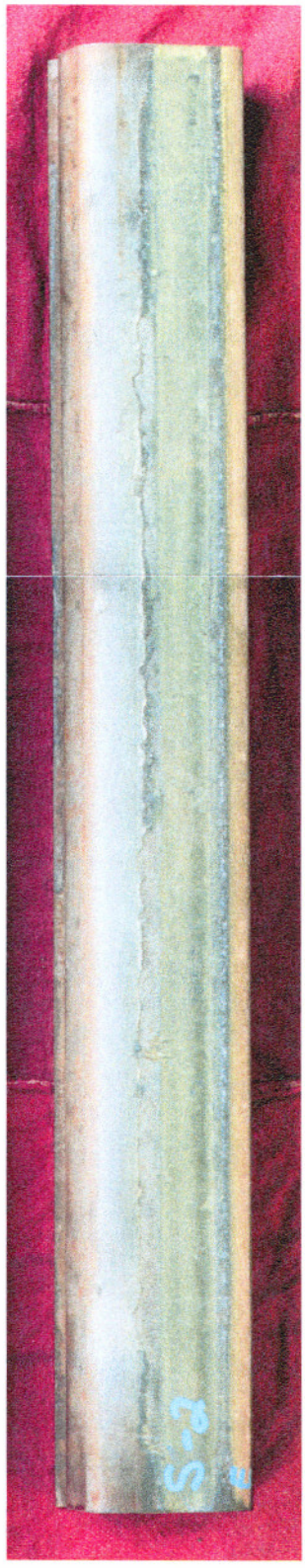

Figure 3.4.5. As-received Track Lab Coupon 4 (TL4/S-2).

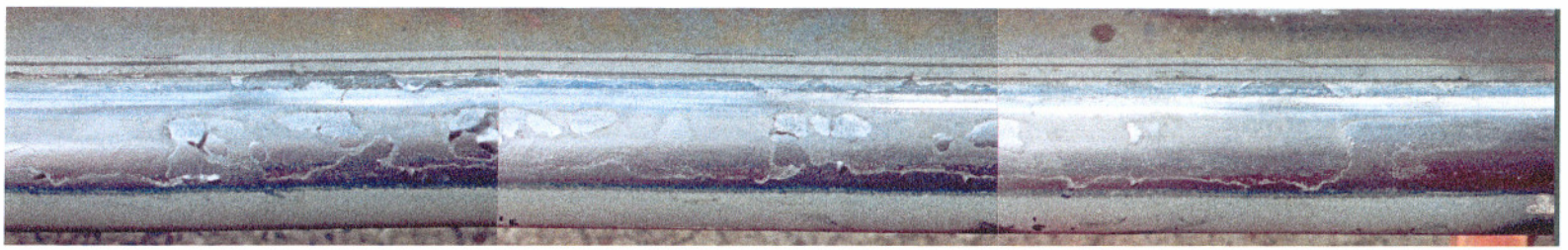

(a)

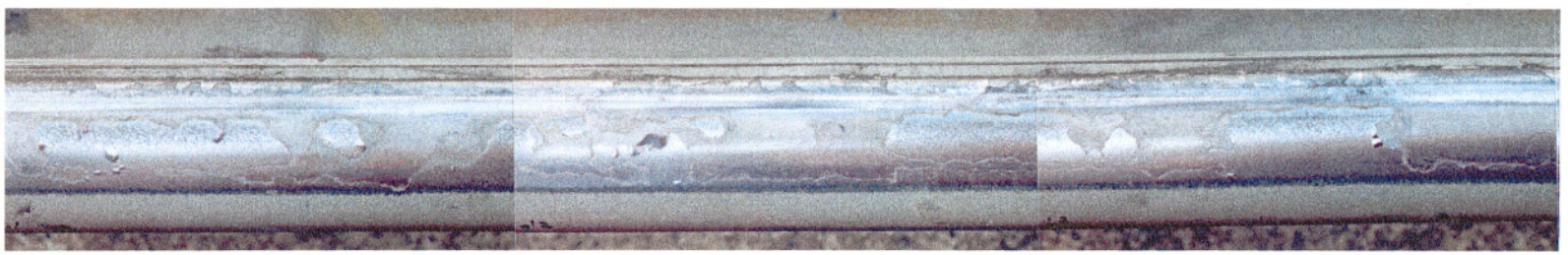

(b)

Figure 3.4.6. Representative sections of as-received FAST rail (FAST).

Figure 3.4.1.1. Oxide banding in RL1 coating.
100x, optical micrograph.

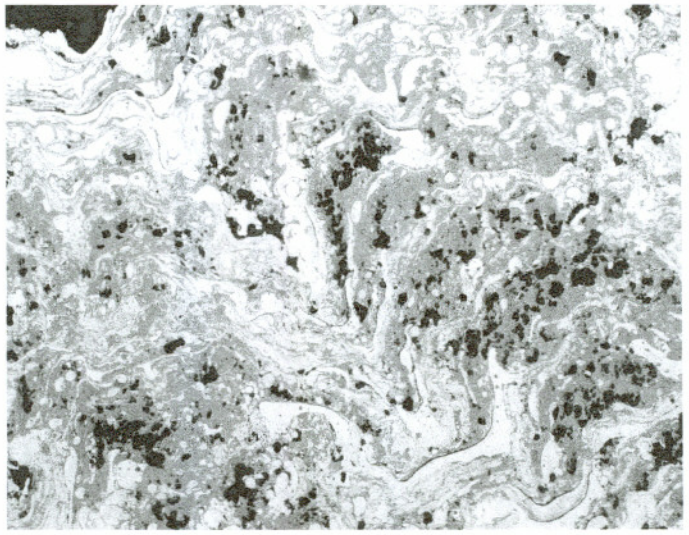

Figure 3.4.1.2. High oxide region in RL1 coating.
200x, optical micrograph.

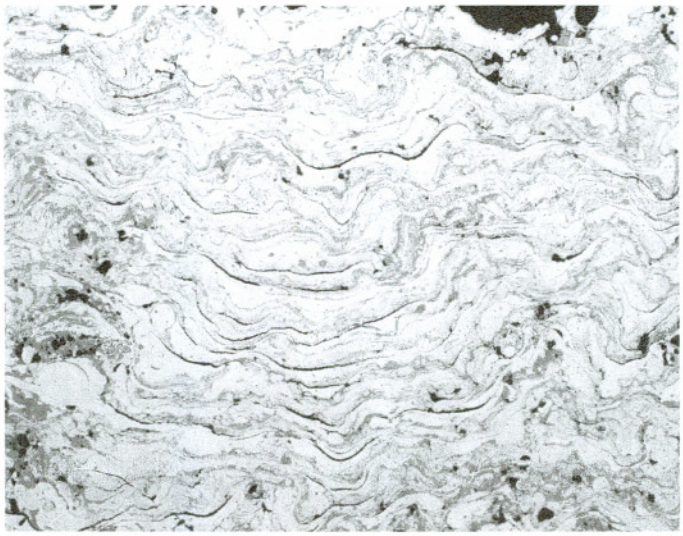

Figure 3.4.1.3. Low oxide region in RL1 coating.
200x, optical micrograph.

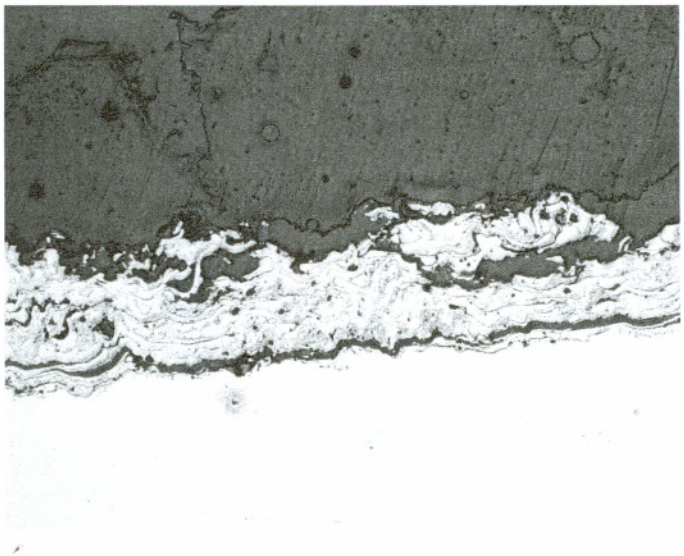

Figure 3.4.1.4. Disintegration of the coating caused by preparation technique.
100x, optical micrograph.

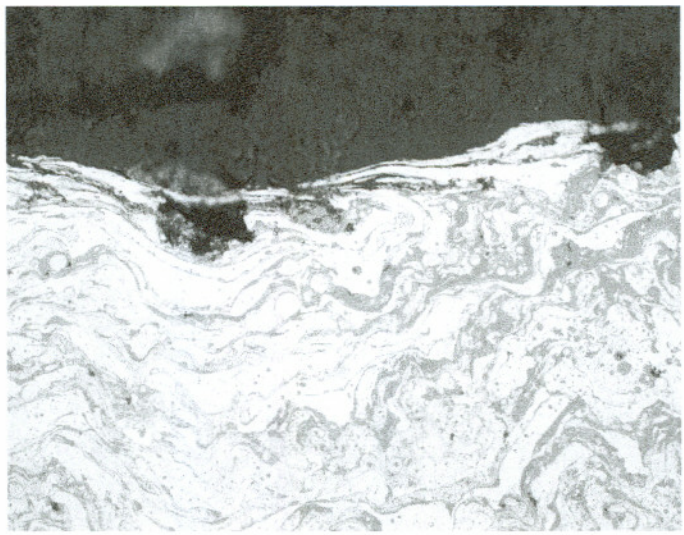

Figure 3.4.1.5. Wear surface of RL1 showing deformation.
400x, optical micrograph.

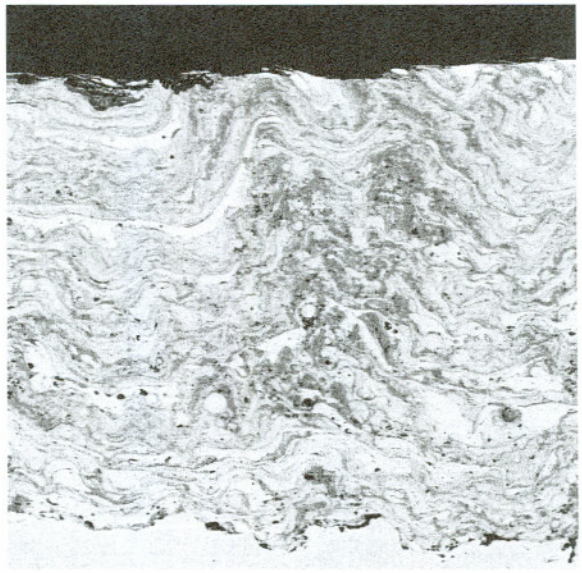

Figure 3.4.1.6. Wear surface of RL1.
150x, backscattered electron image.

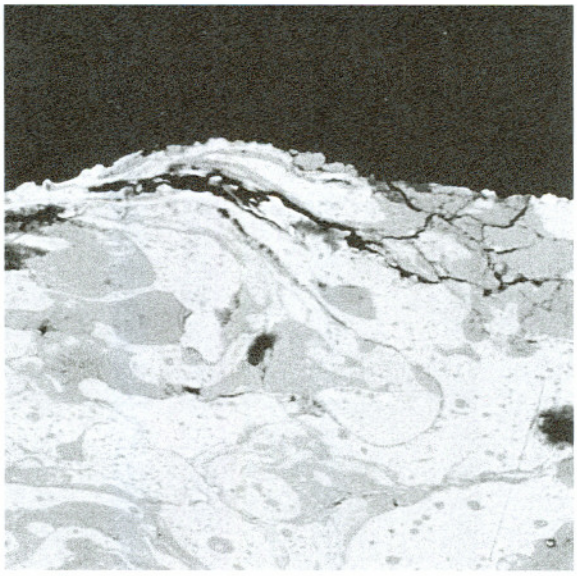

Figure 3.4.1.7. Deformation and oxide cracking in RL1 near center of rail.
1000x, backscattered electron image.

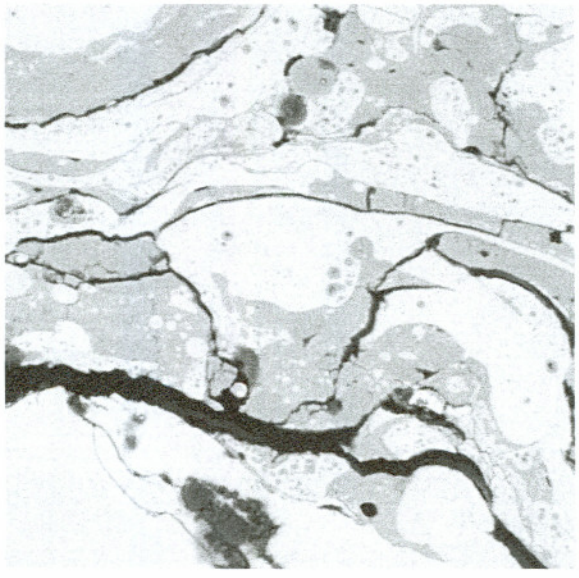

Figure 3.4.1.8. Oxide cracking near interface in RL1.
2000x, backscattered electron image.

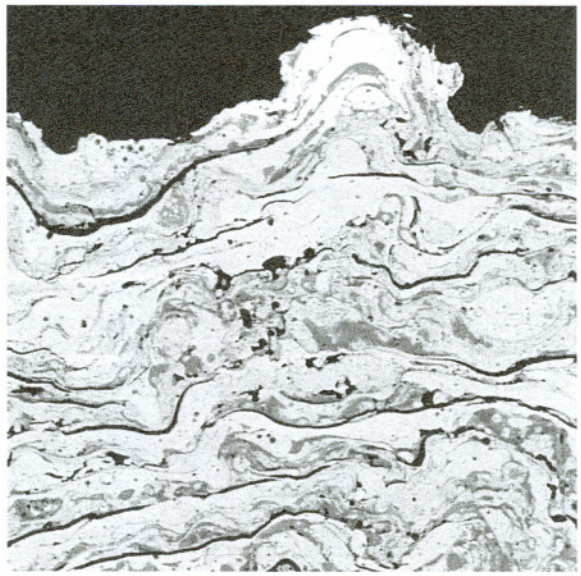

Figure 3.4.1.9. Delamination adjacent to wear surface in RL1.
500x, backscattered electron image.

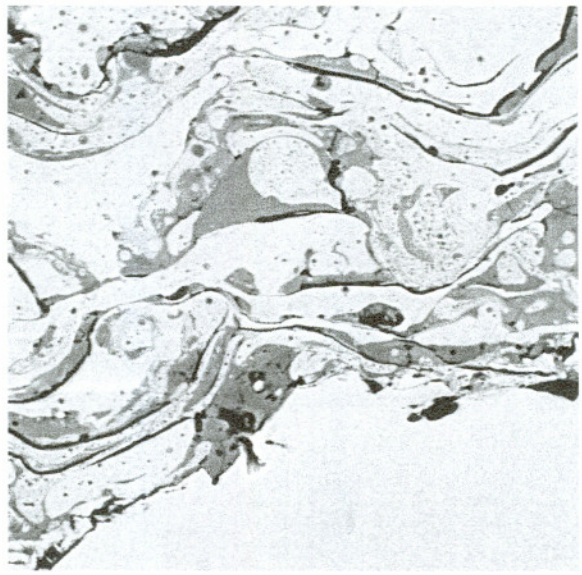

Figure 3.4.1.10. Delamination near coating/substrate interface in RL1.
1000x, backscattered electron image.

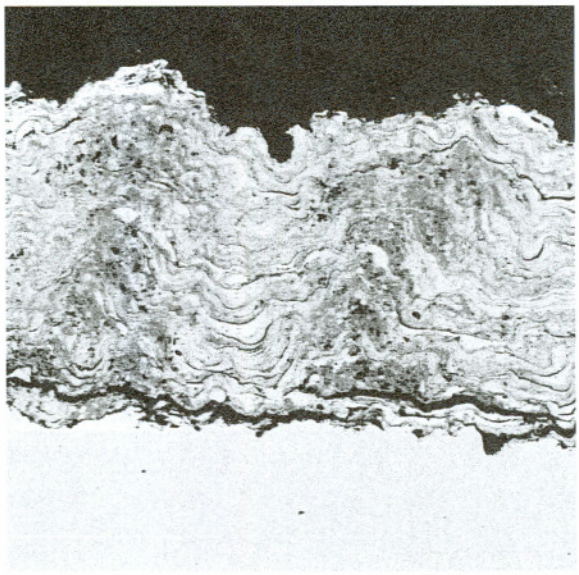

Figure 3.4.1.11. Oxide banding and delamination at interface in RL1.
100x, backscattered electron image.

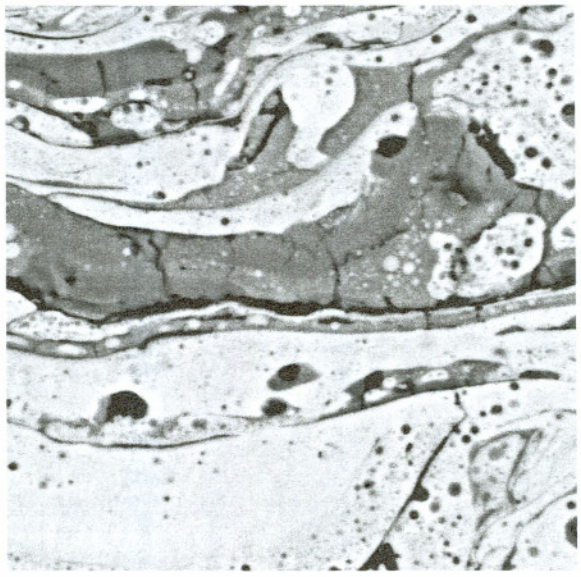

Figure 3.4.1.12. Oxide and steel particle inclusions
in coating microstructure of RL1.
3000x, backscattered electron image.

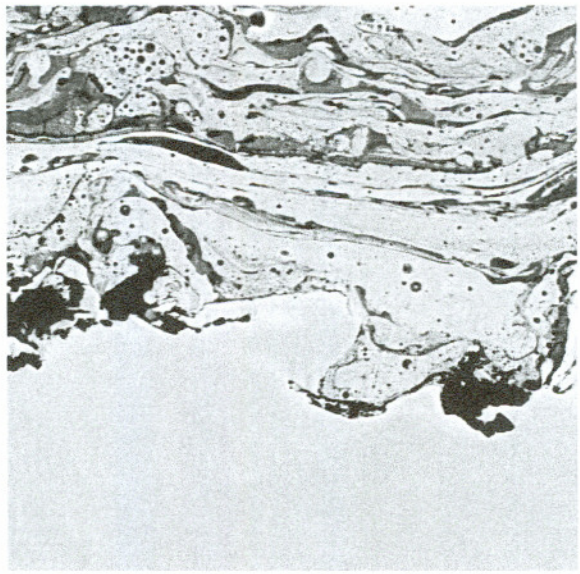

Figure 3.4.1.13. Coating/substrate interface contamination in RL1 caused by grit blasting residue. 1000x, backscattered electron image.

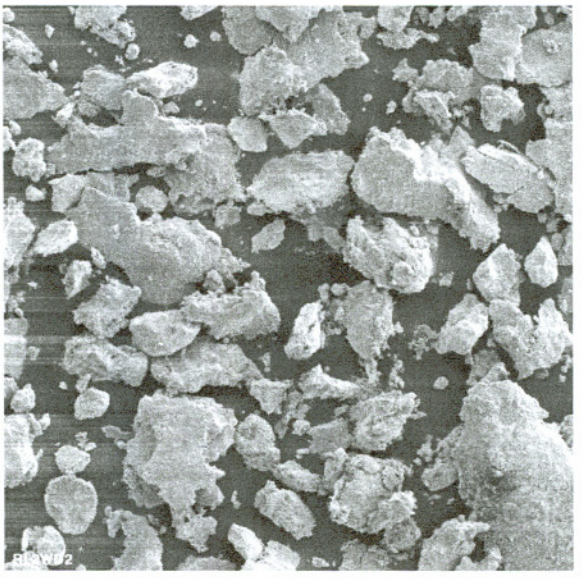

Figure 3.4.2.1. Morphology of RL2 wear debris.
1000x, secondary electron image.

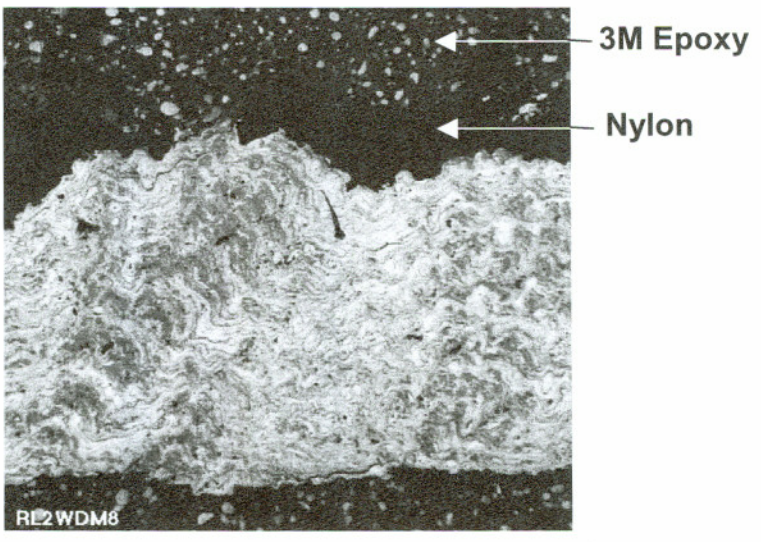

Figure 3.4.2.2. Oxide banding in unworn region of
RL2 wear debris with intact nylon.
50x, optical micrograph.

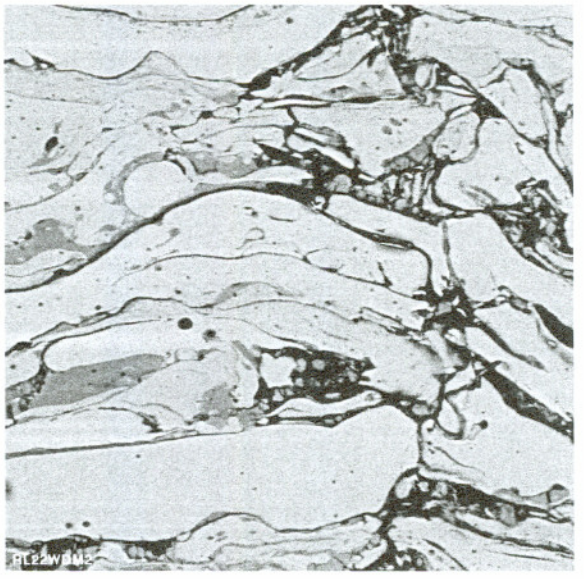

Figure 3.4.2.3. Cracking and delamination in RL2 mounted wear debris.
1000x, backscattered electron image.

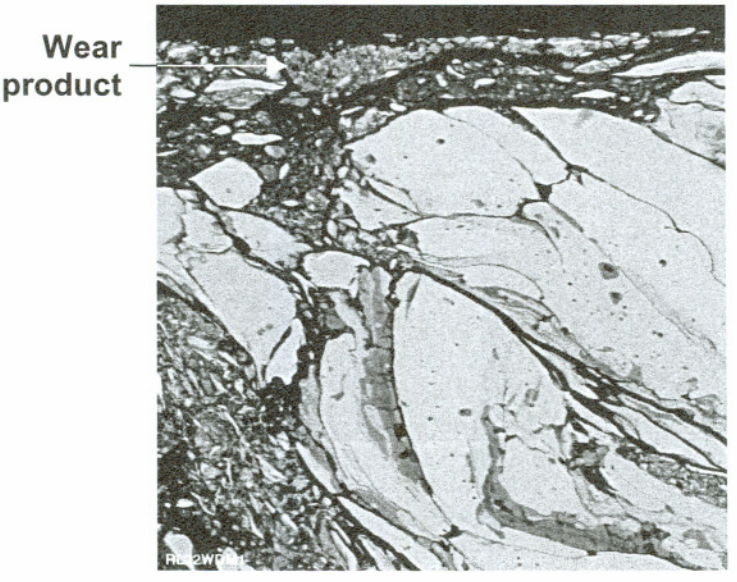

Figure 3.4.2.4. Cracking at surface of RL2 wear debris.
1000x, backscattered electron image.

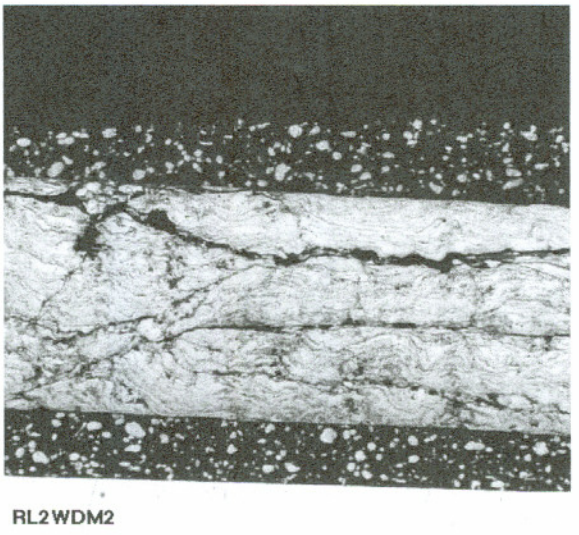

Figure 3.4.2.5. Severely damaged region of RL2 wear debris.
50x, optical micrograph.

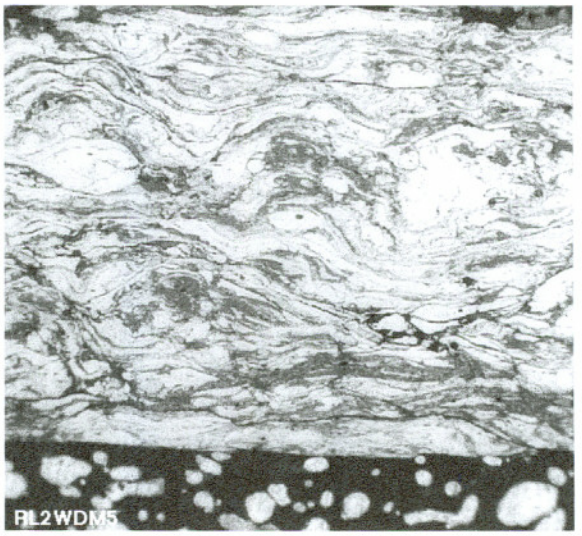

Figure 3.4.2.6. Interlamellar debonding and cracking in RL2 wear debris.
200x, optical micrograph.

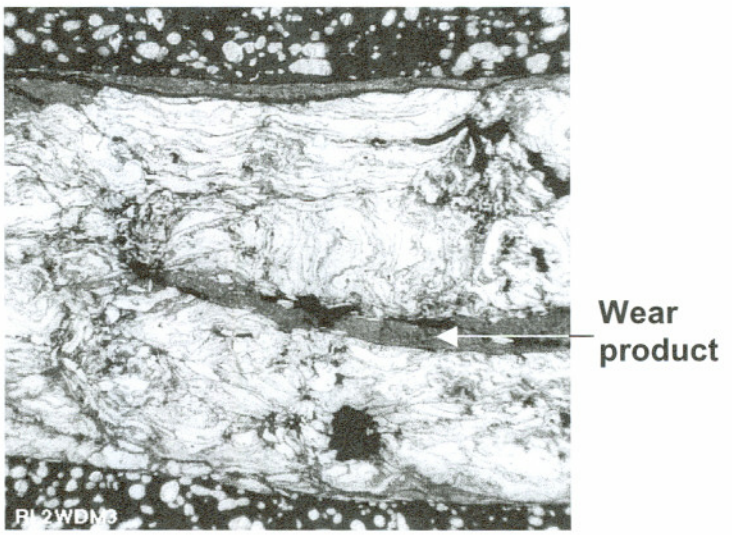

Figure 3.4.2.7. Wear product at RL2 surface and within crack.
100x, optical micrograph.

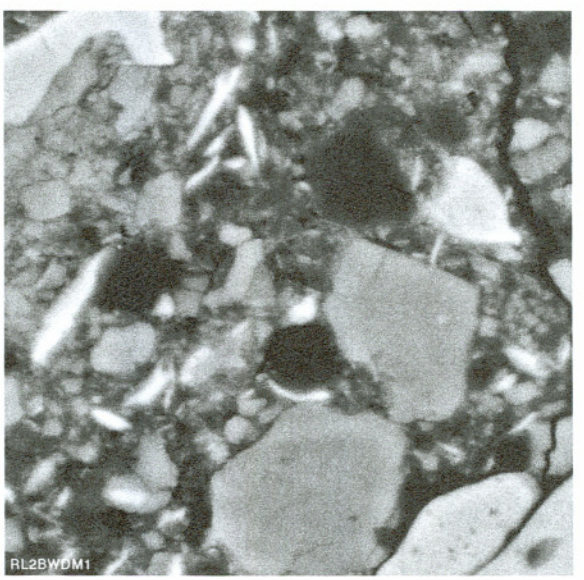

Figure 3.4.2.8. Wear product constituents in RL2 wear debris.
5000x, backscattered electron image.

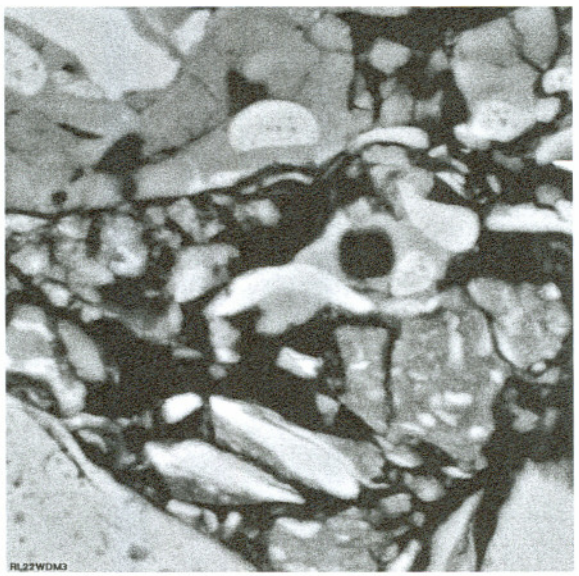

Figure 3.4.2.9. Wear product constituents in RL2 wear debris.
5000x, backscattered electron image.

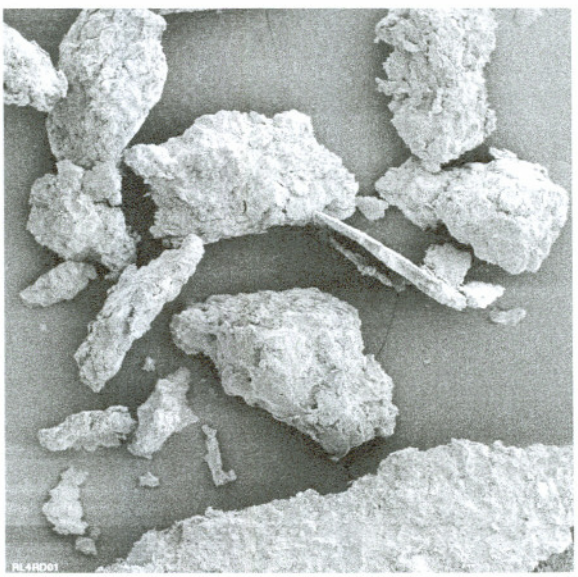

Figure 3.4.3.1. Unmounted wear debris for RL4.
42x, secondary electron image.

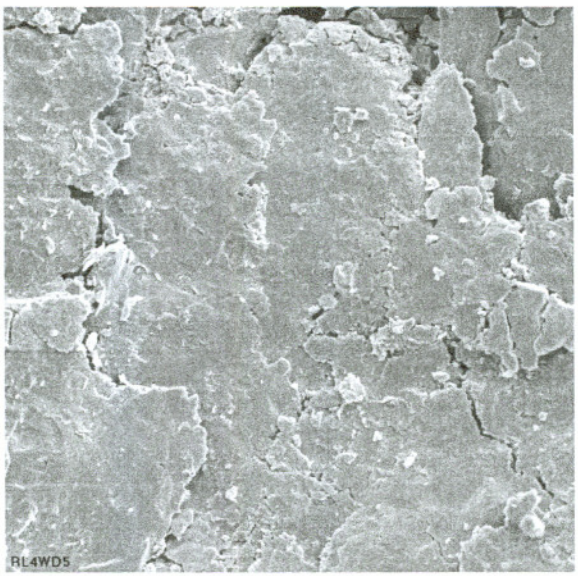

Figure 3.4.3.2. Wear surface of RL4 wear debris.
1000x, secondary electron image.

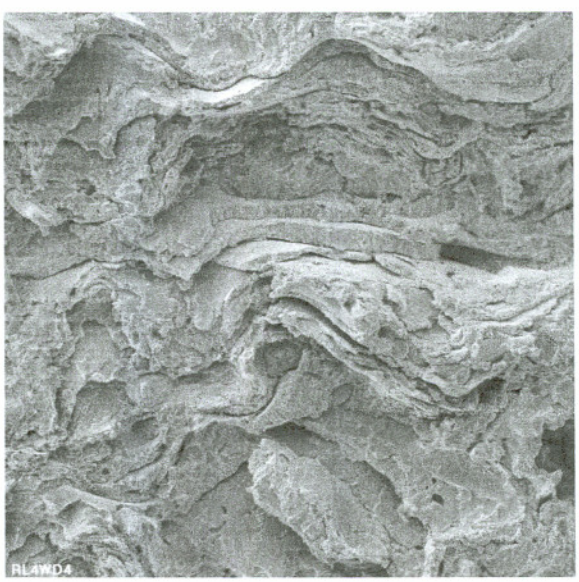

Figure 3.4.3.3. Fracture surface of RL4 wear particle.
500x, secondary electron image.

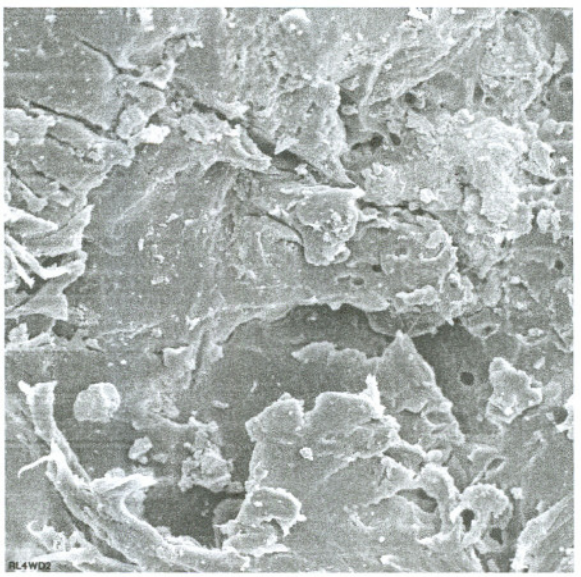

Figure 3.4.3.4. RL4 wear particle surface.
500x, secondary electron image.

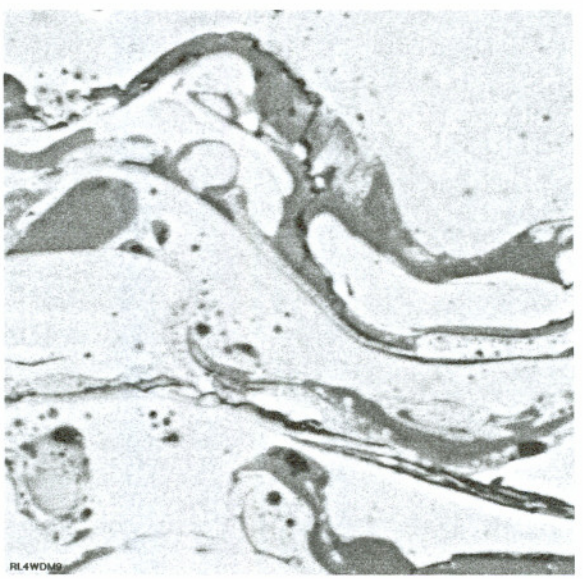

Figure 3.4.3.5. Oxide cracking near RL4 wear debris surface.
3000x, backscattered electron image.

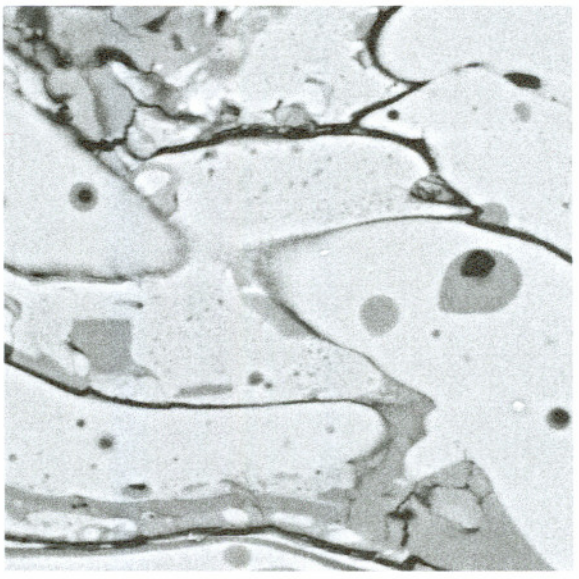

Figure 3.4.3.6. Crack following oxides between metal lamellae in RL4 wear debris. 3000x, backscattered electron image.

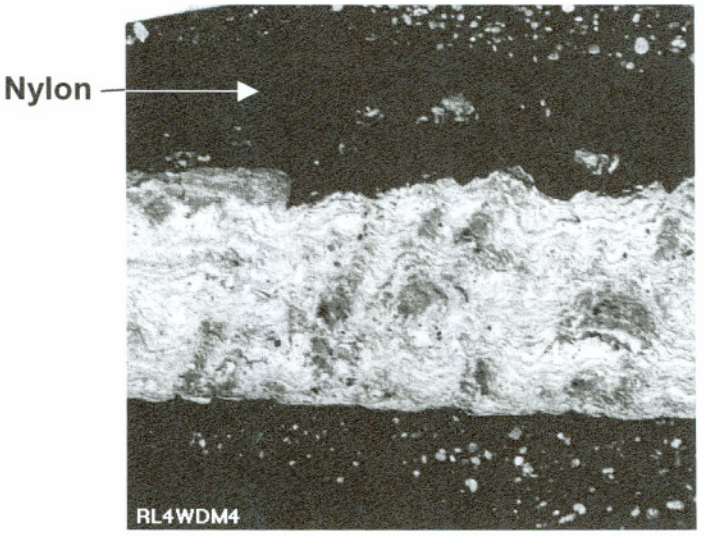

Figure 3.4.3.7. Banded oxides in RL4 wear debris with intact nylon. 50x, optical micrograph.

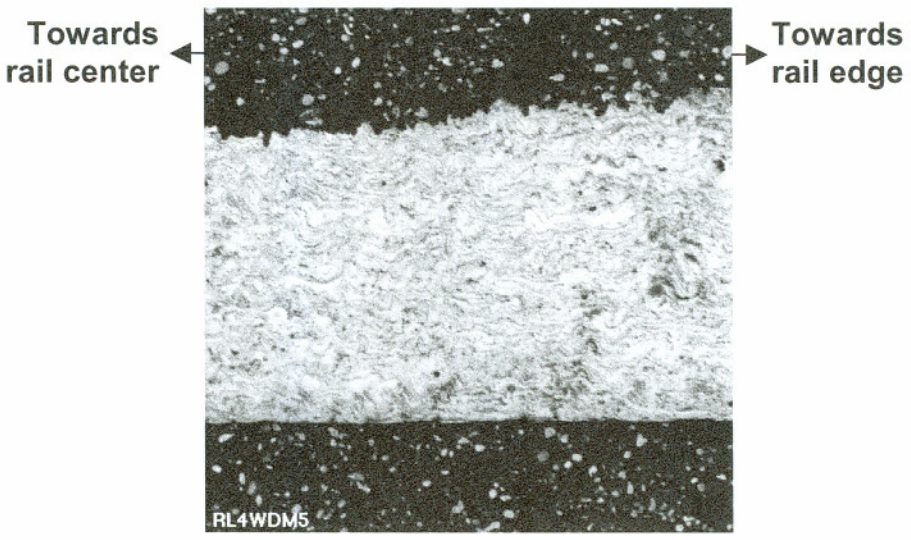

Figure 3.4.3.8. Microstructure in RL4 wear debris.
50x, optical micrograph.

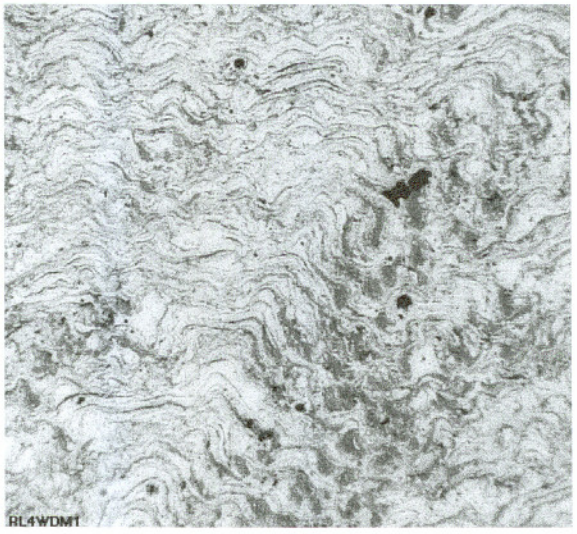

Figure 3.4.3.9. Heterogeneous microstructure in thick RL4
wear debris showing high and low oxide regions.
100x, optical micrograph.

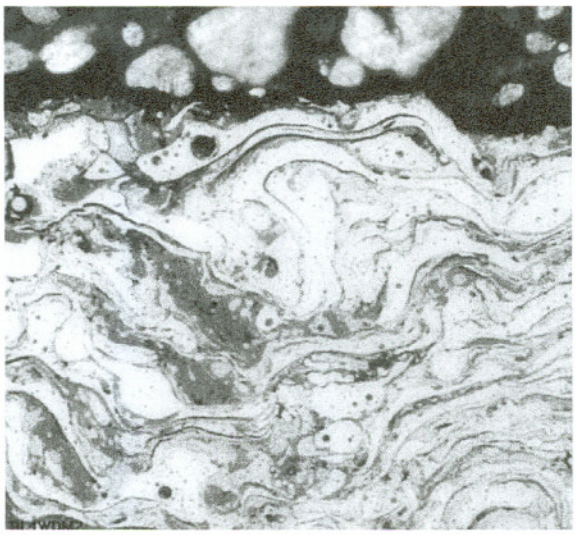

Figure 3.4.3.10. Interlamellar debonding in unworn RL4 wear debris.
400x, optical micrograph.

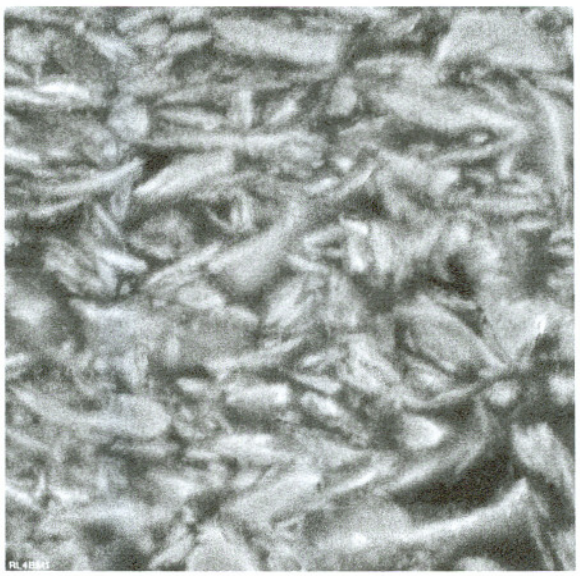

Figure 3.4.3.11. Wear product found in RL4 wear debris.
5000x, backscattered electron image.

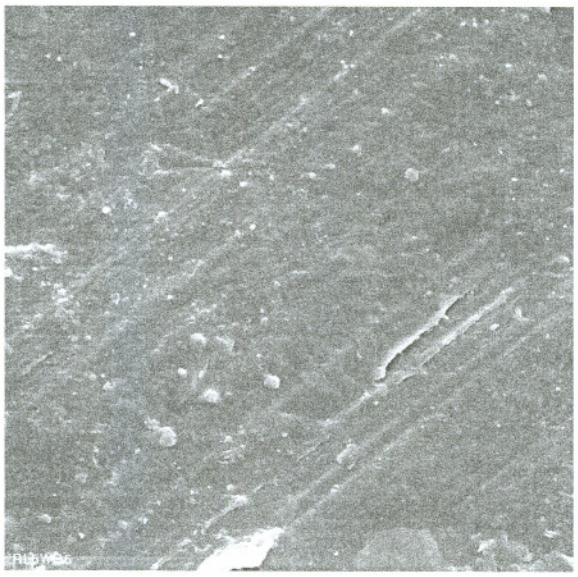

Figure 3.4.4.1. Surface of RL5 nylon wear debris.
1000x, secondary electron image.

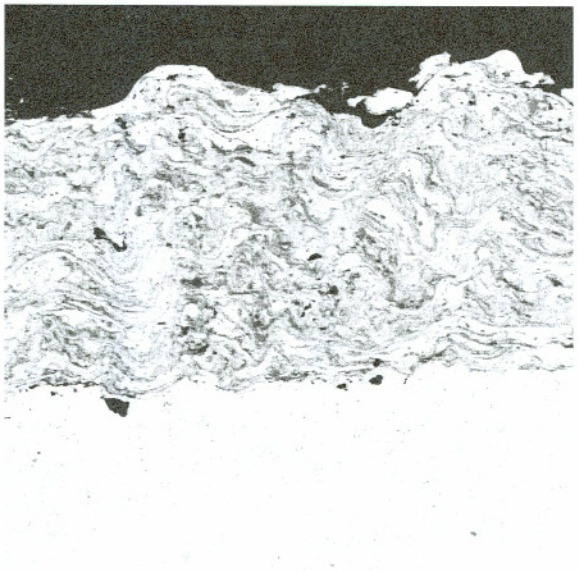

Figure 3.4.5.1. Typical 1080 steel coating microstructure
for TL1 with grit contaminant at interface.
200x, backscattered electron image.

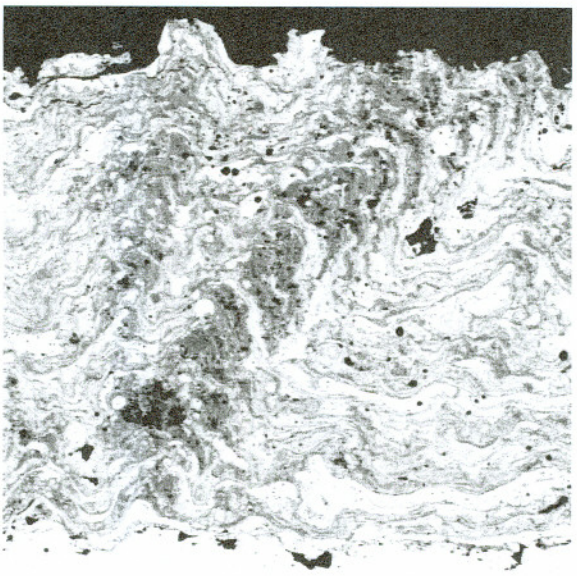

Figure 3.4.5.2. Oxide banding in TL1 coating.
200x, backscattered electron image.

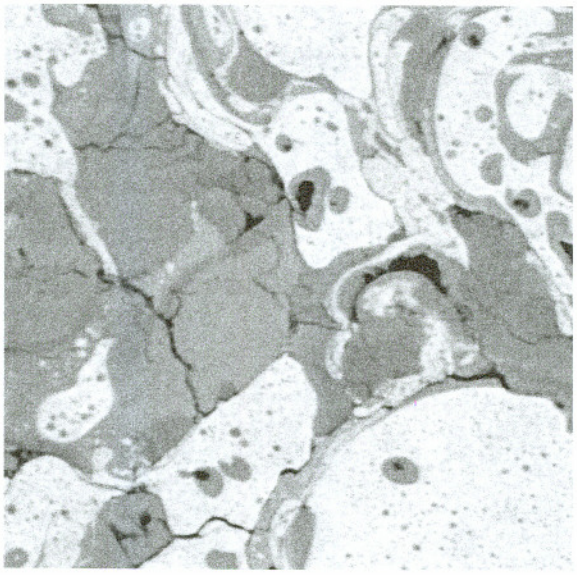

Figure 3.4.5.3. Fine cracks in oxide located near surface of TL1.
5000x, backscattered electron image.

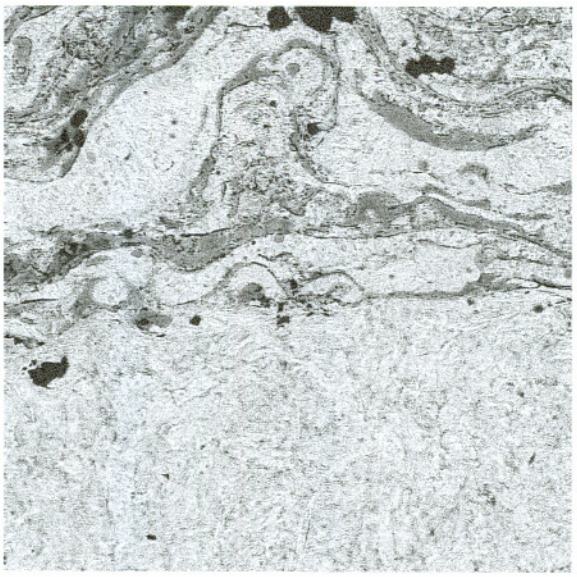

Figure 3.4.5.4. Etched interface between coating and substrate of TL1.
1000x, backscattered electron image.

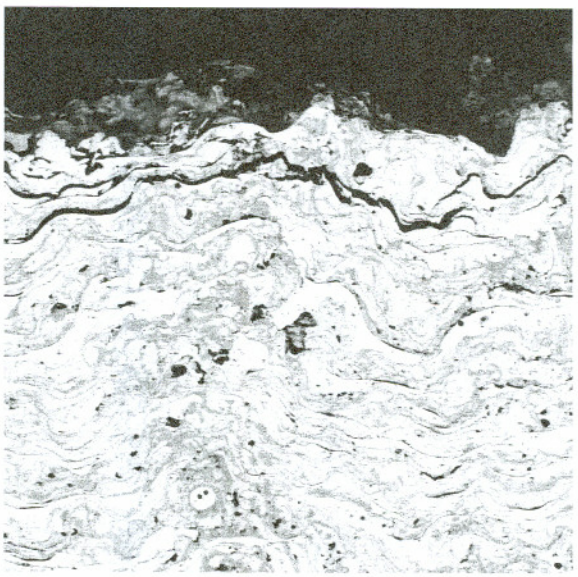

Figure 3.4.5.5. Delamination of surface layers in longitudinal section of TL1.
200x, backscattered electron image.

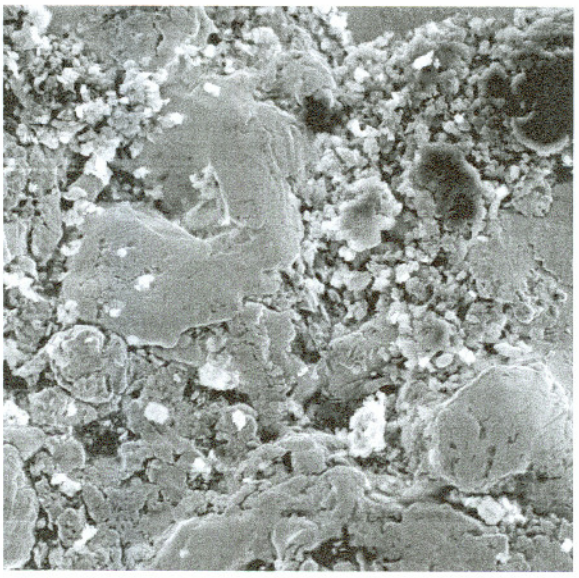

Figure 3.4.5.6. Worn surface showing both metallic and oxide constituents in TL1.
1000x, secondary electron image.

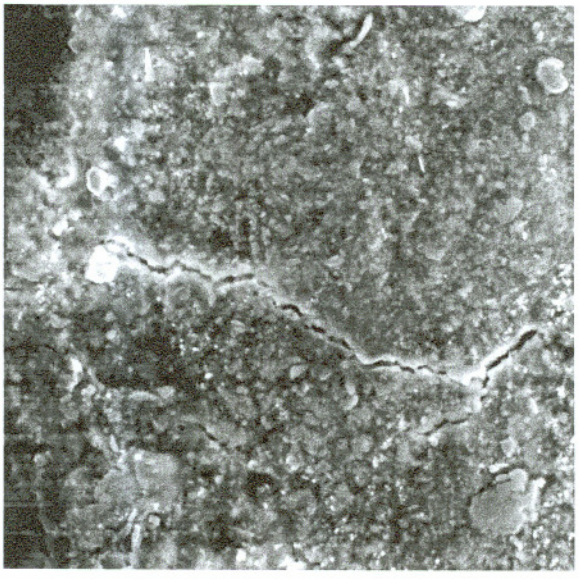

Figure 3.4.5.7. Oxide cracking in surface of TL1.
1000x, secondary electron image.

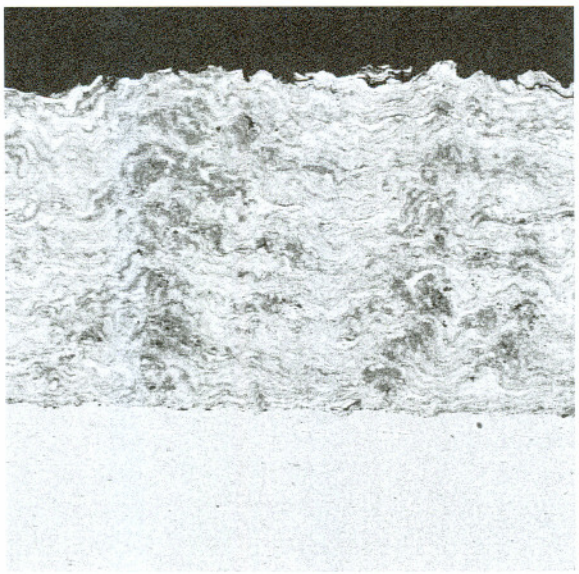

Figure 3.4.6.1. Typical 1080 steel coating microstructure for TL2.
50x, backscattered electron image.

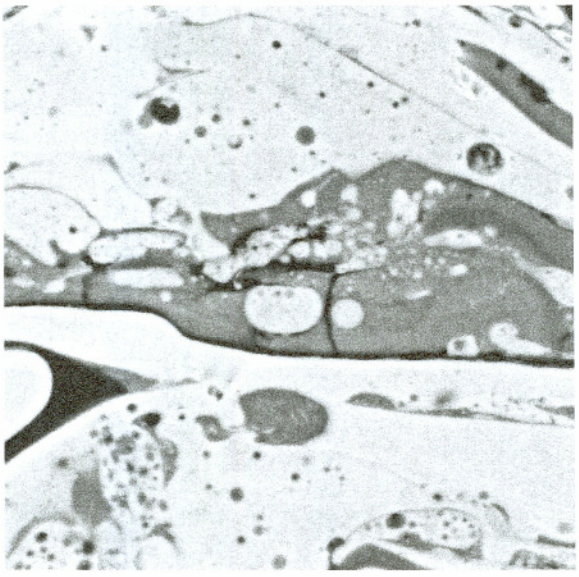

Figure 3.4.6.2. Oxide and steel inclusions in the coating microstructure of TL2.
3000x, backscattered electron image.

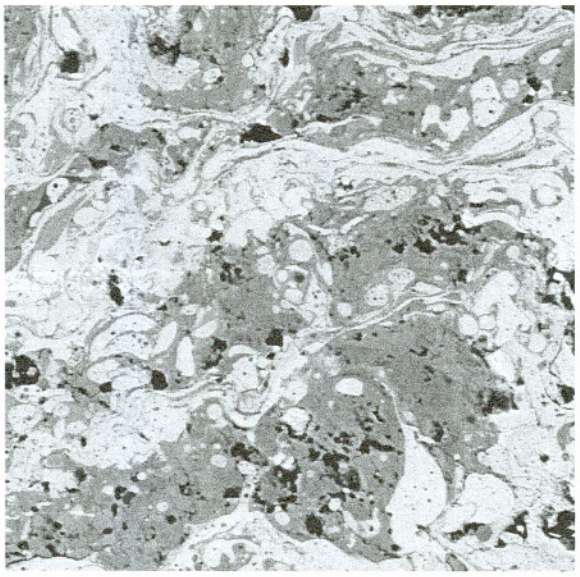

Figure 3.4.6.3. Region of high oxide content and porosity in TL2. 500x, backscattered electron image.

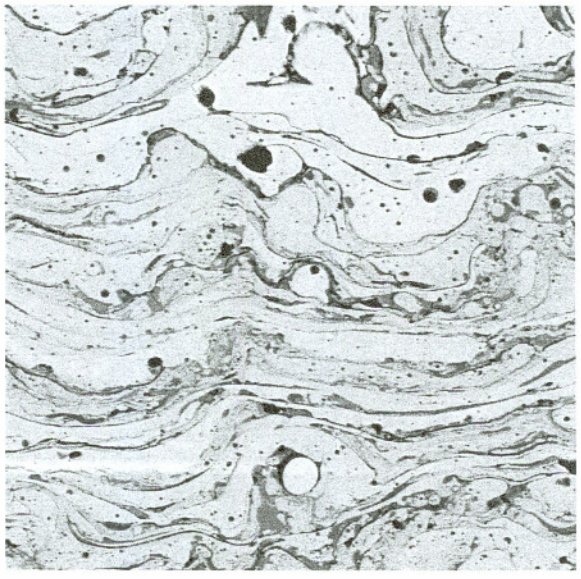

Figure 3.4.6.4. Region of low oxide content and porosity in TL2. 500x, backscattered electron image.

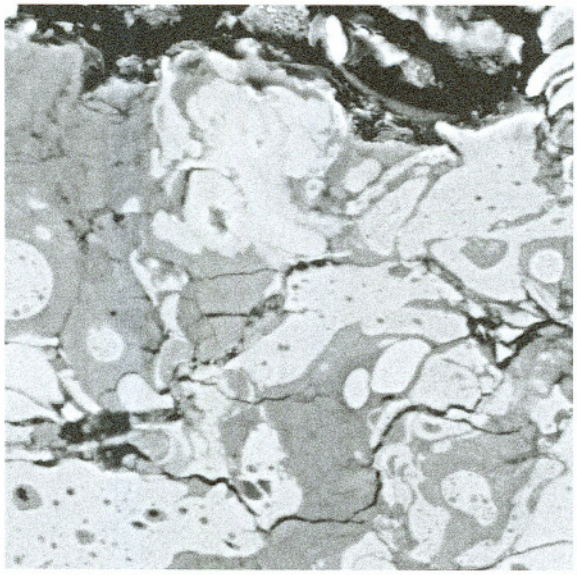

Figure 3.4.6.5. Fine oxide cracks located near surface of tested TL2 coating. 2000x, backscattered electron image.

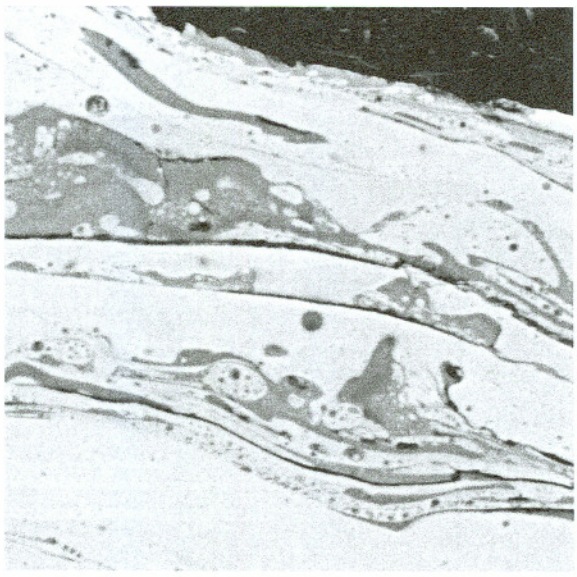

Figure 3.4.6.6. Delamination of the lamellae near coating surface of TL2. 2000x, backscattered electron image.

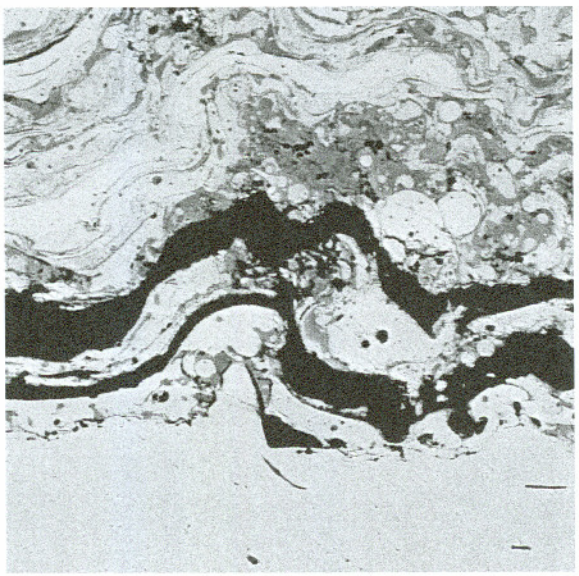

Figure 3.4.6.7. Delamination at the coating/substrate interface of TL2. 500x, backscattered electron image.

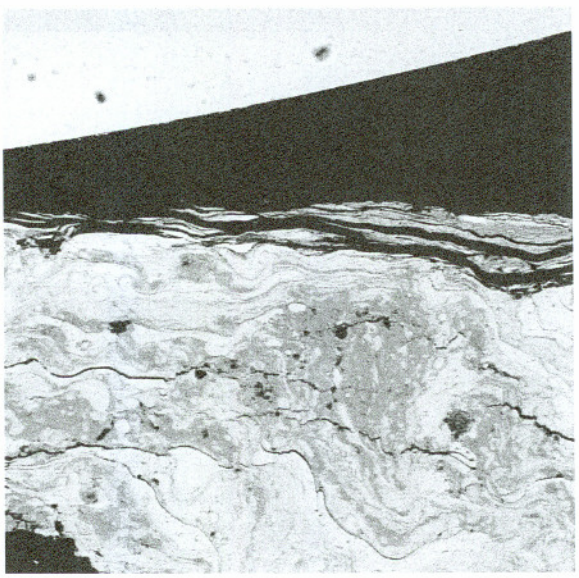

Figure 3.4.6.8. Wear surface of TL2 coating showing deformation. 200x, backscattered electron image.

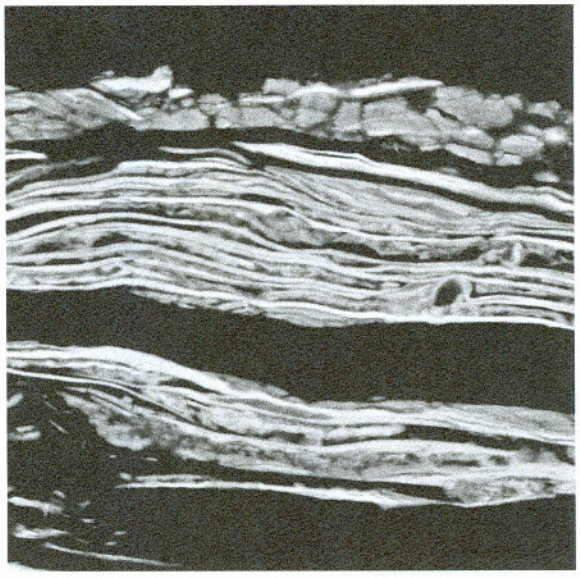

Figure 3.4.6.9. Deformed steel and fractured oxide lamellae in TL2 coating.
2000x, backscattered electron image.

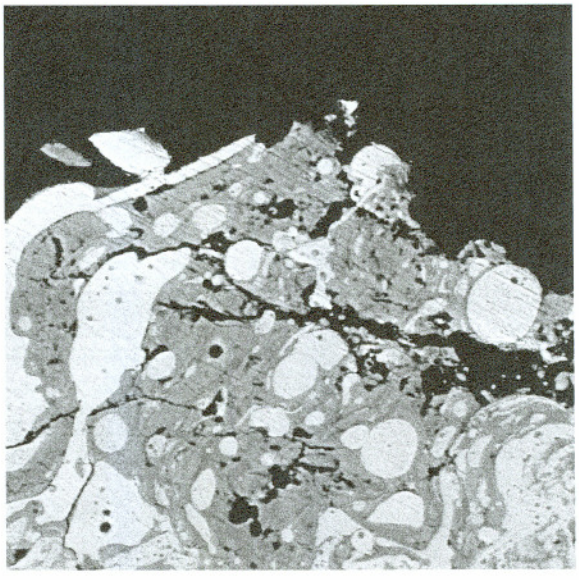

Figure 3.4.6.10. Rough wear surface showing fractured
steel lamellae in TL2 coating.
750x, backscattered electron image.

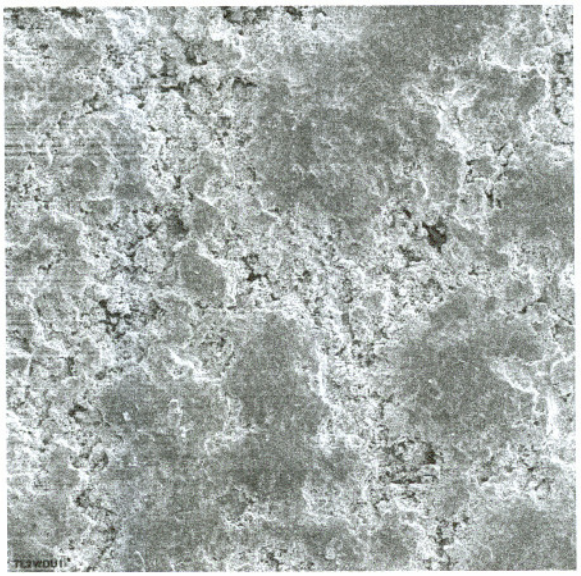

Figure 3.4.6.11. Surfaces found in TL2 wear debris, rough and smooth areas.
100x, secondary electron image.

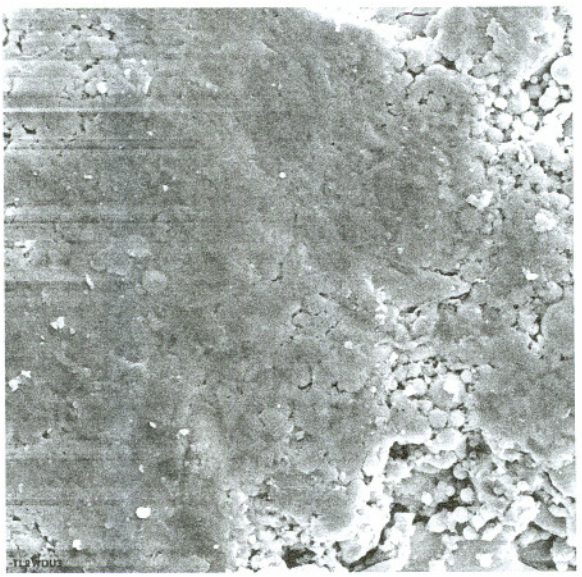

Figure 3.4.6.12. Surfaces found in TL2 wear debris,
unmelted particles adjacent to worn region.
1000x, secondary electron image.

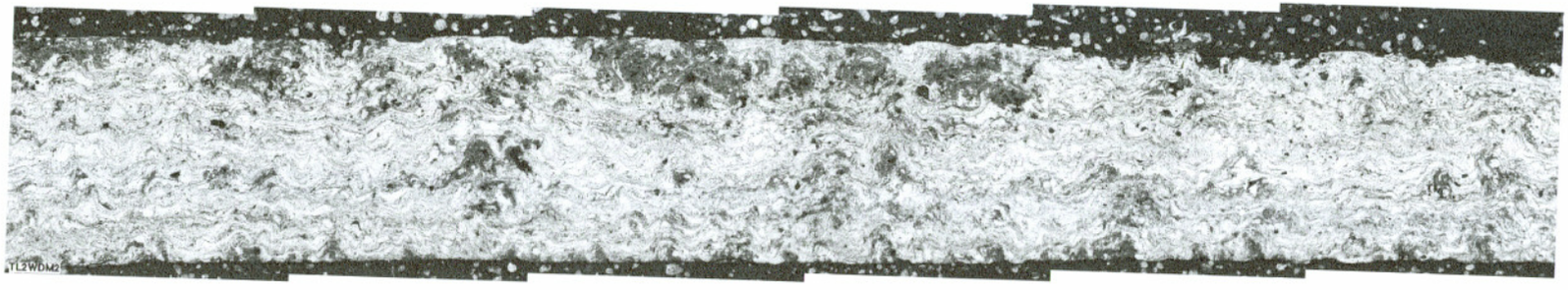

Figure 3.4.6.13. Composite image of TL2 wear debris.
100x, optical micrographs.

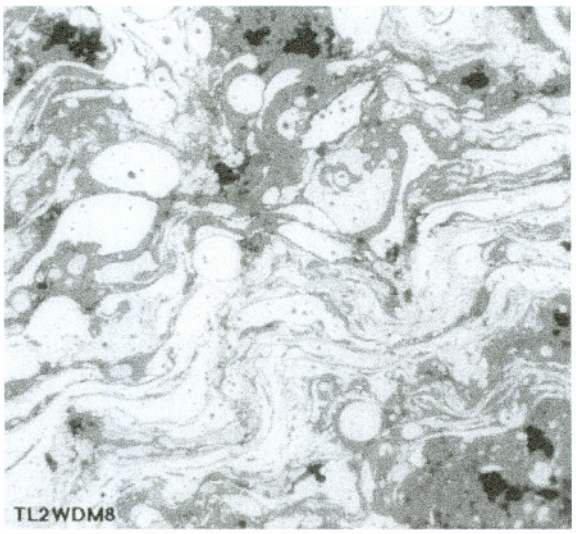

Figure 3.4.6.14. High oxide region in TL2 wear debris.
400x, optical micrograph.

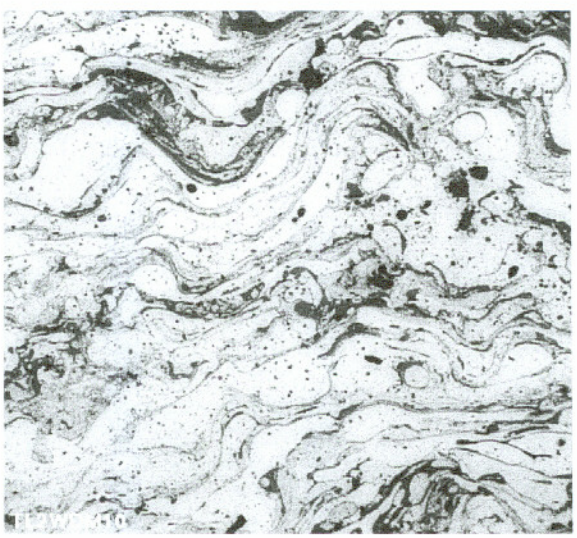

Figure 3.4.6.15. Low oxide region in TL2 wear debris.
400x, optical micrograph.

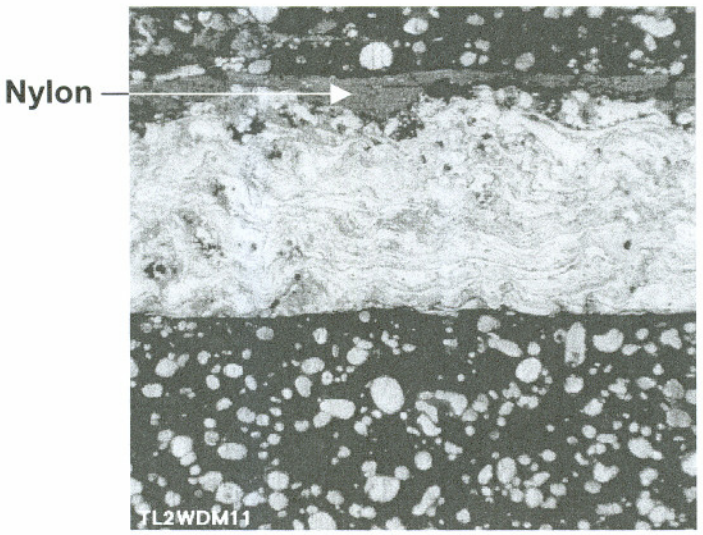

Figure 3.4.6.16. TL2 wear debris with intact nylon coating containing wear product. 100x, optical micrograph.

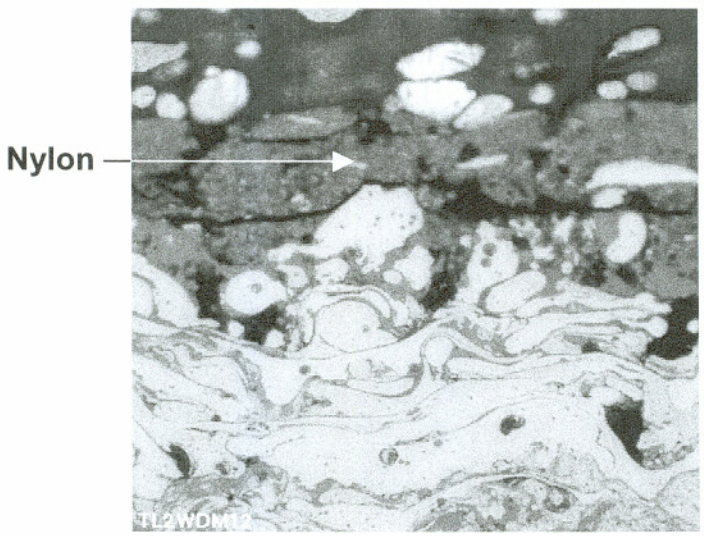

Figure 3.4.6.17. TL2 wear debris nylon coating with wear product. 400x, optical micrograph.

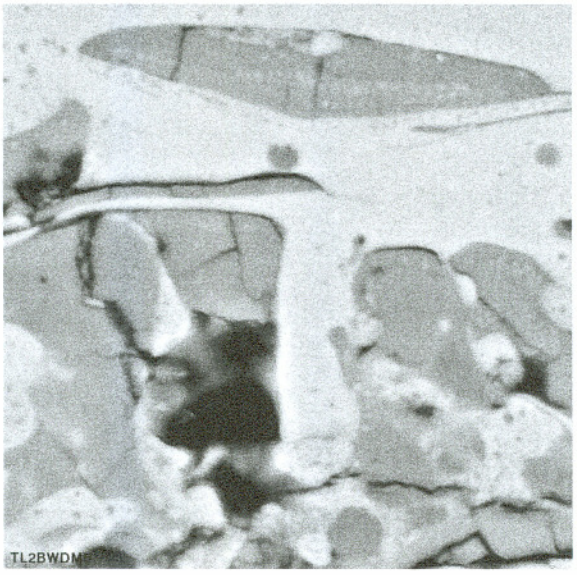

Figure 3.4.6.18. Cracking of oxides within the TL2 coating.
5000x, backscattered electron image.

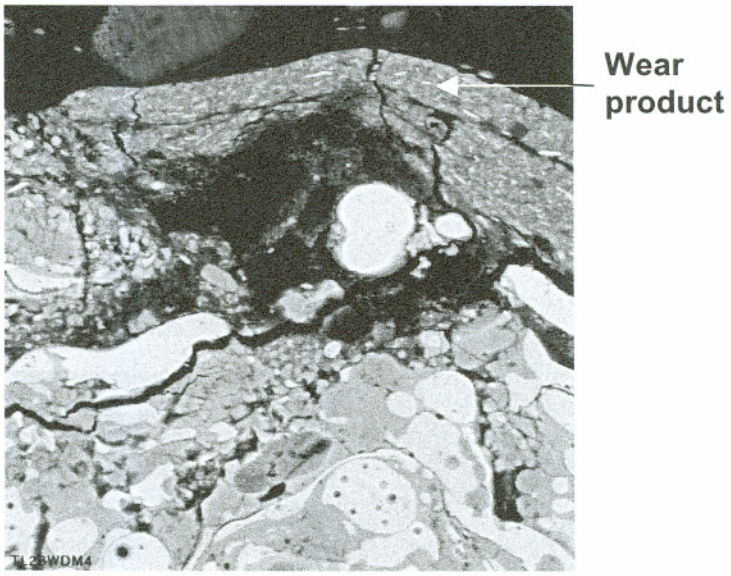

Figure 3.4.6.19. Fractured wear surface of TL2 coating.
1000x, backscattered electron image.

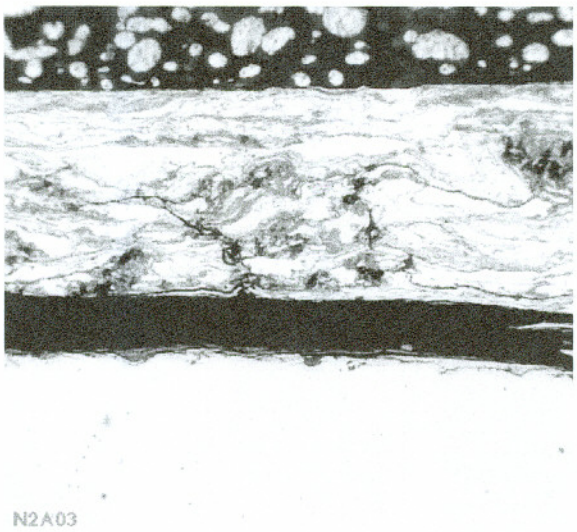

Figure 3.4.7.1. Microstructure of debonded TL3 coating at edge of wear path. 200x, optical micrograph.

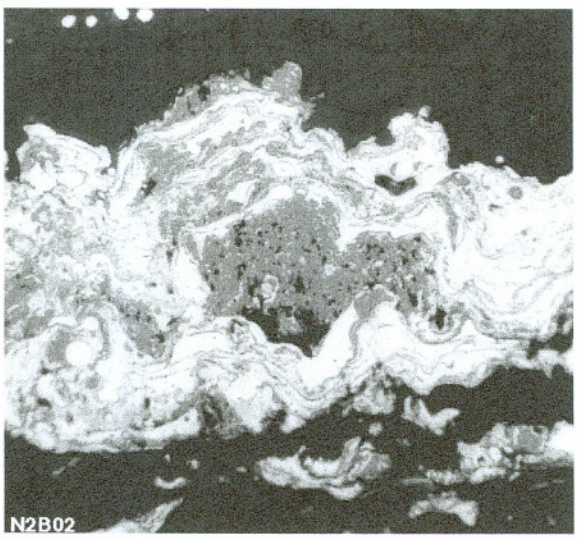

Figure 3.4.7.2. Microstructure of worn TL3 coating at farthest point on field side. 200x, optical micrograph.

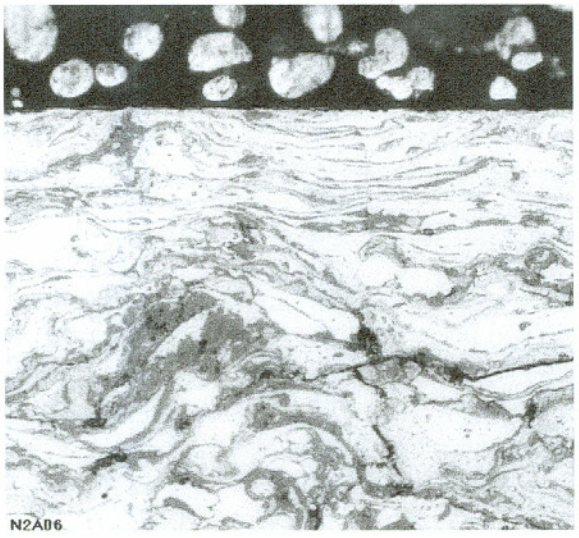

Figure 3.4.7.3. Wear surface of TL3 showing plastic deformation. 200x, optical micrograph.

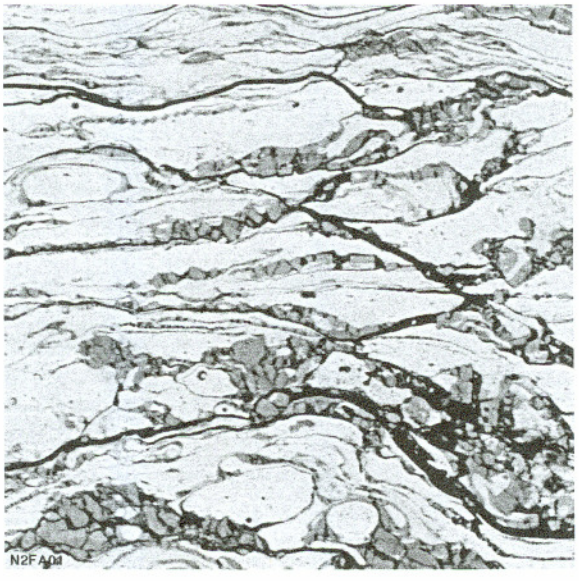

Figure 3.4.7.4. Microstructure of TL3 just beneath the wear surface. 1000x, backscattered electron image.

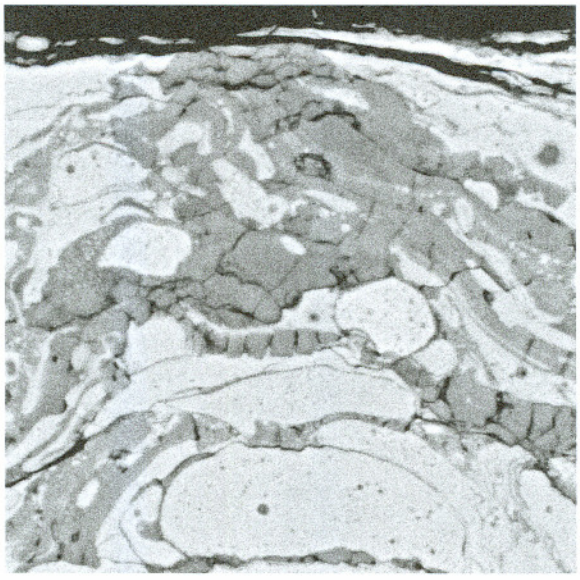

Figure 3.4.7.5. Oxide cracking at surface of TL3.
3000x, backscattered electron image.

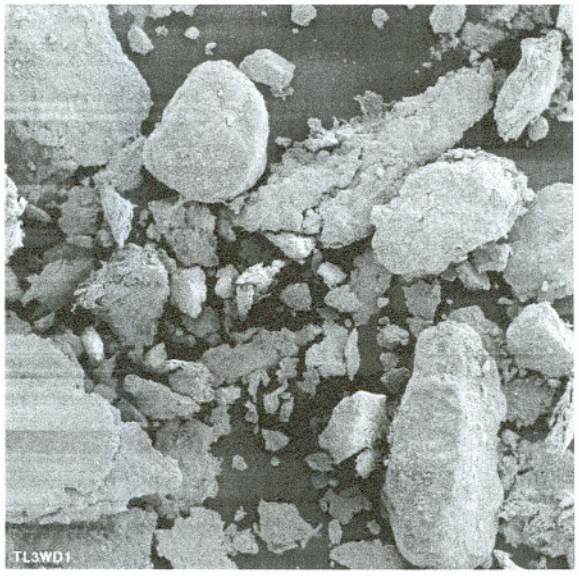

Figure 3.4.7.6. Morphology of TL3 wear particles.
50x, secondary electron image.

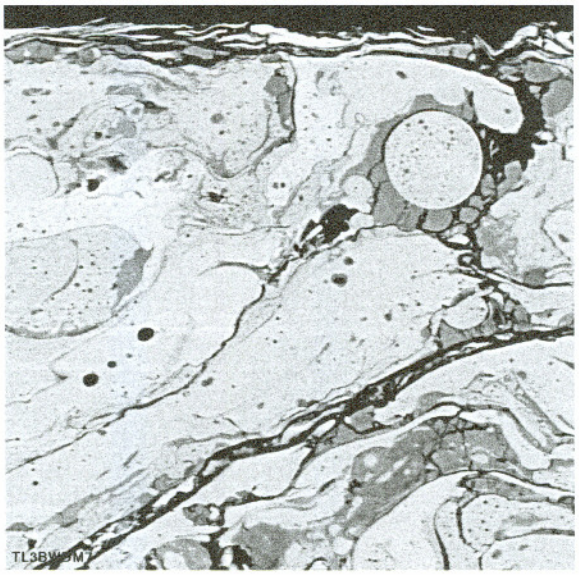

Figure 3.4.7.7. Oxide cracking and interlamellar separation of TL3.
1000x, backscattered electron image.

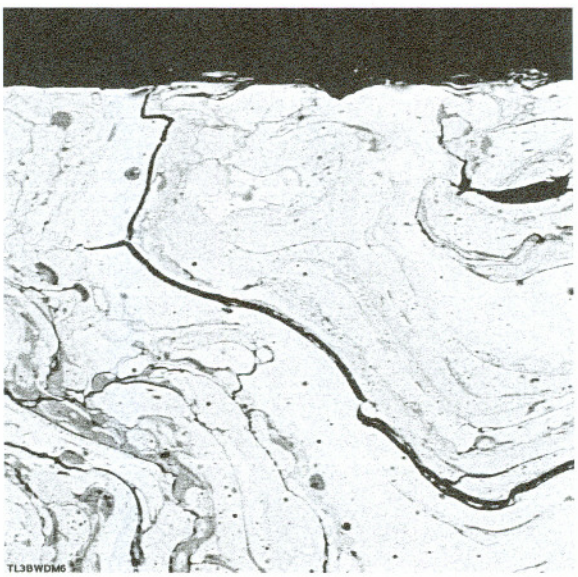

Figure 3.4.7.8. Large and small interlamellar cracks in TL3.
1000x, backscattered electron image.

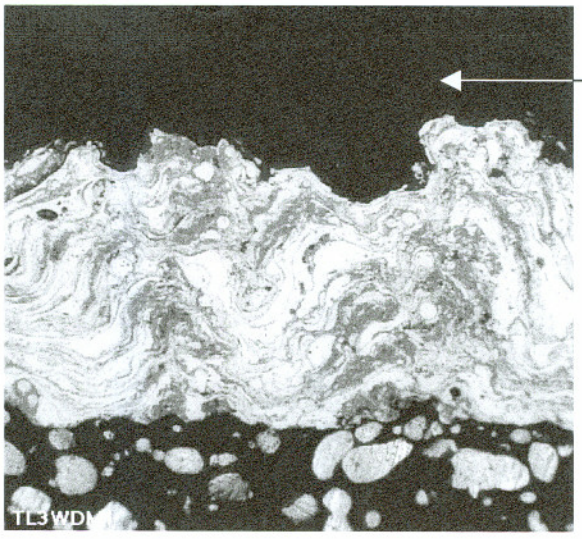

Figure 3.4.7.9. Oxide banding in unworn section of TL3 wear debris with intact nylon. 200x, optical micrograph.

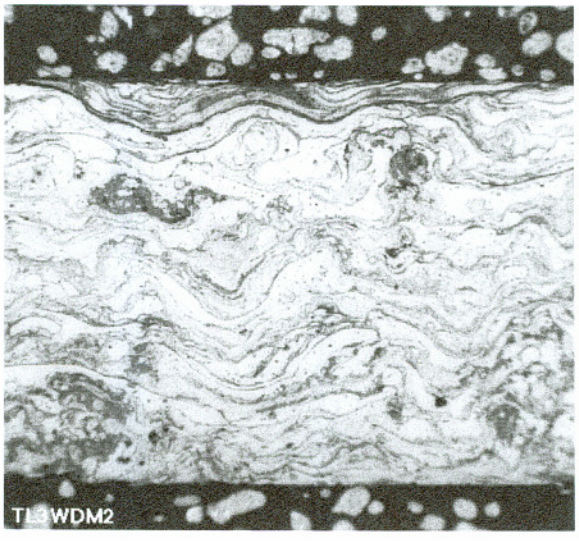

Figure 3.4.7.10. Worn surface of TL3 showing interlamellar separation of wear particle. 200x, optical micrograph.

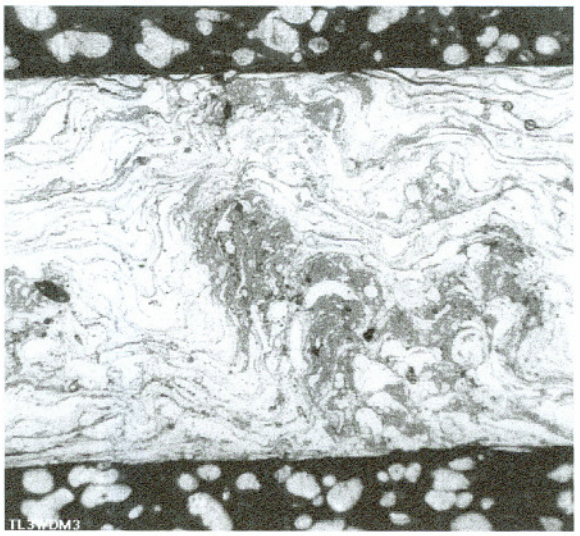

Figure 3.4.7.11. Oxide banding and surface deformation in TL3 wear track.
200x, optical micrograph.

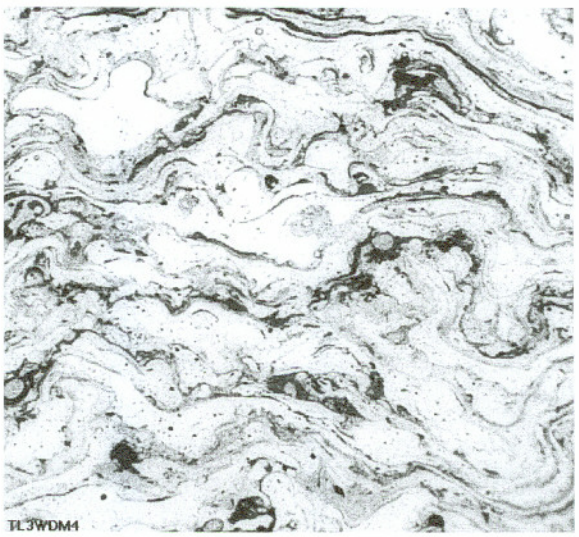

Figure 3.4.7.12. Low oxide microstructure of TL3.
400x, optical micrograph.

Figure 3.4.8.1. Wear surface of TL4 debonded coating with oxide patches and interlamellar debonding. 400x, optical micrograph.

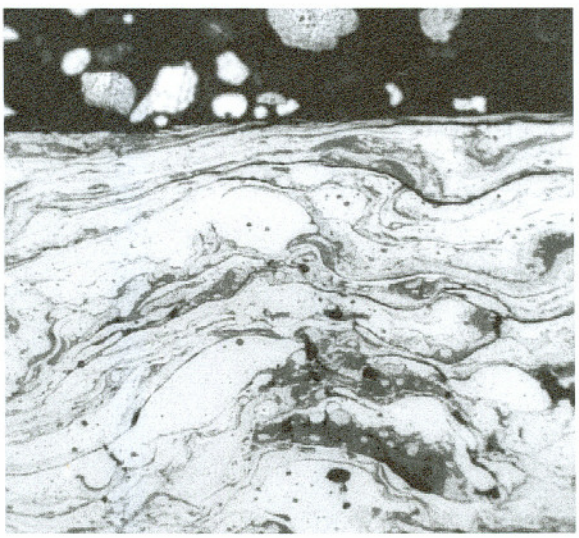

Figure 3.4.8.2. Slight plastic deformation of TL4 wear surface. 400x, optical micrograph.

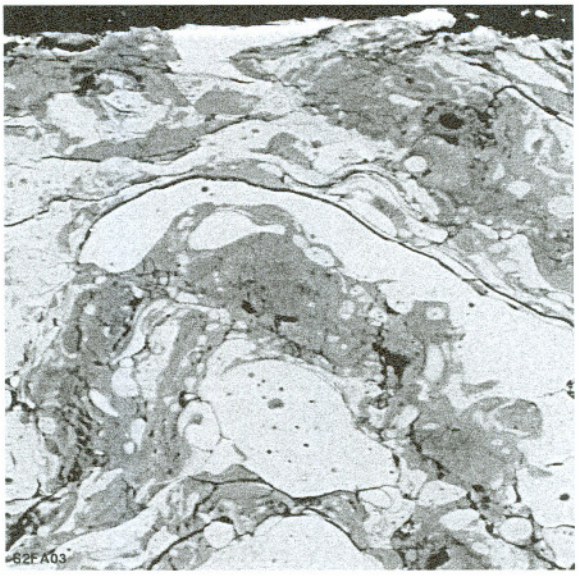

Figure 3.4.8.3. High oxide region in TL4.
800x, backscattered electron image.

Figure 3.4.8.4. Low oxide region in TL4.
1000x, backscattered electron image.

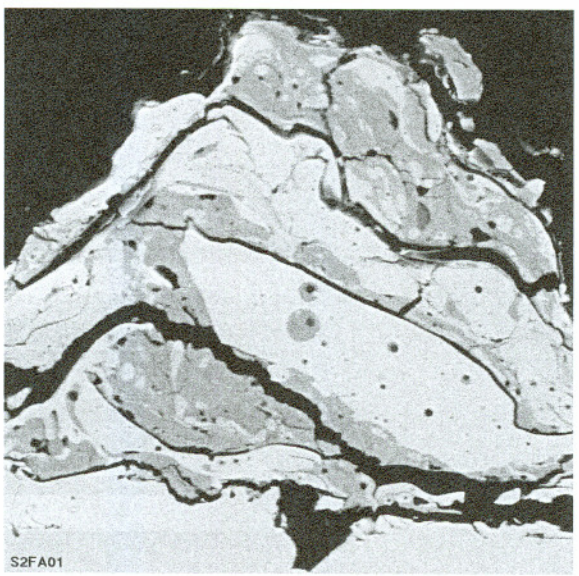

Figure 3.4.8.5. Interlamellar cracking in unworn TL4 coating.
950x, backscattered electron image.

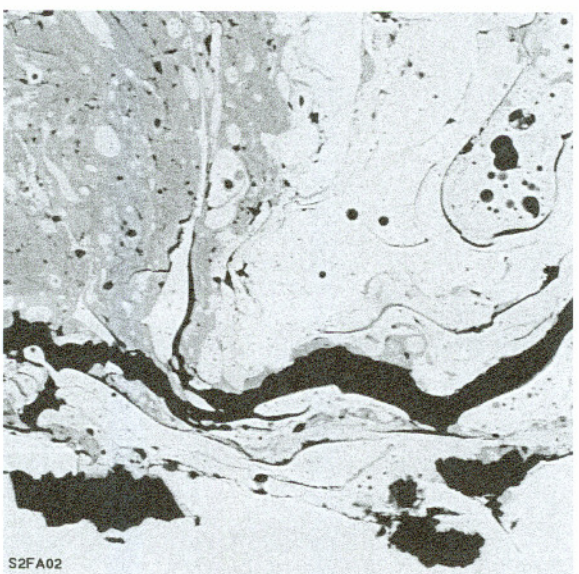

Figure 3.4.8.6. Coating debonding slightly above interface of TL4.
800x, backscattered electron image.

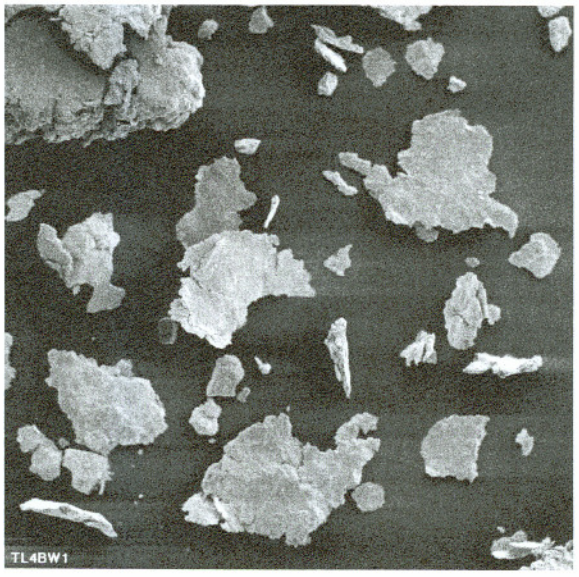

Figure 3.4.8.7. Wear debris particles of TL4.
500x, secondary electron image.

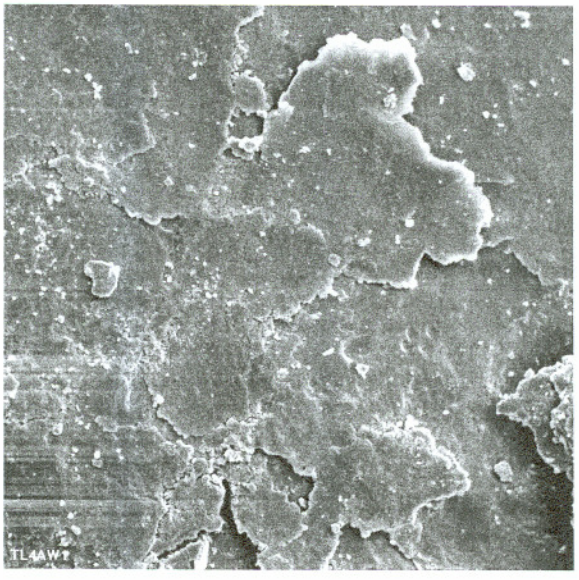

Figure 3.4.8.8. Surface of TL4 wear debris showing initiation of flake-like wear particle.
1000x, secondary electron image.

Figure 3.4.8.9. Regions of varying oxide concentrations in TL4 wear debris. 200x, optical micrograph.

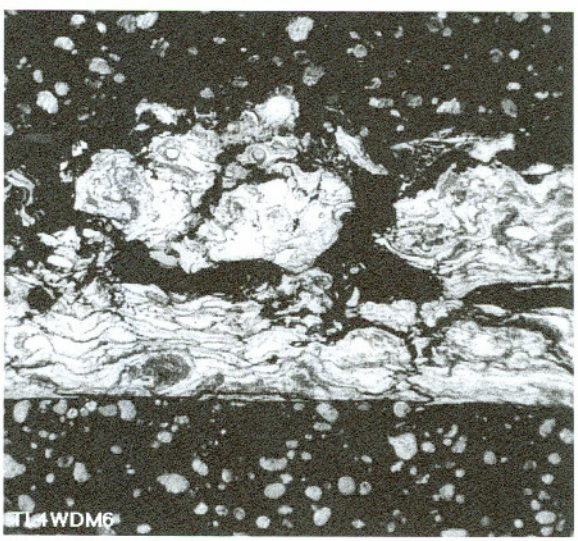

Figure 3.4.8.10. Severe disintegration of TL4 wear debris coating. 100x, optical micrograph.

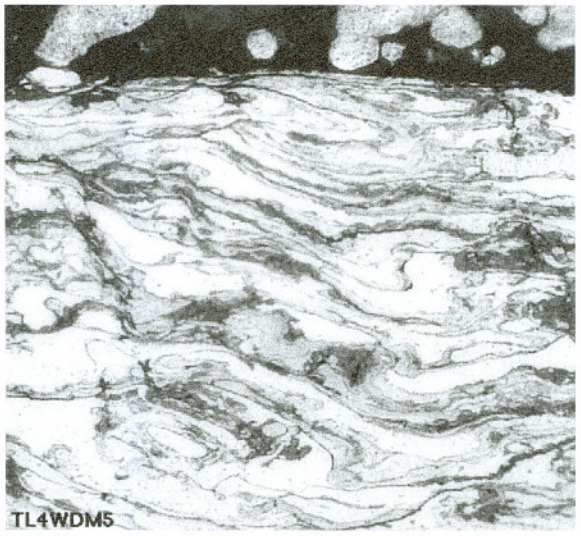

Figure 3.4.8.11. Deformation with elongated oxides in TL4 wear debris.
400x, optical micrograph.

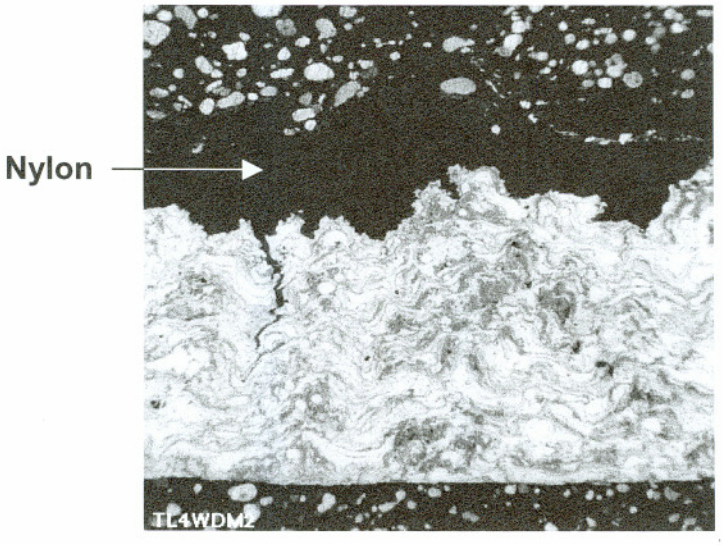

Figure 3.4.8.12. Intact TL4 nylon coating in unworn region.
100x, optical micrograph.

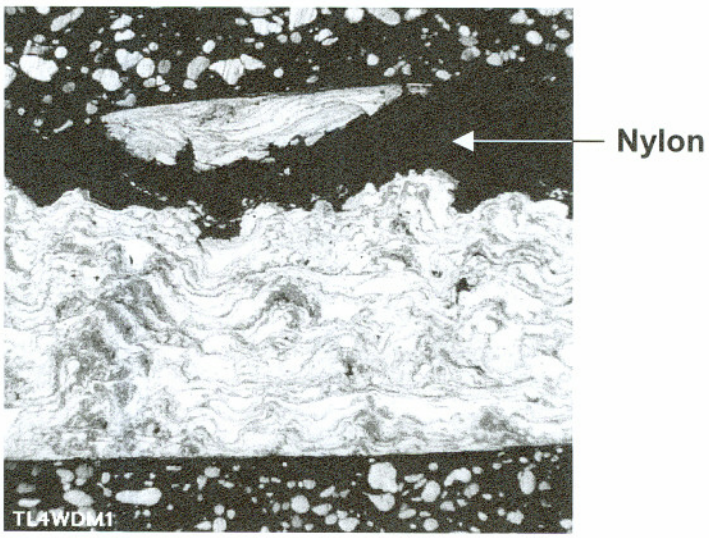

Figure 3.4.8.13. Large coating particle embedded in unworn nylon of TL4 coating. 100x, optical micrograph.

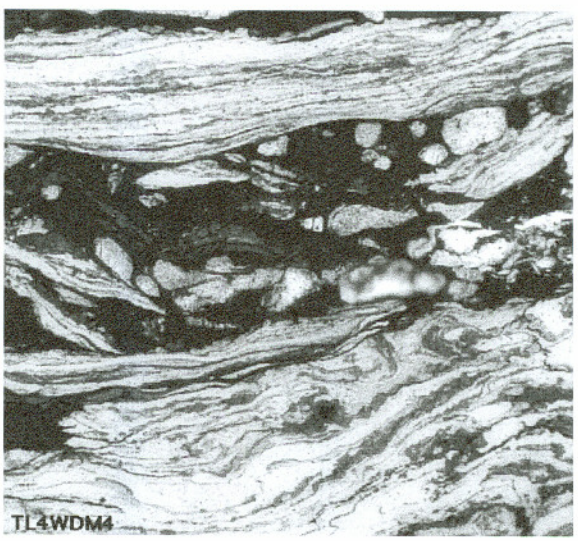

Figure 3.4.8.14. Highly deformed embedded particles at surface of TL4 wear debris. 400x, optical micrograph.

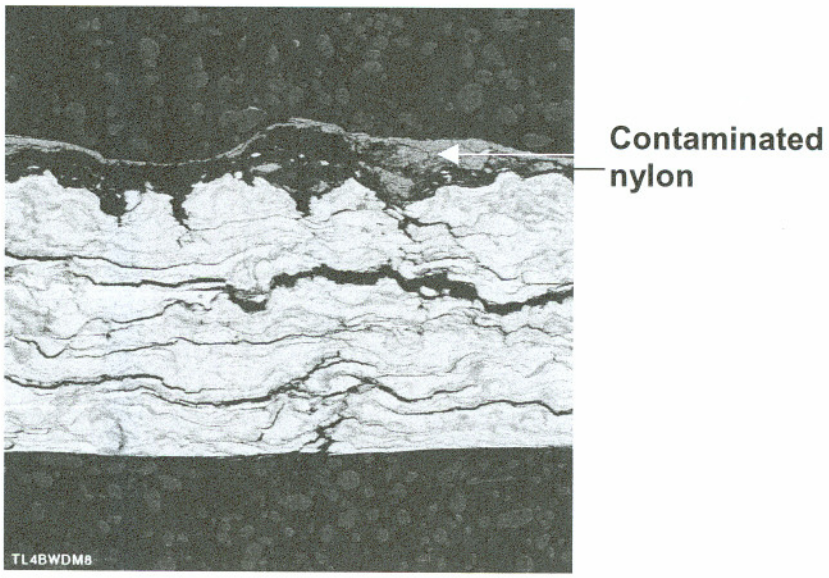

Figure 3.4.8.15. Contamination of the nylon coating by wear debris for TL4.
100x, backscattered electron image.

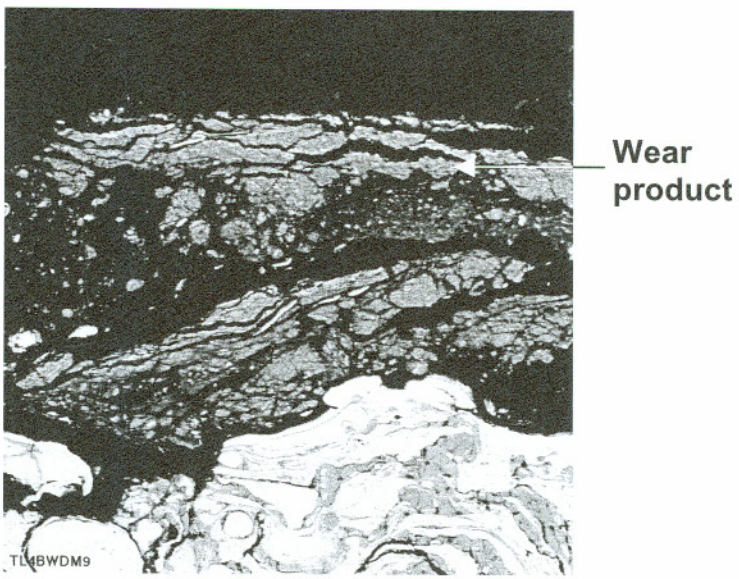

Figure 3.4.8.16. Fractured wear product at TL4 surface.
500x, backscattered electron image.

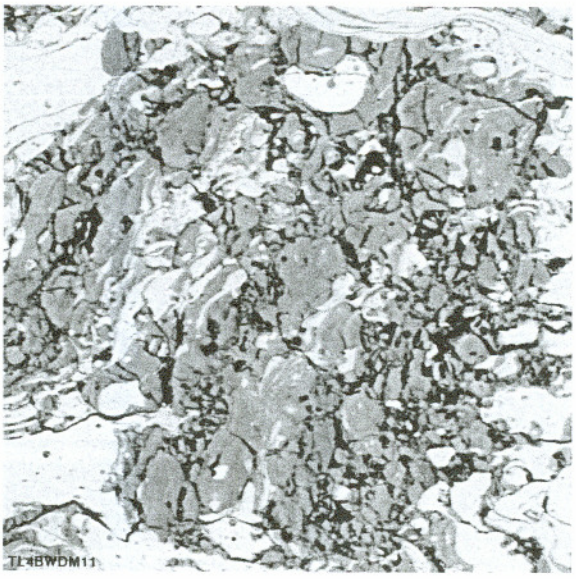

Figure 3.4.8.17. Cracking of oxide rich region in TL4 coating.
1000x, backscattered electron image.

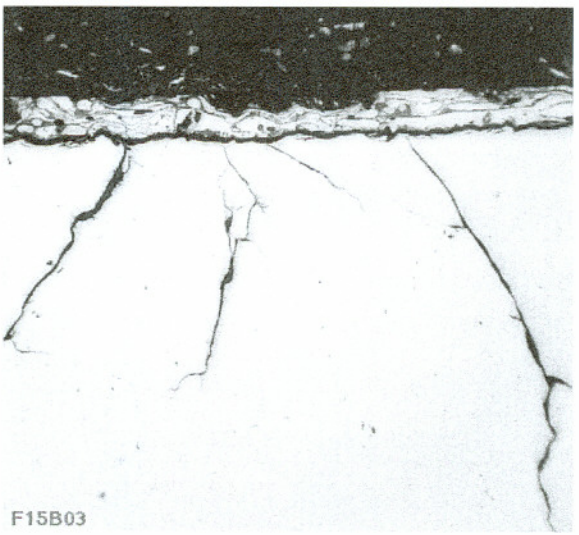

Figure 3.4.9.1. Substrate cracking at the surface of FAST rail wear track.
100x, optical micrograph.

Figure 3.4.9.2. Shear lips in surface of FAST rail gage face.
50x, optical micrograph.

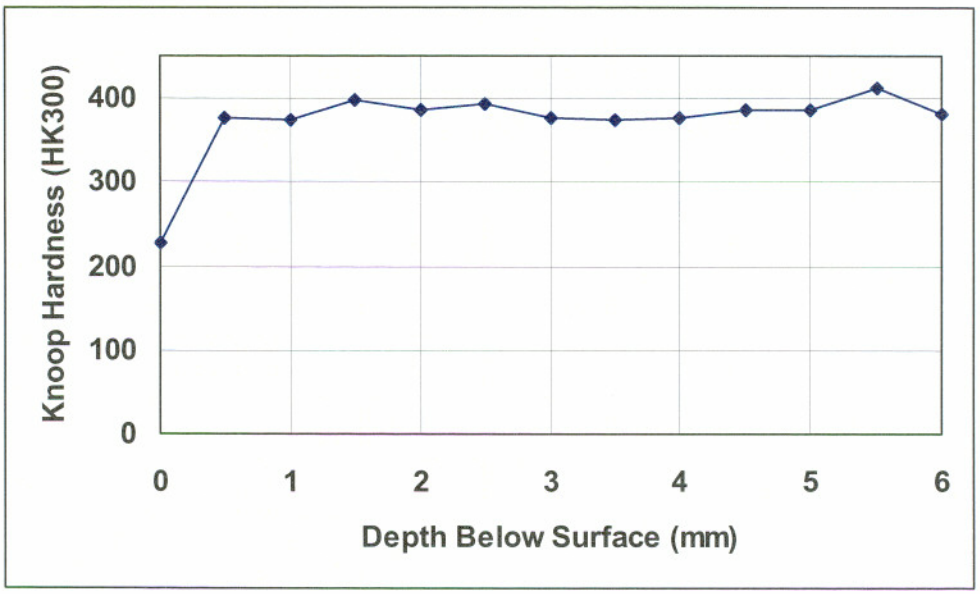

Figure 3.4.9.3. Microhardness traverse for FAST substrate.

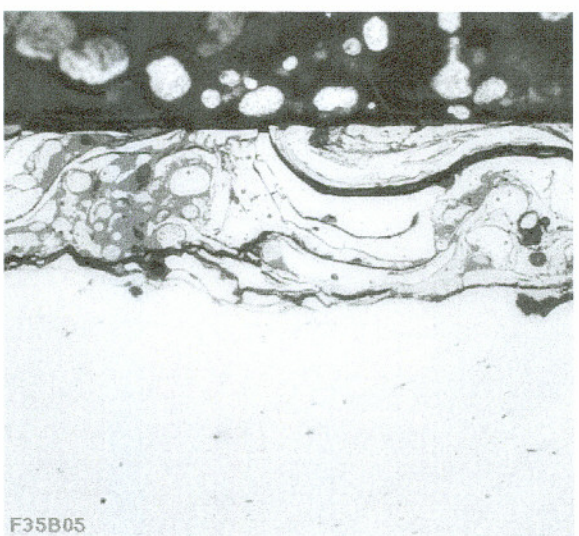

Figure 3.4.9.4. Typical wear surface of FAST.
400x, optical micrograph.

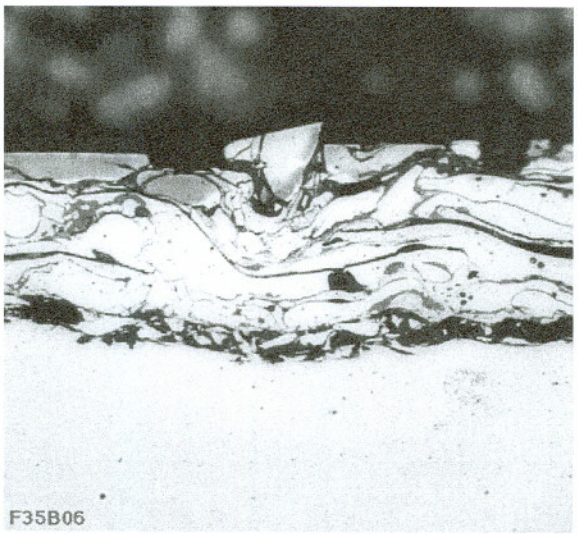

Figure 3.4.9.5. Disintegration of FAST coating at interface.
400x, optical micrograph.

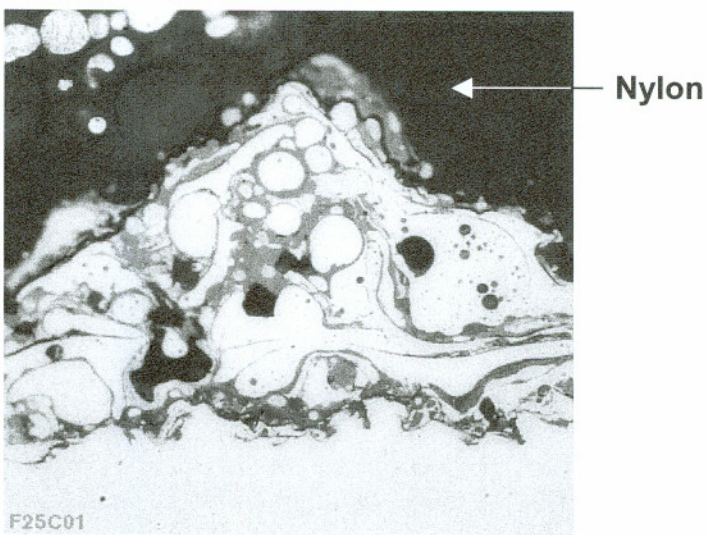

Figure 3.4.9.6. Poor microstructure on field side of FAST rail.
Dark region above coating is unworn nylon.
400x, optical micrograph.

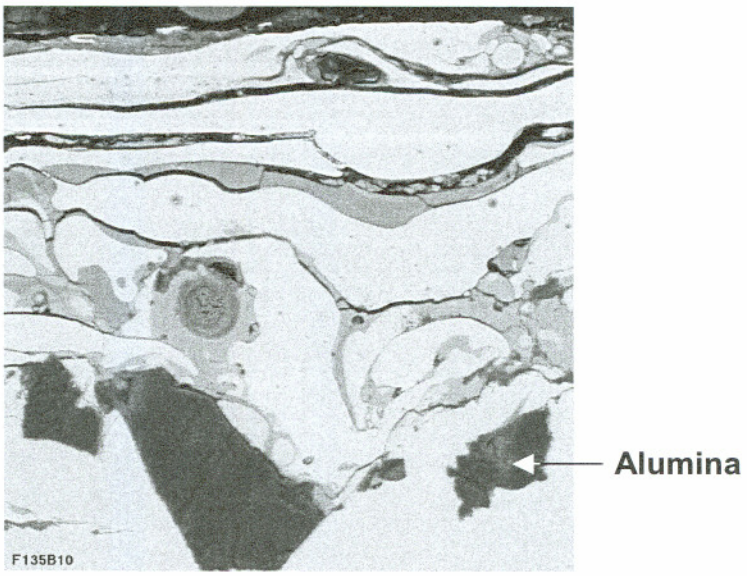

Figure 3.4.9.7. Interlamellar debonding, oxide cracking and interface contamination in FAST specimen. 1000x, backscattered electron image.

Figure 3.4.9.8. Oxide region in FAST with cracking and unmelted particles. 1500x, backscattered electron image.

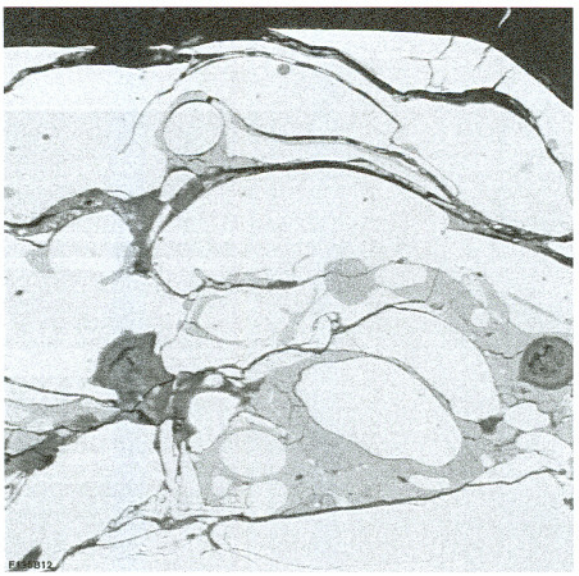

Figure 3.4.9.9. Cracked metal and oxide lamellae in FAST.
1000x, backscattered electron image.

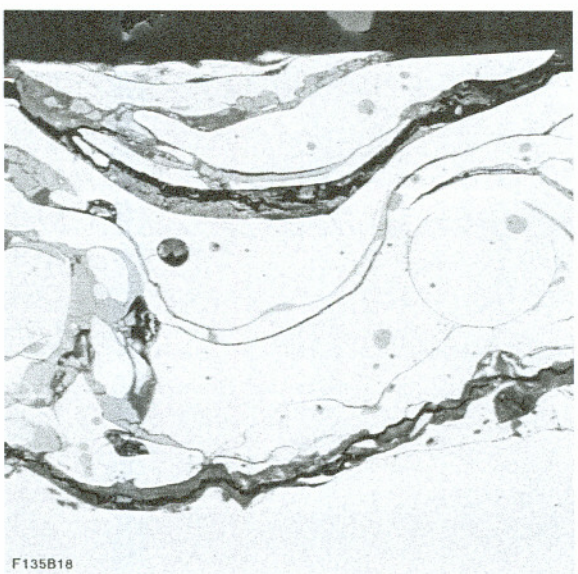

Figure 3.4.9.10. Wear particle formed by interlamellar debonding in FAST.
1000x, backscattered electron image.

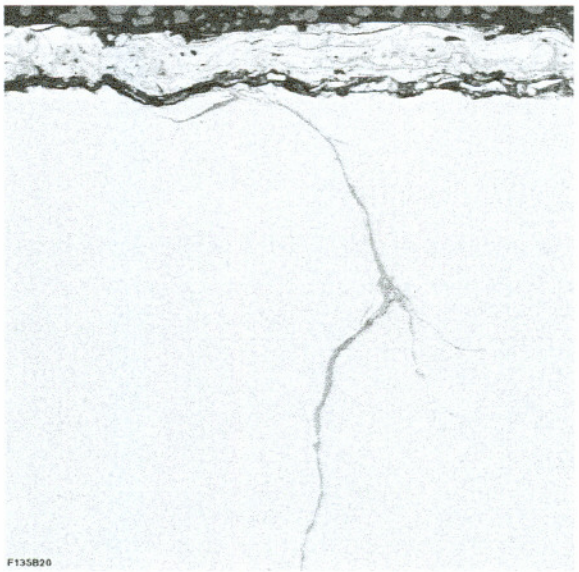

Figure 3.4.9.11. Cracking in FAST rail substrate.
90x, backscattered electron image.

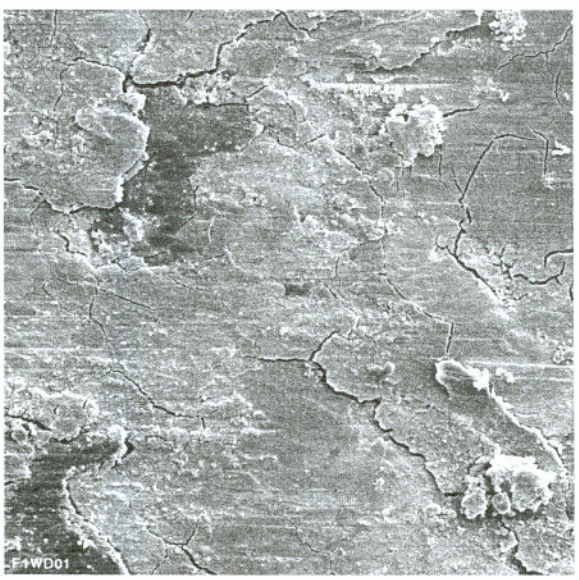

Figure 3.4.9.12. Crack network in surface of unmounted FAST wear debris.
500x, secondary electron image.

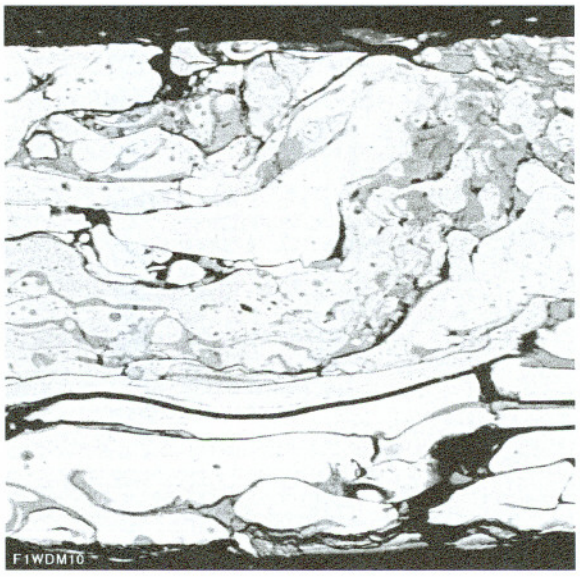

Figure 3.4.9.13. Interlamellar cracking in FAST coating.
1100x, backscattered electron image.

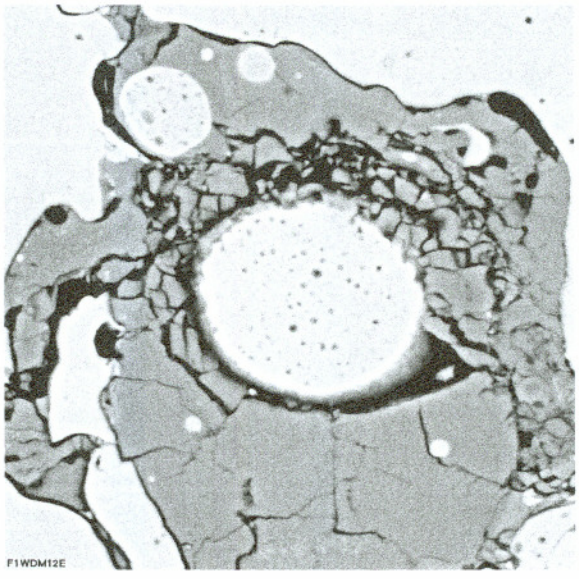

Figure 3.4.9.14. Fractured oxide surrounding unmelted steel particle in FAST coating.
2000x, backscattered electron image.

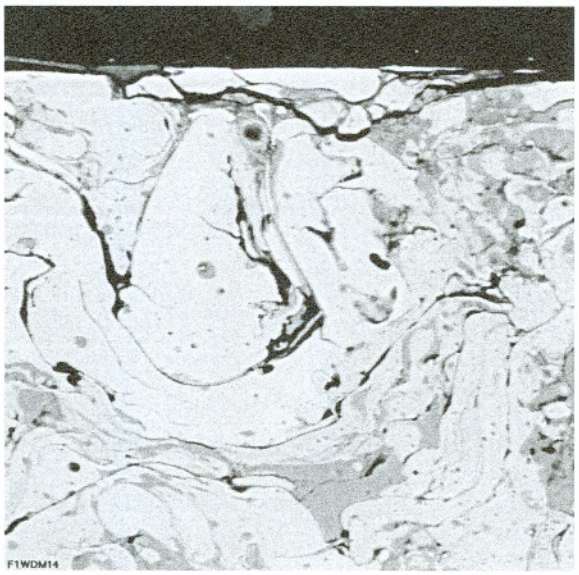

Figure 3.4.9.15. Wear particle formed at FAST surface.
1000x, backscattered electron image.

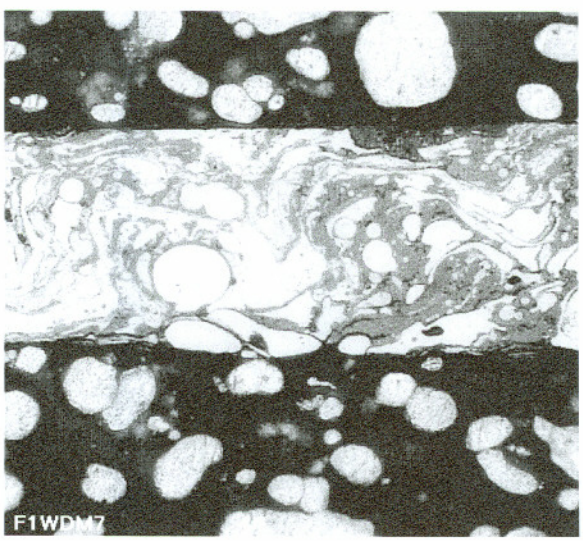

Figure 3.4.9.16. High oxide content region in FAST wear debris.
400x, optical micrograph.

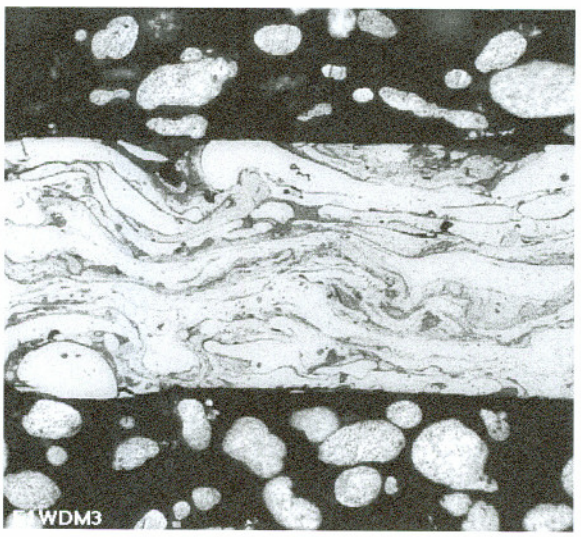

Figure 3.4.9.17. Lower oxide content region in FAST wear debris.
400x, optical micrograph.

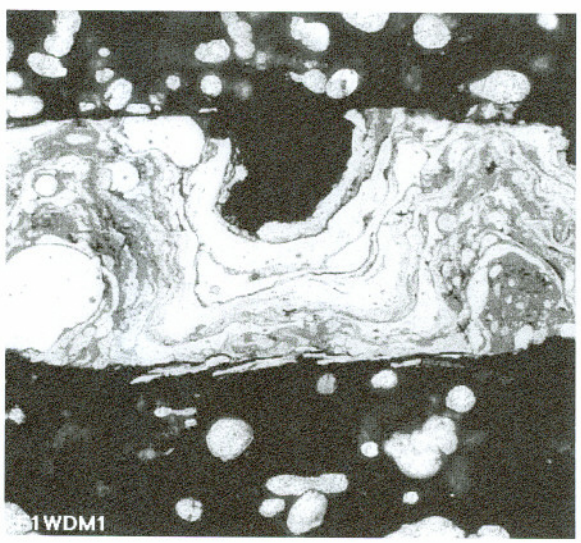

Figure 3.4.9.18. Nylon embedded in cavity in FAST surface.
400x, optical micrograph.

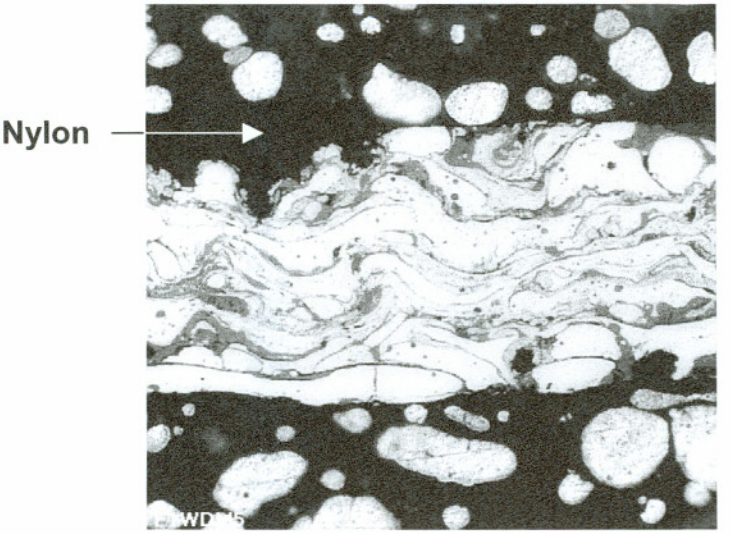

Figure 3.4.9.19. Transition point from worn to unworn coating in FAST wear debris. 400x, optical micrograph.

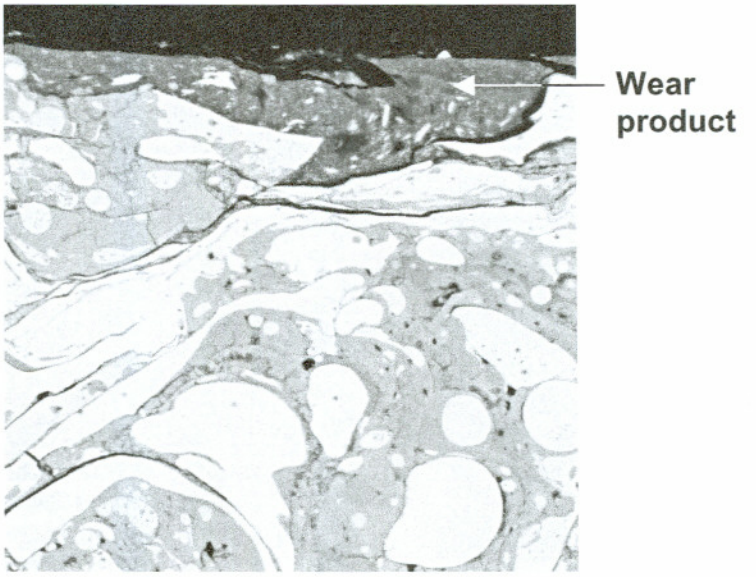

Figure 3.4.9.20. Wear product at surface of FAST specimen. 1250x, backscattered electron image.

References for Chapter 3

1. McMurchie, D., *Development of a 1080 Steel Plasma Sprayed Coating for Slide/Roll Conditions*, Ph.D. Thesis, Oregon Graduate Institute of Science and Technology, 1996.

2. Niebuhr, D. V., *Development of a Self-lubricating Plasma Sprayed Coating for Rolling/Sliding Wear*, Ph.D. Thesis, Oregon Graduate Institute of Science and Technology, 1997.

CHAPTER 4

DISCUSSION

The discussion that follows analyzes research into developing and testing plasma sprayed coatings for use on the track rails of revenue railroad lines. The work covers laboratory studies into the development of both friction enhancing and friction reducing coatings. Selected coatings were subsequently plasma sprayed on full scale test specimens and subjected to testing under simulated revenue rail service conditions.

Previous laboratory assessment covered friction reducing coating development; the laboratory work reported here also covers friction reducing coatings, but concentrates on friction enhancing coatings. A detailed post-test analysis of all full scale test samples is also reported.

The ultimate goal of the friction modification research project was to use plasma sprayed coatings to control the friction level between the wheel and the rail. An important aspect of the project was to develop coatings that would reduce friction along the rail gage face and thereby reduce wear. To achieve this goal, once the candidate materials were identified and the surface preparation techniques finalized, it was then necessary to optimize the plasma spray parameters. This was accomplished using single splat analysis, flat coupon verification, tensile testing and Amsler testing. Using the optimized parameters, full scale test specimens were sprayed. The full scale specimens were tested at FAST using three different tests. On receipt of the tested full scale specimens back at OGI, a post-test analysis was performed to evaluate the failure mechanisms.

Several materials were investigated for their friction altering ability. Stainless steel and titanium were candidate materials considered for their potential to increase the friction between the wheel and the rail, and thereby reduce slip and increase traction. Titanium was later dropped from the research after poor results with stainless steel. Composite steel coatings containing second phase particles of stainless steel or titanium were considered next for increasing friction but also showed poor results. These results led to an investigation into the mechanisms of coating wear and failure using the interrupted test method. Stainless steel coated with nylon was investigated as a friction reducing coating for use in lowering friction in curves.

4.1 PREPARATION OF SUBSTRATES (GRIT BLASTING STUDY)

Coating durability depends, to a great extent, on the ability of a coating to adhere to the substrate. The importance of a properly prepared surface to promote adherence is well known in plasma spraying. A properly prepared surface is free from dirt, grease, and oxide layers that inhibit the metal-to-metal contact between the coating and the substrate. In addition, it is assumed that the rougher the surface, the better the coating adhesion.

Coating adhesion is thought to be a function of three pre-spray processes. The first is cleaning the substrate surface, next is roughening the surface, and finally, cleaning the roughened surface. Typically the substrate is cleaned with detergent and water, rinsed with acetone, and dried with a blast of air prior to roughening. This removes all the grease and oils that potentially could contaminate the roughening process. After roughening, once again the surface is flushed with acetone to remove oils and residual debris particles, and dried. All of these steps are important for coating adhesion and consequently coating wear life. Each process needs to be evaluated, and to assure maximum coating properties and longevity, the processes must be carried out consistently.

One method that both cleans and roughens the surface simultaneously is grit blasting. Grit blasting provides a greater surface area for mechanical bonding to occur and is also thought to increase the energy of the surface by work hardening due to grit impact. There are many parameters to grit blasting that affect the surface roughness of the prepared surface.

This section of the research focuses on evaluating the roughening and cleaning ability of various grit media, and at the same time minimizing subsequent grit-induced contamination. Various experiments were performed to understand the effect of grit blast media and size, impact angle, dwell time and substrate hardness on the surface roughness of steels. Profilometry and microscopy were used to evaluate the roughened surfaces while tensile testing and Amsler testing were used to evaluate the strength of the coatings prepared using different parameters.

4.1.1 Grit Blast Media and Impact Angle Experiments

Steel coupons were prepared using various media, grit sizes and impact angles and then surface profilometry readings were made on the steel coupons after grit blasting to measure surface characteristics. As expected, the results show that the larger grit sizes produce a rougher surface with two exceptions, Table 3.2.1.1. One exception is the 50-70 grit alumina that, although the same size range as the 50-70 grit silica, showed a greater surface roughness than the silica. This may be a result of particle morphology since the silica particles are more rounded than the sharper edged alumina particles, Figure 3.2.1.1. The 25 grit steel shot at 45 degrees, which had a higher average surface roughness than the larger 20 grit alumina, seems to be the other exception. The steel shot, although smaller in size, has a higher density and thus would strike the surface with greater momentum than lower density alumina. However, the error bars (standard deviation) in the graph, Figure 4.1.1 (b), show that there does not seem to be a significant difference between the two materials.

Impact angle results showed no significant effect on surface roughness for any of the alumina and silica samples. The only apparent difference in surface roughness appears to be for the steel shot which had a greater surface roughness for the 45 degree impact angle than the 90 degree impact angle. However, due to the spread in the data shown in Figure 4.1.1 (b) there does not seem to be a significant difference between the two angles.

When examined in the SEM there appeared to be very little difference in the sample surfaces that were prepared using 45 and 90 degree impact angles. Differences could only be found in the relative size of the surface roughness features based on the size of the grit used. Contaminant particles were found to some degree on all the samples examined. Energy dispersive spectroscopy confirmed that the embedded contaminant particles contained Al and O, Figure 3.2.1.2. In addition, W and Co were found embedded on the surface and are believed to result from erosion of the grit blasting nozzle. Energy dispersive spectroscopy of unused alumina grit particles confirmed Al and O, as well as some Ti in the grit particles.

4.1.2 Substrate Hardness

Two different substrates, a new low hardness, hot-rolled rail and a worn high hardness, head-hardened rail were used to study the effect of substrate hardness on surface roughness. Various grit blast media were used in this study, either singly or in combinations. Of the various surface roughness parameters listed in Table 3.2.2.1, R_a is the parameter used most commonly, to describe surface roughness. In all cases the surface roughness was lower for worn head-hardened rail than for the new rail, Figure 4.1.2, as was expected, due to the higher hardness of the head-hardened rail. For the worn rail, the surface roughness values were closer together with the 50/50 mix, steel shot, and two-stage, which were the roughest, and alumina and iron the least. For the new low hardness rail, the surface roughness from steel shot was the highest followed by the 50/50 mix, alumina, two-stage, and lastly, iron shot. The as-sprayed coating surface roughness was twice as high as the grit blasted surfaces.

Since steel shot had the highest R_a and alumina cleaned the fastest, the two-stage process of alumina followed by steel shot was chosen to clean all full scale rail substrates. While this study started out using 20 grit alumina, later work was performed using 36 grit alumina, since 20 grit was no longer available and the grit characteristics between the 20 and 36 grit alumina were very similar.

Figure 3.2.2.2 compares several surfaces made by grit blasting steel coupons with these materials as well as steel shot and 36 and 20 grit alumina. There appear to be gross differences in surface roughness and topography, but the overall surface features are difficult to compare visually since the specific region imaged can greatly influence the comparison due to local variations in the surface roughness. Figures 3.2.2.1 and 3.2.1.1 show the particle morphologies of steel, alumina, and Fe shot. As can be seen the steel particles have large, sharp facets but smooth surfaces while the alumina particles have many irregular surfaces. Since visual differences are difficult to quantify, other methods are required to characterize the surface, such as the various parameters found using surface profilometry.

The profile trace is another tool that can be used to make comparisons between sample surfaces. Surface features appear to be better resolved as shown in the representative profiles found in Figures 3.2.2.3 to 3.2.2.13. For example, the profiles show that the steel grit produced a sharper surface with deeper indentations than either alumina or Fe shot. Despite the greater roughness of steel, it did not clean the surface as well as alumina. A mixture of the two was tried as well as a two-stage process of alumina followed by steel. The two-stage process produced the best profile in terms of peak-to-valley distances and peak count. Simply based on the surface roughness, specifically R_a, the steel grit gives the greatest surface roughness. Based on surface roughness alone the choice would have been steel, however, other factors come into play, which necessitated using alternate grit blasting schemes.

When these results are compared against those for an as-sprayed 1080 steel plasma sprayed coating, the R_a value is much greater, but the number of peaks is lower than those of the grit blasted surfaces, Figure 3.2.3.13. For the plasma sprayed coating there are few, if any, secondary peaks on the main peaks, unlike those for the grit blasted surfaces. The surface of the as-sprayed coating, Figures 3.2.2.14 and 3.2.2.15, shows that roughness is of a different character than that of the grit blasted surfaces, Figure 3.2.2.2. One reason is the profilometer probe was unable to detect all the features of the plasma sprayed coating. Figure 4.1.3 shows schematically how the plasma sprayed coating differs from the grit blasted surface. The intricate, rounded protuberances on the surface that makes a plasma sprayed coating an ideal surface for secondary friction reduction coatings. The surface features interlock with the polymer which provides a better mechanical bond to the surface.

4.1.3 Dwell Time

Dwell time was another factor that influenced surface roughness characteristics. Little change was found in the surface roughness parameters as a function of time, Tables 3.2.3.1 and 3.2.3.2. A dwell time of a few seconds was sufficient to develop a relatively constant roughness profile, Figure 4.1.4. While all of the surfaces showed the presence of embedded grit between the peaks and valleys of the roughened surfaces, Figures 3.2.3.1 and 3.2.3.2, the amount of uncontaminated surface decreased significantly with increasing dwell time. With brittle grit such as alumina, more contamination is expected since it breaks down more rapidly than steel.

Examination of the grit blasted surfaces in cross-section showed a high degree of alumina contamination especially for the higher dwell times, Figures 3.2.3.3 and 3.2.3.4. The lower times preserved the grit integrity to a greater extent and reduced the amount of embedded grit, but the surface oxides were not completely removed, Figure 3.2.3.5 to Figure 3.2.3.7. The surface at 10 seconds dwell appeared to be the least contaminated and the cleanest in terms of removed scale.

Comparison of the composite cross-sections showed that at the longest dwell times the surface roughness appeared to lessen, however, this was not confirmed by profilometry results. Since dwell time did not affect surface roughness, to minimize surface contamination the shortest time was used. With a real rail, it may be contaminated with scale, grease, etc., so cleaning becomes more difficult than with a "new" surface. The extent of the rail contamination makes longer dwell times necessary and may lead to undesirable effects such as embedded grit or work hardening of the surface.

4.1.4. Tensile Testing

Tensile tests assessed the adhesion strength of coatings prepared using various grit blasting methods. The steel shot, 50/50 mixture and the two-stage process showed similar average coating bond strengths but varying ranges. The variations in the readings can be attributed to differences in plasma spraying and in the tensile test variability, which is about ± 5% as found in the "Glue Only" samples in Table 3.2.4.1. Using a greater number of tensile test samples would improve the results obtained.

The effect of post-grit blasting cleaning was evaluated by preparing two sets of samples with the same grit blasting media, one set was cleaned using standard methods and the second set was left unclean. As anticipated, the cleaned surface showed a higher coating adhesion over the unclean surface, Table 3.2.4.1. These results show the importance of eliminating the residual, loose grit blasting particles and debris from the surface prior to plasma spraying as the loose particles can reduce adhesion.

4.1.5 Amsler Testing

Cursory Amsler testing was done on roller samples prepared using different grit blast media and processes. While the results show a wide variability in the test duration, Table 3.2.5.1, the coefficient of friction was relatively constant. It is expected that the grit

blasting method would only affect the life of the coating and not its coefficient of friction. This is also shown by the results presented in Table 3.2.5.2 which show a consistent coefficient of friction for a given slide/roll ratio, but a wide difference in the test duration.

Amsler testing may not be the most ideal method of ranking surface preparation techniques due to the variability inherent in the process. For example, the coating sprayed onto the polished surface (400 grit SiC paper) had a higher coating durability than that of steel shot, Table 3.2.5.2. Some of the variability may be due to the thickness of the coatings, one factor that was difficult to control when spraying coatings at different times. Also the finish on the bottom roller has been variable and is suspected of causing premature coating failure. The stainless steel material used for these tests caused its own set of problems as discussed in further sections.

Previous researchers on this project have investigated other methods of surface preparation for plasma sprayed Amsler rollers, such as knurling, but found little to recommend [1]. This was due to the coarseness of the knurling and the smooth sides of the knurled regions that were difficult to roughen with other grit blasting techniques. More stringent preparation techniques that include a second grit blasting just prior to plasma spraying have also been tried and appeared successful. However, others have had good results without the second grit blasting. It is suspected that differences in the coating microstructure and variations in spraying techniques among individuals, plays a more important role in coating durability.

4.1.6 Summary

The above discussion has shown the difficulties in using various test methods to evaluate the effectiveness of different grit blasting techniques and in making comparisons between the different sets of data. The results obtained from this section can be summarized as follows:

1. Larger grit size produced a rougher surface as determined by the parameter R_a in surface profilometry tests.
2. The harder substrate produces a less rough surface as determined by the parameter R_a in surface profilometry tests.
3. The surface roughness was not sensitive to changes in impact angle.
4. While dwell time did not affect the parameter R_a, it did affect the cleanliness of the surface.
5. Tensile tests show that a clean surface provides better adhesion strength than an unclean surface.

Based on the work reported in this section, the two-stage process (alumina to clean the surface and steel shot to roughen the surface) was used for preparing full scale rail substrate samples for plasma spraying. Further, post-grit blasting cleaning was necessary to maximize coating adhesion.

4.2 PARAMETER OPTIMIZATION STUDY

Three types of spray parameter assessment techniques were used in this study prior to actual spraying onto Amsler test rollers. The parameter optimization methods varied with the coating system and substrate type. For stainless steel coatings, single splat analysis was used. In the case of co-sprayed composite steel coatings, a combination of single splat analysis, coupon verification and adhesion tensile testing was used. Full scale coatings were optimized using coupon verification. Single splat technique allows the assessment of individual splats while the coupon techniques allow assessment of multiple splat build-up. Each technique gives important but different information about spray coating development. The starting points for parameter optimization relied on work done by other investigators at the Oregon Graduate Institute on similar materials.

Single splat analysis is a technique that uses individual splat morphology to identify optimum plasma spraying parameters for a material. Characteristics such as size, shape, particle center condition, and size distribution give information on whether particle heating and velocity are at an optimum. The ideal splat has a flattened, rounded shape, is evenly spread out, and contains a filled center. Poor splat characteristics, including bounce-back of the molten material, missing particle centers, splat starring, and misshapen splats, directly affect the coatings properties and performance. For example, material that has bounced back causes protuberances that can break off when struck by incoming splats and thus form inclusions in the coating.

The technique is performed by passing glass slides rapidly through the plasma plume at the correct working distance and thereby collecting a thin layer of particles onto the slides. If the coating of particles is thin enough, the individual splats can be distinguished and their morphology analyzed as discussed above. Single splat analysis was a technique used by McMurchie [1], and fine tuned for plasma sprayed 1080 steel coatings for potential use in railroad applications as lubricant reservoirs.

Optical examination of the plasma sprayed glass slides using a stereomicroscope showed the characteristics of the sprayed particles for a specific set of parameters. Due to the larger depth of field for the stereomicroscope, coupled with the correct lighting technique and background, the three-dimensional nature of the splats, specifically the bounce-back, was easier to observe. Use of the stereomicroscope was key to this optimization method since it provided immediate feedback on a specific set of parameters. This is an advantage when parameters are first being developed since it removes the time-consuming step of sample preparation.

Coupon parametric assessment was made by plasma spraying the coating material onto a stationary flat coupon with a moving spray gun that traversed back and forth across the sample. The technique used a very simple sample geometry and fixturing set-up and allowed the coating build-up to be assessed. The disadvantage was that it took time not only to prepare the coating cross-sections necessary to evaluate the effectiveness of the parameters, but also to perform image analysis of coating features such as oxide content.

4.2.1 Lubricant-resistant Coatings (Stainless Steel)

The spray parameters developed by McMurchie [1], 230/30/225, were used as a starting point for this work on plasma sprayed stainless steel coatings, Table 3.1.1.1. The nitrogen and hydrogen levels were varied but the working distance was held constant during the tests. The 230 slpm nitrogen parameter set showed the presence of very small particles for each of the hydrogen levels, a factor which contributes to poor coating wear [1]. The 240 slpm nitrogen glass slides were an improvement over the 230 slpm nitrogen set since the splat size distribution was narrower and contained few small splats. The 240 slpm nitrogen/30 slpm hydrogen conditions showed the best splat morphology and size distribution, Figure 3.1.1.1 (a).

One way of confirming the optimum parameters is to bracket the upper and lower extremes of the optimum parameter envelope. For the lower end, a 235 slpm nitrogen and 35 slpm hydrogen parameter set was sprayed, however, this was found to be of poorer quality since it had a wider size distribution, Figure 3.1.1.1 (b). The 250 slpm nitrogen set, sprayed to find the upper limit, showed splats with a high degree of bounce-back indicating that the particle velocity was too great. The most ideal splat morphology and size distribution of the parameter trials occurred with the plasma spraying parameters of 240/30/225. Note that an increase in nitrogen from 230 to 240 slpm was the only parameter changed from those used by McMurchie.

Flat coupons were sprayed to verify the stainless steel parameters determined to be optimum by single splat analysis. Approximately 15 passes were made across each coupon to build up coating thickness. The substrate was not cooled since heat build-up was not severe due to the short spraying time. The optimized microstructure, Figure 3.1.1.2, consisted of a low porosity, two phase lamellar structure of stainless steel and oxide.

4.2.2 Hard Particle Containing Coatings (Composite Steel)

Hard particle containing coatings, also known as composite steel coatings, were made by co-spraying a base 1080 steel wire feedstock material with a secondary powder feedstock material. The secondary feedstock materials, investigated for their ability to increase friction, were stainless steel, titanium, silica and steel shot. Both single splat analysis and coupon verification were used to optimize plasma spraying parameters for this coating type.

Optimizing parameters for hard particle containing coatings was more complicated than those for a single feedstock material since both wire and powder feedstocks were sprayed simultaneously. The parameter optimization was further complicated due to the use of two wires to increase the rate of metal deposition. Parameter development for these

tests was based on prior steel plasma spray research at OGI [1, 2]. The initial parameters for optimization were 230/30/235, which were developed by Niebuhr [2] for his single wire and powder friction reduction work.

In the beginning stages of single splat parameter optimization, both powder and wire were sprayed simultaneously. This was ineffective since it was impossible to tell the wire particles from the powder particles when examined using only the stereomicroscope as there were no visible differences between the two types of particles. In addition, the number of powder particles was very small compared to steel wire particles so that the wire particles overwhelmed any contribution from the powder. Therefore only the powder was optimized using single splat analysis during subsequent tests.

Of the four candidate powder materials, stainless steel and titanium were selected for further testing. The ease of spraying was a major factor in this choice. The other powders, Fe shot and silica, were difficult to spray because of poor powder characteristics. Both the Fe shot and silica powders caused repeated jamming of the powder feeder. Analysis of the silica single splat slides showed pits in the slide surface from unmelted hard particles striking the glass surface. It is believed that the silica particles accelerated too fast and had no time to melt, due to their large size and low density. Left unmelted, silica particles would strike the surface and bounce back off rather than become embedded in the steel coating. In addition to poor spraying characteristics, a factor influencing the elimination of the Fe shot was the inability to easily discriminate it from the rest of the steel coating using microscopy. Since the stainless steel and titanium had good flow characteristics and were easily sprayed, further composite coating optimization focused on these two materials.

The next stage focused on optimizing carrier gas flow rates using single splat analysis, Table 3.1.2.1. Glass slides made for titanium and stainless steel powders showed a more diffuse and less dense coating of particles at the higher carrier gas flow rate of 42 slpm. The lower carrier gas flow rate of 14 slpm showed the particles more tightly concentrated in

the center of the slide. The tighter concentration is preferred since the particles stay in the center of the plume where the optimum heat and velocity transfer can occur. The lower carrier gas flow rate allows the particles to dwell longer in the plume and for more particles to enter the plasma stream.

Due to the inherent difficulties in optimizing two different feedstocks using single splat analysis, all further parameter optimization studies were performed by microstructural analysis of flat coupons and Amsler rollers sprayed with additions of either titanium or stainless steel to 1080 steel. No correlation was found between the amount of powder and the feed wheel type or powder feed rate, Table 3.1.2.2, so it was decided to use the high volume feed wheel and the low feed rate, to maximize the amount of powder and minimize jamming of the powder feed lines, respectively. Little difference was visible in the microstructures for the different parameter sets, Figures 3.1.2.1 through 3.1.2.4.

The powder spray parameters were further refined using tests run with varying powder injection point and gas parameters, Table 3.1.2.3. Both optical and scanning electron microscopy failed to distinguish between the powder phase and the matrix, Figure 3.1.2.5. Even in backscattered mode in the SEM it was difficult to identify the constituents due to the similarity in the average atomic number of the various materials of the coatings, Figures 3.1.2.6 and 3.1.2.7. Thus, it became necessary to use etching, not normally a technique used with plasma sprayed coatings. Due to the lamellar structure, etching generally obscures more information than it reveals. The etchant attacked the 1080 steel while leaving both the stainless and the titanium phases of the coatings unetched, Figures 3.1.2.8 and 3.1.2.9. Etching of sprayed samples enabled image analysis of the powder phase volume fraction to be performed more easily.

There was no trend apparent in the volume fraction of the second phase as a function of spray parameters or powder injector locations, Tables 3.1.2.4 and 3.1.2.5. Surface roughness was thought to be a quick indicator of the amount of powder phase in the coating,

as opposed to the more time-consuming metallographic examination. However, this did not turn out to be the case, since no significant change was found in surface roughness as the powder injection location varied, Tables 3.1.2.6 through 3.1.2.8.

Metallographic coupons used to verify the optimized powder spray parameters were found to have poor microstructures, Figure 3.1.2.7. High porosity and oxide content were found. Porosity can be a result of two different factors: particle pullout during sample preparation or incomplete particle melting during spraying. Porosity generally indicates that the parameters or sample preparation techniques are not optimized. High oxide content is the result of the interaction of the molten particles with the atmosphere through which they travel. The dual wire feed scheme appeared to exhibit higher oxide content in the microstructure than for single wire, possibly due to the greater disturbances in the plume by the two entry points. Coupled with the powder injector this would create even more problems.

Even though the powder feedstock spray parameters, optimized using the glass-slide technique and coupon verification, did not yield high quality sprayed coatings, they were still considered to be the optimum achievable spray parameters and, thus, were still used in co-spraying the composite coated Amsler rollers.

4.2.3 Tensile Tests

Maximum adhesion strength in a coating is desirable, as low cohesive/adhesive strength can lead to coating debonding and spalling. Tensile tests were another way to assess whether plasma spray parameters were optimized. The test matrix for the coatings examined two problems, viz., the effect of plasma spray parameters and the effect of second phase particles.

To examine the effect of spray parameters, samples were sprayed with 1080 steel at 230/30/235, 230/75/235, or 300/75/235, Table 3.1.3.1. Although the tensile test results appear to be different for the spray parameter sets, all tests failed at the coating/substrate interface, Figure 3.1.3.1. Further, considering the spread in the data, there appears to be no significant difference between the three sets. Thus, tensile testing may not be the most useful technique for determining optimum parameters, especially if surface preparation techniques are inadequate as well.

To test the effect of second phase additions on coating strength titanium and stainless steel powder were added to 1080 steel, Table 3.1.3.2. These tests also failed at the coating/substrate interface. However, the tensile strengths are much lower for all of these tests, compared to those described earlier. While detailed analysis was not performed to investigate the results, it is believed that the introduction of the hard particles at the interface are responsible for the low tensile strength of the coatings sprayed with the second phase. The poor results of these coatings cannot be attributed to poor substrate preparation techniques, because the strength is significantly lower (by half) than that for an as-grit blasted surface, i.e., not cleaned after grit blasting, Table 3.2.4.1.

4.2.4 Full Scale Tests

The first set of full scale tests were carried out on rails that were plasma sprayed using the parameters optimized using flat coupon verification and is reported in detail by Niebuhr [2]. These rails failed prematurely during testing. Metallographic examination of the initial full scale test samples had indicated that a poor microstructure was the most probable cause of premature failure. Further fine tuning of the spray parameters, Table 3.1.5.1 was undertaken as part of this and other concurrent research at OGI and is reported in greater detail by Niebuhr [2]. The results of the failure analysis of the initial full scale tests and the full scale tests run on rails sprayed with the re-optimized parameters are discussed in detail in Section 4.4.

4.2.5 Summary

A variety of techniques for parameter optimization are available, some of which work better for specific types of materials and spraying conditions. Parameter optimization is a complicated process, made even more difficult by introducing additional variables. Based on the above discussion, the results can be summarized as follows:

1. Multiple feedstocks and feedstock types complicate the optimization of plasma spraying parameters. The injection of more than one feedstock interrupts the plume, causing perturbations in the flow characteristics of the particles and leads to poor coating properties.
2. Operator variability has significant effect on the results obtained, due to the differences in spraying technique, even though the same procedures are followed.
3. It is difficult to characterize microstructures with multiple components unless there is optical contrast or significant atomic differences between them.
4. Tensile testing is time-consuming and ineffective as a method for optimizing parameters.

4.3 ROLLING/SLIDING WEAR TESTS USING THE AMSLER MACHINE

Past work by other researchers at OGI has shown the effectiveness of using the Amsler machine as a method of ranking the relative performance of monolithic materials for railroad applications, mainly rail steels [3-5]. Rolling contact fatigue, deformation and wear behavior of the rails can be duplicated on the Amsler by varying the different test parameters. This portion of the research focused on understanding the wear behavior of candidate materials for friction control before expensive and time-consuming full scale testing.

Prior to undertaking wear and friction assessment testing, two major steps needed to be completed. The first was the development of standard surface preparation techniques as discussed in Section 4.1 and the second was the development of nominal spraying parameters as discussed in Section 4.2. Next, a way of comparing plasma sprayed materials' coefficient of friction with their monolithic counterparts was required, and thus baseline friction studies were undertaken. Several plasma sprayed materials, and combinations of materials, were evaluated for their friction altering ability, including stainless steel, composite 1080 steel coatings, and stainless steel coated with nylon. The characteristics of coatings sprayed using a higher deposition, dual wire set-up were evaluated and the progression of wear-induced damage for plasma spray coatings was studied using interrupted testing.

4.3.1 Baseline Friction

One of the criteria used to evaluate the plasma sprayed coatings' success was the coating coefficient of friction when compared to the coefficient of friction for uncoated, monolithic steels. Prior to testing the plasma sprayed coatings, it was necessary to gain an understanding of the relationship between the coefficient of friction of uncoated, monolithic material rollers and coated rollers that were tested on the Amsler machine. This understanding was important prior to making quantitative comparisons of the coefficient of friction values for coatings, obtained in this work, to that of other researchers

at OGI and to results in the literature obtained using other test machines and methodologies. The baseline friction work done to measure the coefficient of friction for the uncoated, monolithic materials of interest in modifying friction is reported below.

The materials of interest initially in this research centered around single materials that showed hard to lubricate behavior. Traditionally, stainless steels and titanium have been considered "sticky" materials since they are hard to lubricate and have high coefficients of friction, under dry as well as water lubricated conditions. Typical rail and wheel steel materials were also tested on the Amsler following the same procedure to allow for direct comparison of data.

As can be seen from the test data, Table 3.3.1.2, the titanium self-mated pairs maintained approximately the same coefficient of friction regardless of the contact pressure and lubrication condition. For the titanium/wheel steel roller pairs, the friction coefficient tended to decrease with increasing contact pressures for both the dry and water lubricated tests. The lubrication condition appeared to have little effect on the titanium coefficient of friction. While titanium was originally considered for plasma spraying, due to its high cost and the poor success of the stainless steel coatings (Section 4.3.2), other areas of focus were explored.

The stainless steel materials, Table 3.3.1.3, showed a change in behavior depending on the lubrication condition. For the self-mated roller pairs of 440C, a martensitic stainless steel, and the 308, an austenitic stainless steel, as well as the 1080 steel/308 stainless steel pairs, the friction coefficient ranged from 0.10 to 0.16 during dry Amsler testing. For the tests under dry conditions, the contact pressure appears to have little effect on the value of the friction coefficients. Under water lubrication, the coefficient of friction was higher than under dry conditions and the friction coefficient increased as contact pressure increased. The variations in the friction coefficient for lubricated stainless steels may have been the result of the film formation on the roller surfaces, Figure 3.3.1.1.

For the wheel and rail steel materials, Table 3.3.1.4, in all cases the lubricated tests had a lower coefficient of friction than the dry tests as expected. The water lubricated friction coefficients ranged from 0.26 to 0.29 and showed no trends relating to contact pressure and slide/roll ratios. For the dry tests, the friction coefficients showed a wider spread in values ranging from 0.43 to 0.60. This data is in agreement with the low end of the range in friction coefficients found by Danks [3] in Amsler tests for wheel/rail roller pairs under Type III wear [6] at the end of the roller's useful life. In general, the dry tests showed a trend toward lower friction values at lower contact pressures and lower slide/roll ratios.

For wheel/rail steel pairs tested at 35% slide/roll ratios under dry conditions, wear particles were formed and trapped between the rollers. The degree and speed that the material transfer occurred increased as the load increased. The transition to Type III wear occurred within a few revolutions after the start of the test. For the water lubricated tests at 35% slide/roll ratios, oxide film formation occurred irrespective of the load levels. The coefficient of friction for these tests was fairly constant for the various loads and slide/roll ratios.

4.3.2 Lubricant-resistant Coatings

To study the effects of slide/roll ratio and contact pressure on coating durability and friction coefficient for the stainless steel plasma sprayed coatings, adequate test durations were necessary in order to obtain the coefficient of friction under steady state conditions. The first tests performed failed too early to obtain steady state conditions. The initial Amsler tests started with slide/roll ratios of 35% and contact pressures of 1220 MPa, the standard Amsler test parameters used by McMurchie [1]. Early failure prompted decreasing the slide/roll ratio to 5% and the contact pressure to 900 MPa in order to try to obtain the steady state conditions necessary to find the friction coefficient.

Of the various combinations of test parameters used, Table 3.3.2.1, those tests having high contact pressures and high slide/roll ratios had the highest friction and the highest wear rates. For these tests, Table 4.3.2.1, the average value of the friction coefficient was 0.54 while the average wear rate was 9,430 μg/mm/m. In comparison, the baseline friction values for 308/wheel steel pairs were found to be 0.10 to 0.16. One possible reason for this, based on observation during testing, is that the rough surface of the plasma sprayed coating imprints the surface roughness features into the mated bottom roller during wear-in of the coating. The small protuberances of the coating break off and become embedded in the bottom roller surface. As the test progresses the stainless steel particles, being "sticky," act to pull off more of the coating lamellae until material transfers back and forth in larger and larger patches until the coating fails.

The tests performed at low slide/roll ratios and low contact pressures showed better performance than tests at high slide/roll ratios and high contact pressures. The data for these tests shows reduced friction coefficients and wear rates, Table 4.3.2.2. In addition, the combination of low contact pressure with high slide/roll ratio performed similarly to the higher contact pressure and slide/roll ratios. Comparing these results with those in Table 4.3.2.1 shows that the slide/roll ratio has a more significant effect on the coatings' test performance than does the contact pressure.

Based on the results of the tests described above, the test parameters of 1220 MPa and 5% slide/roll ratio were selected for all further testing of stainless steel. These particular test conditions allowed the rollers to enter steady state wear and thus made it possible to obtain more accurate coefficients of friction and wear rate data. Thus the majority of the stainless steel coating tests were performed at the higher contact pressures and low slide/roll ratios. Data listed in Table 4.3.2.3 compares the coating durability under the low and high values of slide/roll ratio.

For some of the tests, the slide/roll ratio fell below the standard of 5% due to variation in coating thickness. Compared to the testing of monolithic steel rollers, which could be machined to an exact diameter, coating thickness and thus roller diameter, were more difficult to control. Consequently, the coating tests result in greater variability in slide/roll ratios compared to plain steel roller tests. Coating thickness variation effectively changes the ratio between the top (coated) roller and the bottom (uncoated) roller diameters, which affects the slide/roll ratio. Table 4.3.2.4 shows the results of the Amsler tests for these rollers. The contact pressures were 1220 MPa and the coating thickness was 1.5 mm or greater. The lower slide/roll ratios result in lower wear rates and longer test durations.

The effect of coating thickness on the coating wear performance was investigated as well. Table 4.3.2.5 shows the results of three Amsler roller tests performed to failure. The contact pressure in all cases was 1220 MPa. Results indicate that the thicker the coating, the higher the number of revolutions completed.

Tests on the effect of increased secondary gas flow rates showed inconclusive results. Table 4.3.2.6 shows the two higher hydrogen level tests compared with a low hydrogen level test. Since the bottom rollers initiated test shutdown for these tests before the coating failed (as discussed below), it is difficult to determine whether the data is accurate or not. For the case of test A022, which used two bottom rollers before testing was stopped, this is especially true. The deflection strip chart for A022 indicated that the steady state region was not attained before the bottom roller began to fail, Figure 4.3.1. The different slide/roll ratios complicate understanding the results. While the test duration for the 75 slpm hydrogen flow rate is an improvement over the other tests, the friction coefficient is lower.

Over the course of testing the stainless steel rollers, failure was found to occur in three ways: by debonding from the substrate, by formation of edge cracks, and by bottom roller failure, Figures 3.3.2.1 through 3.3.2.3. According to McMurchie [1], plasma sprayed coating debonding can be defined to occur as Type I and Type II debonding modes. (Type I

and Type II debonding modes are not to be confused with Type I and Type II wear modes as described by Bolton and Clayton [6].) Type I debonding was believed to occur as a result of poor substrate surface preparation prior to plasma spraying. The failure typically occurs at low test revolutions and the coating debonds as one piece that maintains the curvature of the substrate. McMurchie found debonding occurred at the coating/substrate interface. Type II debonding was defined to be the result of edge effects. Edge effects are cracks which form parallel to the outer edge of the coating in the overspray region. Because the overspray region is unsupported by the substrate, the cracking leads to material loss at the coating edge. As the test progresses the edge cracks form crack networks which propagate throughout the coating, contributing to coating failure. Type II debonding is observed in high revolution tests and is characterized by the coating debonding as a flat strip and by the formation of crack networks throughout the coating.

Separating the debonding into these two types was not clear cut for the stainless steel coatings. This is because most coatings failed early, less than a thousand revolutions, when compared to the successful 6000 revolution test defined by McMurchie. Initially it was assumed that the surface preparation prior to plasma spraying was inadequate and much time was spent in trying to correct the problem.

The edge effects in stainless steel coatings appear to be more a function of other factors, such as the slide/roll ratio and coating thickness. For example, in the 35% slide/roll ratio tests, edge effects were noted within the first few hundred revolutions. However, edge effects were not noted for the 5% slide/roll ratio tests which, in general, had longer test lives, although, seldom 6000 revolutions.

Failure of the bottom roller from extreme wear was the third defined failure category. The extreme wear of the bottom roller was characterized by faceting and a highly roughened surface, Figure 3.3.2.4. Testing was discontinued at the point that the Amsler machine vibration became too intense. In order to evaluate the contribution of the bottom roller to test

failures, the bottom roller was replaced periodically for one series of tests due to the belief that the overly roughened bottom roller surface contributed to coating failure. Tests were performed to investigate the effect of changing to a fresh bottom roller every 100 revolutions. Table 4.3.2.7 shows the results from these tests. It was found that the detrimental effects of material transfer of the stainless steel were slowed when the bottom roller was changed. When the bottom roller was not changed, the normal wear process, roughening of the roller surfaces followed by material transfer and wear debris creation, continued until failure either by debonding or bottom roller failure. The last bottom roller from test A013 was reused with a fresh, untested top roller coated with stainless steel and sprayed under the same conditions. For this test, the stainless steel coating lasted only 410 revolutions before debonding occurred.

From the tests using multiple bottom rollers, a typical sequence of wear was noted. During the first hundred revolutions, the bottom rollers would enter a wear process similar to that encountered in Type III wear [6]. (Note that Type III wear refers to the wear mechanism found in testing monolithic steel rollers, defined by Bolton and Clayton [6], not to the Type I & Type II coating debonding failures defined by McMurchie [1].) The surfaces became roughened and gouged from transfer of material from the top roller. After the bottom roller was changed, the surface of the top roller flattened out and became less roughened, however, some damage was imparted to the bottom roller, but of a finer nature than previously found. Subsequent bottom rollers showed slight decreases in surface roughening. Faceting was absent, as was edge deformation of the bottom roller.

The top and bottom rollers burnished within the first three or so roller changes. The bottom roller surfaces became brownish colored while the top roller surfaces became a shiny dark gray. Eventually, material transfer began but it started as a thin line, or a series of broken thin lines, which ran around the roller circumference. The roller transfer lines had the characteristic light gray matte appearance observed in previous coating tests. Gradually the

transfer line filled in and widened until the whole coating was roughened. From this point the wear process continued in the same manner as the single bottom roller tests. Figure 4.3.2 shows schematically how this occurred.

The tests performed using a single bottom roller showed some of the same wear process characteristics as the multiple bottom roller tests. The wear process of the stainless steel coatings tested at 1220 MPa and 5% slide/roll ratio followed a similar pattern, but one that was accelerated. Burnishing occurred in some cases but not always. If it occurred, the same material transfer line process took place. Edge cracks were noted in some cases before the coating delaminated. The wear rates, however, between the single and multiple bottom roller tests showed an order of magnitude difference with the multiple bottom roller tests exhibiting the lower wear rates.

The wear process for coatings tested at 1220 MPa and 35% slide/roll ratio was even more severe and accelerated. Severe edge deformation, edge effects and faceting were found within the first few hundred revolutions and the coatings failed very quickly. The wear rates were increased by two orders of magnitude over the multiple bottom roller tests.

Analysis was performed on the stainless steel Amsler test data for dry tests on as-sprayed rollers. Qualitatively, the results showed that the coating life was inversely proportional to the slide/roll ratio and contact pressure. Coating life was found to be directly proportional to coating thickness. It was not possible to simply relate coating life quantitatively to either the contact pressure, the slide/roll ratio or the coating thickness due to the wide variability of the test conditions. In order to study the overall trend of the coating life with respect to contact pressure, the slide/roll ratio, and coating thickness, a new parameter indicating coating longevity, L, was introduced where L is given by

$$L = \frac{t}{P_o \gamma} \times 10^7$$

where t is the coating thickness in mm, P_o is the contact pressure in MPa, and γ is the slide/roll ratio. Figure 4.3.3 shows a graph of L versus the number of revolutions to failure for the individual tests. Regression analysis for a linear relationship between the number of revolutions and L shows a value of $R^2 = 0.76$. Considering that the total number of tests was low and that a greater range of conditions is necessary to yield a better statistical analysis, this seems a reasonable result.

In order to determine the predictive ability of the model, the model was used to check the durability for three stainless steel tests (dry, ground flat), not included in the original analysis, Table 4.3.3.1. For the dry, ground flat data the model appears to predict the test duration with reasonable accuracy for two out of the three tests. The one case that is not accurate at predicting duration has a coefficient of friction below that of the other two, 0.31 compared to 0.41 and 0.44. For the water lubricated, as-sprayed stainless steel coatings, the model does not predict the durability well. These results indicate the limitations of the simple model for predicting durability across a wide range of test conditions. In order to get better predictability over a wider range of variables a more complicated model needs to be developed and a greater number of tests need to be run.

4.3.3 Hard Particle Co-sprayed Composite Steel Coatings

Composite steel coatings were investigated as a means of increasing the friction properties while still retaining the properties of a 1080 steel coating. The composite coating coefficient of friction results, Tables 3.3.3.1 and 3.3.3.2, showed a slight increase over the plain 1080 steel coatings that had an average coefficient of friction of 0.42 to 0.47. The 1080 steel/stainless steel coatings had a coefficient of friction ranging between 0.48 to 0.52 while the 1080 steel/titanium coatings ranged between 0.44 to 0.53. The effect of coating thickness on test duration was inconsistent for both types of coatings and there was no consistent relationship between coating life and the slide/roll ratio.

Failure of the composite 1080 steel/stainless steel coatings occurred by a process similar to that of the stainless steel coatings, Figure 4.3.1. The coatings showed material transfer from small to large circumferential line segments, Figure 3.3.3.1, and roughening of the bottom roller surface. In one case the test was inadvertently started without the load applied. It was noted that the material transfer process was delayed from occurring until the full load was applied. It is thought that work hardening of the surface occurred during the initial light-load portion of the test and this appeared to prevent the transfer of the coating from the top roller to the bottom roller. The coating durability was improved compared to coatings that were not apparently work hardened. An alternate explanation is that the surface protuberances of the stainless steel plasma sprayed coating "imprint" in the bottom roller surface, possibly becoming embedded as the plasma sprayed coating breaks-in to a smoother surface condition. This makes it easier for the splats to become pulled out and start the material transfer process. Examination of McMurchie's bottom rollers showed large amounts of oxides embedded in the surface of the roller.

The as-sprayed surfaces of the 1080 steel/titanium coatings were found to have a rougher surface appearance than normal. The roughness of the top roller surface caused scoring of the bottom roller surface during the first several revolutions of the rollers. Also noted on the top roller coatings were imprints of machining grooves from the bottom rollers. It was not possible to tell by visual inspection if material transfer had occurred. Failure of the coatings usually occurred during the first few hundred revolutions of the test.

4.3.4 1080 Steel Interrupted Tests

Interrupted testing of 1080 steel coatings was carried out to gain a better understanding of the progression of wear damage over the course of a test. Three different sets of 10 rollers each were sprayed. For each set, the average test duration was determined by testing three rollers to failure. Based on these average test durations, the remaining rollers

were tested to different percentages of the calculated average life, Table 3.3.4.1 through Table 3.3.4.3. On completion of the tests, microstructural evaluation of the cross-sectioned rollers sought to chart the progression of wear damage.

For Set 1, roller numbers 2, 6 and 10 were randomly chosen to define the average life. Compared to rollers 2 and 6, roller number 10 failed prematurely due to debonding. Consequently, the average test duration for this set was calculated based on the average duration from rollers 2 and 6; the test duration for roller 10 was redefined as 10% of the average test duration. If a roller failed prior to its originally scheduled percentage of the average test duration, it was re-designated with the actual percentage of the test duration. The average coating life for Set 1 was 2,410 revolutions (average of 2,560 and 2,260), for Set 2 was 1,560 revolutions (average of 1,780 and 1,340), and for Set 3 was 675 revolutions (average of 740, 620 and 670). As can be seen, the maximum coating durability for the three series varies widely. The variability between the three sets is more pronounced than the variability within each set.

One possible reason for the inconsistent test results may have been the variation of the machined surface finishes on the bottom rollers. While some of the rollers had smooth, machined finishes, others showed a rougher, smeared appearance. The poor surface finish of the bottom rollers may account for the amount of material transfer and the deep pitting lines noted on the worn bottom roller surfaces. Figures 4.3.4 (a) to (c) show the amount of wear on the bottom roller after interrupted testing. The tests with the lowest durability (260 revolutions) showed the heaviest wear with severe pits and gouges, whereas the test with the highest durability (2,260 revolutions) showed the least severe surface wear with few minor pits and gouges.

Coating thickness variation may also have played a role in the different test durations. Table 4.3.4.1 and Figure 4.3.5 give the coating thickness for the interrupted tests. The first set had a slightly higher coating thickness than the other two sets. Although the spray

parameters were held constant for all three sets, for the first set, the coatings were deposited in 70 passes within 4 minutes of spray time while the next two sets were deposited in 80 passes within 3.5 minutes of spray time.

The amount of change in coating thickness over the duration of the interrupted test was evaluated to see whether any differences existed between the sets. From the percent change in coating thickness it appears that there is no quantifiable relationship between durability and loss of coating thickness. However, qualitatively, with the exception of the I-1 series, the coating thickness decreases very slightly as the number of revolutions increase. This appears to indicate that either the test durations were too low to enter the steady state wear regime or that other mechanisms predominated during the tests.

Several other characteristics of the coatings, such as microhardness, microstructural features, Tables 3.3.4.9 through 3.3.4.16, and deformation depth, were evaluated to see whether any differences were evident. Table 4.3.4.2 shows the microhardness values for the tests arranged by increasing number of revolutions. The microhardness values for the different interrupted test series are very similar and do not appear to show any change with respect to the number of revolutions, Figure 4.3.6.

The deformation depth, Figure 4.3.7, seems to decrease slightly with increasing revolutions, with the exception of the I-1 series. Since deformation accumulates with each revolution, this result is contrary to expectations. However, wear mechanisms, which compete with deformation, depending on the test conditions would reduce the thickness of the coating. In addition, due to the lamellar structure of the coating, wear often occurs by spalling of large portions of the coating; consequently, the amount of measurable surface deformation could be inconsistent. Since the deformation depth is observed optically and measured based on the appearance of the deformed lamellae, it is possible that measurement error could contribute to the inconsistency.

Figures 4.3.8 through 4.3.13 shows the differences in the deformation found in the coatings for the I-3 set of rollers as the number of revolutions increased. In the first figure, at 70 revolutions, some deformation of the surface is visible as evidenced by the flow lines. Separation of the lamellae at the surface and cracking of the oxides can also be seen. For the next figure, at 170 revolutions, the amount of flow at the surface is more severe. Note that even within this small section of the coating, the depth of deformed material is not consistent. It can be seen that the oxides have started to crack into small particles and have become dispersed within the flow of the metal lamellae. The oxide cracking and dispersion has become even more pronounced at the 340 revolution test, Figure 4.3.10. Large cracks are beginning to appear along the deformation flow lines between the lamellae. In the next micrograph, Figure 4.3.11, at 510 revolutions, the metal lamellae are beginning to fragment and the oxides more finely divided and dispersed. The cracks are becoming deeper and more pronounced, and the lamellae at the surface are starting to separate leading to spalling of large portions of the lamellae. By 620 revolutions, Figure 4.3.12, the cracks have started to form networks that extend downward into the coating bulk and by 670 revolutions, Figure 4.3.13, the networks extend all the way to the interface resulting in coating debonding.

The oxides appear to act in a manner similar to the behavior of sulfide inclusions in monolithic steel in that they act as crack paths in the deformed layers. Figure 4.3.14 through Figure 4.3.16 show a series of oxide crack progression. The large region of oxide can be seen to have become cracked in Figure 4.3.14 but it is still intact, with no signs of deformation. For the higher revolutions, Figure 4.3.15, the oxides have started to disperse with the deformed metal lamellae. By the end of the life of the coating, Figure 4.3.16, the oxides are clearly along the crack propagation paths in the coating.

Since some of the tests failed prematurely, it seemed appropriate to check if any microstructural differences existed that might account for the early failures. The following graphs, Figures 4.3.17 (a) to (c), show the various microstructural constituents as a function of durability. There is no correlation to the number of revolutions for the area fractions of

the oxides, the metal content or the porosity. The rollers from each set were sprayed using the same conditions and thus the microstructures would be expected to be the same. However, none of the microstructural features examined showed any differences between the rollers in each of the sets.

In order to evaluate the progression of wear in the coatings, a wider range in the durability would have been helpful. Obtaining longer lifetimes and spreading out the number of revolutions between each percentage of a full test would have accentuated the differences and made the progression of wear easier to chart. Unfortunately, these tests ran very few cycles in general. If within these few cycles the progression of wear and different elements of the coatings that could have contributed to failure were obvious, it implies that the coating was of a very poor quality.

4.3.5 1080 Steel Dual Wire Tests

Dual wire sprayed coatings were undertaken to explore whether increased deposition rates could be obtained when transferring coating technology to rail using the high-rail concept vehicle proposed to spray rail in track. The results of the dual wire wear tests were disappointing when compared to the results for single wire spray coatings. The dual wire 1080 steel coatings, sprayed with 230/30/235, performed very poorly under dry conditions compared to McMurchie's test results, Table 4.3.5.1. Under water lubricated conditions, the dual wire 1080 steel coatings again performed very poorly, an average of 565 ±11 revolutions. Table 4.3.5.2 compares the results that McMurchie [1] obtained for single wire 1080 steel (plasma sprayed using 230/30/225) under water lubrication with those of the dual wire 1080 steel coatings. Niebuhr's [2] dual 1080 wire sprayed sample, in his 1080 steel/graphite coating work, fared better than the results from these tests. While the spraying parameters were the same, the injector positions for the dual wires were different. The wires in Niebuhr's work were located at 15 and 28 mm from the gun tip, while for this research, the wire injectors were at 15 mm at 45 degrees on opposite sides of the plume.

Note that in Niebuhr's work, graphite powder was simultaneously sprayed at 25 mm at 45 degrees; however, no graphite was found entrapped within the coating. Table 4.3.5.3 shows the results obtained by Niebuhr [2].

Complicated interactions occur in the plume when a second wire is introduced during the spraying process [2, 7]. While the same spray parameters were used in this research as well as in Niebuhr's, the wires were introduced in different manners and locations. A staggered approach appears to improve the wear quality of the coatings. Further improvements may be possible by re-optimizing the spray parameters specifically for dual wire 1080 steel coatings rather than using parameters developed for use with single wire coatings.

4.3.6 Stainless Steel/Nylon Coatings

Stainless steel/nylon coatings are two layer coatings, the first layer sprayed of stainless steel and the top layer of nylon. The nylon acts on the surface of the coating as a friction reducing agent that is in contact with the mating wear surface. Stainless steel was investigated as a primary coating for the application of a friction reducing nylon coating despite the poor wear characteristics shown in the previous sections. This was because stainless steel had a perceived advantage over 1080 steel in that the oxides were thought to be harder. Work from the previous sections has shown that oxides in steel contributed to poor durability of the 1080 steel coatings in rolling/sliding wear interrupted tests. Nylon had been previously plasma sprayed on 1080 steel plasma sprayed coatings for Amsler testing as a friction reduction coating [2].

Amsler test results, Table 3.3.6.1, show that the nylon coating enhanced the durability of the stainless steel coatings and also reduced the coefficient of friction from that of the plain stainless steel coatings. The average life of the nylon covered stainless steel coatings was 12,677 ± 719 revolutions compared to 288 ± 119 for stainless steel alone tested under

the same conditions (test numbers A001, A007 to A010). In some of the tests the nylon was slightly overheated during plasma spraying and appeared a darker brown color. For these tests, nylon on stainless steel showed an improvement at 4,073 ± 905 revolutions indicating that nylon is effective in increasing the stainless steel coating life even when improperly sprayed.

As discussed earlier, wear testing of the nylon coated stainless steel rollers showed a similar pattern of behavior as the plain stainless steel coating. During testing, a dark gray film formed on the top roller surface. At the point where the film broke down (shown by the formation of a shiny gray circumferential line on the roller surface) the wear trace showed a sudden increase in friction, Figure 3.3.6.1. For uncoated stainless steel the friction coefficient ranged from 0.2 to 0.6 during wear testing depending on the amount of material transfer that occurred. The nylon coating wore in a manner similar to that shown in Figure 4.3.2 for stainless steel. In the areas where the nylon had worn off in lines, the surface showed larger than normal, raised particles. As these areas became more pronounced the wear debris emanating from the surface, in the form of large particles, increased.

4.3.7 Summary

The main stumbling block in evaluating the effectiveness of various plasma sprayed coatings under rolling/sliding wear conditions was the premature failure of the coatings; in other words, the tests did not run long enough to show large enough differences as a function of the microstructure. The results obtained from this section can be summarized as follows:

1. Comparing the coefficient of friction of the plasma sprayed coatings to solid, monolithic materials allowed improvements in the coefficient of friction to be ascertained.
2. The coefficient of friction for the stainless steel plasma sprayed coatings was much higher than for the solid stainless steel rollers (mated with wheel steel bottom rollers). This is most likely due to differences in the damage mechanisms in the two cases. On the other hand, the coefficient of friction for the 1080 steel plasma sprayed coatings was slightly lower (~0.45) than for the monolithic wheel/rail pairs (~0.56).
3. During Amsler wear testing, the 1080 steel plasma sprayed coatings deformed, leading to crack networks followed by spalling of the coatings and finally debonding.
4. The addition of nylon on top of stainless steel plasma sprayed coatings improves the durability of the coating. The coefficient of friction for the stainless steel coatings was reduced by the addition of nylon (from ~0.54 to ~0.16). With nylon, the coefficient of friction for stainless steel was very similar to that for monolithic stainless steel mated with wheel steel.
5. Qualitatively, for stainless steel plasma sprayed coatings, the durability of the coatings is directly proportional to the coating thickness and inversely proportional to the slide/roll ratio and contact pressure. The life of the coating can be estimated by a single parameter, L, which combines the effects of the variables mentioned previously.

4.4 FULL SCALE TEST FAILURE ANALYSIS

4.4.1 Coating Microstructure

A plasma sprayed coating consists of several constituents, all of which make up the lamellar structure of the coating, Figure 1.12. The constituents of the coating can be varied to tailor the microstructure to the specific use intended for the coating. Plasma sprayed coatings consist of melted and partially melted particles, unmelted particles, oxidized particles, voids or porosity, and inclusions. Generally, the amount of porosity, unmelted particles, and inclusions should be kept to a minimum for good coating properties. In some coatings oxides can act as a weak link in the coating strength by providing a crack path. The characteristics of a good wear coating are that it should be homogeneous, adhere to the substrate, be durable, and exhibit the necessary wear behavior.

One thing that became apparent, as the failed full scale samples were examined, was that, in most cases, the microstructures of the coatings did not meet expectations. The full scale microstructure contained high amounts of oxide bands, unmelted particles, inclusions, porosity and/or pullout and interface contamination—all detrimental to coating durability. Table 4.4.1 shows an overview of the features found in the various full scale test samples. Especially for the early coatings, it was found that the microstructure was very heterogeneous. The most striking feature of the coatings was the high concentration of oxides in the coating. Regions of extreme oxide banding were found in TL1, TL2 and RL1 and this banding became more severe the farther from the rail centerline. After the condition of these early samples was evaluated, parameters were re-optimized to correct the heterogeneous microstructure. The re-optimization yielded a slight improvement in the degree of oxide banding; instead of bands, the oxides tended to be clumped or grouped. The degree of oxide heterogeneity at the outer extremes of the coating was still more severe than at the center of the coating near the rail centerline.

Besides oxides, other constituents of the coating were found to be problematic such as the high number of inclusion particles. Both metal and oxide inclusions were found in the various full scale sample coatings. Inclusions in these coatings are thought to be the result of bounce-back or splashing of the molten metal or oxidized particles as they strike the surface with too much velocity. Also the sizes of the metal lamellae tended to be non-uniform, sometimes with very large metal lamellae and very small ones.

One of the main requirements for a rail coating was its ability to withstand rail wear for a long enough period, between 10 to 25 MGT, to make it financially feasible before re-coating of the rail was required [8]. Debonding, which indicates poor adherence to the surface, was a serious problem during the full scale tests. The earlier full scale tests (TL1, TL2 and RL1) had shown large scale debonding of the coatings during testing. Since cleanliness and roughness of the coating interface was believed to be a primary factor in coating adherence, an examination of the interfaces between the coating and the substrate was undertaken.

Interface cleanliness was found to be poor for the full scale coatings due to alumina contamination at the coating/substrate interface. Much time was spent in trying to optimize the surface preparation techniques for both the Amsler rollers and the full scale tests. Surface roughening and cleaning for the early samples used alumina grit blasting followed by the acetone rinse and drying with a blast of compressed air. After large scale spalling was found for the tested samples, the surface preparation techniques were re-optimized. The result of which was a new procedure of grit blasting with alumina first, followed by steel shot next, with the same post-grit blasting cleaning process. The alumina was used first because of its ability to better clean the wide variety of surface grit, scale, and other contaminants found on the full scale samples, especially when the rail was used. The steel shot followed the alumina to maximize coating roughness. McMurchie had very good success with his technique of using steel shot on Amsler rollers, however, Amsler rollers had machined

surfaces, clean from all debris with the exception of machining oils. Since the intent of the project was to spray rails in the field, a way of cleaning that would remove a variety of contamination from the rail was required and the two-stage process was very successful.

One problem with the grit blasting procedure was that it was performed by hand. When the sample is a small Amsler roller, Figure 2.11, grit blasting by hand is much easier than with a larger sample. When the sample size gets larger, it gets difficult to maintain a uniform surface preparation technique. For one thing, getting a uniform coverage over the complete surface is difficult. At OGI, Amsler rollers are placed in a suction type blast cabinet and subjected to grit blasting using a hand operated nozzle. For the 60 to 90 cm rail samples, the cabinet was still usable by blasting first one end, then turning it and doing the other end. However, when the sample was greater than this size, like the FAST rail, which was a 3.6 m rail, problems arose. A large portable spray booth that enclosed the rail and contained the grit was made and is shown in Figures 4.4.1.1 (a) and (b).

Using the spray cabinet, a section of the rail was blasted and then moved to another section. Because of the size of the rail it was time-consuming and tedious work. In addition, it was very difficult to judge the consistency and quality of the grit blasting when the portable booth was on the rail. This made it difficult to know when to move from an area or even where the blasting was done due to the inability to see with all the grit dust inside the booth. In addition the complete rail had to be grit blasted twice, first with alumina to clean the surface and then with steel shot to roughen the surface. In light of this, it is easy to understand why alumina contamination at the interface of the full scale coatings was a problem. Effective, uniform cleaning of the substrate (by grit blast) is extremely difficult by hand operation for the large full scale samples.

Compared to coatings sprayed onto small Amsler rollers, the microstructures for the full scale samples varied widely, much more than for Amsler test coatings. Image analysis of the full scale tests was not performed so there is no comparison of oxide volume fraction for

the Amsler tests. However, the microstructures of the Amsler coatings did not show the oxide banding prevalent in the full scale coatings, but rather the oxides were uniformly spread throughout the coatings. Porosity was also another area where the full scale coatings were inferior to the Amsler roller coatings. While it is difficult to determine exactly how much of the porosity found was related to sample preparation techniques, porosity was much higher for the full scale coatings. This may be simply a result of the higher oxide concentrations since more porosity was found in these regions. Porosity was also noted in the regions where oxide/metal inclusions were higher. While some oxide and metal inclusions were seen in the Amsler coatings, they were not as extensive as in the full scale coatings. A wider extreme in metal lamellae sizes also occurred.

When the early coatings showed poor durability under the load and slide/roll conditions they were subjected to in full scale tests, the focus switched to using nylon top coatings to reduce friction (as previously mentioned) and to prolong coating life. The thickness of the nylon was thought to have been between 30 to 50 μm, but, in reality, measurements found much thicker nylon than anticipated, Table 4.4.1. Only with the FAST rail was a sample found in the target thickness range. During the initial stages of the full scale testing, the nylon coating was found to either "bubble" or flake off. This was believed to be due to excess nylon being shed from the surface, but not the whole coating. Evidence from failure analysis supports this, since regions in some samples were found to have worn nylon embedded in the surface crevices adjacent to worn steel. Alternately, the nylon "bubbling" may have been an effect related to overheating while the sample underwent testing. Since so little coating remained in these samples, it is difficult to be sure what happened to the nylon in the more severely damaged regions of the coating over the course of the test. It is also difficult to say whether nylon actually extended coating life since the spraying parameters were different between the nylon coated samples and the samples without nylon coating, even though Amsler tests were found to extend coating life.

Similar types of damage were seen in the full scale test samples, as were seen in the interrupted Amsler test samples. There were two types of damage mechanisms at the surface of the worn coatings. In the presence of nylon, (TL3, TL4 and FAST samples), wear of the surface was noted. This was evidenced by the flat, even surface of the coatings in Figure 3.4.9.19. When nylon was not present, or the nylon coating was exhausted, deformation was visible in the surface layers of the coating, Figure 3.4.6.8. In the deformed areas, oxides were cracked and deformed with the metal lamellae. Crack networks and delamination were also found in these areas. These features are similar to those found in the interrupted Amsler test samples, although the extent was greater, possibly due to the more severe test conditions for the full scale tests. However, it is difficult to chart the progress of damage since the coatings were worn too far and no data was available for intermediate test durations. The limited tests carried out by Niebuhr indicated that a similar sequence of damage occurred for interrupted Amsler tests with nylon (on 1080 steel) coatings, Figures 4.4.1.2.

4.4.2 Thickness and Microhardness

Coating thickness for the full scale test plasma sprayed coatings evolved during the testing after thicker coatings were found to be unsatisfactory. The targeted coating thickness, Table 2.6, for the first tests was 1 mm of plasma sprayed 1080 steel. This thickness originated from initial 1080 steel Amsler roller test experience that targeted a 1mm thick coating. For a limited number of tests, McMurchie had found that there was no correlation between coating thickness ranging around 1 mm and coating durability. Because of the poor durability of the steel coatings in full scale testing, the focus changed to using nylon coated plasma sprayed steel as friction reduction coatings. Initial tests used 30 to 50 μm of nylon sprayed on 1 mm steel. Once again poor results indicated that a change in thickness was necessary. Subsequent full scale testing used a 500 μm base 1080 steel or 308 stainless steel coating which was coated with a second layer of 30 to 50 μm of nylon. As a result of Amsler

testing of nylon coated plasma sprayed steel rollers, it was believed that the thinner base coating led to increased durability due to a reduction in debonding [2]. The thickness was reduced even more by the time the FAST rail was sprayed at 250 μm.

One difficulty experienced in analyzing the results of the full scale tests was in determining whether the targeted coating thickness was obtained. This was thought to be important since comparisons between Amsler tests and full scale tests would be more valid. Since the only data available was from failed samples or wear debris, both worn and unworn regions from these samples were examined for coating thickness. Analysis of both the 8,700 and 18,723 cycle unworn TL4 wear debris samples showed a thickness of 140 μm and 55 μm, respectively, Table 4.4.2. This appears to indicate that the thickness varied at least by a factor of three depending on the location on the rail from where the sample originated. The data shows that the nylon thickness was at a minimum 2 to 3 times greater than projected for all the samples with the exception of the FAST rail. This excessive thickness may have been one reason that the sloughing off of the excess nylon occurred during the break-in period of both the full scale and Amsler testing.

When examining the data, one thing is apparent, the values of the unworn coating thickness are not consistent. One reason for this is that the ultimate thickness depends greatly on the experience of the spray operator. The operator who sprayed the first few samples had less experience than the operator who sprayed the later samples. Also, by design, the coatings were meant to be thinner on the side opposite the running track and gage face of the rail since it was believed that this would help prevent spalling. The problem with using wear debris as a failure analysis tool is that when coating spalled from the surface during the test and was later collected, the section of the rail it came from is not known. The best way to have control of the applied coating thickness is to control the spray process better.

The microhardness of the coatings was examined and it was found that, in general, the worn coatings showed a slightly higher hardness than the unworn. This would be expected since work hardening or deformation would lead to a harder coating. For comparison, 1080 steel microhardness values were around 370 HK_{500} for Amsler rollers [1]. Whether work hardening is an advantage or disadvantage is not known at this time.

4.4.3 Full Scale Test Problems

One of the questions that this project sought to answer was whether Amsler testing was an effective test method for ranking coatings prior to expensive and time-consuming full scale testing. The Amsler has been shown by others [3-5] to be successful for ranking monolithic steel materials. Amsler testing has been used by McMurchie [1] and Niebuhr [2] as a method of ranking various plasma sprayed materials and spray parameters.

In McMurchie's work several different factors such as wire type and diameter, coating surface treatments, and different spray parameters (parameter envelope study) were evaluated. Using the Amsler machine, the durability of coatings sprayed with the different parameters were ranked according to test length. McMurchie was able to achieve good wear results using 1.6 mm diameter weld wire. Niebuhr's work looked at adding various friction lowering second phases, i.e., copper and graphite, to coatings and then testing them on the Amsler. Here also the durability of the coatings ranked the performance of the materials. Durability was not good for coatings with the second phases. Investigating the wear damage process was not a priority compared to obtaining the friction coefficient and wear rate information. The interest was in obtaining a coating that worked, not in basic research into failure mechanisms since this was an application project.

Moving from the small scale Amsler tests to full scale tests created a variety of problems. Testing procedures led to problems in analyzing the data. Since the tests were run at a separate facility, there was little control on how or what information was collected during

the tests. The samples went out for testing and then returned for failure analysis. It is difficult to make sense of the two extremes in information without directly knowing what happened in between.

In some cases not all the tested samples were returned, only wear debris, Table 4.4.3. A cohesive picture is difficult to draw without the full series of samples. Additionally, due to project deadlines, the tests were run out of sequence. The problem this created was that all the tests were completed before the data could be analyzed in a sequential manner. Ideally a tested sample would have been returned, analyzed, and corrections made to the process, and then parameters re-evaluated. Unfortunately, after re-optimization the samples were sprayed as a group. The FAST rail was tested before the TL3 and TL4 samples could be analyzed. When the rolling load machine was upgraded to a newer piece of equipment, problems were encountered in setting and maintaining the required slide/roll ratio. New bearings in the equipment were stiff enough that the wheel "slid" versus rolled, due to the low initial friction of the coated surface.

Mislabeling of the data was another more serious problem. The worn samples for TL3 and TL4 came back labeled only with the markings "N-2" and "S-2" and no information was available as to which sample was designated with which label. By doing energy dispersive spectroscopy of the coatings it was determined that TL3 was the stainless steel sample and TL4 was the 1080 steel sample. Unfortunately, the data received at OGI did not note which set of wear data represented which sample. This alone would not be a problem, since assumptions could be made that the samples were kept straight when tested. However, additional uncertainty was introduced when the wear debris for the tests arrived at OGI labeled TL3 and TL4, and energy dispersive spectroscopy showed that the sample labeled TL3 was only plain steel, while the sample labeled TL4 was stainless steel. (When the samples were sent out from OGI, TL3 was supposed to be stainless steel, while TL4 was supposed to be plain steel.) If both the samples had performed equally well or poorly

then it wouldn't be such a concern. However, the data, Table 3.4.2, shows a sevenfold increase in durability for the TL3 sample over the TL4 sample. Yet it is still not known whether the stainless steel coating or the steel coating did better.

In addition to the lack of information on how the test was carried out, there was little coating left on the samples to analyze. All samples had little or no coating remaining on the wear surface, primarily due to the tests running to failure and even beyond. For both the TL3 and TL4 samples and FAST rail there were only very small flakes of worn coating remaining on the very edges of the wear track, and in most cases, partial debonding of these had occurred. When the coating has debonded it is hard to determine whether cracking and delamination were the result of wear or debonding. For an analysis of the wear mechanism to be performed there needs to be a reasonable amount of worn coating remaining intact on the wear surface.

Another problem was changing from a laboratory setting to a much larger, outdoor setting. The effect of the added variables introduced by the environment, i.e., moisture and, temperature, and dirt, grease and debris carried on the rail car wheels, on the full scale coatings is not known. Previous Amsler testing had shown poor results in water and lubrication studies. The wheels used were roughened and were most likely contaminated and these were transferred onto the sprayed coating during the test. In comparison, laboratory tested bottom rollers were clean, machined surfaces. In fact, unusual wear products that were found on some of the full scale coatings, embedded in the delaminated layers of the coating, appeared to be a finely divided metal product in a matrix material of unknown composition.

For these reasons, to perform a reasonable analysis, a progressive series of tests would need to be run, as in the case of monolithic rail materials where long term studies that chart the changes in hardness and wear profiles have been ongoing. The surfaces of the coating could be visually examined at periodic intervals and documented. Ideally, it would be desirable to have separate samples that could be removed from the test at various test

cycle intervals (like the interrupted tests). From these, cross-sections could be made, the microstructure examined and the progression of damage charted. Additionally, the wear debris could be collected in a systematic manner that precludes misidentification. The disadvantage of this scheme is that, while it would be nice, it would be very expensive and time-consuming. Therefore, a less expensive scheme would be to run the tests, but stop the test while the coating was still intact, with enough left for analysis to be performed on.

During the initial test, TL1, Figure 3.4.2, gross spalling of the coating occurred due to differences in the abrupt height of the coating from the substrate surface. Once large scale spalling damaged the coating, the coating continued to debond easily and thus reduced test durability. The early end of the test made it difficult to test the coating's ability to withstand wear or its ability to change the friction. As a consequence, all subsequent tests, Table 2.6, were feathered at the ends. Feathering was accomplished by reducing the number of spray passes at the ends as the coating thickness was built up. While TL2, Figure 3.4.3, was feathered at the ends, it can still be noted that spalling occurred near the outer edges of the coating, but not at the middle of the coating. It is possible that having feathered ends extended test duration of TL1 (abrupt ends), Table 3.4.2, from 0.12 MGT to 0.32 MGT but it is hard to know for sure. It may be important to have a better understanding of how the full scale test is affected by height differences between adjacent test samples and a better way to monitor the thickness of the ends.

For the rolling load samples, large scale spalling was a problem for all the samples, Table 3.4.1, however, it is hard to make comparisons since only one of the rolling load samples was returned. In the rolling load tests, spalling occurred in the center of the sample and it is unlikely that the edges played a role. More likely the spalling was due to set-up problems with the new rolling load equipment or the conditions under which the test was performed, Figure 2.1.4.

Another problem that occurred in the full scale testing was the use of a used rail for the FAST coating sample. Initially the rail was supposed to be a new rail. After metallographic samples were examined the rail was discovered to have cracking along the top and on one side. The effect of using a cracked substrate on coating durability is not known but it adds another variable to the analysis of the test data.

4.4.4 Spray Problems and Scaling Issues

Parameter optimization consumed much time and energy during the course of the entire "Friction Modification" research project. A great deal of effort went into the development of plasma spray parameters for the 1080 steel sprayed Amsler rollers [1] because parameter optimization for Amsler rollers had turned out to be more complicated than originally anticipated. The parameters developed during McMurchie's research were initially used for spraying the early full scale samples TL1, TL2 and RL1. After the poor test results of these samples and based on the failure analysis findings, parameters were re-optimized for spraying subsequent full scale coating samples.

The re-optimization study looked at a series of spray parameters (based on Amsler tests) that varied the gas parameters and working distance [2]. Rather than using the flat coupon substrate for re-optimization, the geometry of the rail was used, in this case a 5 cm thick section of the rail. These were sprayed in a manner similar to the full scale samples and were sprayed in three discrete rotation steps. The focus in evaluating the results was to change the microstructure in terms of porosity and oxide volume fraction since it was felt that lower oxide content would provide a more durable coating. Based on qualitative examination for these features, it was determined that a specific set of parameters, 230/75/235, was best.

One of the problems with looking for a specific set of features in the microstructure, i.e., oxides or porosity, is that it doesn't take into consideration the coating quality over the

whole rail geometry. With a uniform microstructure like that in the Amsler rollers, this would be sufficient; however, for the full scale coatings, it only gives a snapshot of a specific area of the coating, not the whole. For the rail coatings, in general, a low oxide content region could always be found by selecting the appropriate location on the sample. However, it is the heterogeneous regions with high oxide concentrations that weaken coating properties and thus wear resistance.

A re-examination of the parameter optimization samples showed a heterogeneous microstructure over the whole of the coating width, with the same kinds of features as the full scale samples. These included oxide bands and patches, large metal lamellae, inclusions, porosity, and unmelted particles. Some of the features that were found on the 230/75/235 parameter samples, which were used on later full scale samples, are shown in Figure 4.4.4.1. Examining the entire coating over the rail surface from left to right shows an heterogeneous microstructure and varying coating thickness. On the left side, the coating is thin, unmelted particles and oxide bands are directional towards the rail centerline. As the coating thickens, there are regions of high and low oxide content, in bands and patches. Across the top, the oxide concentrations decrease slightly as the coating thickness increases. Continuing farther, the oxide concentration increases as the coating thins. The coating structures on the sides are built up at a 45 degree angle to the substrate indicating that overspray coated these regions. Also noted was the high correlation between the porosity and the oxide banding/patches. It is very difficult to tell porosity from pullout due to sample preparation of plasma sprayed coatings but because of the brittle nature of the oxides pullout is very likely. Examination of the other (non-optimum) parameter set samples, showed greater oxide banding, porosity and heterogeneity in the microstructure.

While the extent of heterogeneity was similar to that found in the later samples (TL3, TL4, FAST), the fact that it is seen, even in the small, 5 cm sections indicates that parameter optimization for a complex geometry is not trivial. A more in-depth development program to scale up from the small, simple geometry of the Amsler rollers to the large, more

complex geometry of the rail type samples was necessary. The effect of a large heat sink on the coating parameters is another factor that should be considered and is not currently known. Unfortunately, at that point in the research project, there was not enough time to go into the depth of development that was spent on the Amsler parameter optimization. This was coupled with the fact that the complexity for optimizing the full scale sample parameters were not well understood at that point.

4.4.5 Manual Plasma Spraying and Specimen Geometry

Plasma spraying was performed manually for all the samples prepared during this project. The basic difference in the Amsler and full scale sample geometries necessitated different fixturing and spraying methods, Figures 2.4 (a), 2.7 and 4.4.5.1. This created problems with the microstructure of the coatings (Section 4.4.1). While the Amsler roller microstructure was homogeneous, the full scale samples were heterogeneous to varying degrees. The heterogeneous microstructure created a poor coating that did not perform well under full scale testing conditions.

For spraying the Amsler rollers, Figure 2.4 (a), a group of up to five rollers was placed on a graphite bar and attached to a chuck that rotated at 200 rpm. The plasma gun traversed back and forth at a fixed distance across the surface of the rotating rollers for a specific number of passes to build up the coating thickness. Consistency and repeatability of the traverse speed, which varied from operator to operator, created differences in the final coating thickness obtained and the quality of the coatings. For full scale samples, rolling load, track lab and rail, all were sprayed in a manner that was similar to each other but essentially different from the Amsler process.

The full scale process, Figure 2.7, consisted of attaching the sample/rail to a fixture that held the sample length perpendicular to the plasma jet at a specific working distance, Figure 4.4.5.1. The sample/rail remained stationary during spraying while the gun traversed

back and forth along the sample's length (from 0.6 to 3.6 m). At various times in the spraying, the position that the plasma plume contacted the substrate length was changed by hand rotating the sample position, so that coating contour was built up in sections along the sample/rail length. For the rolling load and track lab samples, three discrete rotation steps were used compared to five for the FAST rail. For example, the coating on the top portion of the rail was built up, then the sample rotated and coating built up along the side of the rail. Thus the build-up of the coating for the full scale samples occurred in strips rather than continuously like the Amsler rollers. These overlapping strips, with their regions of non-optimized coatings built up at the outer edges of the strip, appear to have caused the oxide bands.

One problem with the full scale samples' contour is that no matter where the surface is sprayed, non-optimized particles are going to strike the surface, Figure 4.4.5.2 (a). The optimum particle heating and acceleration occur in the center of the plasma plume, and those particles towards the outer edges of the plume are non-optimized. As the coating thickens, the non-optimized particles build up in the same location, one layer on top of another, creating a whole region with poor coating microstructure. This does not happen with the Amsler rollers since the total distance across the rollers is less than 10 cm (for 5 rollers) and the outer edges of the plume do not remain on the rollers as long during spraying, Figure 4.4.5.2 (b). Since the rollers are spinning at 200 rpm, any non-optimized particles are distributed randomly throughout the coating instead of concentrated in regions that weaken the coating structure.

It is believed that differences in individual spraying styles contributed to the poor microstructure as well. Microstructural examination of the full scale coatings found large regions of oxide banding in the first coatings sprayed as discussed previously (RL1, TL1, TL2). The individual who sprayed these early coatings, Table 4.4.2, while following correct spraying procedures, had little experience in plasma spraying and maintaining uniform

speeds. For the later samples (TL3, TL4), a more experienced operator sprayed the coatings using the same procedure. From the differences in individual spraying style, it appears a more uniform coating resulted with the more experienced operator.

The contour of the rail is one that is very difficult to spray, especially when using manual operation. The difficulty is in achieving a consistent, uniform, and repeatable sprayed coating. It appears that manually rotating the sample through 3 to 5 discrete steps [2], which basically sprays the coating in strips, doesn't produce a uniform microstructure. One way of dealing with the problems might be to continuously spin the rail about its axis during spraying. Some sort of an automated method may be preferable, especially since the spray process is affected by the skill of the spray operator. But this would have its drawbacks in safety concerns and by requiring increased fixturing due to the weight of the rail. Different facilities than the spray booth at OGI would also be required. Since only the top and gage face of the rail need to be sprayed, masking of the rest of the rail would be necessary. This would also not be practical for spraying track in service.

4.4.6 Summary

Compared to the time and effort spent in optimizing spray parameters for Amsler roller coatings, too little time was spent on the full scale test coatings. This fact became apparent during failure analysis of the early and re-optimized full scale test coatings. The results obtained from this section can be summarized as follows:

1. The full scale test sample microstructures were of a poor quality and extremely heterogeneous. Although an attempt was made to re-optimize the spraying parameters to improve coating properties, the resulting coatings did not perform much better than the early test samples.
2. The poor performance of the coatings after parameter re-optimization may be due to the fact that only a small section of the rail sample was examined during microstructural evaluation. Optimization of the parameters for full scale test samples needs to consider the quality of the coating over the entire surface sprayed; not just a small portion on the top of the specimen.
3. Compared to the 1080 steel Amsler roller microstructures, the full scale test microstructures were of a much lower quality.
4. The majority of the full scale test samples appeared to fail due to a complete debonding of the coating from the substrate. Contamination in the form of alumina particles, from the grit blasting operation, was found at the coating/substrate interface in all the samples examined, and is most likely a contributing factor to the debonding failure of the coatings.
5. The size of the full scale rail samples made it difficult for manual grit blasting to be effective in preparing the surface for plasma spraying.
6. The size and geometry of the full scale samples made it difficult to optimize parameters and obtain a consistently good coating over the entire surface of the sample. Further, the variations in operator technique and skill are more obvious in the spraying of the large full scale geometry.

7. Addition of nylon on the steel plasma sprayed coatings for friction reduction led to slightly improved test durability.
8. The thinner coatings appeared to last longer in the full scale tests. However, since the thinner coatings also had a layer of nylon on top of the steel coating, it is difficult to definitely state that the thinner coatings led to improved durability.
9. The laboratory scale Amsler test does not appear to be a good indicator of the performance of the coating in the full scale tests. This is primarily because the microstructures vary in going from a small scale Amsler roller to a large scale rail sample.
10. Having the full scale tests run by a third party led to lack of control over the actual testing (i.e., tests were run too long, very little coating was left on the samples) and data collection causing confusion in the results.

Table 4.3.2.1. Amsler results for high contact pressures and high slide/roll ratio.

Test No.	Contact Pressure (MPa)	Slide/Roll Ratio (%)	Friction Coefficient	Wear Rate (µg/mm/m)	Test Duration (revs.)
A009	1220	34	0.54	11391	326
A007 [1]	1220	33	0.54	10887	200
A010	1220	33	0.54	10086	471
A008 [1]	1220	33	0.54	5359	272

[1] Tests stopped when edge cracking occurred.

Table 4.3.2.2. Amsler results for low slide/roll ratio and low contact pressure.

Test No.	Contact Pressure (MPa)	Slide/Roll Ratio (%)	Friction Coefficient	Wear Rate (µg/mm/m)	Test Duration (revs.)
A004	900	5	0.33	156	2808
A005	900	36	0.54	4774	480

Table 4.3.2.3. Comparison of Amsler results for low and high values of slide/roll ratio.

Test No.	Contact Pressure (MPa)	Slide/Roll Ratio (%)	Friction Coefficient	Wear Rate (µg/mm/m)	Test Duration (revs.)
A006	1220	5	0.36	448	571
A018	1220	5	0.39	871	1141
A009	1220	34	0.54	11391	326
A007	1220	33	0.54	5359	200

Table 4.3.2.4. Amsler results for slide/roll ratios less than 5%.

Test No.	Contact Pressure (MPa)	Slide/Roll Ratio (%)	Friction Coefficient	Wear Rate (µg/mm/m)	Test Duration (revs.)
A011	1220	2	0.20	9	7554
A012	1220	2	0.31	116	9139
A019	1220	3	0.44	252	5734

Table 4.3.2.5. Amsler results showing effect of coating thickness.

Test No.	Thickness (mm)	Slide/Roll Ratio (%)	Friction Coefficient	Wear Rate (µg/mm/m)	Test Duration (revs.)
A015	0.38	9	0.44	1730	353
A006	0.87	5	0.36	448	571
A017	1.52	5	0.38	187	2763

Table 4.3.2.6. Amsler results for varied secondary gas levels of hydrogen.

Test No.	Hydrogen Level (slpm)	Slide/Roll Ratio (%)	Friction Coefficient	Wear Rate (µg/mm/m)	Test Duration (revs.)
A018	30	5	0.39	871	1141
A022*	60	6	0.43	1172	679 (1359)[1]
A023	75	6	0.31	442	4339

[1] Number in parenthesis indicate values obtained using second bottom roller.

Table 4.3.2.7. Amsler results for multiple bottom roller tests.

Test No.	No. of Bottom Rollers	Slide/Roll Ratio (%)	Friction Coefficient	Wear Rate (µg/mm/m)	Test Duration (revs.)
A013	9	7	0.26	7	915
A014	6	7	0.40	17	553
A016	6	9	0.17	31	553

Table 4.3.3.1. Verification of model for the parameter L, Po = 1220 MPa.

Test No.	Test Type	Friction Coefficient	Slide/Roll Ratio (%)	Thickness (mm)	Test Duration	
					Actual (revs.)	Predicted (revs.)
A002	308L Si - Dry ground flat	0.41	36.0	0.86	290	212
A023		0.31	6.4	1.3	4339	1803
A019		0.44	3.2	1.84	5734	5105
A038	308L Si – water as-sprayed	0.57	34.2	0.91	299	236
A036		0.32	7.6	0.85	4611	993
A037		0.35	7.5	0.86	13170	1018

Table 4.3.4.1. Coating thickness for interrupted tests.

Test No.	Durability (revs.)	% of Average Life	Thickness (μm)		
			Before Test	After Test	% Change
I1-10	260	10	560	414 ± 5	26.1%
I1-1	320	15	700	599 ± 12	14.4%
I1-3	570	25	670	475 ± 13	29.1%
I1-2	2560	100	660	524 ± 9	20.6%
I1-6	2260	100	560	427 ± 10	23.75%
I2-2	510	30	500	429 ± 12	14.2%
I2-6	600	40	490	404 ± 6	17.6%
I2-1	680	40	500	394 ± 9	21.2%
I2-7	970	60	480	339 ± 7	29.4%
I2-3	1780	100	450	339 ± 7	24.7%
I3-7	70	10	500	419 ± 11	16.2%
I3-6	170	25	500	356 ± 6	28.8%
I3-5	340	50	480	367 ± 9	23.5%
I3-4	510	75	470	359 ± 7	23.6%
I3-2	620	100	480	342 ± 5	28.8%
I3-3	670	100	480	334 ± 5	30.4%
I3-1	740	100	410	353 ± 7	13.9%

Table 4.3.4.2. Microhardness for interrupted tests.

Test No.	Durability (revs.)	% of Average Life	Hardness (HK_{300})
I1-10	260	10	439 ± 43
I1-1	320	15	428 ± 12
I1-3	570	25	427 ± 18
I1-2	2560	100	402 ± 20
I1-6	2260	100	439 ± 26
I2-2	510	30	423 ± 22
I2-6	600	40	442 ± 22
I2-1	680	40	461 ± 18
I2-7	970	60	446 ± 30
I2-3	1780	100	431 ± 46
I3-7	70	10	410 ± 62
I3-6	170	25	432 ± 67
I3-5	340	50	444 ± 40
I3-4	510	75	424 ± 34
I3-2	620	100	430 ± 22
I3-3	670	100	455 ± 21
I3-1	740	100	420 ± 23

Table 4.3.5.1. Comparison of dual versus single wire 1080 steel dry Amsler tests.

Test No.	Contact Pressure (MPa)	Slide/Roll Ratio	Friction Coefficient	Thickness (mm)	Test Duration (revs.)
AMST140 [1]	1220	37	--	0.61	6000
AMST129 [1]	1220	37	--	.067	2000
A043	1220	34.6	0.50	0.5	127
A044	1220	34.6	0.53	0.5	127

Table 4.3.5.2. Comparison of dual versus single wire1080 steel water lubricated Amsler tests.

Test No.	Contact Pressure (MPa)	Slide/Roll Ratio	Friction Coefficient	Thickness (mm)	Test Duration (revs.)
AMST174 [1]	1220	35	0.26	0.88	4890
A039	1220	6	0.22	0.64	700
A040	1220	6	0.23	0.65	440
A041	1220	5	0.22	1.32	520
A042	1220	5	0.21	1.27	600

Table 4.3.5.3. Comparison of dual wire 1080 steel dry Amsler tests [2].

Test No.	Contact Pressure (MPa)	Slide/Roll Ratio	Friction Coefficient	Thickness (mm)	Test Duration (revs.)
G23 #1	1220	4.56	0.46	0.98	3800 [1]
G20	1220	4.61	0.46	1.07	1000 [2]
G21 #1	1220	6.64	0.46	0.87	2100 [2]

[1] Coating debonded.
[2] Test terminated.

Table 4.4.1. Summary of microstructural features found in full scale samples.

Characteristic	Sample							
	RL1	RL2	RL4	TL1	TL2	TL3	TL4	FAST
Oxide cracking	✔	✔	✔	✔	✔	✔	✔	✔
Delamination	✔	✔	✔	✔	✔	✔	✔	✔
Unmelted particles	✔	✔	–	✔	✔	✔	✔	✔
Inclusions	✔	–	✔	✔	✔	✔	✔	✔
Porosity/pullout	✔	✔	✔	✔	✔	✔	✔	✔
Alumina contamination	✔	–	–	✔	✔	–	✔	✔
Height differential at ends	✔	–	–	✔	–	–	–	–
Coating spalling	✔	✔	–	✔	✔	–	–	–
Deformation	✔	–	–	–	✔	✔	✔	–
Heterogeneous –								
Oxide bands	✔	✔	✔	✔	✔	–	✔	–
Oxide patches	✔	–	✔	–	✔	✔	✔	✔
Spray operator	1	2	2	1	1	2	2	2

Table 4.4.2. Thickness and microhardness for full scale test samples.

Sample	Coating		Wear Debris		Nylon
	Thickness (μm)	Hardness (HK_{300})	Thickness (μm)	Hardness (HK_{300})	Thickness (μm)
RL1 – unworn	241 – 633	403 – 412			
RL1 – worn	454 – 510	445			
RL2 – unworn			719 – 963	352 – 376	144
RL2 – worn			72	386	N/A
RL4 – unworn			1092 – 1200	349 – 401	149
TL1 – unworn	209 – 436	357			
TL1 – worn	390 – 469	421 – 467			
TL2 – unworn	672 – 1235	339 – 382	582	375	
TL2 – worn	1047 – 1225	474 – 498	436 – 704	378 – 460	
TL3 – unworn	255 – 285	315 – 356	228	358	190
TL3 – worn	240	322 – 332	342	416	N/A
TL4 – unworn	165 – 188	363 – 385			136 – 142
TL4 – worn	176 – 252	418 – 452			N/A
TL4 – unworn (8,700 cycles)			460	306	140
TL4 – unworn (18,723 cycles)			390	N/A	55
TL4 – worn (18,723 cycles)			357 – 371	375	N/A
FAST – unworn	66 – 90	190 – 328	76	N/A	48
FAST - worn	66 – 123	248 – 318	82 – 103	254 – 334	N/A

Data is the range for averages of multiple samples.

Table 4.4.3. Summary of full scale samples received at OGI for analysis.

Samples Received	Sample								
	RL1	**RL2**	**RL4**	**RL5** [1]	**TL1**	**TL2**	**TL3**	**TL4**	**FAST**
Rail sample	✔				✔	✔	✔	✔	✔
Wear debris		✔	✔	✔		✔	✔	✔	✔

[1] For RL5 only nylon wear debris was received.

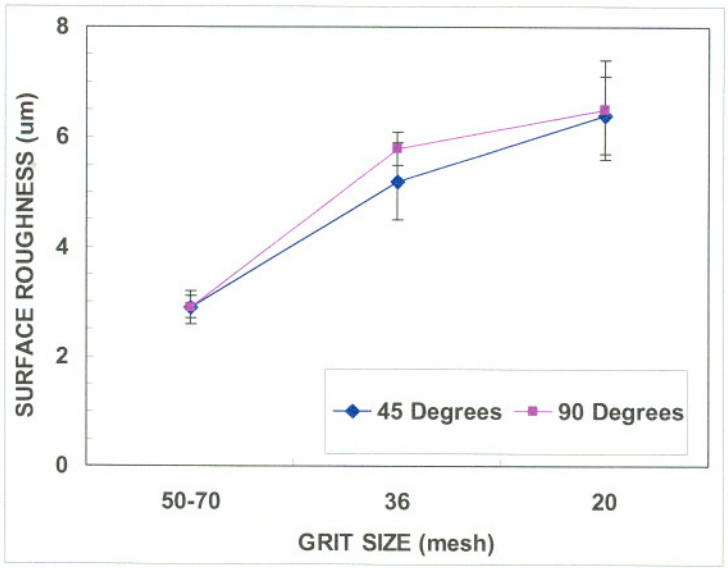

(a)

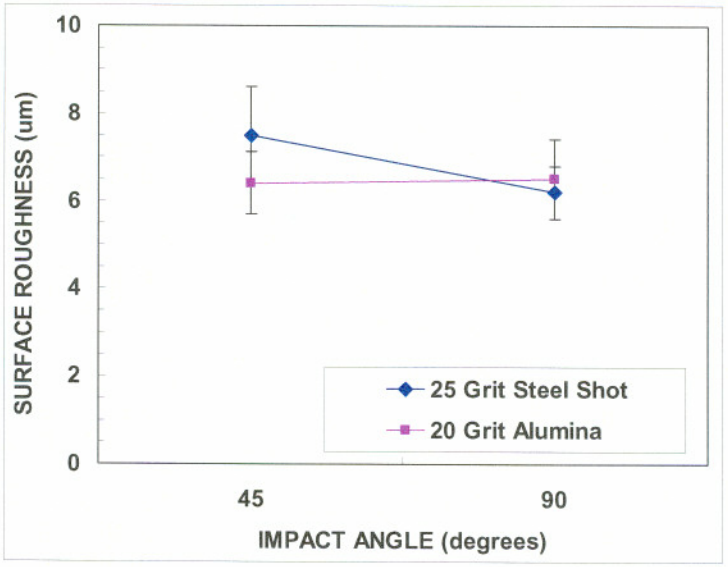

(b)

Figure 4.1.1. Graphs of (a) surface roughness vs. alumina grit size and (b) surface roughness vs. grit size for 25 grit steel shot and 20 grit alumina.

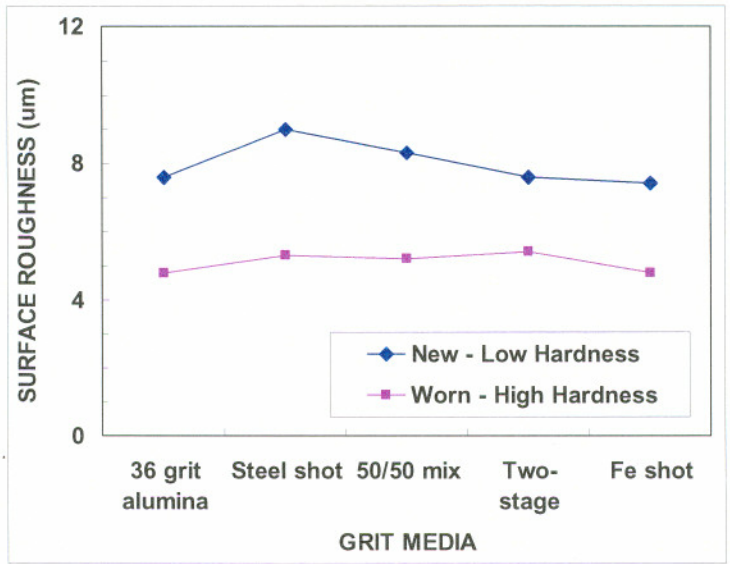

Figure 4.1.2. Surface roughness vs. grit media for two different substrates.

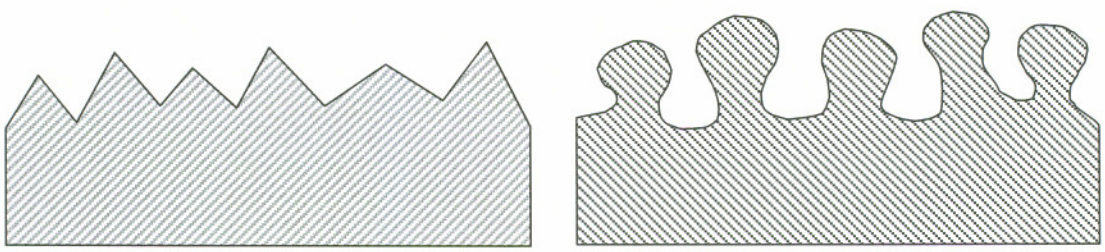

(a) (b)

Figure 4.1.3. Schematic of (a) grit blasted surface and (b) as-sprayed surface.

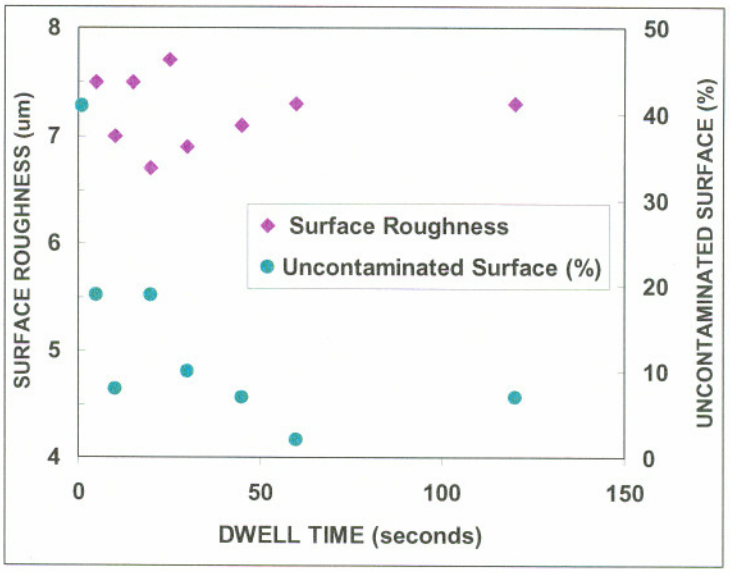

Figure 4.1.4. Surface roughness and percentage of uncontaminated surface vs. dwell time.

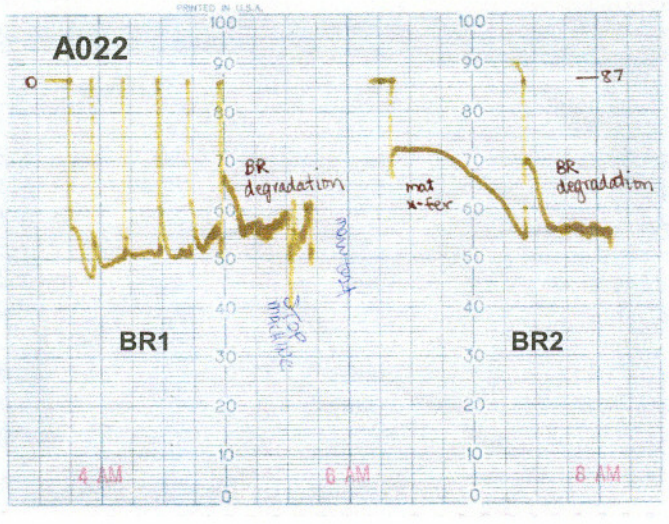

Figure 4.3.1. Amsler test friction trace for plasma sprayed stainless steel, test number A022.

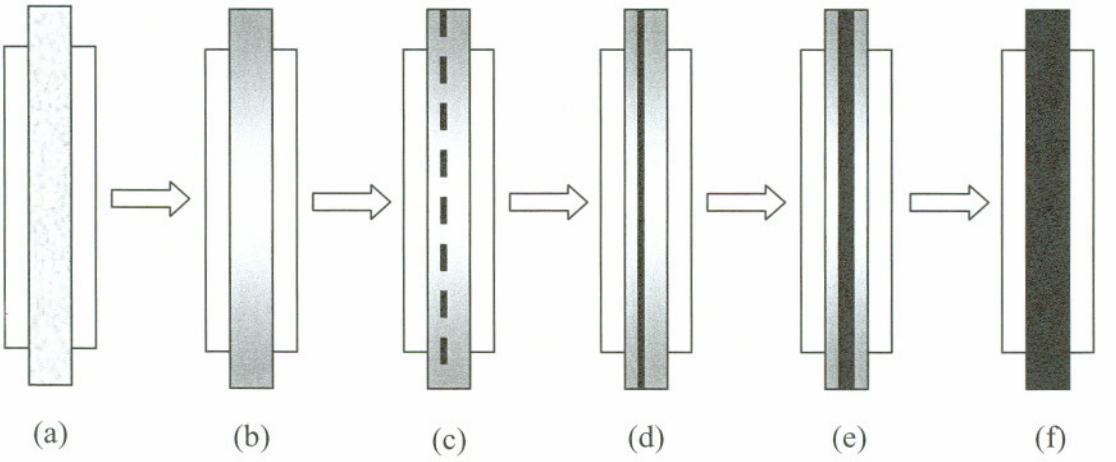

Figure 4.3.2. Typical wear sequence for stainless steel sprayed rollers during an Amsler test, (a) as-sprayed, (b) darkened, burnished surface, (c) broken line of material transfer, (d) solid line of material transfer, and (e) and (f) line widens until entire surface transfers material.

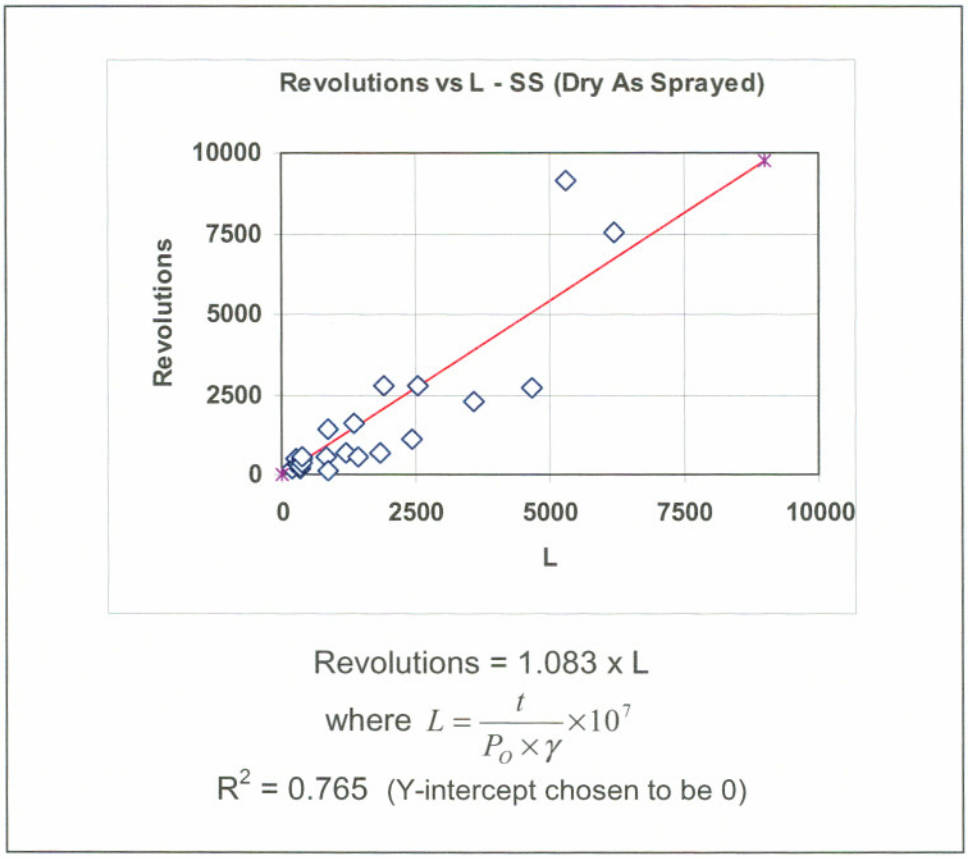

Figure 4.3.3. Graph of Amsler test durability vs. the parameter "L."

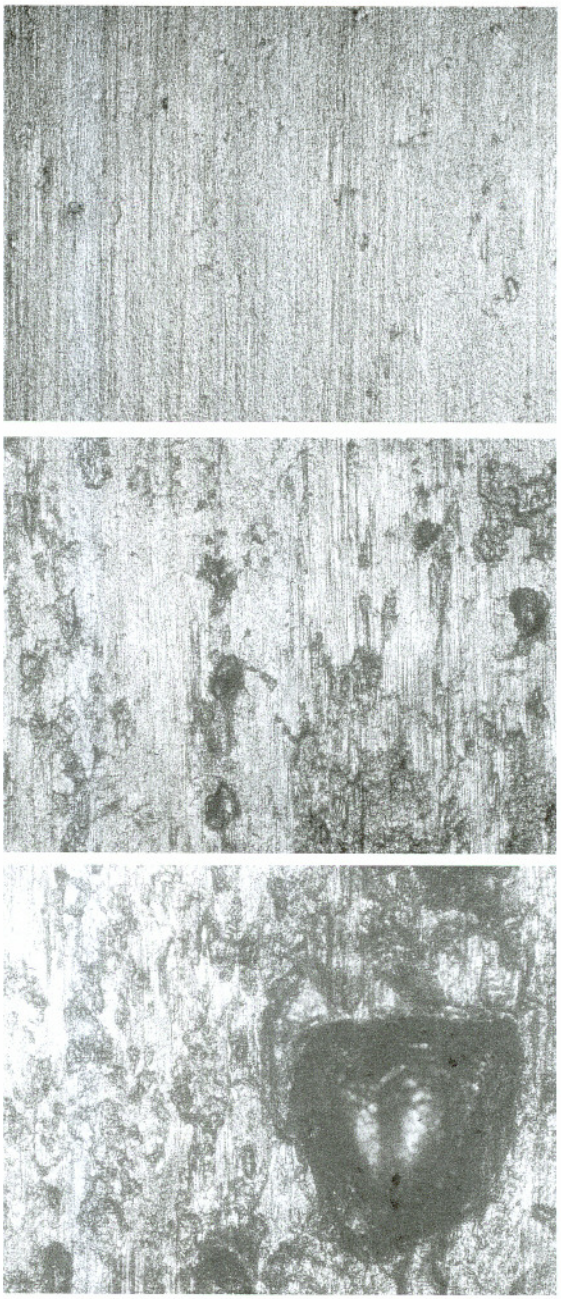

Figure 4.3.4. Appearance of bottom rollers after interrupted testing, (a) mild wear after 2,260 revolutions, (b) medium wear after 420 revolutions, and (c) severe wear after 260 revolutions.

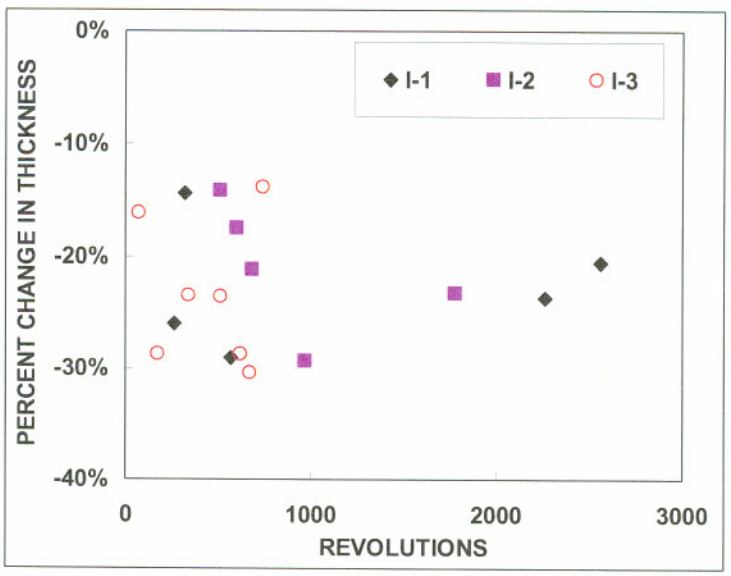

Figure 4.3.5. Change in coating thickness as a function of durability for interrupted tests.

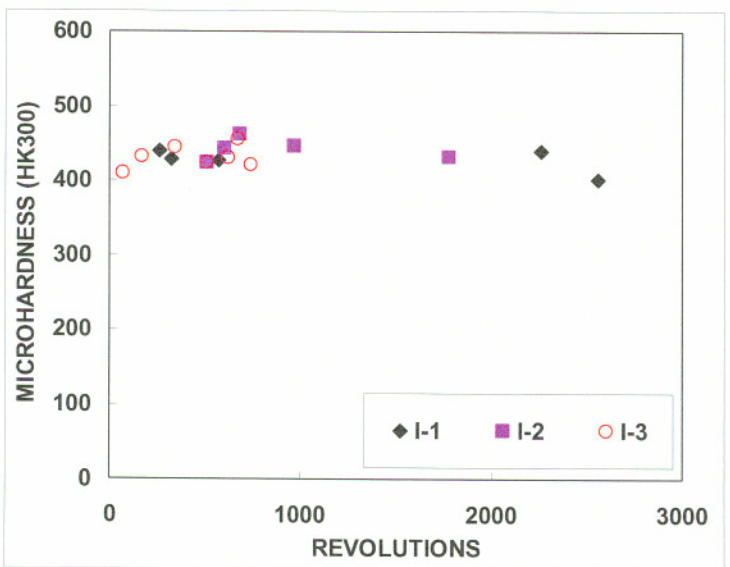

Figure 4.3.6. Microhardness as a function of durability for interrupted tests.

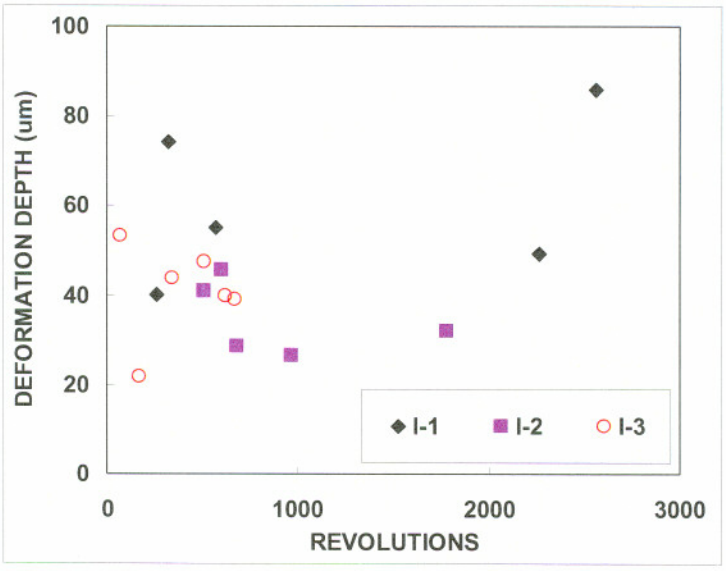

Figure 4.3.7. Deformation depth as a function of durability for interrupted tests.

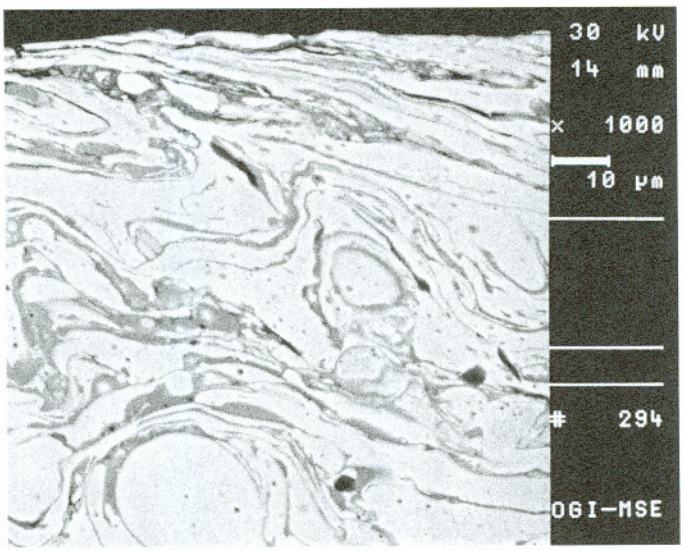

Figure 4.3.8. Appearance of surface for I3-7 at 70 revolutions. 1000x, backscattered electron image.

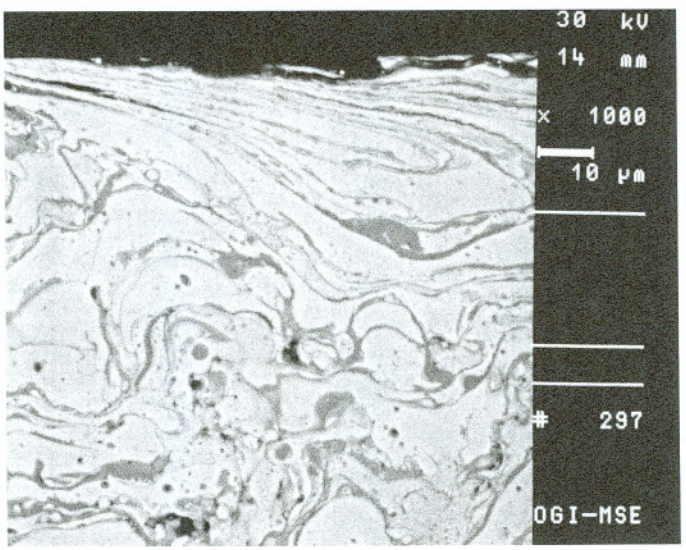

Figure 4.3.9. Appearance of surface for I3-6 at 170 revolutions. 1000x, backscattered electron image.

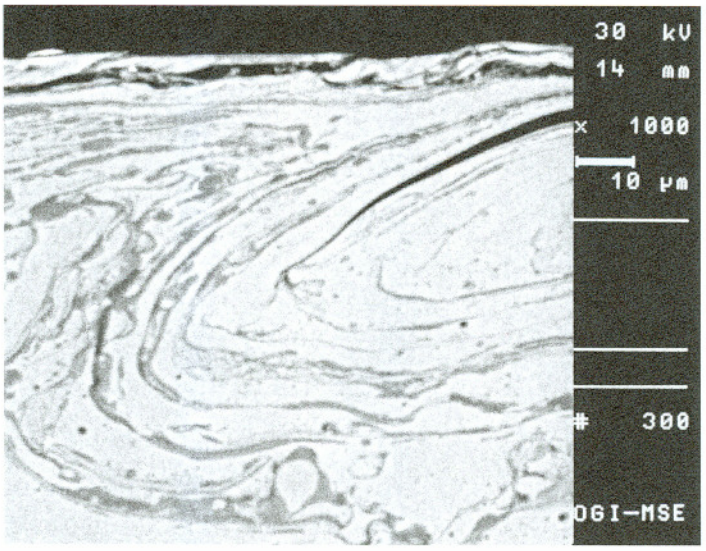

Figure 4.3.10. Appearance of surface for I3-5 at 340 revolutions. 1000x, backscattered electron image.

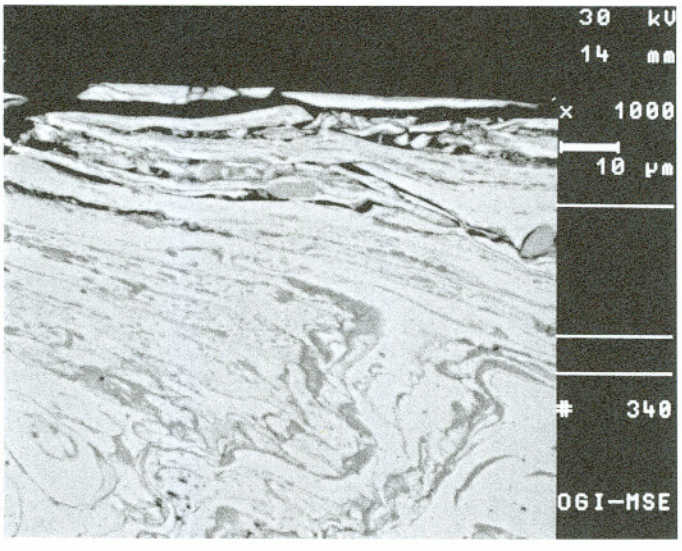

Figure 4.3.11. Appearance of surface for I3-4 at 510 revolutions. 1000x, backscattered electron image.

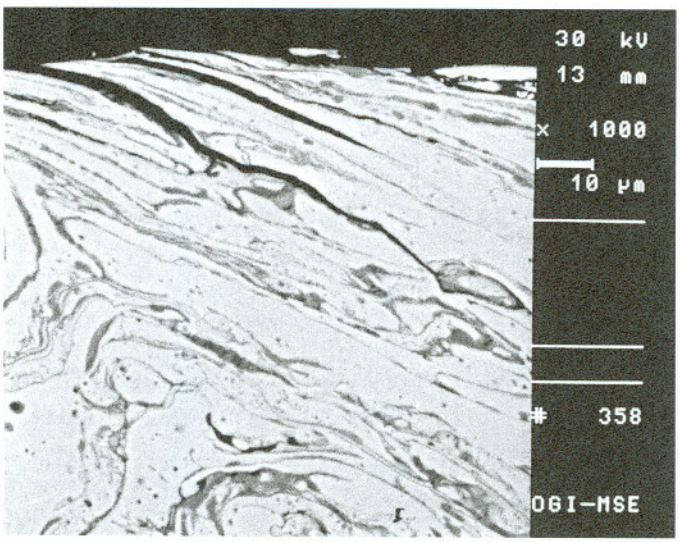

Figure 4.3.12. Appearance of surface for I3-2 at 620 revolutions. 1000x, backscattered electron image.

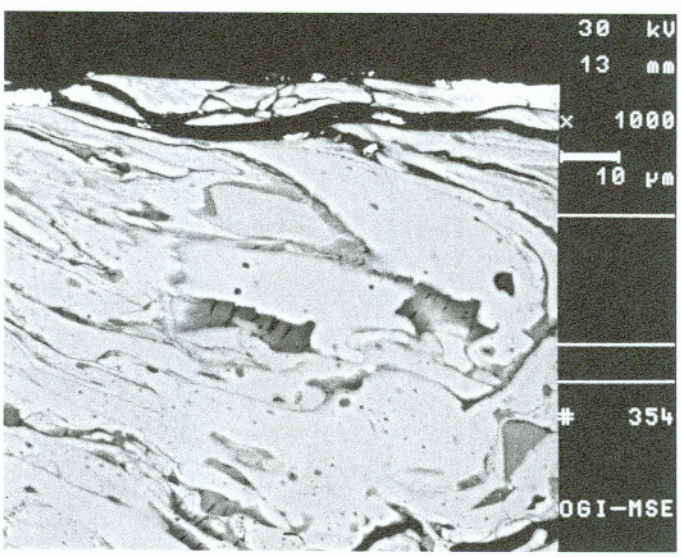

Figure 4.3.13. Appearance of surface for I3-3 at 670 revolutions. 1000x, backscattered electron image.

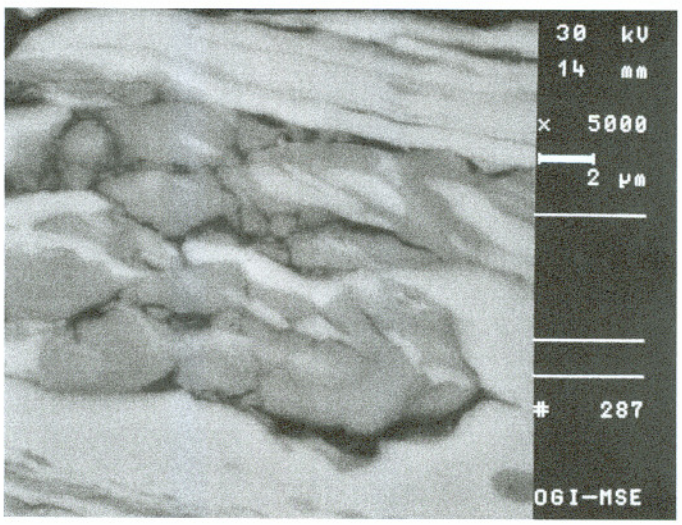

Figure 4.3.14. Appearance of oxides for I3-7 at 70 revolutions. 1000x, backscattered electron image.

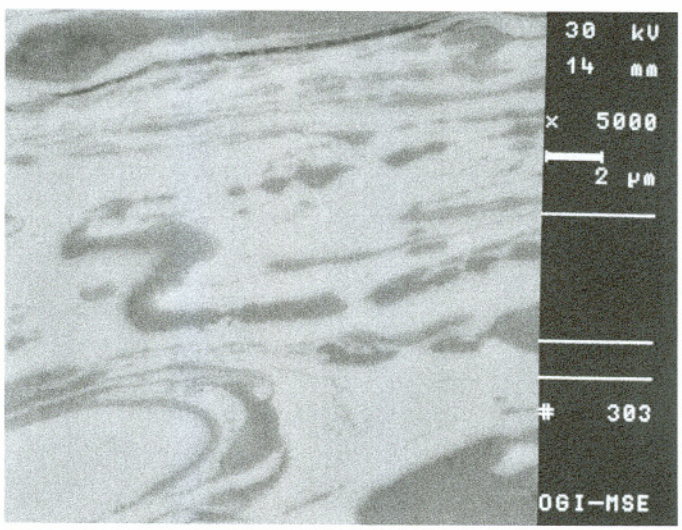

Figure 4.3.15. Appearance of oxides for I3-5 at 340 revolutions. 5000x, backscattered electron image.

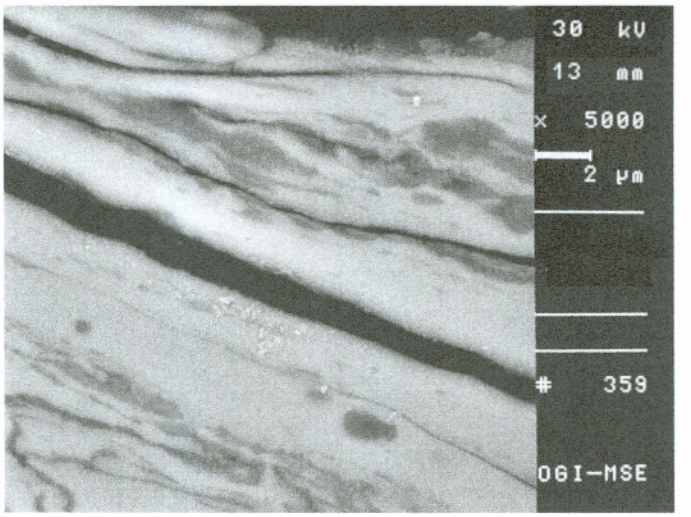

Figure 4.3.16. Appearance of oxides for I3-2 at 620 revolutions. 5000x, backscattered electron image.

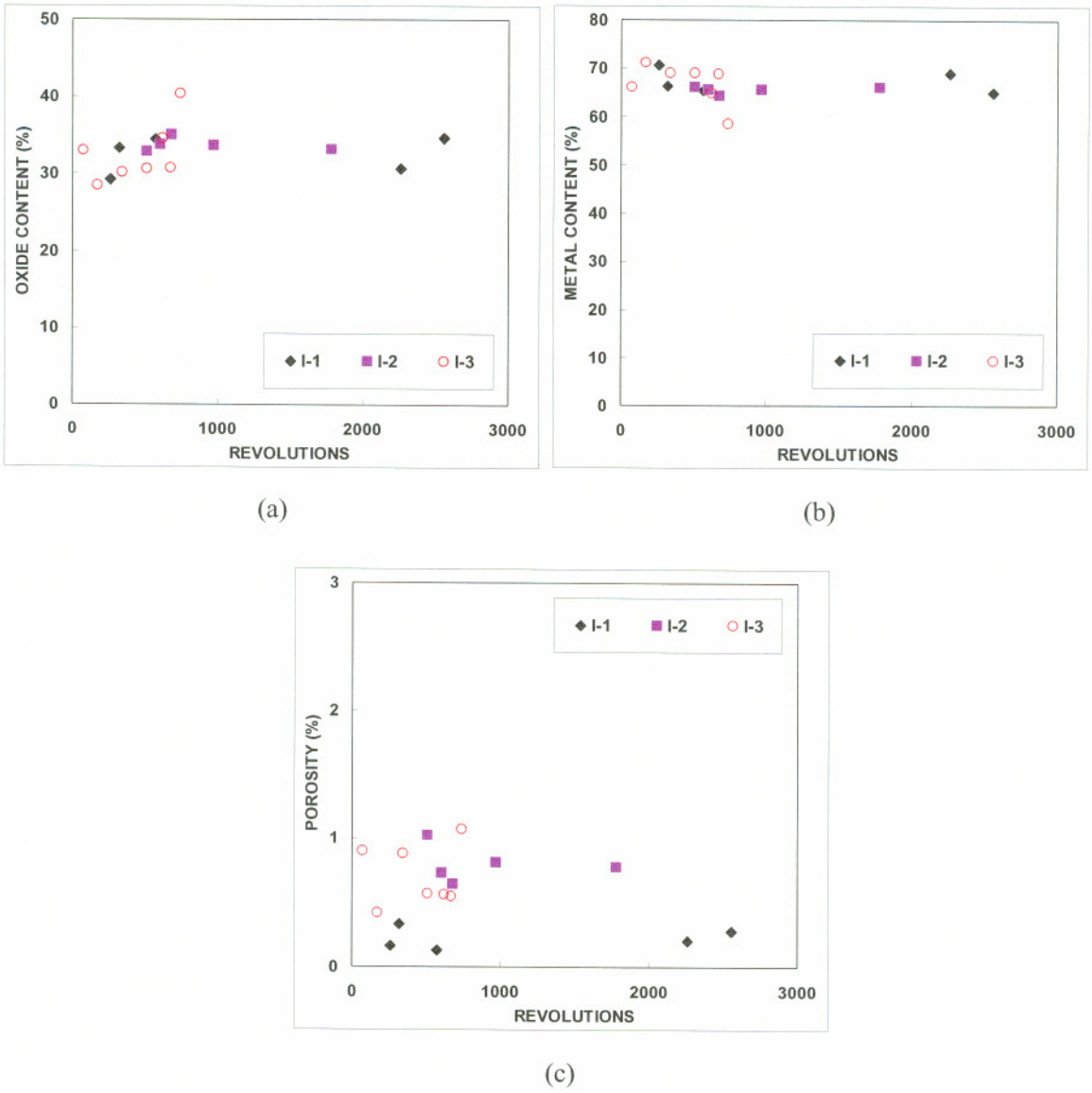

Figure 4.3.17. Various microstructural constituents as a function of durability for interrupted tests, (a) oxide content, (b) metal content and (c) porosity.

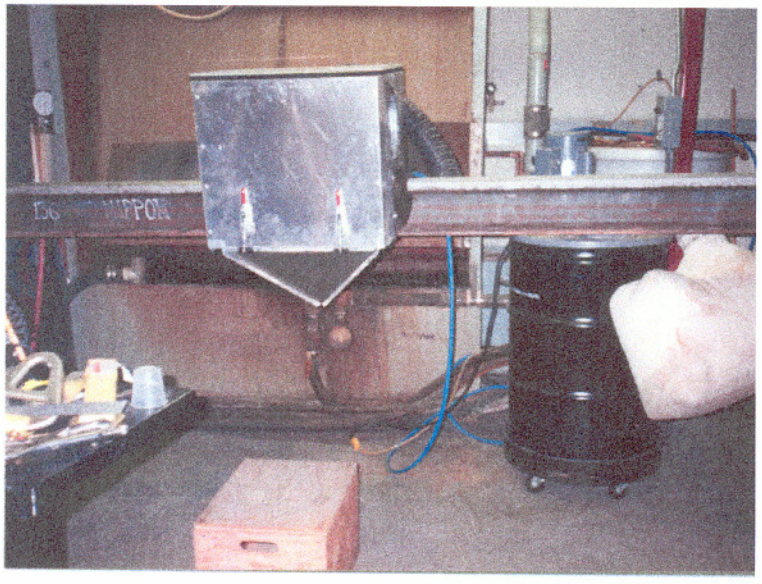

(a)

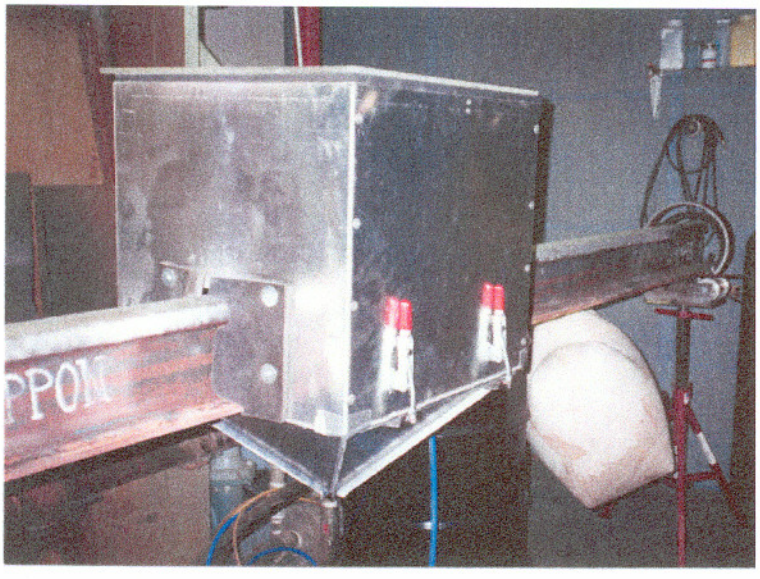

(b)

Figure 4.4.1.1. Portable grit blasting booth for cleaning large rails.

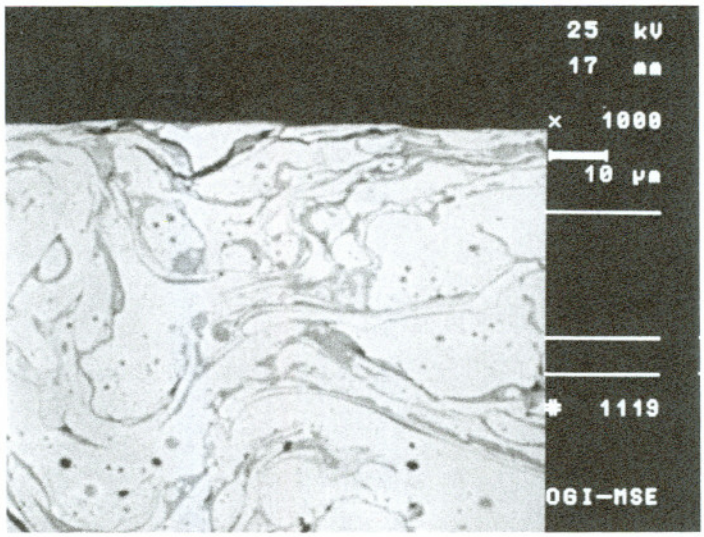

(a)

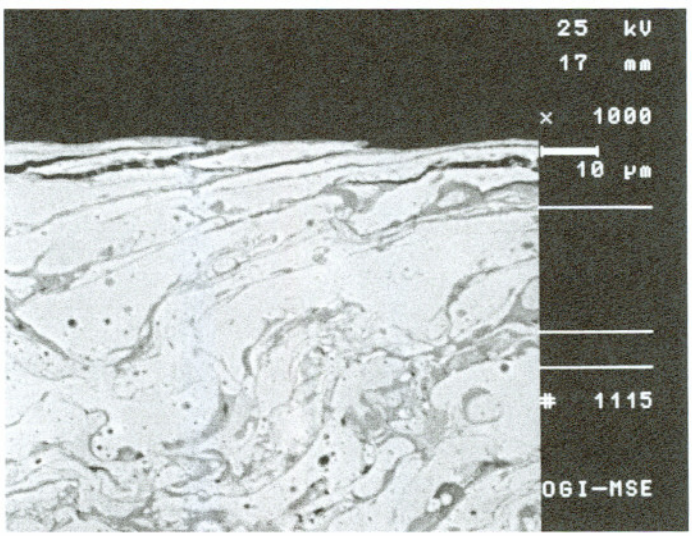

(b)

Figure 4.4.1.2. Wear surfaces of interrupted Amsler tests on 1080 steel/nylon rollers showing (a) little deformation at 4,000 revolutions and (b) increased deformation at 8,920 revolutions. 1000x, backscattered electron images.

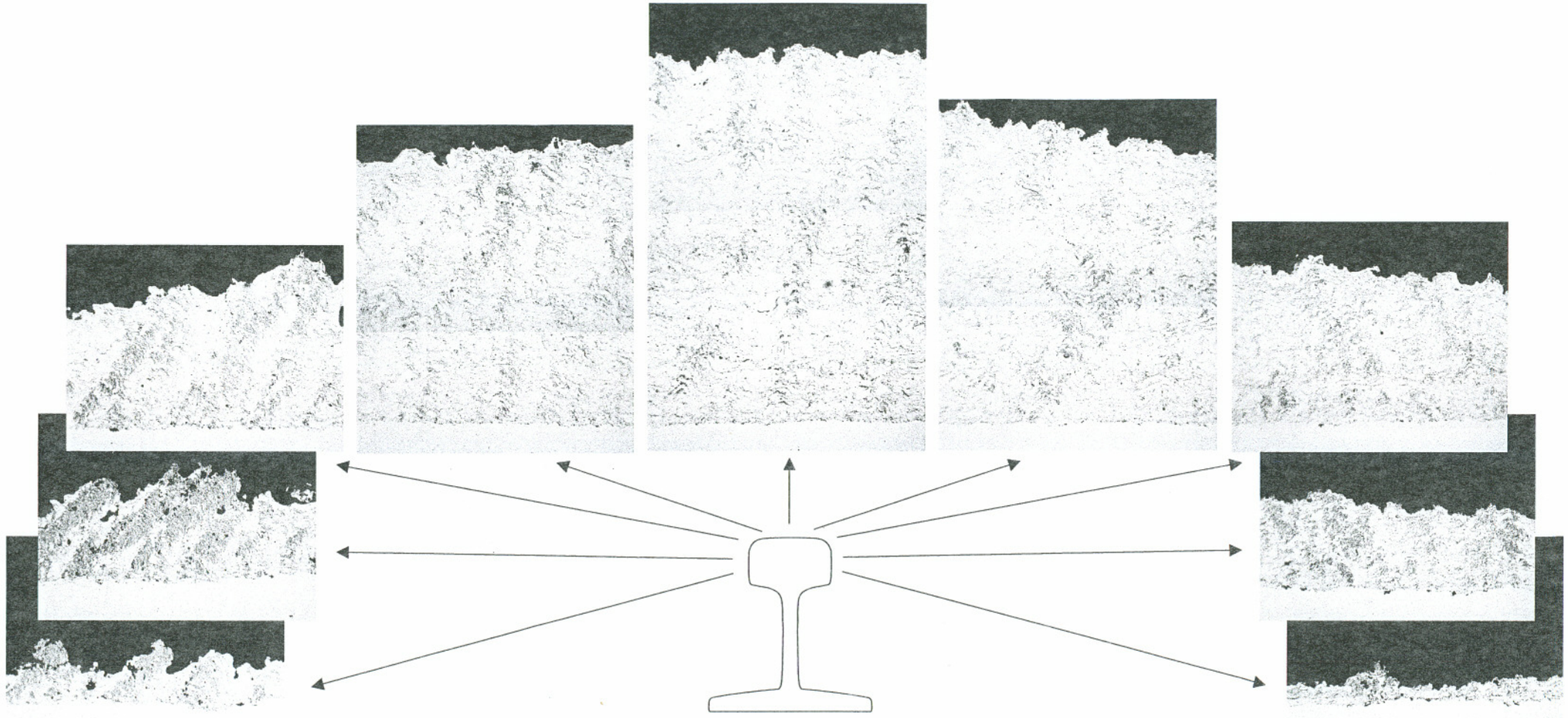

Figure 4.4.4.1. Microstructure at various locations on rail head for samples sprayed using re-optimized parameters. 100x, optical micrographs.

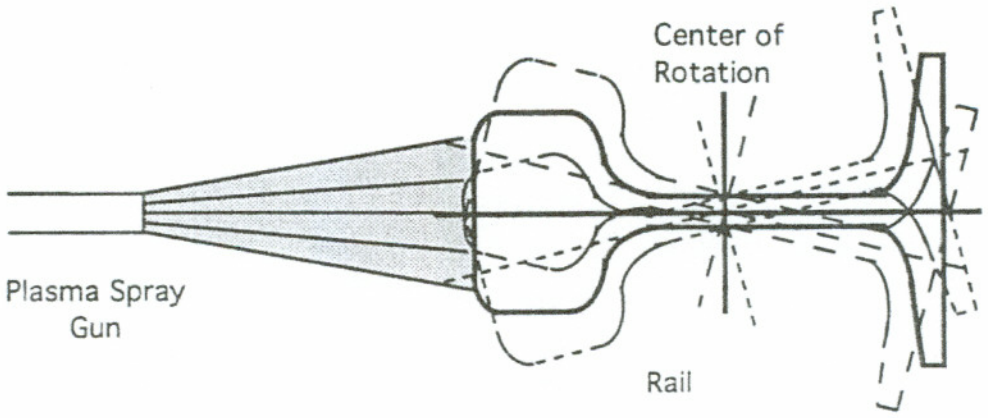

Figure 4.4.5.1. Schematic of rail during plasma spraying.

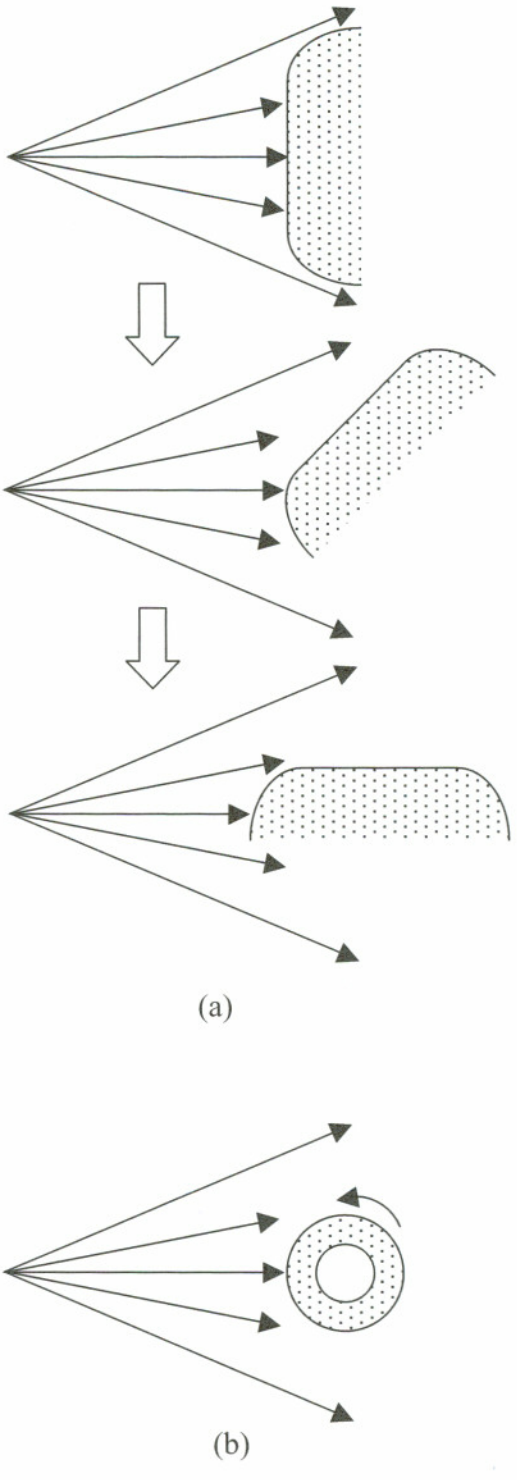

Figure 4.4.5.2. Schematic of (a) rail and (b) Amsler roller during plasma spraying.

References for Chapter 4

1. McMurchie, D., *Development of a 1080 Steel Plasma Sprayed Coating for Slide/Roll Conditions*, Ph.D. Thesis, Oregon Graduate Institute of Science and Technology, 1996.

2. Niebuhr, D. V., *Development of a Self-lubricating Plasma Sprayed Coating for Rolling/Sliding Wear*, Ph.D. Thesis, Oregon Graduate Institute of Science and Technology, 1997.

3. Danks, D., *Wear and Microstructure of Eutectoid Steels*, Ph.D. Thesis, Oregon Graduate Center, 1989.

4. Ramaswamy, D., *Wear Behavior of Bainitic Steels*, Ph.D. Thesis, Oregon Graduate Institute of Science and Technology, 1991.

5. Dikshit, V. A., *Rolling Contact Fatigue Behavior of Pearlitic Rail Steel*, Ph.D. Thesis, Oregon Graduate Institute of Science and Technology, 1992.

6. Bolton, P. J. and Clayton, P., Rolling-Sliding Wear in Rail and Tyre Steels. *Wear*, Vol. 93, 1984, pp. 145-165.

7. Scholl, M., Plasma Spraying with Wire Feedstock. *Proceedings of the 7th National Thermal Spray Conference, Boston, MA, June 1994*, pp. 491-496.

8. Sawley, K., Plasma Arc Coatings: Review of Progress and Options for Future. Communication to Dr. Milton Scholl of the Oregon Graduate Institute of Science and Technology, March 1997.

CHAPTER 5

CONCLUSIONS

1. Larger grit sizes and softer substrates produced a rougher surface as determined by the parameter R_a in surface profilometry tests.
2. The surface roughness was not sensitive to changes in impact angle.
3. While dwell time did not affect the parameter R_a, it did affect the cleanliness of the surface and increased contamination in the form of embedded grit and grit fines.
4. Tensile tests show that a clean surface provides better adhesion strength than an unclean surface.
5. Multiple feedstock and feedstock types complicate the optimization of plasma spraying parameters and obtaining consistently good coating properties.
6. It is difficult to characterize microstructures with multiple components unless there is optical contrast or significant atomic differences between them.
7. Comparing plasma sprayed coatings to monolithic materials, the coefficient of friction for the stainless steel plasma sprayed coatings was higher than for the solid stainless steel rollers (mated with wheel steel bottom rollers). The coefficient of friction for the 1080 steel plasma sprayed coatings was slightly lower than for the monolithic wheel/rail pairs.
8. During interrupted Amsler wear testing, the 1080 steel plasma sprayed coatings deformed leading to crack networks followed by spalling of the coatings and finally debonding.

9. Transfer of stainless steel from the top roller to the bottom roller increases the wear rate and coefficient of friction and decreases coating durability. Interrupting the transfer process by using fresh bottom rollers decreases the wear rate and the coefficient of friction.

10. In Amsler testing, the addition of nylon on top of stainless steel plasma sprayed coatings reduces the coefficient of friction and surface deformation and improves the durability of the coating.

11. For Amsler testing of stainless steel plasma sprayed coatings, the durability of the coatings is directly proportional to the coating thickness and inversely proportional to the slide/roll ratio and contact pressure. The life of the stainless steel plasma sprayed coating can be estimated by a single parameter, L, which combines the effects of the variables mentioned above.

12. The full scale test sample microstructures were of a poor quality and extremely heterogeneous. Although an attempt was made to re-optimize the spraying parameters to improve coating properties, the resulting coatings did not perform much better than the early test samples.

13. Optimization of the parameters for full scale test samples needs to consider the quality of the coating over the entire surface sprayed; not just a small portion on the top of the specimen.

14. Compared to the 1080 steel Amsler roller microstructures, the full scale test microstructures were of a much lower quality.

15. Full scale wear testing resulted in damage to the coatings including coating delamination, coating/substrate debonding, oxide and metal lamellae cracking, plastic flow at the surface, and the formation of wear particles.

16. Oxides act as crack paths in the coatings contributing to coating failure.

17. Contamination in the form of alumina particles from the grit blasting operation, was found at the coating/substrate interface in all the full scale test samples examined, and is most likely a contributing factor to the debonding failure of the coatings.
18. Uniform and effective surface preparation was difficult to obtain due to the size and geometry of the full scale test samples.
19. The size and geometry of the full scale samples and the spraying method made it difficult to optimize parameters and obtain a consistently good coating over the entire surface of the sample since a greater portion of the coating was built up by particles in the non-optimum region of the spray plume, than for Amsler rollers.
20. Variations in operator skill and technique caused differences in parameter optimization results and full scale sample plasma sprayed coating microstructures.
21. The addition of nylon on the steel plasma sprayed coatings for friction reduction on full scale samples led to slightly improved test durability.
22. Due to the variations in the tests, it is difficult to say whether having a thinner base coating in the 1080/nylon test had a beneficial impact on full scale coating durability.
23. The laboratory scale Amsler test does not appear to be a good indicator of the performance of the coating in the full scale tests. This is primarily because the microstructures vary when going from a small scale Amsler roller to a large scale rail sample.
24. It is difficult to make comparisons between the various full scale test samples due to the wide variations in the spray parameters, coating materials and thickness and test conditions.
25. Having the full scale tests run by a third party led to lack of control over the actual testing, data collection and result accuracy.

BIOGRAPHICAL NOTE

Heidi was born in Columbus, Ohio and raised in Seattle, Washington. She attended Highline Community College in Midway, Washington, and transferred to the University of Washington in Seattle, Washington. After completing her Bachelor of Science degree in Metallurgical Engineering she attended the Oregon Graduate Institute of Science and Technology in Beaverton, Oregon. She currently resides in Aloha, Oregon with four wonderful, rescued cats.